



Special Issue Reprint

Themed Issue in Honor of Prof. Maciej J. Nowak, for His Contributions to the Field of Photochemistry of Matrix-Isolated Species

Edited by
Rui Fausto and Robert Kołos

mdpi.com/journal/photochem



**Themed Issue in Honor of Prof. Maciej
J. Nowak, for His Contributions to the
Field of Photochemistry of
Matrix-Isolated Species**

Themed Issue in Honor of Prof. Maciej J. Nowak, for His Contributions to the Field of Photochemistry of Matrix-Isolated Species

Guest Editors

Rui Fausto

Robert Kołos



Basel • Beijing • Wuhan • Barcelona • Belgrade • Novi Sad • Cluj • Manchester

Guest Editors

Rui Fausto
Department of Chemistry
University of Coimbra
Coimbra
Portugal

Robert Kołos
Laboratory Astrochemistry
Group
Institute of Physical
Chemistry, PAS
Warsaw
Poland

Editorial Office

MDPI AG
St. Alban-Anlage 66
4052 Basel, Switzerland

This is a reprint of the Special Issue, published open access by the journal *Photochem* (ISSN 2673-7256), freely accessible at: www.mdpi.com/journal/photochem/special_issues/Matrix_Isolated.

For citation purposes, cite each article independently as indicated on the article page online and as indicated below:

Lastname, A.A.; Lastname, B.B. Article Title. <i>Journal Name</i> Year , <i>Volume Number</i> , Page Range.
--

ISBN 978-3-7258-1210-3 (Hbk)

ISBN 978-3-7258-1209-7 (PDF)

<https://doi.org/10.3390/books978-3-7258-1209-7>

© 2024 by the authors. Articles in this book are Open Access and distributed under the Creative Commons Attribution (CC BY) license. The book as a whole is distributed by MDPI under the terms and conditions of the Creative Commons Attribution-NonCommercial-NoDerivs (CC BY-NC-ND) license (<https://creativecommons.org/licenses/by-nc-nd/4.0/>).

Contents

About the Editors	vii
Preface	ix
Fumiyuki Ito	
Observation of Light-Induced Reactions of Olefin–Ozone Complexes in Cryogenic Matrices Using Fourier-Transform Infrared Spectroscopy Reprinted from: <i>Photochem</i> 2022 , <i>2</i> , 150–164, https://doi.org/10.3390/photochem2010012	1
İsa Sıdır, Yadigar Gülseven Sıdır, Sándor Góbi, Halil Berber and Rui Fausto	
UV-Induced Benzyloxy Rotamerization in an <i>Ortho</i> OH-Substituted Aryl Schiff Base Reprinted from: <i>Photochem</i> 2022 , <i>2</i> , 376–389, https://doi.org/10.3390/photochem2020026	16
Igor Reva, Hanna Rostkowska and Leszek Lapinski	
Phototransformations of 2,3-Diamino-2-Butenedinitrile (DAMN) Monomers Isolated in Low-Temperature Argon Matrix Reprinted from: <i>Photochem</i> 2022 , <i>2</i> , 448–462, https://doi.org/10.3390/photochem2020031	30
Sándor Góbi, Gopi Ragupathy, Gábor Bazsó and György Tarczay	
Vibrational-Excitation-Induced and Spontaneous Conformational Changes in Solid <i>Para</i> -H ₂ —Diminished Matrix Effects Reprinted from: <i>Photochem</i> 2022 , <i>2</i> , 563–579, https://doi.org/10.3390/photochem2030039	45
Yoriko Wada, Hiroshi Akagi, Takayuki Kumada, Ryuji Itakura and Tomonari Wakabayashi	
Mass-Resolved Momentum Imaging of Three Dichloroethylene Isomers by Femtosecond Laser-Induced Coulomb Explosion Reprinted from: <i>Photochem</i> 2022 , <i>2</i> , 798–809, https://doi.org/10.3390/photochem2030051	62
Urszula Szczepaniak, Robert Kołos, Jean-Claude Guillemin and Claudine Crépin	
Phosphorescence of C ₅ N [−] in Rare Gas Solids Reprinted from: <i>Photochem</i> 2022 , <i>2</i> , 263–271, https://doi.org/10.3390/photochem2020019	74
Jacek Dobkowski, Igor V. Sazanovich, Aleksander Gorski and Jacek Waluk	
Energy Relaxation of Porphycene in Atomic and Molecular Cryogenic Matrices Reprinted from: <i>Photochem</i> 2022 , <i>2</i> , 299–307, https://doi.org/10.3390/photochem2020021	83
Heloïse Leboucher, Joëlle Mascetti, Christian Aupetit, Jennifer A. Noble and Aude Simon	
Water Clusters in Interaction with Corannulene in a Rare Gas Matrix: Structures, Stability and IR Spectra Reprinted from: <i>Photochem</i> 2022 , <i>2</i> , 237–262, https://doi.org/10.3390/photochem2020018	92
Tomonari Wakabayashi, Urszula Szczepaniak, Kaito Tanaka, Satomi Saito, Keisuke Fukumoto, Riku Ohnishi, et al.	
Phosphorescence of Hydrogen-Capped Linear Polyynes C ₈ H ₂ , C ₁₀ H ₂ and C ₁₂ H ₂ in Solid Hexane Matrices at 20 K Reprinted from: <i>Photochem</i> 2022 , <i>2</i> , 181–201, https://doi.org/10.3390/photochem2010014	118
Md Al Mamunur Rashid, Mofizur Rahman, ASM Obaidullah Mahmud, Ali Shazzad Mohammad Morshed, Md Masudul Haque and Md Mobarak Hossain	
UV-Vis Spectrophotometer as an Alternative Technique for the Determination of Hydroquinone in Vinyl Acetate Monomer Reprinted from: <i>Photochem</i> 2022 , <i>2</i> , 435–447, https://doi.org/10.3390/photochem2020030	139

About the Editors

Rui Fausto

Professor Rui Fausto graduated, received his PhD and habilitated from the University of Coimbra, and presently is a visiting Professor at the Istanbul Kultur University (Turkey), and heads the research group on Computational Chemistry, Spectroscopy and Thermodynamics of the Coimbra Chemistry Centre, Institute of Molecular Sciences, at the Department of Chemistry, University of Coimbra. The group uses low-temperature matrix isolation coupled with infrared spectroscopy, as well as micro-Raman spectroscopy and computational approaches to address topics that include the study of vibrationally induced and quantum mechanical tunnelling-driven organic chemistry reactions, conformationally dependent photochemistry, and the structure and reactivity of short-living intermediates, among others.

Robert Kołos

Professor Robert Kołos graduated from the University of Warsaw, received his PhD and habilitated at the Institute of Physical Chemistry of the Polish Academy of Sciences, and presently heads the Laboratory Astrochemistry group at IPC PAS. The group mainly uses low-temperature matrix isolation coupled to vibrational and electronic spectroscopy. The scientific topics include, but are not limited to, the photochemistry and photophysics of small nitriles and related organonpictogen molecules with recognized or potential astrochemical importance.

Preface

This Special Issue of *Photochem* is dedicated to Professor Maciej J. Nowak for his contributions to our understanding of the photochemistry of matrix-isolated species. The Special Issue comprises 10 articles that span a broad range of interests and issues, encompassing both experimental and theoretical investigations.

Professor Maciej J. Nowak was born and educated in Warsaw (Poland). He completed his MSc degree at the University of Warsaw (Department of Physics) in 1971 and started his work there at the Department of Physics, with the Atomic and Molecular Optics Research Group of the Institute of Experimental Physics, where he worked on the study of molecular interactions (mainly H-bonding) in solid phase and liquids. He obtained his PhD in Physics (1979) under the supervision of Prof. Krystyna Szczepaniak at the Department of Biophysics of the same university. During his doctoral work and career at the Institute of Physics of the Polish Academy of Sciences (where he is still active), Prof. Nowak has revealed the fundamental structural details and reactivity patterns of nucleic acid bases, initially in the gas phase, and most of the time using the matrix isolation method as the main research technique, together with infrared spectroscopy. Prof. Nowak was one of the European pioneers of matrix isolation spectroscopy applied to observe photochemical reactions, particularly those involving nucleic acid bases and related compounds.

He has been awarded an Alexander von Humboldt fellowship that allowed him to spend two years (1981–1982) at the Department of Physical Chemistry of the Philipps-Universität (Marburg, Germany) in the research group of Prof. Werner A.P. Luck. Subsequently, he established a modern laboratory for matrix isolation studies at the Institute of Physics PAS in Warsaw, which he has led since 1986. In the research that followed, Prof. Nowak focused on the determination of the structure of the most stable forms of the nucleic acid bases (uracil, thymine, cytosine, adenine) isolated in low-temperature matrices, and he published some of the most complete, seminal papers on these chemical systems. In 2010, he obtained the title of a Professor in Physics and the full professorship at the Institute of Physics PAS. In 2019, he retired but continued working part-time at the institute.

Prof. Nowak has published over 125 articles in the most prestigious scientific journals, reporting the results of his research. In one of his first articles (together with the group of Prof. William B. Person), he demonstrated, for the first time, the successful application of *ab initio* (HF) calculations to IR spectroscopy of heterocyclic molecules. Today, quantum chemical predictions of vibrational spectra are commonly applied in experimental research. Later on, as a result of a collaboration with Profs. Ludwik Adamowicz and Andrzej Leś, Prof. Maciej Nowak published a long series of articles where enthalpy differences between the tautomers of nucleic acid bases and related compounds (some species being the products of photoexcitation of more stable precursors isolated in cryogenic matrices) were obtained. Additionally, in collaboration with Prof. Andrzej L. Sobolewski, a specialist in quantum chemical calculations of the excited electronic states, he presented new perspectives of photoreactivity in different chemical systems, including his alma mater substances, i.e., nucleic acid bases. During the last 20 years, a long-lasting and fruitful collaboration has been established between the groups of Prof. Nowak and Prof. Rui Fausto (University of Coimbra, Portugal), with the particular involvement of Drs. Leszek Lapinski (from Warsaw) and Igor Reva (from Coimbra). Specifically, the most important results obtained from this collaboration were the identification of cytosine isomers and interconversion between cytosine isomers induced by UV or NIR irradiation, the investigation of the effects of NIR-selective excitation of overtone vibrations of isolated flexible molecules leading to conformational changes, and the direct observation of different chemical processes taking place

via the quantum mechanical tunnelling effect. More recently, Prof. Nowak has also been interested in investigations of the influence of solid hydrogen matrix environments in the course of H atom transfer oxo \rightarrow hydroxy and thion \rightarrow thiol phototautomeric processes occurring (or not occurring) in oxo and thio compounds isolated in Ar and H₂ matrices.

Although the home institute of Prof. Maciej Nowak is not dedicated to education, he has been involved in teaching university students and has been engaged in the education of PhD students from his own laboratory and the doctoral school. In his own words: "*my passion is the experiment*". Indeed, during his whole career, he was actively engaged in constructing experimental equipment, preparing experiments and carrying them out, usually with the support and assistance of Drs. Leszek Lapinski and Hanna Rostkowska, his long-standing co-workers (and good friends) at the Institute of Physics PAS.

We must thank all our colleagues who contributed to this Special Issue celebrating the scientific career of Prof. Nowak and his achievements in photochemistry and photophysics of matrix-isolated species. Additionally, we would like to express our appreciation to the diligent reviewers whose meticulous evaluations have elevated the scientific rigor and quality of the submitted articles.

Rui Fausto and Robert Kołos

Guest Editors

Article

Observation of Light-Induced Reactions of Olefin–Ozone Complexes in Cryogenic Matrices Using Fourier-Transform Infrared Spectroscopy

Fumiyuki Ito

National Institute of Advanced Industrial Science and Technology (AIST), Tsukuba 305-8569, Japan; f-ito@aist.go.jp

Abstract: Each olefin (ethylene, trans-1,3-butadiene, isoprene, dimethyl butadiene (DMB)) and ozone molecules were codeposited on a CsI window at cryogenic temperature, and the products of photolysis with ultraviolet–visible light were observed using Fourier-transform infrared spectroscopy. The products of the C₂H₄–O₃ system could be assigned to glyoxal (CHO–CHO), ethylene oxide (c-C₂H₄O), CO, and CO₂. The formation of CHO–CHO and c-C₂H₄ and the absence of H₂CO and HCOOH indicated that the main reaction channels did not involve C–C bond breaking. Based on this simple scheme, the photoproducts of different olefin–O₃ systems were assigned, and the vibrational features predicted by density functional theory calculations were compared with the observed spectra. Regarding butadiene, spectral matches between the observations and calculations seemed reasonable, while assignments for isoprene ambiguities of and DMB remain, mainly because of the limited availability of authentic sample spectra.

Keywords: matrix-isolation; infrared spectroscopy; olefin; ozone; charge–transfer complex

Citation: Ito, F. Observation of Light-Induced Reactions of Olefin–Ozone Complexes in Cryogenic Matrices Using Fourier-Transform Infrared Spectroscopy. *Photochem* **2022**, *2*, 150–164. <https://doi.org/10.3390/photochem2010012>

Received: 20 January 2022

Accepted: 22 February 2022

Published: 24 February 2022

Publisher's Note: MDPI stays neutral with regard to jurisdictional claims in published maps and institutional affiliations.



Copyright: © 2022 by the author. Licensee MDPI, Basel, Switzerland. This article is an open access article distributed under the terms and conditions of the Creative Commons Attribution (CC BY) license (<https://creativecommons.org/licenses/by/4.0/>).

1. Introduction

The products of oxidation of volatile organic compounds (VOCs) contribute to secondary organic aerosols (SOAs) in the atmosphere and influence climate and local air quality [1]. In this respect, unsaturated VOCs such as ethylene (C₂H₄) [2] and isoprene (C₅H₈) [3], have been intensively investigated. The key reactants for the oxidation processes are ozone (O₃), hydroxyl (OH), and nitrate (NO₃) radicals. Ozone forms charge–transfer (CT) complexes with various organic molecules, and exhibits strong CT bands in the ultraviolet–visible (UV–VIS) region [4–7]. The oxidation processes involve reactions in both light and dark conditions; therefore, it is important to understand how light-induced oxidation proceeds in the olefin–ozone system.

The purpose of this study is to investigate the light-induced reactions of olefin–O₃ systems spectroscopically in a cryogenic noble gas matrix to minimize the effect of thermal excitation of reactants. Numerous investigations have been conducted on reactions of olefin–O₃ systems experimentally [8–23] and theoretically [24–26]. Many of the gas phase studies have been focused on ozonolysis in dark conditions, and have been done at moderate temperatures [8–13]. Quite recently, these reactions have been under further scrutiny at lower temperature by using new experimental techniques [14,15]. In matrices, on the other hand, studies on low temperature reactions have been done for decades [16–23]. In situ observations of light-induced reactions of olefin–O₃ systems at cryogenic temperature are, to the best of our knowledge, not so abundant [23]. Ault and coworkers have performed systematic studies on these systems [24–27], and we will refer to them in comparison with this study.

In the present study, two samples, i.e., olefin/Ar (olefin = ethylene (C₂H₄), 1,3-butadiene (C₄H₆), isoprene (C₅H₈), dimethyl butadiene (C₆H₁₀)) and O₃/Ar premixed samples, were co-deposited on a cold CsI window via separate pulse valves and irradiated

by several light sources at various wavelengths. The observed vibrational features of the photoproducts were compared with existing spectral data and the simulated features obtained using quantum chemical calculations, as performed previously [28,29].

2. Materials and Methods

2.1. Experiment

Gaseous ethylene and butadiene were purchased from GL Sciences and TCI, respectively, and used without further purification. Isoprene and dimethyl butadiene (WAKO) were degassed in freeze–pump–thaw cycles before sample preparation. Ozone was generated using a homemade ozonizer made of O_2 gas, trapped in a liquid N_2 -cooled silica gel, and subjected to vacuum distillation to remove residual O_2 . Each gaseous sample was diluted with Ar at various ratios and stored in a shielded glass vessel. Olefin/Ar and O_3 /Ar samples were codeposited onto a cold CsI window through separate pulse valves at 9–30 K, with a repetition rate of 10 Hz and pulse width of 450 μs . Matrix-isolated species were irradiated by several light sources, including continuous wave (CW) diode lasers at 405, 670, and 800 nm, pulsed nanosecond lasers at 532 and 780 nm (LOTIS LS-2137/2 and LT-2211A), and a CW Xe discharge lamp (ENERGETIQ EQ-99FC) with sets of optical filters. The typical exposure time was 10–30 min. Infrared (IR) spectra before and after photolysis were recorded with a JASCO FT/IR-6100 spectrometer, and the results were used to obtain the difference spectra for each system. Spectra were recorded in the region of 650–4000 cm^{-1} with a resolution of 0.5 cm^{-1} . A schematic of the experimental setup is presented in Figure 1. Details of the instrumentation can be found in our previous articles [28,29]. The obtained difference spectra for C_2H_4 , C_4H_6 , C_5H_8 , and C_6H_{10} are displayed in Figures 2–5, respectively. Spectral changes upon isotopic substitution ($^{16}O \rightarrow ^{18}O$) are listed for the three systems in Figure 6. Ozone ($^{18}O_3$) was prepared using the same procedure as used for the preparation of normal species from $^{18}O_2$ (Matheson).

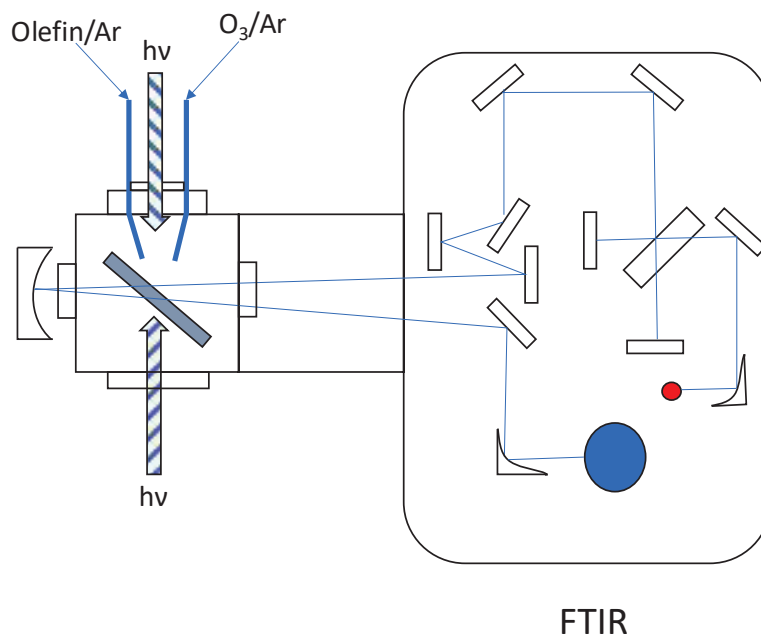


Figure 1. A schematic of the experimental setup for the olefin–ozone photolysis. Two pulse valves were used to deposit olefin/Ar and O_3 /Ar samples separately. The photolysis beam was introduced from two optical ports, via optical fiber (for CW light source) or transfer optics (pulsed laser).

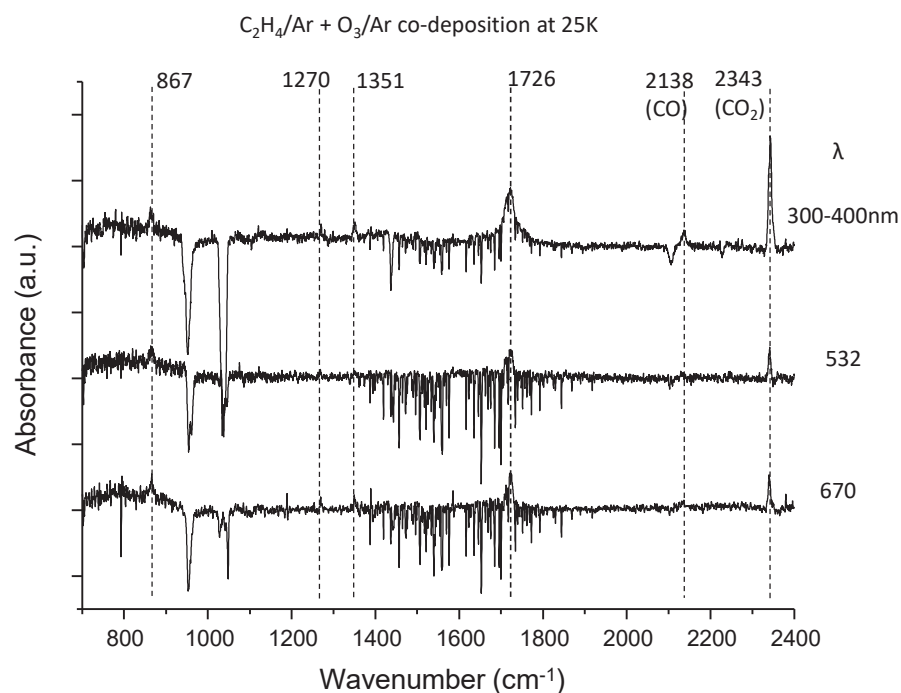


Figure 2. The difference spectra for the ethylene–ozone system upon irradiation at three wavelengths in the fingerprint region. The near-UV light was obtained from a CW Xe discharge lamp through an optical filter. The 532 nm light was taken from the second-harmonic wave of nano-second pulse Nd:YAG laser, while the 670 nm light was obtained from the CW diode laser.

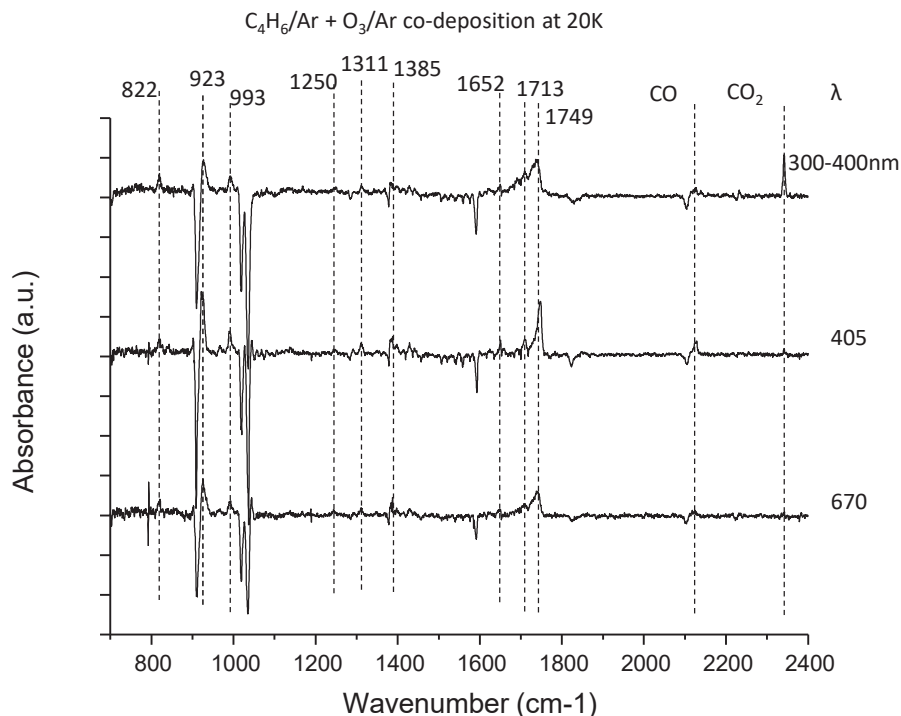


Figure 3. The difference spectra for the 1,3-butadiene–ozone system upon irradiation at three wavelengths in the fingerprint region. The near-UV light was obtained from the CW Xe discharge lamp through the optical filter, while others are supplied by CW diode laser.

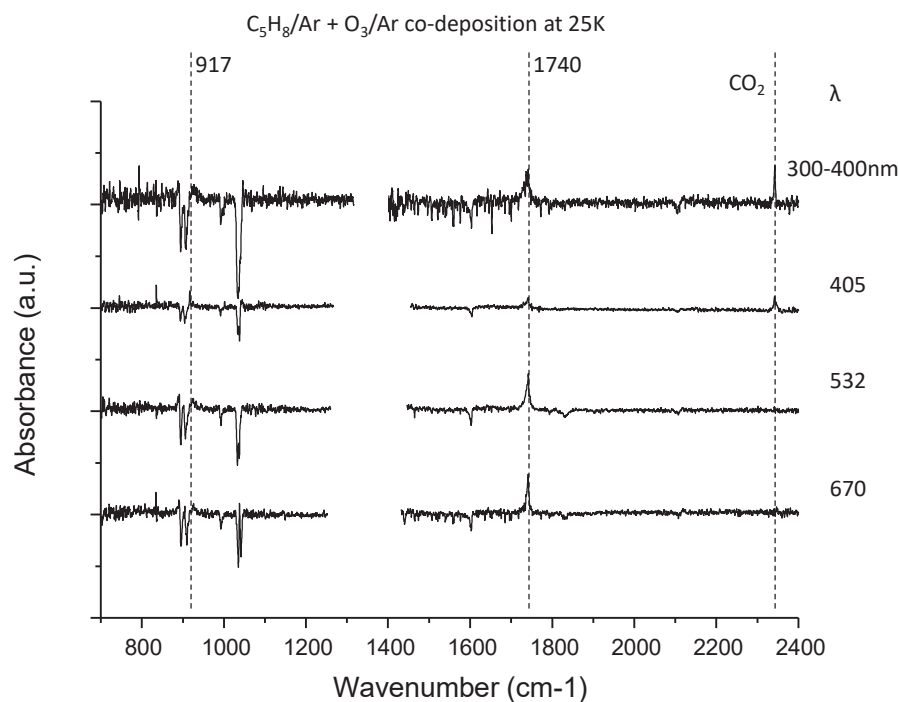


Figure 4. The difference spectra for the isoprene–ozone system upon irradiation at four wavelengths in the fingerprint region. The near-UV light was obtained from the CW Xe discharge lamp through the optical filter. The 532 nm light was taken from the second-harmonic wave of nano-second pulse Nd: YAG laser, while others were supplied from the CW diode laser. The region with light intensity degradation due to optical fringes and atmospheric water was trimmed in each trace.

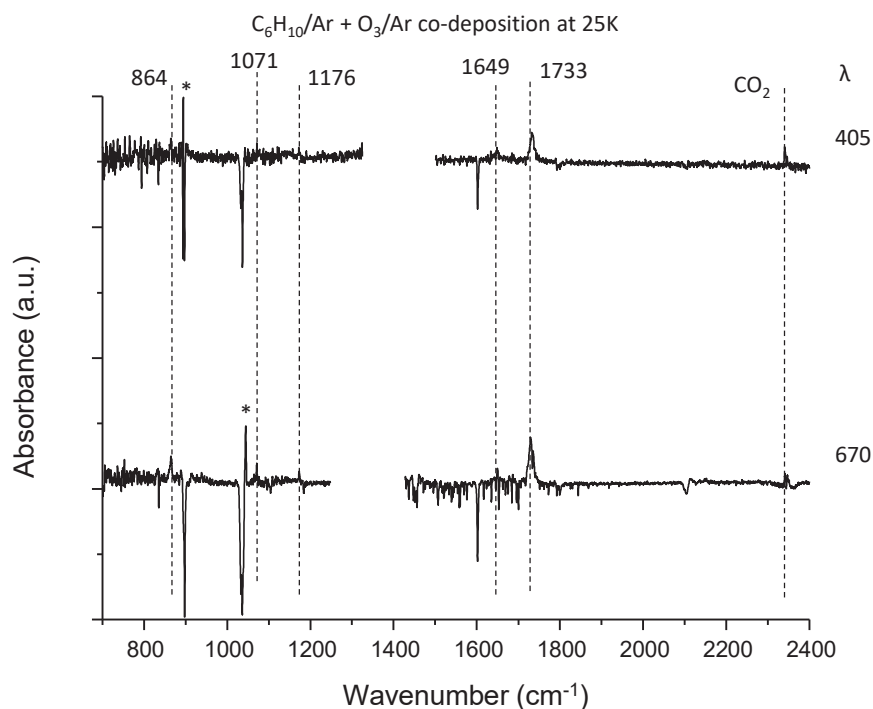


Figure 5. The difference spectra for the dimethylbutadiene–ozone system upon irradiation in the fingerprint region. Two CW diode laser sources were used to photolyze this system at 405 and 670 nm. Peaks with asterisks (*) were not reproducible. The region with light intensity degradation due to optical fringes and atmospheric water was trimmed in each trace.

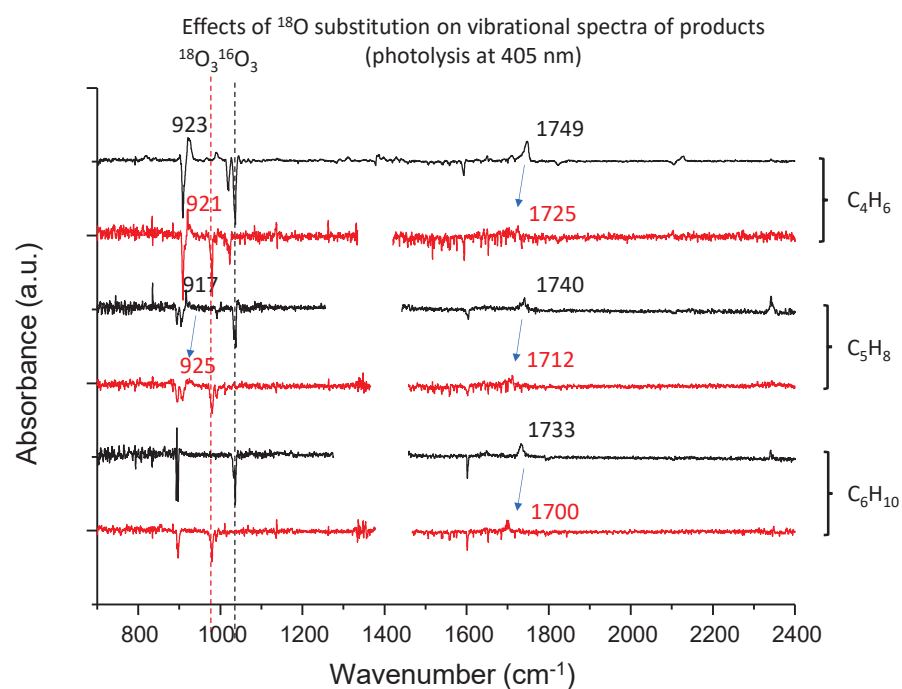


Figure 6. The difference spectra for the three systems with $^{16}\text{O}_3$ (black trace) and $^{18}\text{O}_3$ (red trace) being compared with each other. The region with light intensity degradation due to optical fringes and atmospheric water was trimmed in each trace.

2.2. Calculation

For the assignment of photoproducts, density functional theory (DFT) calculations were carried out for candidate molecules. Structure optimization and vibrational calculation for each stable species were performed at the dcp-b3lyp/6-31 + G (2d,2p) level [30]. Anharmonic vibrational frequencies for all fundamental bands of each species were obtained with vibrational second-order perturbation treatment [31,32] for direct comparison with the observed vibrational peak position without frequency scaling. All calculations were completed with Gaussian09 (Rev. 02) [33].

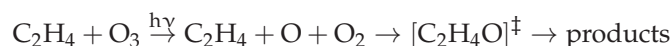
3. Results

3.1. $\text{C}_2\text{H}_4\text{-O}_3$ System

Figure 2 shows the difference spectra for the ethylene–ozone system upon irradiation; the photoproducts produce positive peaks, whereas reactants show depletion. Below 15 K, the difference spectra showed no decrease in reactants nor the emergence of photoproducts. This indicated that thermal diffusion after deposition was crucial to achieving close contact between C_2H_4 and O_3 in the matrix. Four peaks could be ascribed to the photoproducts, and two of them (at 2138 and 2343 cm^{-1}) were readily assigned to CO and CO_2 , respectively. While the peaks at 867 cm^{-1} and 1270 cm^{-1} were assigned to the ν_5 and ν_3 bands of ethylene oxide ($\text{c-C}_2\text{H}_4$) [34], respectively, the assignment of the most intense band at 1726 cm^{-1} was not straightforward, because it was not due to the aldehydes (H_2CO [35] and CH_3CHO [36]) or the carboxylic acids (HCOOH [37] and CH_3COOH [38]) as expected. Finally, we assigned this peak to trans-glyoxal (CHO-CHO), in conformation with previous matrix data [39]. The remaining peak at 1351 cm^{-1} could not be assigned to a known species. Although it was in good agreement with ν_7 of CH_3CHO , a ν_8 band with comparable intensity could not be located. Therefore, it was left unassigned. From existing data on the IR band intensities of these molecules [40–42], it was found that the depletion of C_2H_4 and O_3 obeyed $\sim 1:1$ stoichiometry. The mass balance of C atoms in these photoreactions could be estimated to be more than 43% in total, and more than 70% for UV-photolysis. Therefore,

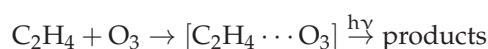
it is reasonable to conclude that the photoreactions of the $C_2H_4-O_3$ system mainly proceed without C–C bond breaking.

It is known that the reaction of C_2H_4 and an oxygen atom (3P) in the gas phase at room temperature produces mainly CH_3CHO and fragmented products due to the high excess energy of the C_2H_4O adduct [43]. Conversely, in liquid N_2 , the addition reaction leads to the simultaneous formation of $c-C_2H_4O$ and CH_3CHO with a comparable branching ratio, owing to the rapid energy release of the adduct into the cold media [44]. The absence of CH_3CHO in the photoproducts in the Ar matrix suggests that the photoreaction of the $C_2H_4 + O_3$ system is not stepwise as follows:



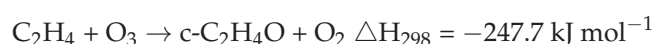
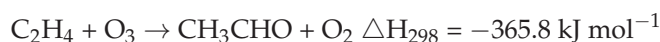
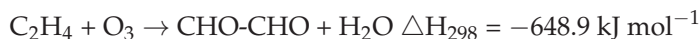
where $[C_2H_4O]^\ddagger$ stands for a transition state.

It seems more reasonable to assume the following concerted reaction instead:



where $[C_2H_4 \cdots O_3]$ represents a CT complex. Contrarily, the decrease in CO and CO_2 during photolysis at longer wavelengths may indicate that they originate from the UV dissociation of photoproducts (mainly CHO–CHO).

Production of CHO–CHO from this system is reasonable in view of the following energetics:



Understanding the reasons behind why CH_3CHO was not observed in the photoproducts of this system is difficult. Theoretically, the isomerization of $c-C_2H_4O$ to CH_3CHO and vice versa is hampered by the high activation energy barriers [45]; therefore, we can safely state that CH_3CHO is not a primary product in the photolysis of the $C_2H_4-O_3$ complex at cryogenic temperatures. In the dehydration reaction, glyoxal and H_2O molecules are produced simultaneously. The apparent absence of H_2O in the observed spectra is due to a compound effect of optical fringes and the ineffective removal of atmospheric water vapor, even with a purge system by dry N_2 flow. Since it was practically impossible to assign photoproducts in this region for larger olefins, the corresponding part was trimmed in Figures 4–7; see each figure caption.

The ozonolysis of C_2H_4 (dark reaction) initiated at an elevated temperature, with an energy threshold of $5.2 \text{ kCal mol}^{-1}$ [46]. Thus, this study shows the initial stage of photoreactions followed by complicated chains of the oxidation processes, leading to secondary organic aerosol (SOA) formation at ambient temperature.

Therefore, it is assumed that the primary photolysis of olefin– O_3 systems occurs in the following ways:



and



as observed for the $C_2H_4-O_3$ system. The primary products predicted from these two schemes for each olefin are shown in Figure 7. Regarding the dehydration products from $C_5H_8-O_3$ and $C_6H_{10}-O_3$ systems, it was difficult to derive glyoxal-like molecules by removing one O_2 and two H_2 atoms symmetrically from the Criegee intermediates (see the bottom trace of Figure 7). Thereafter, other types of molecules, including an oxirane skeleton and a formyl group, were assumed. The name of each molecule was obtained from PubChem via the Add-ons of the ACD/ChemSketch software. Simulated spectra for the

predicted products were obtained from anharmonic vibrational calculations, as described in Section 2.2, and compared with the experimental spectra in Figures 8–10.

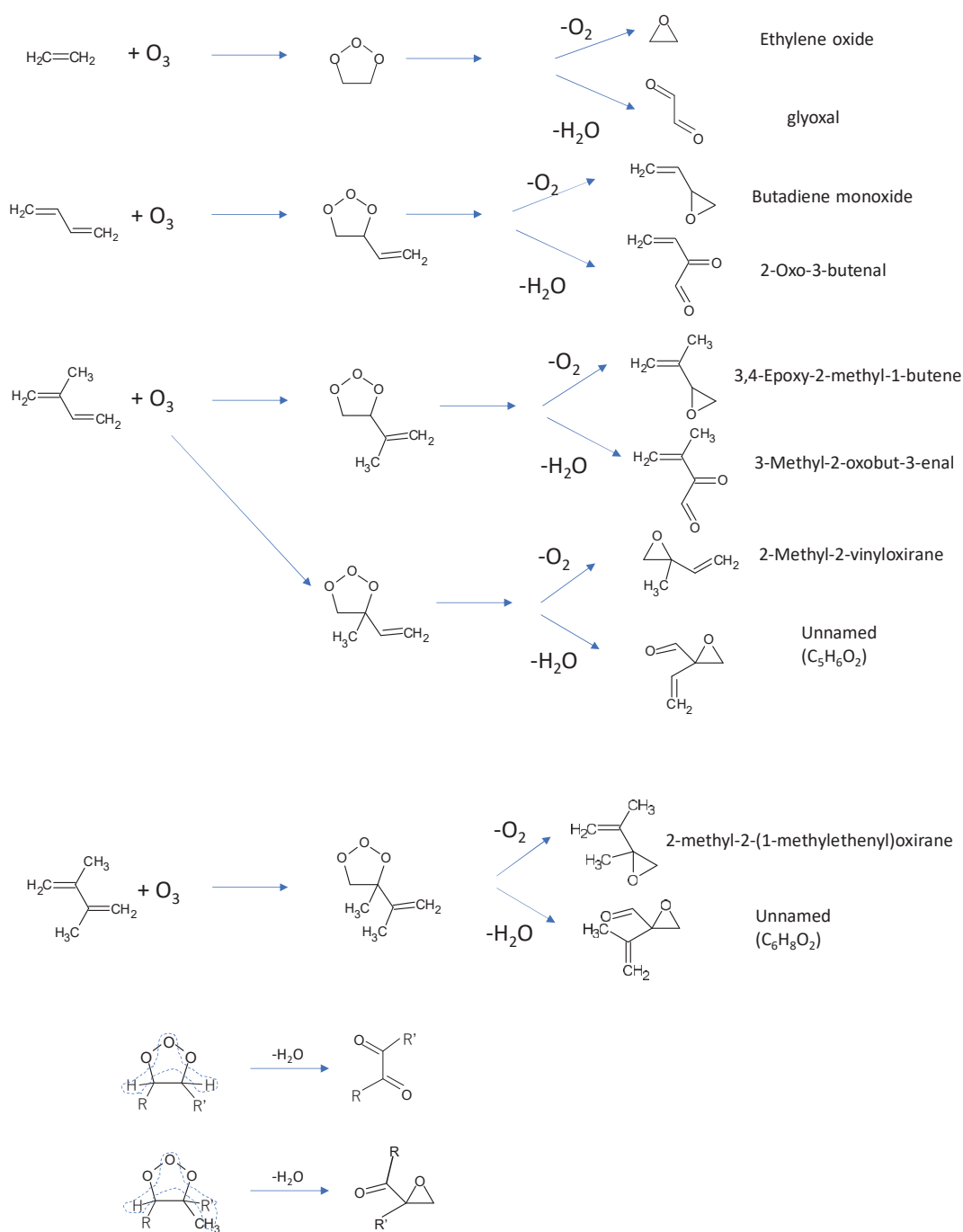


Figure 7. Plausible photoproducts for the olefin- O_3 systems predicted from two types of reaction paths for the $C_2H_4-O_3$ system.

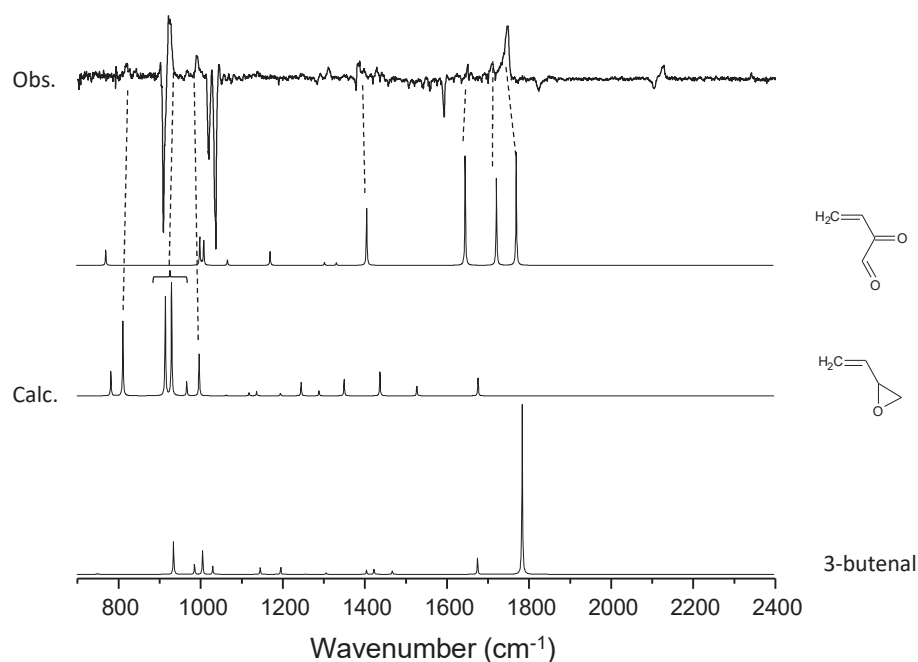


Figure 8. A comparison of the experimental spectra with simulated spectra for the candidate molecules for the $\text{C}_4\text{H}_6\text{-O}_3$ system.

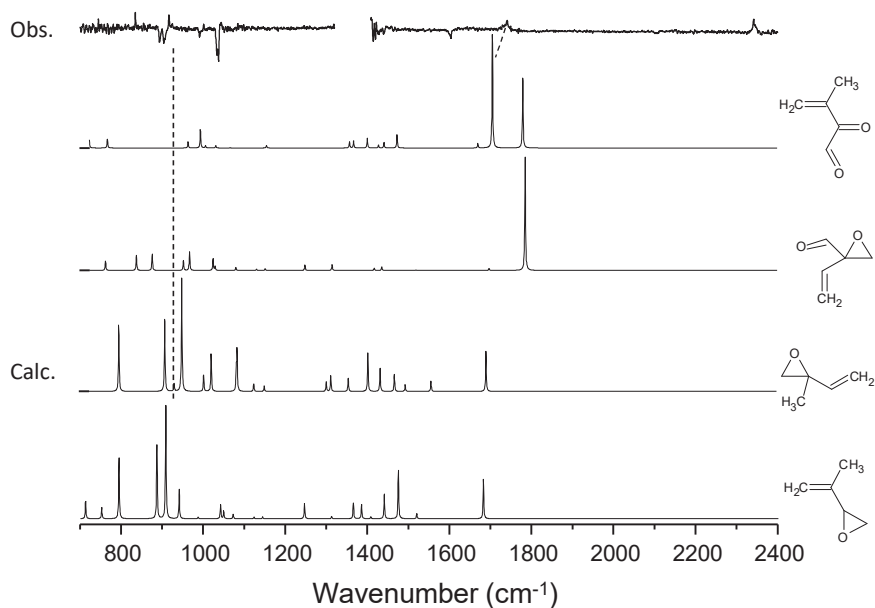


Figure 9. A comparison of the experimental spectra with simulated spectra for the candidate molecules for the $\text{C}_5\text{H}_8\text{-O}_3$ system.

3.2. $\text{C}_4\text{H}_6\text{-O}_3$ System

Figure 3 shows the difference spectra of the 1,3-butadiene–ozone system upon irradiation similar to that of the $\text{C}_2\text{H}_4\text{-O}_3$ system. In addition to the peaks for CO and CO_2 , four vibrational peaks were observed as the photoproducts. Notably, the peak at 1749 cm^{-1} was broad and degraded at longer wavelengths. As mentioned above, the production of CO and CO_2 is suppressed during photolysis at longer wavelengths. The observed peaks reproduced the result of Ault [27]. Based on the reaction schemes in Figure 7, the following were assigned to the vibrational peaks of the photoproducts:

$$822, 923, 993\text{ cm}^{-1}: \text{butadiene monoxide}$$

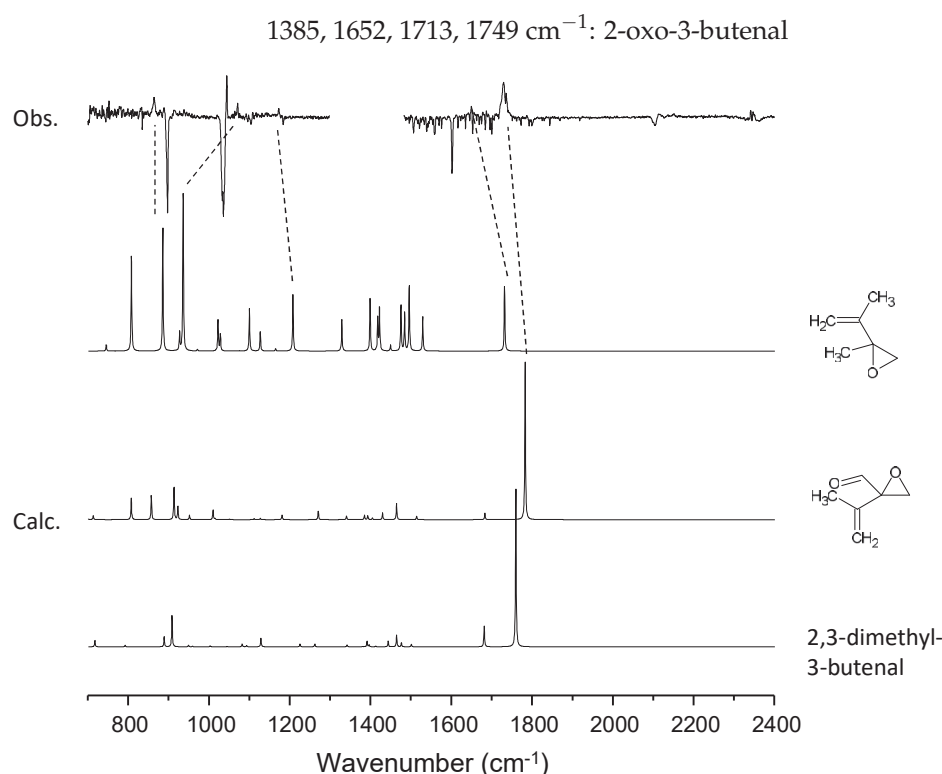


Figure 10. A comparison of the experimental spectra with simulated spectra for the candidate molecules for the $\text{C}_6\text{H}_{10}\text{-O}_3$ system.

The gas-phase spectrum for butadiene monoxide in the National Institute of Standards and Technology (NIST) database conformed to the present matrix-isolation peaks. The peaks assigned to butadiene monoxide also conformed to those observed in the Ar matrix produced from visible laser photolysis of the $\text{C}_4\text{H}_6\text{-NO}_2$ system [47]. Conversely, for the 2-oxo-3-butenal, no experimental spectrum is available, so direct comparison was not possible. Instead, the anharmonic vibrational calculation showed a good match with the observed peak positions (Figure 8). Ault assigned the peaks at 1385, 1652, 1749 cm^{-1} to 3-butenal and the peak at 1713 cm^{-1} to 2-butenal. Tanaka et al. reported a vibrational peak of 3-butenal at 1735 cm^{-1} [47], and this position is not consistent with the assignment of ref. [27]. The spectral matches between observation and calculation in Figure 8 showed better agreement for 2-oxo-3-butenal, and it would be more conclusive to assign these peaks to the glyoxal-like 2-oxo-3-butenal. The isotopic shift ($^{16}\text{O} \rightarrow ^{18}\text{O}$) of this band is 24 cm^{-1} , which is comparable to the calculated anharmonic wavenumber shift for 2-oxo-3-butenal (36 cm^{-1}). The two peaks at 1250 and 1311 cm^{-1} could not be assigned to these two molecules and remain unidentified. Besides, we cannot rule out the possibility that peaks of other photoproducts overlap with the 1749 cm^{-1} peak, in view of the broad and strong spectral feature.

3.3. $\text{C}_5\text{H}_8\text{-O}_3$ System

Figure 4 shows the difference spectra for the isoprene–ozone system upon irradiation. Due to its limited sensitivity, only two peaks at 917 and 1740 cm^{-1} were observed in addition to the peak for CO_2 . In contrast, the inequivalence of the two double bonds in isoprene provides two possible isoprene–ozone complexes, and thus, four photoproducts are predicted (see Figure 7). We carried out DFT calculations at the B3LYP/aug-cc-pVTZ level for the CT complexes, and found that both CT complexes are comparably stable (energy difference < 50 cm^{-1}). It is thus reasonable to assume that they coexist. Among these four candidate molecules, the spectral database contained the spectra for only 2-methyl-2-vinyloxirane in the form of transmission and ATR spectra for liquid films [48].

The experimental spectra showed a strong peak at 890 cm^{-1} that does not conform to the peak at 917 cm^{-1} . Tanaka et al. observed visible laser photoproducts in the isoprene- NO_2 system and assigned the 930 cm^{-1} peak to this molecule. Since these two peaks cannot be misidentified, the 917 cm^{-1} peak was assigned to 3,4-epoxy-2-methyl-1-butene. Although the 917 cm^{-1} peak was close to the O-O stretching band of the simplest Criegee intermediate CH_2OO [49], such possibility was ruled out from the very small isotope shift upon $^{16}\text{O} \rightarrow ^{18}\text{O}$ substitution; see Figure 6.

Regarding the 1740 cm^{-1} band, the two candidate molecules exhibited similar simulated patterns, and it is not clear which is more plausible. Because of the considerable energy difference between them, the peak was temporarily assigned to 3-methyl-2-oxobut-3-enal. As shown in Figure 9, the spectral match remains qualitative owing to the limited spectroscopic data available. The isotopic shift ($^{16}\text{O} \rightarrow ^{18}\text{O}$) of this band is 28 cm^{-1} , which is comparable to the calculated anharmonic wavenumber shift for this molecule (34 cm^{-1}).

3.4. $\text{C}_6\text{H}_{10}\text{-O}_3$ System

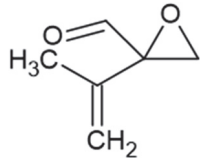
Figure 5 shows the difference spectra for the dimethyl butadiene-ozone system upon irradiation. Five peaks were observed at 864 , 1071 , 1176 , 1649 and 1733 cm^{-1} , in addition to the CO_2 peak. Notably, the production of CO_2 is negligible even at 405 nm , implying the absence of a glyoxal-like product. Tanaka et al. observed peaks at 865 , 1070 , 1175 in the visible laser photolysis of a DMB- NO_2 system in Ar and assigned them to 2-methyl-2-(1-methylethenyl) oxirane [47]. They did not report the peak at 1649 cm^{-1} , and it may be obscured by the strong peak of nitrite radical at 1657 cm^{-1} . They observed a peak at 1731 cm^{-1} and assigned it to 2,3-dimethyl-3-butenal. Our assignments of the three low lying peaks were consistent with theirs, although it is not clear which molecule the 1733 cm^{-1} band is assignable to; no experimental IR data are available for the authentic samples of the two candidate molecules. Anharmonic vibrational calculations for these two species provided essentially the same spectral patterns, and the qualitative match between the experiment and calculation is similar to that of the $\text{C}_5\text{H}_8\text{-O}_3$ system, as shown in Figure 10. The isotopic shift ($^{16}\text{O} \rightarrow ^{18}\text{O}$) of this band is 33 cm^{-1} , comparable to the calculated anharmonic wavenumber shift for the molecule (38 cm^{-1}).

4. Discussions

The peak positions of the photoproducts in this study are listed in Table 1, together with their assignments. As described above, the vibrational peaks for the photoproducts for each of the three olefin-ozone systems can be interpreted consistently by assuming there was no C-C bond cleavage upon irradiation. It would be reasonable to conclude that the CT bands of these ozone complexes do not have significant absorption cross-sections in the longer wavelength limit of the visible region, because we could not detect products of photolysis at 780 and 800 nm . Regarding the $\text{C}_2\text{H}_4\text{-O}_3$ system, we could not observe photoproducts spectroscopically upon irradiation at 405 nm , and there might be a "gap" in the CT band around this wavelength, whereas no such depletion of photolysis was found for other olefins. The observation of CT bands has been reported for some organic molecule-ozone complexes [4–7]. Jonnalagadda et al. measured the CT band for the $\text{C}_2\text{H}_4\text{-O}_3$ complex in the Xe matrix [6]. The spectrum shows a maximum at ca. 300 nm and a decrease in the longer wavelength region. This is consistent with the photolytic efficiency observed in this study, except for the possible gap at approximately 405 nm . One possible source of this small discrepancy might be the difference in host atoms; Xe is more polarizable than Ar and, therefore, may influence the CT band profile via host-guest interactions. The enhancement of the CT band for the allene- O_3 complex in Xe was found to be the host effect [4]. We also attempted to observe the CT band of the $\text{C}_2\text{H}_4\text{-O}_3$ complex in the Ar matrix using a UV-VIS spectrometer (StellarNet Qmini2 WIDE-V), but the strong scattering of the host matrix did not allow for reproducible detection. Instead, we carried out two types of theoretical calculations for the CT band using time-dependent DFT (TD-DFT) and a configuration interaction including only single excitation (CIS). An optimized

structure for the $C_2H_4-O_3$ complex in the electronic ground state was obtained at the cam-B3LYP /aug-cc-pVTZ level, and it was used as the reference geometry for the excited state calculations. The range-separated function was employed because it provides a better description for excited states of CT complexes [50–52]. The results shown in Figure 11 indicate that CIS predicts a bimodal absorption profile, whereas TD-DFT derives a strong absorption band in between. It seems that the CIS calculation qualitatively reproduced the observed photolytic efficiency.

Table 1. Observed vibrational peaks of photoproducts and their assignments. The name of each molecule was obtained from PubChem. The molecule in the last row cannot be found in the database, so its structure is presented instead.

Olefin	Peak Position (cm^{-1})	Assignment	Calc.
C_2H_4	867	Ethyleneoxide ν_5 (ring deform)	
	1270	Ethyleneoxide ν_3 (ring stretch)	
	1351	unidentified	
	1726	Glyoxal ν_{10} (C=O stretch)	
C_4H_6	822	butadiene monoxide (ring deform)	
	923	butadiene monoxide (ring deform)	
	993	butadiene monoxide (CH ₂ =C bend)	
	1250	unidentified	
	1311	unidentified	
	1385	2-oxo-3-butenal (CH ₂ bend)	1408
	1652	2-oxo-3-butenal (C=C stretch)	1648
	1713	2-oxo-3-butenal (C=O stretch)	1725
C_5H_8	917	3,4-epoxy-2-methyl-1-butene (ring deform)	907
	1740	3-methyl-2-oxobut-3-enal (C = O stretch)	1696
C_6H_{10}	864	2-methyl-2-(1-methylethenyl) oxirane (ring deform)	864
	1071	2-methyl-2-(1-methylethenyl)oxirane (CH ₂ =C bend)	917
	1176	2-methyl-2-(1-methylethenyl)oxirane (CH ₂ =C bend)	1180
	1649	2-methyl-2-(1-methylethenyl)oxirane (C=C stretch)	1690
	1733	 (C=O stretch)	1782
	Or 2,3-dimethyl-3-butenal (C=O stretch)	1759	

In this study, the types of photoproducts derived were not dependent on the wavelength of the light source. Kamata et al. [53] and Kon et al. [54] reported the switching of photoreaction channels at visible wavelengths. It is still not clear how and why such differences arise, which presents another issue to be solved.

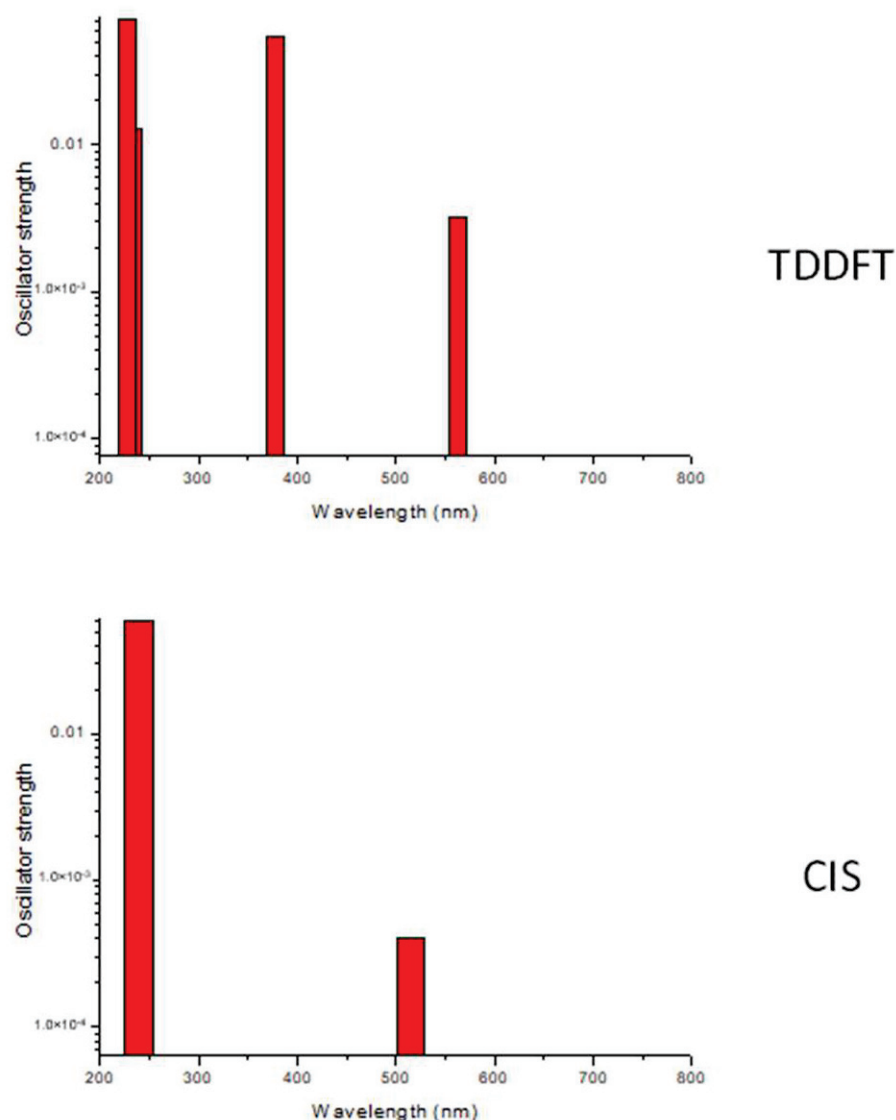


Figure 11. The simulated spectra for the CT bands for the ethylene–ozone complex by TD-DFT and CIS methods.

5. Conclusions

In this study, we experimentally observed the photolysis of four types of olefin–ozone complexes and presented the possible assignment of photoproducts. Regarding the $C_2H_4-O_3$ and $C_4H_6-O_3$ systems, the spectral match between observation and prediction seemed satisfactory, but those for the other systems remain ambiguous, mainly because of the unavailability of authentic sample spectra. We must stress that the work of Tanaka et al. on diene– NO_2 systems [47] was very helpful in narrowing down candidate molecules, even though we had to rely on the simulated spectra for the temporary assignment of many of these products. Further research is required to verify the assignments. Finally, the importance of the low carbon balance for the $C_2H_4-O_3$ system reaction that amounts to 70% at most, as described above, indicates that there are some other reaction channels followed by the photoexcitation of the CT band, whose products were not identified by infrared spectroscopy. The application of other experimental techniques is required in future.

Funding: This research received no external funding.

Institutional Review Board Statement: Not applicable.

Informed Consent Statement: Not applicable.

Data Availability Statement: Raw output files of DFT calculations in this study are available from the author upon request.

Acknowledgments: We would like to thank Akai and Kamata (TUAT) for valuable information on the effective separation and purification technique of ozone. We would also like to thank anonymous referees who provided useful and detailed comments on earlier versions of the manuscript.

Conflicts of Interest: We declare no conflict of interest regarding the financial and personal issues that could influence the work reported in this paper.

References

1. Seinfeld, J.H.; Pandis, S.N. *Atmospheric Chemistry and Physics: From Air Pollution to Climate Change*; Wiley: New York, NY, USA, 1998.
2. Johnson, D.; Marston, G. The gas-phase ozonolysis of unsaturated volatile organic compounds in the troposphere. *Chem. Soc. Rev.* **2008**, *37*, 699–716. [CrossRef] [PubMed]
3. Wennberg, P.O.; Bates, K.H.; Crounse, J.D.; Dodson, L.G.; McVay, R.C.; Mertens, L.A.; Nguyen, T.B.; Praske, E.; Schwantes, R.H.; Smarte, M.D.; et al. Gas-Phase Reactions of Isoprene and Its Major Oxidation Products. *Chem. Rev.* **2018**, *118*, 3337–3390. [CrossRef]
4. Singmaster, K.A.; Pimentel, G.C. Photolysis of Allene-Ozone Mixtures at 647 nm in Cryogenic Matrices Part 1. Formation of allene oxide. *J. Mol. Struct.* **1989**, *194*, 215–238. [CrossRef]
5. Singmaster, K.A.; Pimentel, G.C. Spectroscopic Detection of Ozone-Olefin Charge-Transfer Complexes in Cryogenic Matrices. *J. Phys. Chem.* **1990**, *94*, 5226–5229. [CrossRef]
6. Jonnalagadda, S.; Chan, S.; Garrido, J.; Bond, J.; Singmaster, K.A. Detection of Ethylene-Ozone and Cyclohexene-Ozone Charge-Transfer Complexes in Cryogenic Matrices. *J. Am. Chem. Soc.* **1995**, *117*, 562–563. [CrossRef]
7. Pinelo, L.F.; Kugel, R.W.; Ault, B.S. Charge-Transfer Complexes and Photochemistry of Ozone with Ferrocene and n-Butylferrocene: A UV–vis Matrix-Isolation Study. *J. Phys. Chem. A* **2015**, *119*, 10272–10278. [CrossRef]
8. Herron, J.T.; Huie, R.E. Stopped-Flow Studies of the Mechanisms of Ozone-Alkene Reactions in the Gas Phase. *Ethylene. J. Am. Chem. Soc.* **1977**, *99*, 5430–5435. [CrossRef]
9. Niki, H.; Maker, P.D.; Savage, C.M.; Breltenbach, L.P. A FT IR Study of a Transitory Product in the Gas-Phase Ozone-Ethylene Reaction. *J. Phys. Chem.* **1981**, *85*, 1024–1027. [CrossRef]
10. Su, F.; Calverl, J.G.; Shaw, J.H. A FT IR Spectroscopic Study of the Ozone-Ethene Reaction Mechanism in O₂-Rich Mixtures. *J. Phys. Chem.* **1980**, *84*, 239–246. [CrossRef]
11. Horie, O.; Moortgat, G.K. Decomposition pathways of the excited Criegee intermediates in the ozonolysis of simple alkenes. *Atmos. Environ. A* **1991**, *25*, 1881–1896. [CrossRef]
12. Neeb, P.; Horie, O.; Moortgat, G.K. The nature of the transitory product in the gas-phase ozonolysis of ethene. *Chem. Phys. Lett.* **1995**, *246*, 150–156. [CrossRef]
13. Neeb, P.; Horie, O.; Moortgat, G.K. The Ethene—Ozone Reaction in the Gas Phase. *J. Phys. Chem. A* **1998**, *102*, 6778–6785. [CrossRef]
14. Porterfield, J.P.; Eibenberger, S.; Patterson, D.; McCarthy, M.C. The ozonolysis of isoprene in a cryogenic buffer gas cell by high resolution microwave spectroscopy. *Phys. Chem. Chem. Phys.* **2018**, *20*, 16828–16834. [CrossRef] [PubMed]
15. Rouso, A.C.; Hansen, N.; Jasper, A.W.; Ju, Y. Low-Temperature Oxidation of Ethylene by Ozone in a Jet-Stirred Reactor. *J. Phys. Chem. A* **2018**, *122*, 8674–8685. [CrossRef]
16. Kühne, H.; Vaccani, S.; Ha, T.-K.; Bauder, A.; Günthard, H.H. Infrared-matrix and microwave spectroscopy of the ethylene-ozone gas-phase reaction. *Chem. Phys. Lett.* **1976**, *38*, 449–455. [CrossRef]
17. Kühne, H.; Günthard, H.H. Spectroscopic Study of the Ozone-Ethylene Reaction. Matrix-Infrared Spectra of Three Isotopic Ethylene Ozonides. *J. Phys. Chem.* **1976**, *80*, 1238–1247. [CrossRef]
18. Nelander, B.; Nord, L. The reaction between ethylene and ozone. A matrix study. *Tetrahedron Lett.* **1977**, *32*, 2821–2822. [CrossRef]
19. Hawkins, M.; Kohlmiller, C.K.; Andrews, L. Matrix Infrared Spectra and Photolysis and Pyrolysis of Isotopic Secondary Ozonides of Ethylene. *J. Phys. Chem.* **1982**, *86*, 3154–3166. [CrossRef]
20. Kohlmiller, C.K.; Andrews, L. Infrared Spectrum of the Primary Ozonide of Ethylene in Solid Xenon. *J. Am. Chem. Soc.* **1981**, *103*, 2578–2583. [CrossRef]
21. Andrews, L.; Kohlmiller, C.K. Infrared Spectra and Photochemistry of the Primary and Secondary Ozonides of Propene, trans-2-Butene, and Methylpropene in Solid Argon. *J. Phys. Chem.* **1982**, *86*, 4548–4557. [CrossRef]
22. Samuni, U.; Haas, Y.; Fajgar, R.; Pola, J. Matrix effects in the low-temperature oxonation of ethylene, tetramethylethylene and 1-hexene. *J. Mol. Struct.* **1998**, *449*, 177–201. [CrossRef]
23. Clark, R.J.H.; Foley, L.J. Photochemically Induced Reactions of Ozone with 1,2-Dibromoethene and 1,2-Dichloroethene: An FT-IR Matrix Isolation Study. *J. Phys. Chem. A* **2002**, *106*, 3356–3364. [CrossRef]
24. Clay, M.; Ault, B.S. Infrared matrix isolation and theoretical study of the initial intermediates in the reaction of ozone with cis-2-butene. *J. Phys. Chem. A* **2010**, *114*, 2799–2805. [CrossRef] [PubMed]

25. Hoops, M.D.; Ault, B.S. Matrix isolation study of the early intermediates in the ozonolysis of cyclopentene and cyclopentadiene: Observation of two criegee intermediates. *J. Am. Chem. Soc.* **2009**, *131*, 2853–2863. [CrossRef]
26. Kugel, R.W.; Ault, B.S. Infrared matrix isolation and theoretical studies of reactions of ozone with bicyclic alkenes: α -pinene, norbornene, and norbornadiene. *J. Phys. Chem. A* **2015**, *119*, 312–322. [CrossRef]
27. Ault, B.S. Matrix isolation study of the reaction of O (3P) with 1,3 butadiene: Unexpected formation of ethylketone. *J. Mol. Struct.* **2019**, *1176*, 47–53. [CrossRef]
28. Ito, F. Infrared and quantum chemical studies of isoprene-methanol complexes in noble gas matrices. *J. Mol. Spectrosc.* **2019**, *362*, 90–95. [CrossRef]
29. Ito, F. Infrared and density functional theory studies of isoprene-water complexes in noble gas matrices. *J. Mol. Spectrosc.* **2017**, *341*, 27–34. [CrossRef]
30. Torres, E.; DiLabio, G.A. A (Nearly) Universally Applicable Method for Modeling Noncovalent Interactions Using B3LYP. *J. Phys. Chem. Lett.* **2012**, *3*, 1738–1744. [CrossRef]
31. Barone, V. Vibrational zero-point energies and thermodynamic functions beyond the harmonic approximation. *J. Chem. Phys.* **2004**, *120*, 3059–3065. [CrossRef]
32. Barone, V. Anharmonic vibrational properties by a fully automated second-order perturbative approach. *J. Chem. Phys.* **2005**, *122*, 014108. [CrossRef] [PubMed]
33. Frisch, M.J.; Trucks, G.W.; Schlegel, H.B.; Scuseria, G.E.; Robb, M.A.; Cheeseman, J.R.; Scalmani, G.; Barone, V.; Petersson, G.A.; Nakatsuji, H.; et al. *Gaussian 09, Revision A.02*; Gaussian, Inc.: Wallingford, CT, USA, 2009.
34. Ault, B.S. Matrix Isolation Study of the Complexes of Small-ring Heterocycles. *J. Mol. Struct.* **1985**, *127*, 343–356. [CrossRef]
35. Khoshkhoo, H.; Nixon, E.R. Infrared and Raman spectra of formaldehyde in argon and nitrogen matrices. *Spectrochim. Acta A* **1973**, *29*, 603–612. [CrossRef]
36. Wiberg, K.B.; Thiel, Y.; Goodman, L.; Leszczynski, J. Acetaldehyde: Harmonic Frequencies, Force Field, and Infrared Intensities. *J. Phys. Chem.* **1995**, *99*, 13850–13864. [CrossRef]
37. Maçõas, E.M.S.; Lundell, J.; Pettersson, M.; Khriachtchev, L.; Fausto, R.; Räsänen, M. Vibrational spectroscopy of cis- and trans-formic acid in solid argon. *J. Mol. Spectrosc.* **2003**, *219*, 70–80. [CrossRef]
38. Macoas, E.M.S.; Khriachtchev, L.; Pettersson, M.; Fausto, R.; Rasanen, M. Rotational isomerism of acetic acid isolated in rare-gas matrices: Effect of medium and isotopic substitution on IR-induced isomerization quantum yield and cis \rightarrow trans tunneling rate. *J. Chem. Phys.* **2004**, *121*, 1331–1338. [CrossRef]
39. Diem, M.; MacDonald, B.G.; Lee, E.K.C. Photolysis and Laser-Excited Fluorescence and Phosphorescence Emission of trans-Glyoxal in an Argon Matrix at 13 K. *J. Phys. Chem.* **1981**, *85*, 2227–2232. [CrossRef]
40. Pugh, L.A.; Rao, K.N. Intensities from infrared spectra. In *Molecular Spectroscopy: Modern Research*; Rao, K.N., Ed.; Academic Press: Cambridge, MA, USA, 1976; Volume 2, pp. 165–226.
41. Profeta, L.T.M.; Sams, R.L.; Johnson, T.J. Quantitative Infrared Intensity Studies of Vapor-Phase Glyoxal, Methylglyoxal, and 2,3-Butanedione (Diacetyl) with Vibrational Assignments. *J. Phys. Chem. A* **2011**, *115*, 9886–9900. [CrossRef]
42. Adler-Golden, S.M.; Langhoff, S.R.; Bauschlicher, C.W., Jr.; Carney, G.D. Theoretical calculation of ozone vibrational infrared intensities. *J. Chem. Phys.* **1985**, *83*, 255–264. [CrossRef]
43. Cvetanovic, R.J. Reaction of Oxygen Atoms with Ethylene. *J. Chem. Phys.* **1955**, *23*, 1375–1380. [CrossRef]
44. Hirokami, S.; Cvetanovic, R.J. Reaction of Oxygen Atoms, O(3P), with Olefins in Liquid Nitrogen Solution at 77 K. *J. Am. Chem. Soc.* **1974**, *96*, 3738–3746. [CrossRef]
45. Yang, X.; Maeda, S.; Ohno, K. Insight into Global Reaction Mechanism of [C2, H4, O] System from ab initio Calculations by the Scaled Hypersphere Search Method. *J. Phys. Chem. A* **2007**, *111*, 5099–5110. [CrossRef] [PubMed]
46. Atkinson, R.; Carter, W.P.L. Kinetics and Mechanisms of the Gas-Phase Reactions of Ozone with Organic Compounds under Atmospheric Conditions. *Chem. Rev.* **1984**, *84*, 437–470. [CrossRef]
47. Tanaka, N.; Kajii, Y.; Shibuya, K.; Nakata, M. Visible Light Induced Reactions of NO₂ with Conjugated Dienes in a Low-Temperature Ar Matrix. *J. Phys. Chem.* **1993**, *97*, 7048–7053. [CrossRef]
48. 2-Methyl-2-vinylloxirane | C₅H₈O - PubChem. Available online: <https://pubchem.ncbi.nlm.nih.gov/compound/92166> (accessed on 23 February 2022).
49. Su, Y.-T.; Huang, Y.-H.; Witek, H.A.; Lee, Y.-P. Infrared Absorption Spectrum of the Simplest Criegee Intermediate CH₂OO. *Science* **2013**, *340*, 174–176. [CrossRef]
50. Dreuw, A.; Weisman, J.L.; Head-Gordon, M. Long-range charge-transfer excited states in time-dependent density functional theory require non-local exchange. *J. Chem. Phys.* **2003**, *119*, 2943–2946. [CrossRef]
51. Adamo, C.; Jacquemin, D. The calculations of excited-state properties with Time-Dependent Density Functional Theory. *Chem. Soc. Rev.* **2013**, *42*, 845–856. [CrossRef]
52. Campetella, M.; Maschietto, F.; Frisch, M.J.; Scalmani, G.; Ciofini, I.; Adamo, C. Charge Transfer Excitations in TDDFT: A Ghost-Hunter Index. *J. Comput. Chem.* **2017**, *38*, 2151–2156. [CrossRef]

53. Kamata, K.; Yoshioka, R.; Akai, N.; Nakata, M. Visible-light-Induced Reaction of an Ozone–Trimethylamine Complex Studied by Matrix-Isolation IR and Visible Absorption Spectroscopies. *J. Phys. Chem. A* **2020**, *124*, 9973–9979. [CrossRef]
54. Kon, A.; Inano, N.; Terada, N.; Kamata, K.; Akai, N.; Nakata, M. Photoreactions of Ozone–Tetrahydrothiophene, Ozone–Pyrrolidine, and Ozone–Thiazolidine Complexes Studied Using Matrix-Isolation IR and Visible Absorption Spectroscopies. *J. Phys. Chem. A* **2021**, *125*, 2114–2120. [CrossRef]

Article

UV-Induced Benzyloxy Rotamerization in an *Ortho* OH-Substituted Aryl Schiff Base

İsa Sıdır ^{1,2,*}, Yadigar Gülseven Sıdır ^{1,2}, Sándor Góbi ^{2,3}, Halil Berber ⁴ and Rui Fausto ^{2,*}¹ Department of Physics, Bitlis Eren University, 13000 Bitlis, Turkey; yadigar.gulseven@gmail.com² CQC-IMS, Department of Chemistry, University of Coimbra, 3004-535 Coimbra, Portugal; sgobi@qui.uc.pt³ MTA-ELTE Lendület Laboratory Astrochemistry Research Group, Institute of Chemistry, ELTE Eötvös Loránd University, H-1518 Budapest, Hungary⁴ Department of Chemistry, Eskişehir Technical University, 26470 Eskişehir, Turkey; hlberber@eskisehir.edu.tr

* Correspondence: isidir@beu.edu.tr (İ.S.); rfausto@ci.uc.pt (R.F.)

Abstract: A new benzyloxy containing ortho hydroxyl-substituted aryl Schiff base, trans 2-((2-(benzyloxy)benzylidene)amino)phenol (abbreviated as BBAP), was synthesized and characterized by ¹H-, ¹³C-NMR and infrared spectroscopic techniques and elemental analysis. The conformational landscape of the compound, as well as its infrared spectra in argon and N₂ cryogenic matrices (10 K) were investigated, followed by the study of the effects of in situ UV irradiation of the matrix-isolated compound. The structural information was obtained through an extensive series of quantum chemical calculations performed at the DFT(B3LYP)/6-311++G(d,p) level of theory, which enabled to identify 3 low-energy OH...N intramolecularly H-bonded conformers of the molecule that were later found to be present in the as-deposited cryogenic matrices. The 3 experimentally relevant conformers of BBAP differ in the geometry of the benzyloxy substituent, and were discovered to interconvert upon in situ UV irradiation (λ = 230 nm) of the matrix-isolated compound. This is the first report on UV-induced conformational changes taking place in a benzyloxy fragment for a matrix-isolated compound.

Citation: Sıdır, İ.; Gülseven Sıdır, Y.; Góbi, S.; Berber, H.; Fausto, R. UV-Induced Benzyloxy Rotamerization in an *Ortho* OH-Substituted Aryl Schiff Base.

Photochem **2022**, *2*, 376–389. <https://doi.org/10.3390/photochem2020026>

Academic Editor: Yasuharu Yoshimi

Received: 26 April 2022

Accepted: 12 May 2022

Published: 25 May 2022

Publisher's Note: MDPI stays neutral with regard to jurisdictional claims in published maps and institutional affiliations.



Copyright: © 2022 by the authors. Licensee MDPI, Basel, Switzerland. This article is an open access article distributed under the terms and conditions of the Creative Commons Attribution (CC BY) license (<https://creativecommons.org/licenses/by/4.0/>).

Keywords: UV-induced ring rotamerization; 2-((2-(benzyloxy)benzylidene)amino)phenol; matrix isolation; DFT(B3LYP)/6-311++G(d,p); molecular conformation; benzyloxy rotamerization

1. Introduction

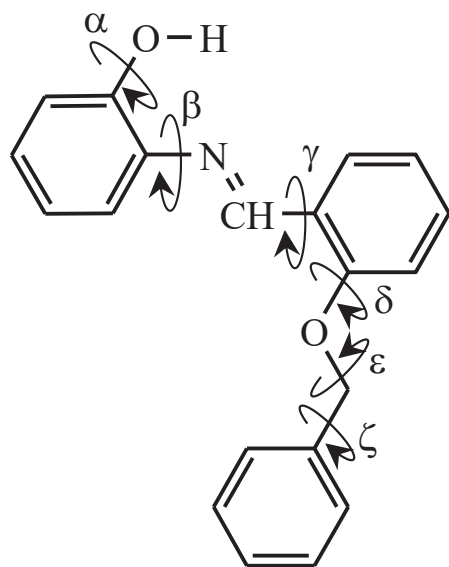
Schiff bases are common organic structures (also known as azomethines; R₁R₂C = NR₃, with R₁, R₂ = alkyl, aryl or H, and R₃ = alkyl or aryl) that can usually be easily synthesized through a one-step synthetic procedure, which involves the reaction of primary amines with carbonyl compounds [1,2]. Aryl Schiff bases have their azomethine characteristic group connected to a benzene ring, and are the most relevant members of this family of compounds due to their wide spectrum of applications, particularly as corrosion inhibitors [3], catalyst carriers [4,5], thermo-stable materials [6–8], metal ion complexing agents [9], optical data storage systems [10–12], molecular switches [13,14], and sensors [15,16]. These compounds also have many uses in molecular electronics, computing, [17,18] and medicine [19–21].

In aryl Schiff bases, the presence of a hydroxyl group in the *ortho* position the azomethine group leads to the formation of an intramolecular resonance-stabilized O–H...N hydrogen bond, which has a positive effect on the thermodynamic stability of the whole molecule [22,23]. In addition, in these compounds, enol-imine/keto-amine tautomerism, as well as *cis/trans* (or *E/Z*) isomerism around the azomethine C=N bond, are, in general, easily accessible, particularly as a result of their photo-excitation. The photo-induced enol-imine/keto-amine tautomerism in *ortho* hydroxyl-substituted aryl Schiff bases has been the subject of many studies and is known to take place via excited-state intramolecular proton transfer (ESIPT) [24–29].

We have been investigating the structure and reactivity of *ortho* hydroxyl-substituted aryl Schiff bases using a concerted approach that included the experimental study of the

molecules of the compounds isolated in low-temperature inert matrices and the theoretical evaluation of their conformational landscape by means of quantum chemical theoretical methods [28–30]. Emphasis has been given to the evaluation of the photochemical behavior of the matrix-isolated compounds when subjected to ultraviolet (UV) irradiation, as, for example, the UV-induced methoxy rotamerization of a methoxy-substituted *ortho*-hydroxy aryl Schiff base and the *E*-enol/*Z*-enol and *E*-enol/*E*-keto photo-isomerizations undergone by *N*-salicylidene-*p*-carboxyaniline [28,29], as well as to quantum mechanical H-atom tunneling reactions taking place in the cryogenic matrices [30].

In the present study, we have investigated *trans* 2-((2-(benzyloxy)benzylidene)amino) phenol (BBAP), which is an *ortho*-OH substituted aryl Schiff base bearing a benzyloxy substituent (Scheme 1). This substituent is a conformationally flexible moiety, with three internal rotations that may lead to different conformers (δ , ϵ and ζ in Scheme 1). The work focused on the characterization of the conformational space of the molecule, through the identification of its lowest-energy conformers, the study of the infrared spectrum of BBAP isolated in cryogenic Ar and N₂ matrices, and the evaluation of the processes that took place upon UV irradiation of the matrix-isolated compound. Extensive quantum chemical calculations were performed within the density functional theory (DFT) framework, in order to characterize the molecule conformationally and to identify the most relevant intramolecular interactions that determine the nature of the lowest-energy forms of BBAP. As it is shown in the next sections of this article, the calculations render 3 low-energy conformers of the compound, with energies within ca. 4 kJ mol⁻¹, which could be trapped from the gas phase into the cryogenic matrices and characterized vibrationally. These conformers differ in the geometry of the benzyloxy moiety, and are stabilized by the characteristic stabilizing intramolecular O–H⋯N hydrogen bond established between the phenolic O–H group (as H-donor) and the azomethine nitrogen atom (as acceptor), and by the absence of significant steric hindrance. In situ narrowband UV irradiation of the matrix-isolated compound at $\lambda = 230$ nm was found to induce interconversions between the low-energy conformers initially present in the matrices (i.e., it was found to lead to rotamerization within the benzyloxy group) but no evidence was found either for *trans*→*cis* (C=N) isomerization or enol-imine/keto-amine tautomerization. To the best of our knowledge, this is the first report on the UV-induced conformational changes that take place in a benzyloxy fragment of a matrix-isolated compound.

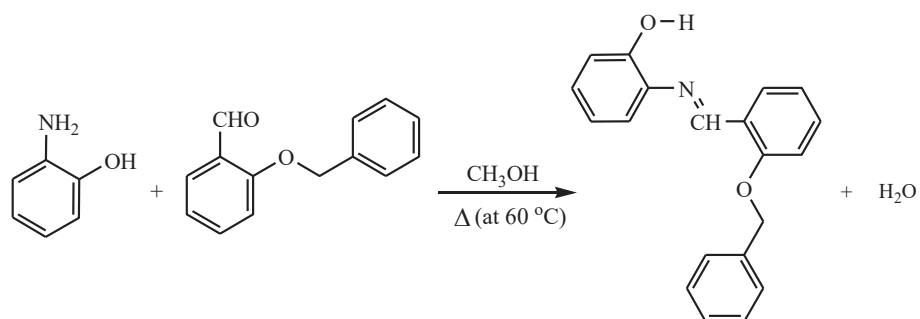


Scheme 1. Structure of BBAP, highlighting the conformationally relevant internal rotation axes (designated by the Greek letters).

2. Experimental and Computational Methods

2.1. Synthesis Procedure and Characterization

2-((2-(Benzyloxy)benzylidene)amino)phenol (BBAP) was synthesized from 2-aminophenol and 2-(benzyloxy)benzaldehyde (Scheme 2), following the general procedure previously reported [25–30]. 2-Aminophenol (1.091 g, 0.01 mol) and 2-(benzyloxy)benzaldehyde (2.12 g, 0.01 mol) were first dissolved in 25 mL of methanol by heating, and the solutions were then added slowly. After the substance precipitated, the mixture was stirred for another 1–2 h, at $T = 60\text{ }^{\circ}\text{C}$. The precipitated product was filtered, purified by recrystallization in methanol and dried in a vacuum desiccator at room temperature. The infrared (IR) spectrum of the purified crystalline material (in a KBr pellet, at room temperature) and the ^1H - and ^{13}C -NMR spectra in deuterated dimethylsulfoxide ($\text{DMSO-}d_6$) solution were found to be compatible with the desired product. These are provided as supporting materials (Figures S1–S3). The synthesis exclusively yielded the *E* ($\text{C}=\text{N}$) enol-imine isomeric form of the compound, with no evidence of the formation of either the *Z* ($\text{C}=\text{N}$) isomer or of the keto-amine tautomeric species.



Scheme 2. Synthesis of BBAP.

The IR spectrum was recorded by using a Perkin Elmer FTIR 100 spectrometer, and the ^1H - and ^{13}C -NMR spectra were obtained in a Bruker Biospin UltrashieldTM NMR spectrometer, at room temperature. The melting point (m.p.) of the compound was measured using a Gallenkamp Sanyo Heater device. Elemental analysis was performed using a CNHS-932 LECO apparatus.

IR (KBr disc, $\nu\text{ cm}^{-1}$): 3369 (O–H); 3097–3006 (C–H, aromatic); 2928–2843 (C–H, aliphatic); 1621 (C=N); 1587–1448 (C=C, aromatic); 1027 (CH₂–O–C). ^1H -NMR (300 MHz, $\text{DMSO-}d_6$, δ ppm): 9.02 (s, 1H); 9.00 (s, 1H); 8.21 (dd, $J = 7.7, 1.7\text{ Hz}$, 1H); 7.61–6.69 (m, 13H); 5.26 (s, 2H). ^{13}C -NMR (75 MHz, $\text{DMSO-}d_6$, δ ppm): 158.67 (s); 155.04 (s); 151.30 (s); 139.26 (s); 137.31 (s); 133.27 (s); 129.01 (s); 128.40 (s); 128.01 (s); 127.53 (s); 125.14 (s); 121.33 (s); 120.05 (s); 119.97 (s); 116.48 (s); 113.87 (s). Elemental analysis: $\text{C}_{20}\text{H}_{17}\text{NO}_2$, Calc. (Obs.): C, 79.19 (79.05); H, 5.65 (5.79); N, 4.62 (4.70). m. p.: 83–84 $^{\circ}\text{C}$.

2.2. Matrix-Isolation and UV-Irradiation Experiments

To obtain the cryogenic matrices of the compound, a solid sample of BBAP was sublimated by using a homemade Knudsen cell, connected to the vacuum chamber of the cryostat (APD Cryogenics closed-cycle helium refrigeration system, with a DE-202A expander) and co-deposited with a large excess of argon (Ar) or nitrogen (N_2) (both obtained from Air Liquide) onto a cold ($10.0 \pm 0.1\text{ K}$) CsI substrate, mounted at the cold tip of the cryostat. The solute:matrix ratio was $\sim 1:1000$, to provide the adequate isolation of the compound.

The infrared spectra of the matrices were collected using a Nicolet 6700 FTIR spectrometer, equipped with a mercury cadmium telluride (MCT) detector and a KBr beam splitter, in the $4000\text{--}400\text{ cm}^{-1}$ range and with 0.5 cm^{-1} resolution. The instrument was purged by a stream of dry/ CO_2 -filtered air in order to avoid interference from atmospheric H_2O and CO_2 .

UV irradiation of the matrix-isolated BBAP was performed at $\lambda = 230$ nm, through the outer KBr window of the cryostat, using UV light provided by a Spectra Physics MOPO-SL optical parametric oscillator (OPO), pumped by a pulsed (pulse duration 10 ns, repetition rate 10 Hz) Quanta Ray Pro-Series Nd-YAG laser.

2.3. Quantum Chemical Calculations

All calculations were carried out using the GAUSSIAN 09 (Revision C.01) program [31]. The ground-state geometries, relative energies, and infrared spectra of the different forms of BBAP were obtained at the DFT(B3LYP)/6-311++G(d,p) level of theory [32–37], the calculated harmonic vibrational frequencies were subsequently scaled by the factor 0.955, above 1800 cm^{-1} , and by the factor 0.983, below 1800 cm^{-1} , to correct them for the effect of basis set limitation, for the neglected part of electron correlation and, mainly, for the anharmonicity effects.

Assignment of the vibrational spectra was carried out with the help of the animation module of ChemCraft (version 1.8) [38]. In the simulated spectra presented in the figures, the IR bands were broadened by Lorentzian profiles (fwhm = 2 cm^{-1}), centered at the calculated (scaled) wavenumbers.

The UV spectrum of BBAP in the gas phase was calculated within the time-dependent-DFT (TD-DFT) theoretical framework, with the same functional and basis set used in the performed ground-state calculations [39,40].

3. Results and Discussion

3.1. Geometrical Features and Energies of BBAP Isomeric Structures

The BBAP molecule possesses six internal degrees of conformational freedom, besides *cis* and *trans* isomerism around the C=N azomethine bond. However, all the low-energy conformers of the synthesized *trans* C=N isomer (*E* isomer) have the geometry of the phenolic moiety determined by the stabilizing intramolecular O–H \cdots N hydrogen bond established between the phenolic O–H group (as H-donor) and the azomethine nitrogen atom (as acceptor), as it is characteristic for *ortho* OH-substituted aryl Schiff bases [22,23,28–30], which was pointed out in the introduction. The calculations for different arrangements around the C–O(H) and C–N bonds led to conformers whose energies are 28–51 kJ mol^{-1} higher than that of the most stable conformer (see Table S1 and Figure S4) and are irrelevant in practical terms. In this way, the number of significant conformational degrees of freedom was reduced to four, which correspond to the internal rotations around the two exocyclic C–C bonds and the two ether C–O bonds (see Scheme 1). A systematic search on the potential energy surface of the molecule considering these four internal rotations as scanning coordinates allowed us to identify 11 different conformers (all having an equivalent-by-symmetry form), of which three are low-energy forms, with relative energies within ca. 4 kJ mol^{-1} , and the remaining have energies higher than that of the most stable conformer, by 13–29 kJ mol^{-1} (Table 1).

The structures of the three lowest-energy conformers of BBAP are shown in Figure 1. The calculated relative electronic energies (with and without the inclusion of the zero-point correction) and standard Gibbs energies (at 298.15 K) of the 11 conformers of BBAP, bearing the intramolecular O–H \cdots N hydrogen bond, and their estimated populations in the room-temperature (RT) gas-phase equilibrium are shown in Table 1. Relevant dihedral angles for these conformers are given in Table 2.

All three of the most stable conformers of BBAP (I, II and III: see Figure 1) share a common geometry, except that of the benzyloxy substituent. In the most stable form (I), the C–O–CH₂–C dihedral angle (ϵ) angle is $\sim 180^\circ$ (*anti* arrangement), while in conformers II and III, this dihedral defines a *gauche* arrangement, being -78.7 and 79.2° , respectively. On the other hand, the O–CH₂–C–C (ζ) dihedral angles in II and III correspond to a geometry where one of the methylene C–H bonds is nearly perpendicular to the phenyl ring of the benzyloxy substituent, while, in the case of conformer I, it is the C–O bond that is approximately perpendicular to the ring. As a whole, the geometric arrangements defined

by the ϵ and ζ axes in the different conformers make conformer II a more open structure, relative to forms I and III; the phenyl ring of the benzyloxy moiety in II points away from the main plane of the molecule, while in III it points towards this plane. Form I presents an intermediate geometry regarding this structural feature (see Figure 1).

Conformers II and III have similar energies, which are higher than that of conformer I by 3.52 and 3.65 kJ mol⁻¹ (3.91 and 4.16 kJ mol⁻¹, when the zero-point correction is considered). Since the OH...H hydrogen bond distance was predicted by the calculations to be ~2.06 Å in all three conformers, their energy difference should be attributed to the specific geometric arrangement of their benzyloxy substituent. In conformer I, the ether O atom was better placed than in both forms II and III to allow for its lone electron pairs to conjugate with the π -electron cloud of the phenyl ring, which might justify its lower energy.

Table 1. B3LYP/6-311++G(d,p) calculated relative electronic energies (ΔE_{el}), zero-point corrected electronic energies ($\Delta E_{(0)}$), and standard Gibbs energies ($\Delta G_{298.15}$) for the low-energy conformers of *trans* BBAP, and their estimated room temperature gas-phase equilibrium conformational populations ($P_{298.15}$)^a.

Conformer	ΔE_{el}	$\Delta E_{(0)}$	$\Delta G_{298.15}$	$P_{298.15}$ (%)
I	0.00	0.00	0.00	89
II	3.52	3.91	6.83	6
III	3.65	4.16	7.13	5
IV	13.29	13.01	14.63	
V	15.23	14.58	14.09	
VI	12.83	12.23	14.09	
VII	14.37	14.14	16.80	
VIII	21.64	21.17	25.05	
IX	21.88	20.57	24.27	
X	22.09	20.76	22.50	
XI	28.74	27.18	27.92	

^a Energies in kJ mol⁻¹, relative to conformer I. See Figures 1 and S5 for structures of the conformers.

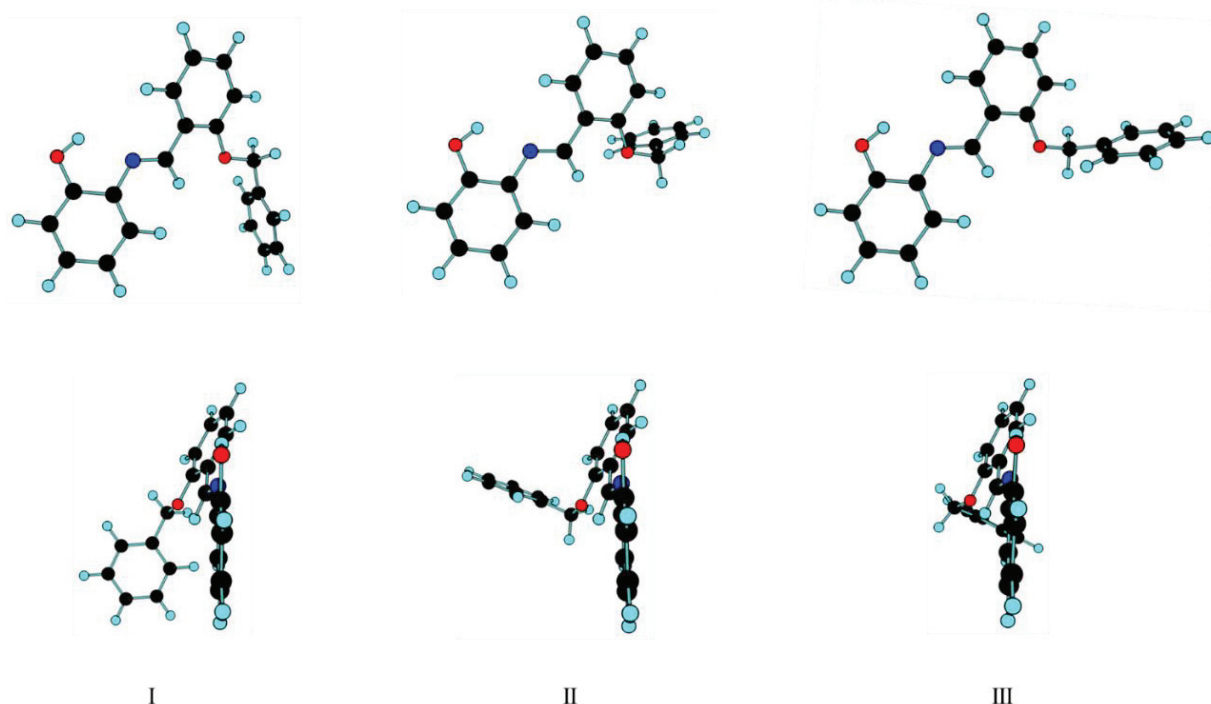


Figure 1. B3LYP/6-311++G(d,p) optimized structures for the three lowest energy conformers (I, II and III) of BBAP (two views). Each conformer has a symmetry-equivalent form. See Table 1 for relative energies, and Table 2 for values of the conformationally relevant dihedral angles.

Table 2. B3LYP/6-311++G(d,p) optimized conformationally-relevant dihedral angles (°) of the low-energy conformers of *trans* BBAP^a.

	C–N=C–C	H–O–C–C _N	C _H –C–N=C	N=C–C–C _H	C _H –C–O–C	C–O–CH ₂ –C	O–CH ₂ –C–C
Conformer		α	β	γ	δ	ε	ζ
I	–177.4	–2.7	21.7	6.7	–0.7	–179.5	80.1/–98.9
II	–177.0	–3.1	23.4	8.3	5.6	–78.7	–31.5/151.4
III	–177.5	–2.9	22.4	4.9	–6.7	79.3	29.5/–153.3
IV	–176.4	–3.2	22.8	13.6	–95.8	74.2	68.6/–111.2
V	–179.1	–2.3	16.4	–3.0	87.0	–77.8	–64.6/115.5
VI	–179.3	–3.2	16.2	179.3	–0.3	–179.3	–84.2/95.1
VII	–179.2	–1.5	12.4	177.1	2.4	–77.6	–30.8/152.1
VIII	179.9	–1.7	25.9	–175.3	–105.4	74.2	68.7/–111.0
IX	–179.4	–3.9	28.1	179.5	–98.5	174.9	–27.3/154.7
X	–179.7	–3.2	29.7	–177.1	–100.1	170.5	–67.4/112.8
XI	–177.9	–2.1	30.9	–152.6	72.2	–169.4	88.6/–90.4

^a See Figures 1 and S5 for structures of the conformers.

The standard Gibbs energies (at 298.15 K) of conformers II and III are 6.83 and 7.13 kJ mol^{–1} higher than that of conformer I, which led to estimated populations for I, II and III in the gas-phase equilibrium (at room temperature: RT) of ca. 89%, 6% and 5%, respectively. It is interesting to note that the calculated entropy (at RT) for conformer I was ~634 J mol^{–1} K^{–1}, being larger than those estimated for conformers II and III (~623 J mol^{–1} K^{–1}), indicating that the conformational flexibility of the benzyloxy group in conformer I is higher than in conformers II and III. This is in agreement with the relative values of the calculated torsional frequencies around the ζ axis for the three conformers: 11 cm^{–1} for I, 33 cm^{–1} for II, and 29 cm^{–1} for III, which demonstrates that the potential energy profile for this torsional mode is considerably flatter around the minimum I, compared to II and III.

The structures of the remaining conformers bearing the stabilizing intramolecular OH···N hydrogen bond (IV–XI) are shown in Figure S5 (supporting information). Forms IV and V (with relative energies of 13.29 and 15.23 kJ mol^{–1}, respectively) are related to conformers II and III, respectively, regarding the value of the ε dihedral angle, but have a different arrangement about the ζ axis, which leads to an increased steric hindrance between the two nearby-located phenyl rings, thus accounting for their higher relative energy compared to II and III. On the other hand, forms VI–XI have the N=C–C–C_H (γ) dihedral angle *anti* (contrarily to forms I–V, which have a *syn* arrangement). The energies of these conformers are higher than that of the most stable conformer, I, by ~13–29 kJ mol^{–1}, as a result of the destabilizing interactions between the benzyloxy and phenol moieties (see Figure S4). In the two lowest energy conformers of this group (VI and VII), a weak O–H···O intramolecular hydrogen bond (~2.80–2.90 Å) exists between the phenol group and the benzyloxy oxygen atom, which justifies their lowest-energy compared to the remaining conformers (VIII–XI), where such interaction is absent.

Figure 2 shows the potential energy profile for interconversion between the three lowest-energy conformers of BBAP. In this figure, the symmetry-equivalent forms of I, II and III are designated as I', II' and III', respectively. The scanning coordinate is the C–O–CH₂–C dihedral angle (ε) and the starting geometries for the different scans that were used to build the figure were those of I', II and III. In the figure, the values assumed by the O–CH₂–C–C angle (ζ, where the ring carbon atom is that defining the smallest dihedral angle among the two possible in the starting conformer) along the scans are also shown, since, at certain critical geometries along the scans, the arrangement of the phenyl group, as defined by the ζ angle, changed in order to relief steric hindrance.

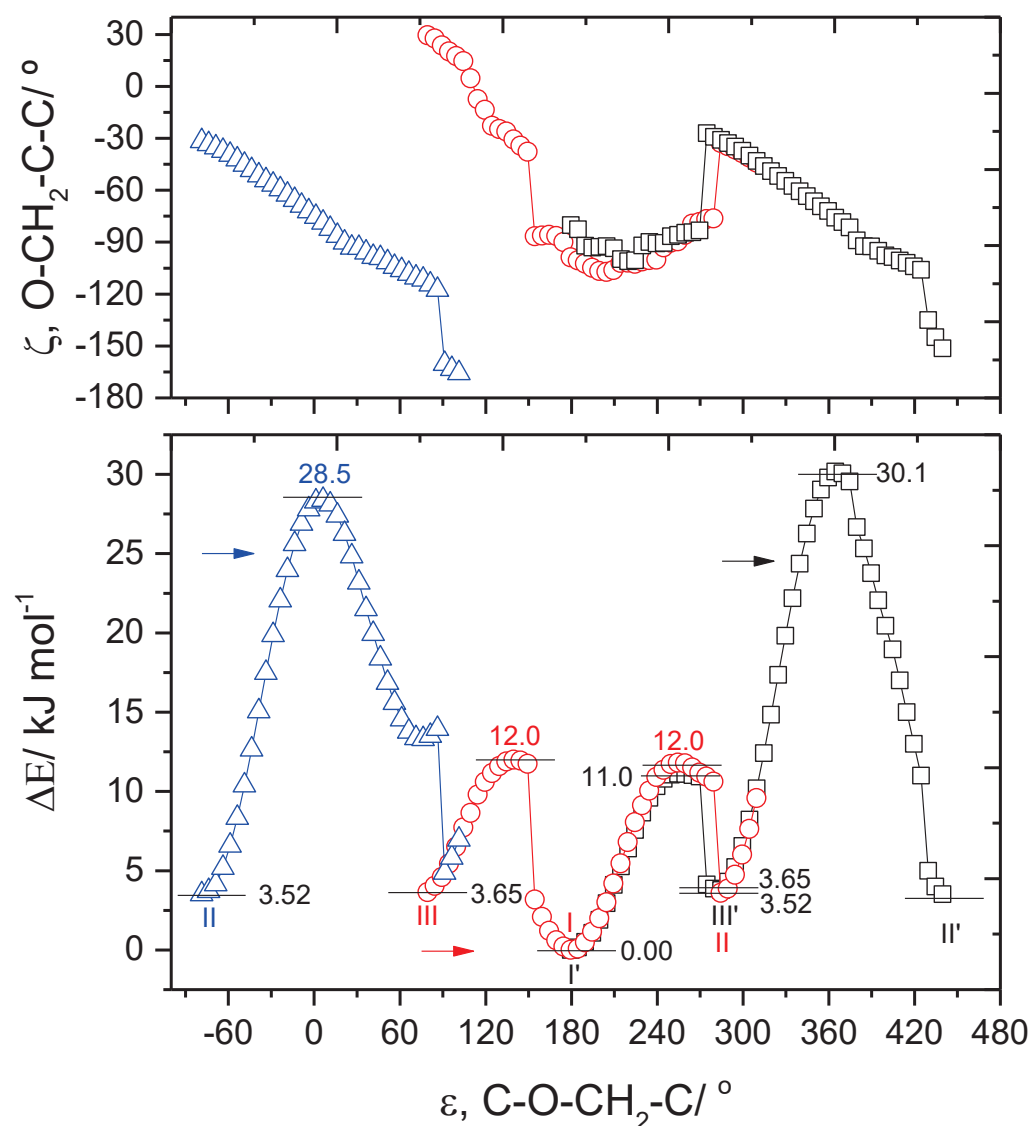


Figure 2. Potential energy profiles for interconversion between conformers I, II and III (and their symmetry-related forms I', II' and III'), obtained by performing relaxed scans (shown in different colors) with the C–O–CH₂–C (ϵ) dihedral angle as scanning coordinates. The initial geometries chosen for the scans and the direction of the scans are indicated by the arrows.

In starting the scan at the geometry of II, towards the geometry of III (i.e., increasing the value of ϵ : the blue line in Figure 2), the energy raises until the transition structure, which stayed 25 kJ mol⁻¹ higher in energy than conformer II, and then starts to decrease. At $\epsilon \sim 90^\circ$, there is an abrupt decrease of energy, which is determined by the change of the orientation of the phenyl group, as seen in the change of the ζ angle to the characteristic value of conformer III (ca. -150°). This change results from the steric hindrance between the two phenyl groups. The interesting point to notice is that this change of orientation of the phenyl group takes place along the scan for a value of the scanning coordinate, ϵ , that is larger than that of conformer III (the ζ angle is initially that of conformer II, ca. -30° , and decreases smoothly till ca. -120° , the point at which the ring flip takes place) so that this latter form is not effectively reached in this way. Nevertheless, after the flip of the phenyl group, the molecule is taken to the potential energy well of conformer III, which meant that, in practical terms, the conversion II \rightarrow III is achieved after the relaxation of the structure obtained after the change of orientation of the phenyl group.

When the scan starts at the geometry of conformer III, for increasing values of ϵ (the red line in Figure 2), conformer I is reached after the reorientation of the phenyl group at $\epsilon \sim 150^\circ$, which also implies a fast decrease of energy around this geometry. The energy barrier separating III from I is about 8.5 kJ mol^{-1} (12 kJ mol^{-1} in the reverse direction). The continuation of the scan towards II allowed to reach this latter conformer via a barrier of 12 kJ mol^{-1} ($\sim 8.5 \text{ kJ mol}^{-1}$ in the reverse direction). These low-energy barriers demonstrate the easiness of the processes for interconversion between the three conformers.

The performed scan that starts from the geometry of I' (black line in Figure 2), for increasing values of ϵ , yields form III' (through an energy barrier of $\sim 11 \text{ kJ mol}^{-1}$) after the reorientation of the phenyl group at $\epsilon \sim 270^\circ$, which then converts to form II' through a barrier of ca. 30 kJ mol^{-1} . The slightly higher barrier when the scan goes from III' to II', compared to that obtained when the scan goes from II to III, results from the slightly different interactions at the geometries at which the flip of the phenyl group takes place when the scan is performed in the two different directions.

The most important conclusions that can be extracted from the results shown in Figure 2 are, on the one side, that the energy barriers separating the different forms are large enough to allow their trapping from the gas phase into the cryogenic matrices without significant conformational cooling during matrix deposition [41,42], and, on the other side, that they are sufficiently low to provide the molecule with substantial conformational flexibility around this coordinate in the gas phase. One can also expect that the interconversion barriers in the excited states are also not very large.

3.2. Infrared Spectrum of Matrix-Isolated BBAP

Monomers of BBAP were isolated from the gas phase into cryogenic (10 K) Ar and N₂ matrices, as described in Section 2.2. The experimental IR spectra obtained in both matrices are presented in Figure 3, alongside the simulated IR spectrum, that was constructed by adding the DFT(B3LYP)/6-311++G(d,p) calculated spectra of conformers I, II and III, weighted by their estimated populations in the gas phase prior to deposition. As stated before, these three conformers were the only forms of BBAP expected to be significantly populated in the gas phase, with the lowest energy conformer, I, strongly dominating (see Table 1). Since the calculations also indicated that the energy barriers separating these conformers from each other would be large enough to prevent their interconversion during matrix deposition, the presence of these three conformers in the as-deposited matrices was expected. The agreement between the experimental and the simulated spectra, shown in Figure 3 is excellent, what is in consonance with the presence in the as-deposited matrices of the 3 conformers in relative amounts similar to those estimated theoretically. However, the expected amounts of conformers II and III present in the matrices were considerably smaller than that of conformer I (6 and 5% vs. 89%), which, together with the fact that the spectra of the three conformers were very much similar (in particular, those of II and III, that were very much coincident regarding their frequencies and that differed mostly in the relative band intensities) due to their structural resemblance, made the identification of marker bands for conformers II and III very difficult. Band assignments are provided in Table S2 (supporting information), where no assignments to individual conformers are given. It should, however, be highlighted that the results of the performed UV irradiation of the matrices, which are presented in the next section, clearly show that all three conformers are, in fact, present in the matrices, though the assignment of the bands to individual conformers could not be done either based on those results, as explained below.

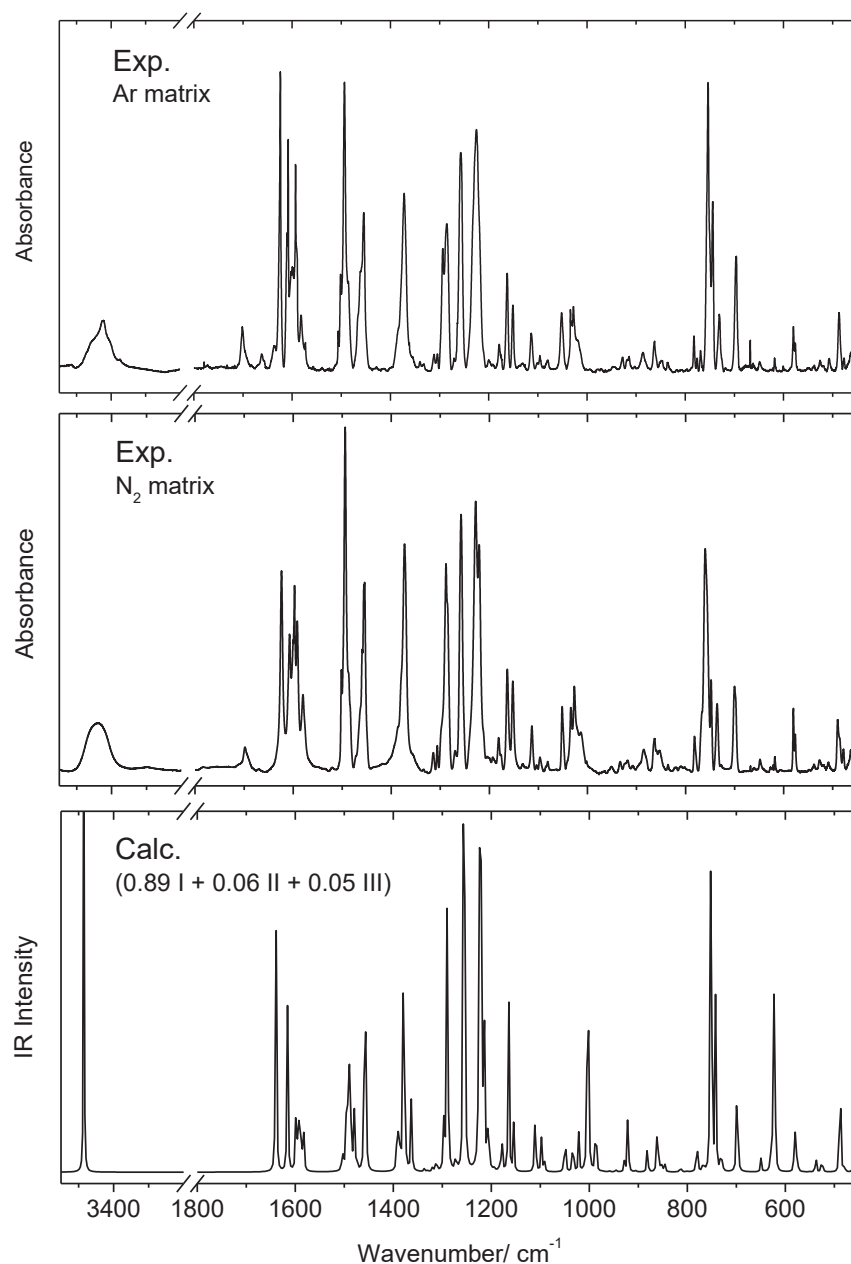


Figure 3. As-deposited IR spectra of BBAP, isolated in Ar (*top panel*) and N₂ (*middle panel*) matrices (10 K), and simulated IR spectrum, built using the calculated infrared spectra of conformers I, II and III, weighted by their estimated populations in the matrices (*lower panel*). Calculated wavenumbers were scaled as described in Section 2.3. The experimental bands at ca. 667 cm⁻¹ were due to traces of atmospheric CO₂.

3.3. Narrowband UV-Induced Rotamerization of Phenyl Ring

The effects of in situ UV irradiation of matrix-isolated BBAP in both Ar and N₂ matrices were investigated. The matrices were irradiated at $\lambda = 230$ nm for 50 min, the irradiation wavelength being chosen taking into account the TD-DFT-calculated UV spectrum of the compound (see Figure S6, in the supporting information).

The different spectra obtained by subtracting the IR spectra of the as-deposited matrices from those of the UV-irradiated matrices are shown in Figure 4.

The first point that we observed was the fact that irradiation did not result in the appearance of new bands in the spectra but led only to changes in the relative intensities of the bands. This observation indicated that no new species were being generated upon the

performed irradiations, in particular, that neither the *trans*→*cis* (C=N) isomerization nor the enol-imine/keto-amine tautomerization were taking place. Otherwise, the observed redistribution of the band intensities revealed that the amount of the BBAP conformers that were initially present in the matrices were changing—i.e., that UV irradiation resulted in rotamerization within the benzyloxy group.

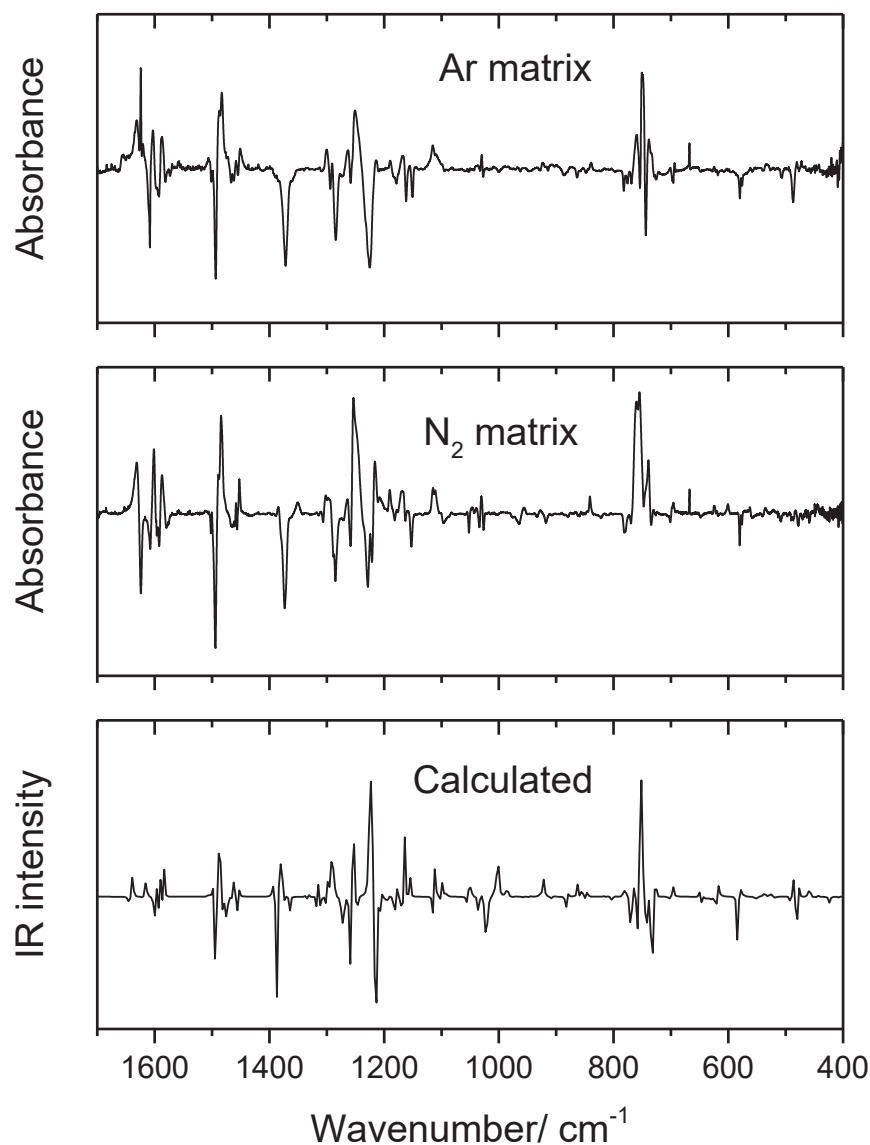


Figure 4. Top and middle panels: IR difference spectra (spectrum obtained after 50 min. of UV irradiation at 230 nm minus as-deposited spectrum) obtained in Ar and in N₂ (10 K). Lower panel: Simulated infrared difference spectrum was built based on the calculated spectra of BBAP conformers I, II and III, with intensities scaled as $0.43 \times \text{I} + 0.57 \times \text{III} - \text{II}$. Calculated wavenumbers were scaled as described in Section 2.3. The experimental bands at ca. 667 cm^{-1} were due to traces of atmospheric CO₂.

Detailed comparison of the experimental results with the calculated spectra of conformers I, II and III allowed us to conclude that the amount of conformer II present in the matrices after irradiation diminished, while the amount of conformers I and III increased. A simulated IR difference spectrum defined as $a_1 \times S_{\text{IR}}(\text{I}) + a_3 \times S_{\text{IR}}(\text{III}) - S_{\text{IR}}(\text{II})$, where $S_{\text{IR}}(x)$ represents the calculated spectrum of conformer x , and the coefficients a_x apply to the intensities ($a_1 + a_3 = 1$), was then obtained by adjusting the coefficients a_1 and a_3 to reproduce, as best as possible, the experimental difference spectra. A good solution was

obtained for $a_1 = 0.43$ and $a_3 = 0.57$ (see Figure 4), which indicated that, upon irradiation, the population of conformer III increased somewhat more than that of conformer I.

Unfortunately, the assignment of individual bands to specific conformers could not be done, even taking into account the results of the UV irradiation experiments. As mentioned in Section 3.2, the spectra of the three conformers are very similar, in particular, those of conformers II and III. Hence, since irradiation led to the consumption of conformer II and the formation of conformer III (and I, which also has most of its bands coincident with those of conformers II and III: see Table S2), the appearance of negative bands in the difference spectra, shown in Figure 4, does not mean that these bands are only ascribable to conformer II; in the same way, the fact that the bands appear as positive in the difference spectra does not imply that this conformer does not also contribute to their intensity. Nevertheless, the presence of the three conformers in the matrices is beyond doubt, as is the fact that the UV irradiation of the matrices leads to their interconversion.

The detailed explanation for the specific observations resulting from the UV irradiation of the matrices escapes the scope of this study, since it requires high-level excited-states theoretical calculations and also a detailed study of the constraints imposed by the matrix morphology to the involved transformations. Nevertheless, a general picture can be presented, based on simple considerations that are in agreement with the observations. The first consideration relies on the fact that all three of the conformers—I, II and III—have similar UV absorbance spectra. This means that they were simultaneously excited by the performed irradiation of the matrices, and the system should tend to a photostationary state. Thus, the observed changes in the relative populations of the conformers were a reflex of the occurrence of the different photo-induced interconversions between the three conformers towards the photo-stationary state. In the absence of rigorous theoretical data on the different reaction parameters for each individual isomerization process, one cannot say anything regarding the relative efficiency and extension of the different processes. Assuming that they have probabilities that are intrinsically identical, then the final result should be dependent largely on matrix effects. The critical variable in this case would be the volume available in the primary matrix cage for the conformational changes within the benzyloxy fragment to take place. In this regard, conformers I, II and III of BBAP are significantly different, with conformer II being a considerably more open structure than conformers I and III and, thus, requiring a much larger embedment volume in the matrices to accommodate the benzyloxy fragment, which is, in this case, more deviated from the plane of the main fragment of the molecule (see Figure 1). On the other hand, conformer III is the most closed form, requiring the smallest volume to properly accommodate the benzyloxy fragment among the three conformers. The conformational changes would take place without important changes of the original matrix-site morphology, which would cost a large amount of energy for matrix rearrangement. Under these circumstances, one would expect that volume constraints to the efficiency of the conformational conversions were maximized for those leading to the formation of conformer II and minimized for those leading to the formation of conformer III, thus justifying the observed changes in the relative populations of the conformers. We could also expect that the photoisomerization in Ar and N₂ would show some difference due to the difference in lattice parameters for these two host crystals. Nevertheless, no striking differences were observed in the results obtained in the two matrices (though around the 750 cm⁻¹, the difference spectra, obtained in the two matrices and shown in Figure 4, differ somewhat from each other). The apparent relative lack of high-sensitivity of the observed photoisomerization to the matrix host may be due to the comparatively large volume of the rotating group compared to the host-matrix particles (either Ar atom or N₂ molecule).

4. Conclusions

In this study, the conformational space of the molecule of benzyloxy substituted *ortho*-OH substituted aryl Schiff base *trans* 2-((2-(benzyloxy)benzylidene)amino)phenol (BBAP) has been investigated by an extensive series of quantum chemical calculations, undertaken

within the density functional theory framework. Thirty-one distinct conformers of the compound were identified, with the three most stable conformers (I–III) having considerably lower energies than all the remaining forms. The most relevant intramolecular interactions in BBAP were evaluated and used to explain the relative energies of the different conformers, with emphasis given to the lowest-energy forms, whose relative energies stay within ca. 4 kJ mol^{-1} . These conformers differ in the geometry of the benzyloxy moiety, and are stabilized by an intramolecular O–H \cdots N hydrogen bond, established between the phenolic O–H group (as H-donor) and the azomethine nitrogen atom (as acceptor), and by the absence of significant steric hindrance.

The compound was synthesized from 2-aminophenol and 2-(benzyloxy)benzaldehyde and isolated in cryogenic argon and N₂ matrices. The three lowest-energy conformers (I–III) predicted theoretically have been successfully trapped into the low-temperature matrices (10 K), and the IR spectra of the compound in both solid Ar and N₂ have been assigned. Subsequently, in situ UV irradiation ($\lambda = 230 \text{ nm}$) of the matrix-isolated compound was carried on. It was concluded that the performed irradiation induced interconversions between the 3 low-energy conformers of BBAP initially present in the matrices, i.e., rotamerization within the benzyloxy group, while no evidence was found both for *trans*→*cis* (C=N) isomerization and enol-imine/keto-amine tautomerization. An explanation for the observed conformational population changes upon UV irradiation was proposed, which considered the attainment of a photo-stationary state upon irradiation, together with the different primary cages occupied by the reactant molecules. Conformer II has a considerably more open structure than conformers I and III and, thus, requires a much larger embedment volume in the matrices to accommodate the benzyloxy fragment, while conformer III requires the smallest volume among the three conformers. Since the photo-induced conformational changes shall take place without important changes of the original matrix-site morphology (which would cost a large amount of energy), volume constraints to the efficiency of the conformational conversions are maximized for those leading to formation of conformer II and minimized for those leading to conformer III, thus justifying the observed changes in the relative populations of the conformers, with that of II reducing and those of I and III increasing, with the last being the one increasing the most. To the best of our knowledge, this is the first report on UV-induced conformational changes taking place in a benzyloxy fragment of a matrix-isolated compound.

Supplementary Materials: The following supporting information can be downloaded at: <https://www.mdpi.com/article/10.3390/photochem2020026/s1>. Figures S1–S7 with IR, ¹H- and ¹³C-NMR spectra of BBAP, pictures of higher-energy conformers of BBAP, and TD-DFT(B3LYP)/6-311++G(d,p) calculated and experimental UV-vis spectrum of BBAP. Tables S1 and S2 with DFT(B3LYP)/6-311++G(d,p) calculated relative energies of the high-energy conformers of BBAP and proposed band assignments for the IR spectra of matrix-isolated BBAP (in Ar and N₂ matrices).

Author Contributions: H.B. synthesized the compound, performed its characterization by IR and NMR spectroscopies, and elemental analysis. Y.G.S. performed the DFT calculations. İ.S. and S.G. collected the experimental infrared spectra, performed the initial analysis of the data, and wrote the first draft of the manuscript. R.F. consolidated the data interpretation, and wrote the final draft of the manuscript. All authors have read and agreed to the published version of the manuscript.

Funding: This research received no external funding.

Acknowledgments: The authors greatly appreciate Bitlis Eren University Research Foundation for financial support (Projects BEBAP-2014.05 and BEBAP-2013.04) and for the computational facilities, the Portuguese Science Foundation (“Fundação para a Ciência e a Tecnologia”—FCT; Projects CQC-IMS UIDB/00313/2020 and UIDP/00313/2020—National Funds), and the Chemistry Department, Faculty of Sciences, Eskişehir Technical University.

Conflicts of Interest: The authors declare no conflict of interest.

References

1. Borisova, N.E.; Reshetova, M.D.; Ustyniuk, Y.A. Metal-Free Methods in the Synthesis of Macrocyclic Schiff Bases. *Chem. Rev.* **2007**, *107*, 46–79. [CrossRef] [PubMed]
2. Vigato, P.A.; Tamburini, S.; Bertolo, L. The development of compartmental macrocyclic Schiff bases and related polyamine derivatives. *Coord. Chem. Rev.* **2007**, *251*, 1311–1492. [CrossRef]
3. Emregül, K.C.; Düzgün, E.; Atakol, O. The application of some polydentate Schiff base compounds containing aminic nitrogens as corrosion inhibitors for mild steel in acidic media. *Corros. Sci.* **2006**, *48*, 3243–3260. [CrossRef]
4. Drozdak, R.; Allaert, B.; Ledoux, N.; Dragutan, I.; Dragutan, V.; Verpoort, F. Ruthenium complexes bearing bidentate Schiff base ligands as efficient catalysts for organic and polymer syntheses. *Coord. Chem. Rev.* **2005**, *249*, 3055–3074. [CrossRef]
5. Sessler, J.L.; Melfi, P.J.; Pantos, G.D. Uranium complexes of multidentate N-donor ligands. *Coord. Chem. Rev.* **2006**, *250*, 816–843. [CrossRef]
6. Yang, C.-J.; Jenekhe, S.A. Conjugated aromatic polyimines. 2. Synthesis, structure, and properties of new aromatic polyazomethines. *Macromolecules* **1995**, *28*, 1180–1196. [CrossRef]
7. Destri, S.; Khotina, I.A.; Porzio, W. 3-Hexyl Tetra-Substituted Sesquithienylene-Phenylene Polyazomethines with High Molecular Weight. Mechanistic Considerations. *Macromolecules* **1998**, *31*, 1079–1086. [CrossRef]
8. Grigoras, M.; Catanescu, O.; Simionescu, C.I. Poly(azomethine)s. *Rev. Roum. Chim.* **2001**, *46*, 927–939.
9. Kaya, I.; Vilayetoglu, A.R.; Mart, H. The synthesis and properties of oligosalicylaldehyde and its Schiff base oligomers. *Polymer* **2001**, *42*, 4859–4865. [CrossRef]
10. Wu, P.; Bhamidipati, M.; Coles, M.; Rao, D. Biological nano-ceramic materials for holographic data storage. *Chem. Phys. Lett.* **2004**, *400*, 506–510. [CrossRef]
11. Yuan, W.; Sun, L.; Tang, H.; Wen, Y.; Jiang, G.; Huang, W.; Jiang, L.; Song, Y.; Tian, H.; Zhu, D. A novel thermally stable spironaphthoxazine and its application in rewritable high density optical data storage. *Adv. Mater.* **2005**, *17*, 156–160. [CrossRef]
12. Yanez, C.O.; Andrade, C.D.; Yao, S.; Luchita, G.; Bondar, M.V.; Belfield, K.D. Photosensitive polymeric materials for two-photon 3D WORM optical data storage systems. *ACS Appl. Mater. Interfaces* **2009**, *1*, 2219–2229. [CrossRef] [PubMed]
13. Melloni, A.; Rossi Paccani, R.; Donati, D.; Zanirato, V.; Sinicropi, A.; Parisi, M.L.; Martin, E.; Ryazantsev, M.; Ding, W.J.; Frutos, L.M. Modeling, preparation, and characterization of a dipole moment switch driven by Z/E photoisomerization. *J. Am. Chem. Soc.* **2010**, *132*, 9310–9319. [CrossRef]
14. Staykov, A.; Watanabe, M.; Ishihara, T.; Yoshizawa, K. Photoswitching of conductance through salicylidene methylamine. *J. Phys. Chem. C* **2014**, *118*, 27539–27548. [CrossRef]
15. Dalapati, S.; Jana, S.; Guchhait, N. Anion recognition by simple chromogenic and chromo-fluorogenic salicylidene Schiff base or reduced-Schiff base receptors. *Spectrochim. Acta A Mol. Biomol. Spectrosc.* **2014**, *129*, 499–508. [CrossRef] [PubMed]
16. Zhang, X.; Yin, J.; Yoon, J. Recent advances in development of chiral fluorescent and colorimetric sensors. *Chem. Rev.* **2014**, *114*, 4918–4959. [CrossRef]
17. Hadjoudis, E.; Mavridis, I.M. Photochromism and thermochromism of Schiff bases in the solid state: Structural aspects. *Chem. Soc. Rev.* **2004**, *33*, 579–588. [CrossRef]
18. Amimoto, K.; Kawato, T. Photochromism of organic compounds in the crystal state. *J. Photochem. Photobiol. C Photochem. Rev.* **2005**, *6*, 207–226. [CrossRef]
19. Larkin, D.R. The role of catalysts in the air oxidation of aliphatic aldehydes. *J. Org. Chem.* **1990**, *55*, 1563–1568. [CrossRef]
20. Vančo, J.; Švajlenová, O.; Račanská, E.; Muselík, J.; Valentová, J. Antiradical activity of different copper (II) Schiff base complexes and their effect on alloxan-induced diabetes. *J. Trace Elem. Med. Biol.* **2004**, *18*, 155–161. [CrossRef]
21. Jarzabek, B.; Kaczmarczyk, B.; Sęk, D. Characteristic and spectroscopic properties of the Schiff-base model compounds. *Spectrochim. Acta. A Mol. Biomol. Spectrosc.* **2009**, *74*, 949–954. [CrossRef] [PubMed]
22. Raczuk, E.; Dmochowska, B.; Samaszko-Fierstek, J.; Madaj, J. Different Schiff Bases—Structure, Importance and Classification. *Molecules* **2022**, *27*, 787. [CrossRef] [PubMed]
23. Król-Starzomska, I.; Filarowski, A.; Rospenk, M.; Koll, A.; Melikova, S. Proton Transfer Equilibria in Schiff Bases with Steric Repulsion. *J. Phys. Chem. A* **2004**, *108*, 2131–2138. [CrossRef]
24. Minkin, V.I.; Tsukanov, A.V.; Dubonosov, A.D.; Bren, V.A. Tautomeric Schiff bases: Iono-, solvato-, thermo- and photochromism. *J. Mol. Struct.* **2011**, *998*, 179–191. [CrossRef]
25. Sıdır, Y.G.; Pırbudak, G.; Berber, H.; Sıdır, İ. Study on the electronic and photophysical properties of the substitute-((2-phenoxybenzylidene) amino) phenol derivatives: Synthesis, solvatochromism, electric dipole moments and DFT calculations. *J. Mol. Liq.* **2017**, *242*, 1096–1110. [CrossRef]
26. Sıdır, Y.G.; Berber, H.; Sıdır, İ. The Dipole Moments and Solvatochromism of ((4-(Benzyloxy) benzylidene) amino) phenol Compounds as Solvatochromic Materials. *J. Solut. Chem.* **2019**, *48*, 775–806. [CrossRef]
27. Sıdır, Y.G.; Aslan, C.; Berber, H.; Sıdır, İ. The electronic structure, solvatochromism, and electric dipole moments of new Schiff base derivatives using absorbance and fluorescence spectra. *Struct. Chem.* **2019**, *30*, 835–851. [CrossRef]
28. Avadanei, M.; Cozan, V.; Shova, S.; Paixão, J.A. Solid state photochromism and thermochromism of two related N-salicylidene anilines. *Chem. Phys.* **2014**, *444*, 43–51. [CrossRef]
29. Sıdır, İ.; Sıdır, Y.G.; Göbi, S.; Berber, H.; İldiz, G.O.; Fausto, R. UV-induced –OCH₃ rotamerization in a matrix-isolated methoxy-substituted ortho-hydroxyaryl Schiff base. *Photochem. Photobiol. Sci.* **2022**. [CrossRef]

30. Sıdır, İ.; Gülseven Sıdır, Y.; Góbi, S.; Berber, H.; Fausto, R. Structural Relevance of Intramolecular H-Bonding in Ortho-Hydroxyaryl Schiff Bases: The Case of 3-(5-bromo-2-hydroxybenzylideneamino) Phenol. *Molecules* **2021**, *26*, 2814. [CrossRef]
31. Frisch, M.; Trucks, G.W.; Schlegel, H.B.; Scuseria, G.E.; Robb, M.A.; Cheeseman, J.R.; Scalmani, G.; Barone, V.; Mennucci, B.; Petersson, G.A.; et al. *Gaussian 09*; Gaussian, Inc.: Wallingford, CT, USA, 2009.
32. Becke, A.D. Density-functional exchange-energy approximation with correct asymptotic behavior. *Phys. Rev. A* **1988**, *38*, 3098–3100. [CrossRef] [PubMed]
33. Lee, C.; Yang, W.; Parr, R.G. Development of the Colle-Salvetti correlation-energy formula into a functional of the electron density. *Phys. Rev. B Condens. Matter* **1988**, *37*, 785–789. [CrossRef] [PubMed]
34. Vosko, S.H.; Wilk, L.; Nusair, M. Accurate spin-dependent electron liquid correlation energies for local spin density calculations: A critical analysis. *Can. J. Phys.* **1980**, *58*, 1200–1211. [CrossRef]
35. McLean, A.D.; Chandler, G.S. Contracted Gaussian basis sets for molecular calculations. I. Second row atoms, $Z = 11$ –18. *J. Chem. Phys.* **1980**, *72*, 5639–5648. [CrossRef]
36. Krishnan, R.; Binkley, J.S.; Seeger, R.; Pople, J.A. Self-consistent molecular orbital methods. XX. A basis set for correlated wave functions. *J. Chem. Phys.* **1980**, *72*, 650–654. [CrossRef]
37. Frisch, M.J.; Pople, J.A.; Binkley, J.S. Self-consistent molecular orbital methods 25. Supplementary functions for Gaussian basis sets. *J. Chem. Phys.* **1984**, *80*, 3265–3269. [CrossRef]
38. Chemcraft—Graphical Program for Visualization of Quantum Chemistry Computations. Available online: <https://www.chemcraftprog.com/> (accessed on 3 January 2022).
39. Bauernschmitt, R.; Ahlrichs, R. Treatment of electronic excitations within the adiabatic approximation of time dependent density functional theory. *Chem. Phys. Lett.* **1996**, *256*, 454–464. [CrossRef]
40. Stratmann, R.E.; Scuseria, G.E.; Frisch, M.J. An efficient implementation of time-dependent density-functional theory for the calculation of excitation energies of large molecules. *J. Chem. Phys.* **1998**, *109*, 8218–8224. [CrossRef]
41. Reva, I.D.; Stepanian, S.G.; Adamowicz, L.; Fausto, F. Missing Conformers: Comparative Study of Conformational Cooling in Cyanoacetic Acid and Methyl Cyanoacetate Isolated in Low Temperature Inert Gas Matrixes. *Chem. Phys. Lett.* **2003**, *374*, 631–638. [CrossRef]
42. Rosado, M.T.S.; Lopes Jesus, A.J.; Reva, I.D.; Fausto, R.; Redinha, J.S. Conformational Cooling Dynamics in Matrix-Isolated 1,3-butanediol. *J. Phys. Chem. A* **2009**, *113*, 7499–7507. [CrossRef]

Article

Phototransformations of 2,3-Diamino-2-Butenedinitrile (DAMN) Monomers Isolated in Low-Temperature Argon Matrix

 Igor Reva ^{1,*}, Hanna Rostkowska ² and Leszek Lapinski ²
¹ University of Coimbra, CIEPQPF, Department of Chemical Engineering, 3030-790 Coimbra, Portugal

² Institute of Physics, Polish Academy of Sciences, Al. Lotników 32/46, 02-668 Warszawa, Poland; rostk@ifpan.edu.pl (H.R.); lapin@ifpan.edu.pl (L.L.)

* Correspondence: reva@eq.uc.pt

Abstract: UV-induced transformations were studied for monomers of 2,3-diamino-2-butenedinitrile (DAMN) isolated in argon matrices. Photoinduced hydrogen-atom transfer was found to be the major process occurring upon UV ($\lambda > 320$ nm or $\lambda > 295$ nm) excitation of matrix-isolated DAMN monomers. As a result of the transfer of a hydrogen atom from an amino group to a nitrile fragment, a tautomer of DAMN involving a ketenimine group was generated. Identification of this photo-produced species was based on comparison of its experimental IR spectrum with the spectrum theoretically predicted for the ketenimine form. Another product photogenerated upon UV ($\lambda > 320$ nm, $\lambda > 295$ nm, or $\lambda > 270$ nm) irradiation of DAMN isolated in Ar matrices was identified as 4-amino-1H-imidazole-5-carbonitrile (AICN). The structure of this photoproduct was unambiguously assigned on the basis of an exact match of wavenumbers of the bands in the IR spectrum of this photogenerated species and the wavenumbers of IR bands of AICN trapped (in a separate experiment) from the gas phase into an Ar matrix.

Keywords: photochemistry; IR spectra; matrix isolation; DAMN; AICN; ketenimine; hydrogen-atom transfer

Citation: Reva, I.; Rostkowska, H.; Lapinski, L. Phototransformations of 2,3-Diamino-2-Butenedinitrile (DAMN) Monomers Isolated in Low-Temperature Argon Matrix. *Photochem* **2022**, *2*, 448–462. <https://doi.org/10.3390/photochem2020031>

Academic Editor: Elena Cariati

Received: 30 May 2022

Accepted: 14 June 2022

Published: 16 June 2022

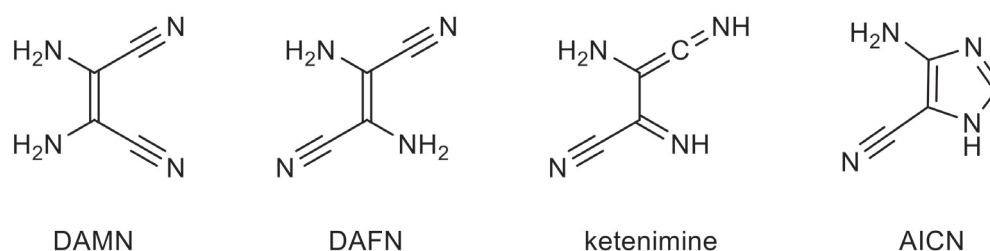
Publisher's Note: MDPI stays neutral with regard to jurisdictional claims in published maps and institutional affiliations.



Copyright: © 2022 by the authors. Licensee MDPI, Basel, Switzerland. This article is an open access article distributed under the terms and conditions of the Creative Commons Attribution (CC BY) license (<https://creativecommons.org/licenses/by/4.0/>).

1. Introduction

2,3-Diaminomaleonitrile (DAMN) and 2,3-diaminofumaronitrile (DAFN) are the *cis* and *trans* isomers of 2,3-diamino-2-butenedinitrile (Scheme 1). According to their formula, $C_4N_4H_4$, these compounds can be treated as tetramers of HCN. Indeed, DAMN has been identified as one of the products of HCN polymerization [1–6]. Moreover, it was demonstrated that DAMN transforms to DAFN in the very well-known *cis*–*trans* photoisomerization process [7]. Then, this *trans* isomer (DAFN) can photochemically convert [8–11] into the cyclic imidazole derivative (4-amino-1H-imidazole-5-carbonitrile AICN, Scheme 1). The photoinduced DAMN-to-DAFN isomerization and formation of AICN are believed to play a key role in the formation of purine nucleobases on early Earth [9–13].



Scheme 1. The *cis* (DAMN) and *trans* (DAFN) isomers of 2,3-diamino-2-butenedinitrile, their ketenimine tautomer, and 4-amino-1H-imidazole-5-carbonitrile (AICN).

The mechanistic description of the photoprocess transforming DAMN/DAFN into AICN was the subject of several experimental and theoretical studies [11,13]. Different molecular structures were proposed as potential intermediates on the route from DAMN/DAFN to AICN. One of such structures is ketenimine (Scheme 1) resulting from the photoinduced intramolecular hydrogen-atom transfer in DAFN. However, conversion of an enaminonitrile (such as DAMN/DAFN) to a structure with the imidazole ring must involve not only hydrogen-atom transfer processes, but also cleavage of one of the CC bonds and formation of a new CN bond. That is why structures with four-membered ring (azetines) or with three-membered-ring (azirines) should also be considered as potential intermediates involved in the photoinduced DAMN/DAFN \rightarrow AICN process.

In the current work, the photoinduced transformations were studied for monomeric DAMN molecules isolated in low-temperature argon matrices. One of the goals of the present study was a reliable identification of a ketenimine tautomer (Scheme 1) as a product of phototransformations of the DAMN molecules. The experimental investigation was also aimed at finding convincing spectral indications of the photochemical DAMN/DAFN \rightarrow AICN transformation.

2. Experimental Methods

Samples of the compounds investigated in the current study, 2,3-diamino-maleonitrile (DAMN) purity > 98%, and 4-amino-1*H*-imidazole-5-carbonitrile (AICN) purity > 95%, were purchased from Sigma-Aldrich. Before a matrix-isolation experiment, a solid sample of a studied compound was placed in a miniature glass oven located inside the vacuum chamber of a cryostat with a Sumitomo SRDK-408D2 closed-cycle cooler. Then, the cryostat was evacuated, and the solid compound was heated by a resistive wire wrapped around the glass oven. The vapor of the compound was deposited, together with large excess of argon, onto a CsI window cooled to 12 K. The mid-IR spectra were recorded in the 4000–500 cm^{-1} range with 0.5 cm^{-1} resolution using a Thermo Nicolet iS50R FTIR spectrometer equipped with a KBr beam splitter and a DTGS detector with a KBr window. The spectra in the lower-wavenumber 700–300 cm^{-1} range were recorded using the same spectrometer but with a “solid substrate” beam splitter and a DTGS detector with a polyethylene window. Matrix-isolated monomers of the studied compounds were irradiated with UV light from a high-pressure mercury lamp fitted with a water filter and an appropriate cut-off Schott filter (WG360, WG335, WG320, WG295, or UG11 transmitting light with $\lambda > 360$ nm, $\lambda > 335$ nm, $\lambda > 320$ nm, $\lambda > 295$ nm, or $\lambda > 270$ nm, respectively).

3. Computational Details

Geometries of DAMN and DAFN molecules, as well as geometries of the species that may be generated upon UV irradiation of DAMN/DAFN, were fully optimized at the DFT(B3LYP) level of theory [14–16]. At the optimized geometries, harmonic vibrational frequencies and infrared intensities were computed at the same DFT (B3LYP) level. To approximately correct for the neglected anharmonicity, the harmonic DFT frequencies were scaled by factors of 0.950 (for wavenumbers higher than 3200 cm^{-1}) and 0.980 (for wavenumbers lower than 1800 cm^{-1}), used in our previous works [17,18]. For wavenumbers from the 3200–1800 cm^{-1} range, we used a factor of 0.957, obtained from the ratio between the frequency of the standalone band due to the C \equiv N stretching mode observed in this work for matrix-isolated DAMN (2225 cm^{-1}) and the frequency of the respective mode computed for the DAMN monomer (2324 cm^{-1}). These data were used to simulate the IR spectra using the ChemCraft software [19]. The peaks centered at the scaled wavenumbers were convoluted with Lorentzian functions having a full width at half-maximum (fwhm) equal to 2 cm^{-1} and peak heights equal to the computed infrared intensities. The above theoretical computations were carried out with the Gaussian 09 set of programs [20], using the standard 6-311++G(d,p) basis set [21–23].

For the estimation of the isomerization barriers, the geometries of the respective transition states (TS) were fully optimized [24,25]. The harmonic vibrational frequencies were

computed at the DFT (B3LYP)/6-311++G(d,p) level of theory to verify that the found stationary point has one imaginary frequency. Thereafter, we mapped out the intrinsic reaction coordinate (IRC) [26], starting from the TS in both directions, until a local minimum was detected on each side. For the IRC following, we employed the Hessian-based predictor-corrector integrator in the Cartesian (non-mass-weighted) coordinate system as implemented in the Gaussian 16 electronic structure package [27]. This allowed a comparison of the shapes of different barriers, expressed in the generalized multidimensional coordinates.

Vertical excitation energies of the low-energy electronic excited singlet states were computed at the same DFT(B3LYP)/6-311++G(d,p) level, using time-dependent DFT approach [28,29]. For the graphical representation, each computed electronic transition was convoluted with a Lorentzian function having a half width at half-maximum (hwhm) equal to 0.248 eV (2000 cm^{-1}).

4. Results

4.1. Molecular Structures of DAMN and DAFN

Optimization of the structure of DAMN (the *cis* isomer of 2,3-diamino-2-butenedinitrile), performed at the DFT(B3LYP)/6-311++G(d,p) level, led to identification of only one minimum on the potential energy surface (PES). This minimum corresponds to the structure with the C_2 symmetry axis (Figure 1). In such a structure, the amino groups are symmetrically involved in a cyclic hydrogen-bond-like intramolecular interaction. This interaction may be similar to that found in the ammonia dimer [30–33].

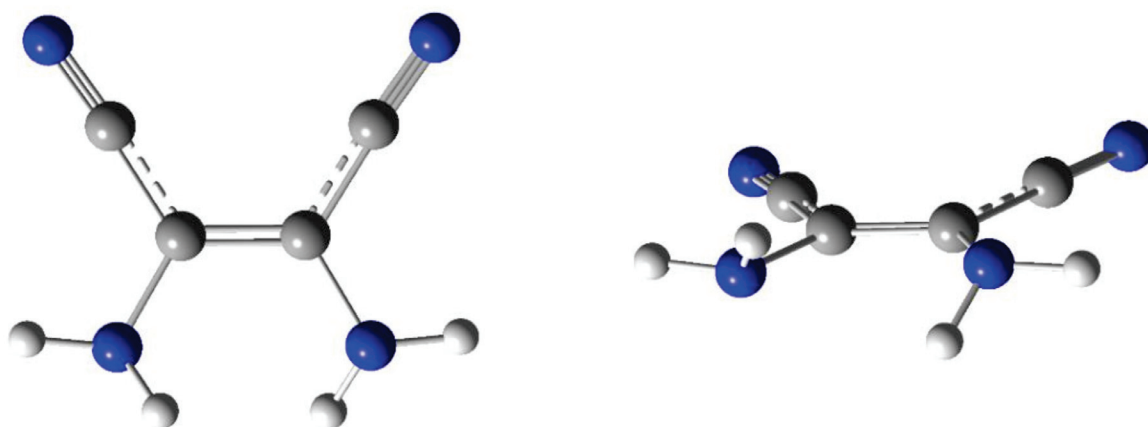


Figure 1. Optimized geometry of the DAMN molecule: two projections of the lowest-energy form with C_2 symmetry. Color codes: blue—nitrogen, gray—carbon, white—hydrogen.

Two low-energy minima were found on the PES of DAFN (the *trans* isomer of 2,3-diamino-2-butenedinitrile). These minima correspond to nearly planar structures of the molecule; however, in both of them, the amino groups are slightly pyramidal. In the lowest-energy structure, the lone electron pairs of the NH_2 nitrogen atoms point to the same side of the “plane” formed by the heavy atoms. This structure belongs to the C_2 symmetry group (Figure 2 and Appendix A, Figure A1). The other structure has a center of symmetry and belongs to the C_i symmetry group. In this form, the lone electron pairs of the NH_2 nitrogen atoms point to the opposite sides of the approximate plane of the DAFN molecule. The energy of this latter C_i form is only slightly higher (by 0.46 kJ mol^{-1} , including the zero-point vibrational energy correction) than the energy of the C_2 structure.

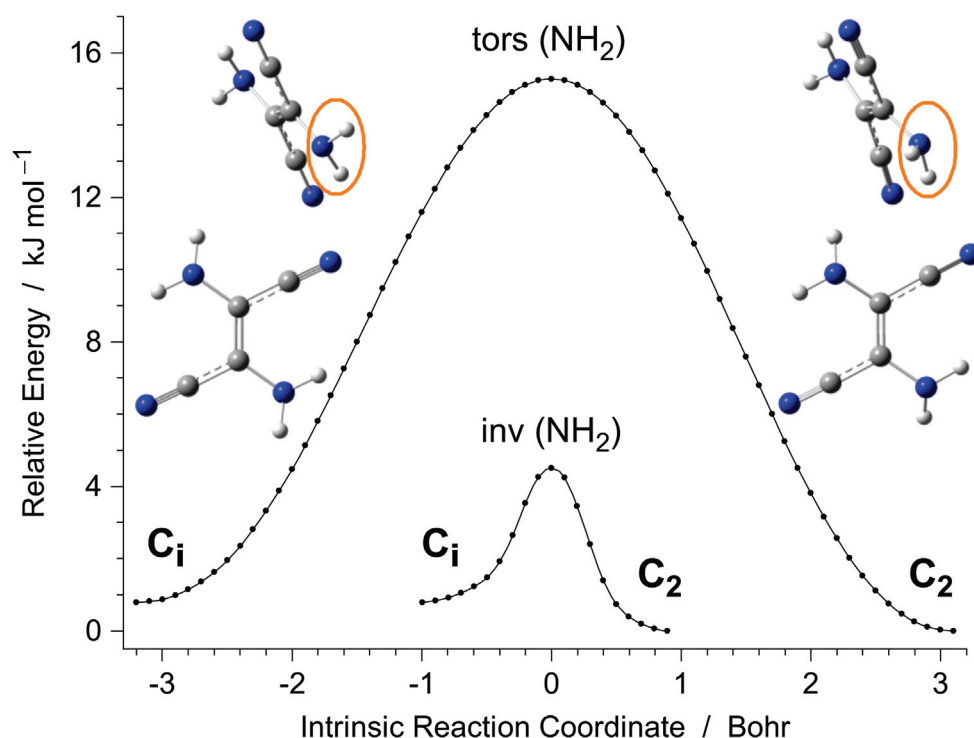


Figure 2. Potential energy minima due to C_i and C_2 structures of DAFN. The barriers separating these minima were computed at the DFT(B3LYP)/6-311++G(d,p) level by following the PES of the DAFN system along the torsional (tors) or inversional (inv) intrinsic reaction coordinate. The insets show the geometries of two DAFN minima, with emphasis (orange ovals) on the one amino group which changes the pyramidalization. Color codes: blue—nitrogen, gray—carbon, white—hydrogen.

Transition of one of these forms into the other by rotation of one of the amino groups around the C–N bond is related with a moderately high ($\sim 15 \text{ kJ mol}^{-1}$) barrier. However, the transition between the C_2 and C_i structures by inversion of one of the amino groups is related with such a low barrier (4.5 kJ mol^{-1}) that its crossing would occur on the subpicosecond time scale. Hence, both the C_2 and C_i structures can be treated as a single quasiplanar form of the real DAFN molecule. Existence of the two closely lying C_2 and C_i minima on the PES of DAFN should result in distortions of the shape of the multidimensional potential energy well. This is expected to make some vibrations of the molecule significantly anharmonic.

4.2. Infrared Spectrum of DAMN Isolated in Low-Temperature Ar Matrices

The infrared spectrum of DAMN monomers isolated in an Ar matrix is presented in Figure 3. This spectrum is well reproduced by the results of theoretical calculation carried out at the DFT (B3LYP)/6-311++G(d,p) level for DAMN structure with C_2 symmetry.

In the high-wavenumber region of the experimental spectrum, the bands due to anti-symmetric stretching vibrations of the NH_2 groups appear at 3470 and 3459 cm^{-1} , whereas the bands due to symmetric stretching vibrations of the NH_2 groups appear at 3367 and 3362 cm^{-1} . In the above descriptions, “antisymmetric” and “symmetric” terms refer to local symmetry of each of the NH_2 groups. The characteristic band due to the stretching vibration of the triple $\text{C}\equiv\text{N}$ bond appears at 2225 cm^{-1} in the spectral region free of any other IR bands. Typically, the stretching modes of the triple $\text{C}\equiv\text{N}$ bonds in nitriles give rise to weak bands in IR spectra [34]. However, a relatively high IR intensity ($103.7 \text{ km mol}^{-1}$) of the $\text{C}\equiv\text{N}$ stretching mode in DAMN results from the antisymmetric coupling of stretching modes due to two nitrile groups. The other (symmetric) coupling gives rise to the mode with much lower IR-intensity (12.8 km mol^{-1}). Strong IR bands assigned to the NH_2 scissoring vibrations are found in the experimental spectrum at 1640 , 1620 , and 1601 cm^{-1} .

A fingerprint pattern of the bands at 1357, 1295, and 1234 cm^{-1} is formed by three IR absorptions due to the NH_2 rocking vibrations coupled with the stretching vibrations of the single C–N bonds. This pattern of three bands is very well reproduced by the theoretical calculations. In the spectral range below 750 cm^{-1} , there are significant discrepancies between the bands observed in the experimental spectrum and the pattern of bands predicted by theoretical calculation carried out within the harmonic approximation. The reason for that is the contribution of the NH_2 vibrations in the inversional direction (together with the C–C \equiv N bending vibrations) to the normal modes with frequencies lower than 750 cm^{-1} . The vibrational modes involving NH_2 inversional movement are usually quite poorly reproduced by the calculations performed within the harmonic approximation. Moreover, the commonly used perturbational approach to correct for anharmonicity fails to help in such cases.

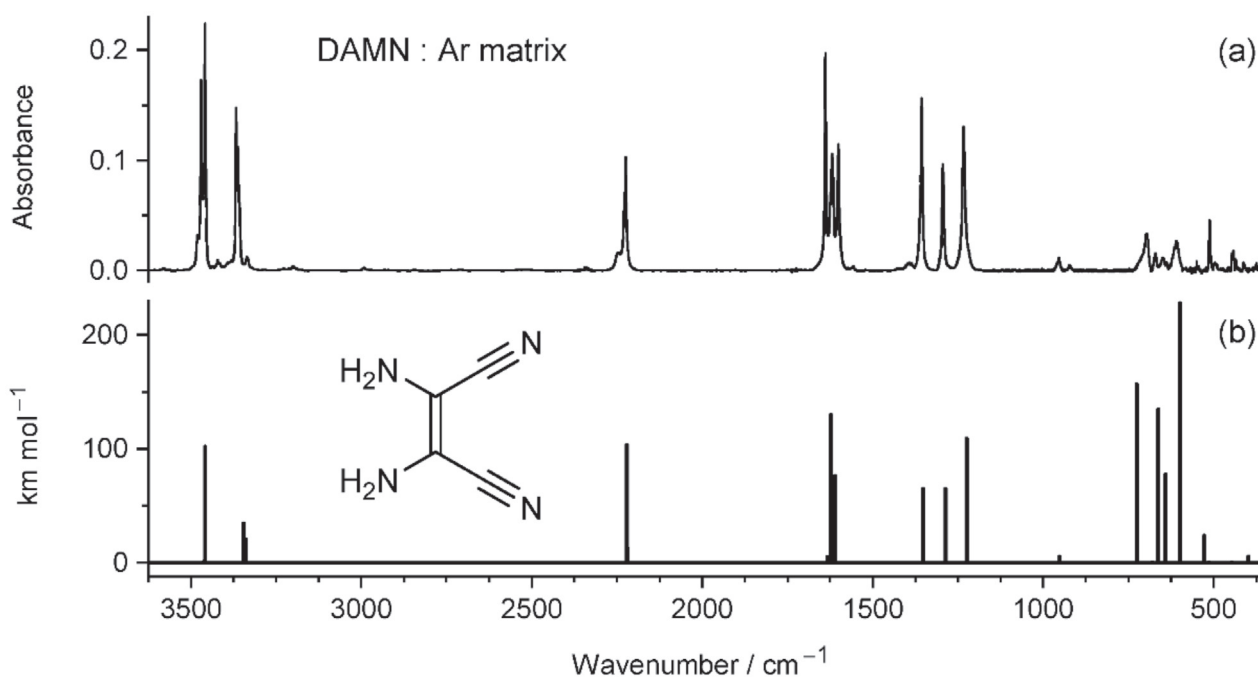


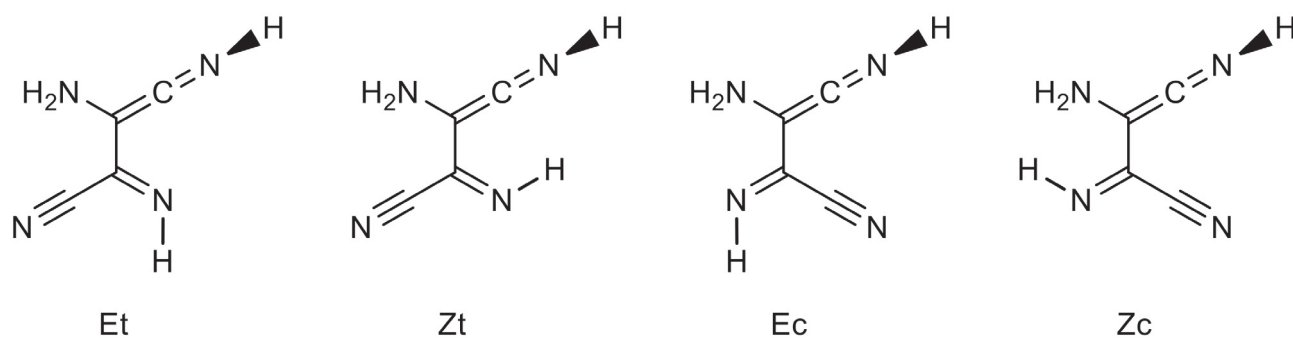
Figure 3. (a) Infrared spectrum of 2,3-diaminomaleonitrile (DAMN) monomers isolated in an Ar matrix at 12 K, compared with (b) theoretical IR spectrum of this compound computed at the DFT (B3LYP)/6-311++G(d,p) level.

4.3. Photoproducts Generated upon UV Excitation of Matrix-Isolated DAMN

Monomers of DAMN isolated in an Ar matrix at 12 K were exposed to UV light of different wavelengths, limited from the short-wavelength side by an appropriate cut-off filter. Irradiation of matrix-isolated DAMN with UV light ($\lambda > 360$ nm or $\lambda > 335$ nm) did not result in any photochemical transformations of the compound. Exposure of the matrix to UV ($\lambda > 320$ nm) radiation induced a very slow decrease of the IR bands due to the DAMN reactant and appearance of a set of new IR bands. The observed photochemical changes were more vigorous when the matrix was exposed to UV ($\lambda > 295$ nm) light.

In the spectrum of the photoproducted species, the most appealing is the intense IR absorption at 2026 cm^{-1} (Figure 4). The wavenumber of this band is characteristic of the “antisymmetric” stretching vibration of the C=C=N fragment in the –C=C=N–H ketenimine group [35–41]. The frequency of this vibration is well predicted by the theoretical calculations carried out for the ketenimine tautomer of DAMN/DAFN. In addition, a high IR intensity (605–535 km mol^{-1}) was theoretically predicted in agreement with the experimental observation. This suggests that ketenimine photoproduct was generated upon UV excitation by hydrogen-atom transfer from an amino group to the nitrogen atom of one of the C \equiv N groups. Another intense IR band appears in the spectrum of the photoproducted

species at 906 cm^{-1} . This band can be assigned to the bending of the $\text{C}=\text{N}-\text{H}$ fragment of the $-\text{C}=\text{C}=\text{N}-\text{H}$ ketenimine group. A medium-intensity band found at 1572 cm^{-1} is due to the stretching vibration of the $\text{C}=\text{N}$ bond in the $-\text{C}=\text{NH}$ imine group. The overall agreement between the IR spectrum theoretically predicted for the ketenimine form of DAMN/DAFN and the spectrum of the new IR bands appearing after UV irradiation of matrix isolated DAMN confirms that the ketenimine tautomer is the main product generated in this process.



Scheme 2. Structures of main isomers of ketenimine; (i) E/Z stands for the anti/syn orientations of the imine group; (ii) *t/c* stands for the *trans/cis* configuration around the central CC bond (see text for details). See Appendix B, Figure A2 for the optimized geometries, including the pairs of structures with different orientations of the amino group.

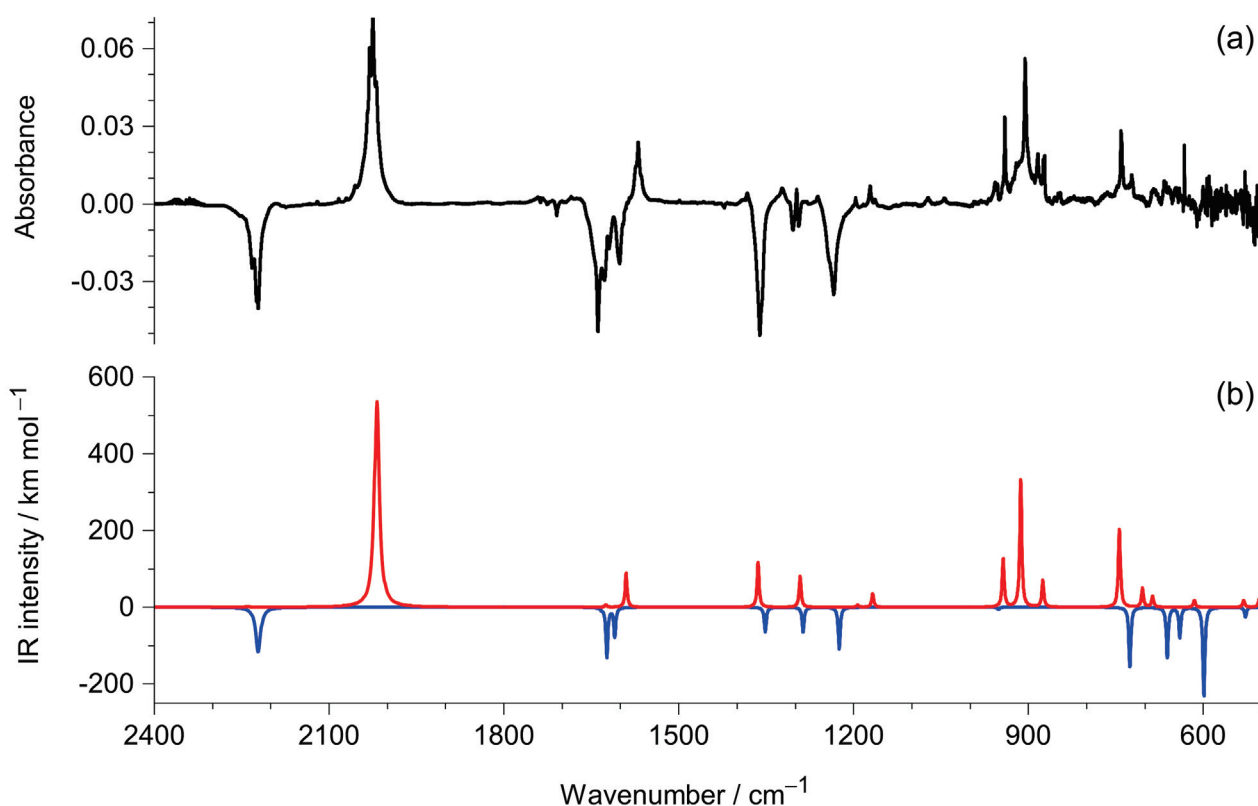


Figure 4. (a) Infrared spectrum recorded after UV ($\lambda > 295\text{ nm}$) irradiation of DAMN monomers isolated in an Ar matrix minus infrared spectrum recorded immediately after deposition of the matrix; (b) Theoretical spectra of DAMN (blue) and ketenimine (red) Zt isomer (see Scheme 2) computed at the DFT (B3LYP)/6-311++G(d,p) level. The intensities of the theoretical bands predicted for the DAMN molecule were multiplied by -1 .

In all possible structures of the ketenimine form of DAMN/DAFN, the hydrogen atom of the $-C=C=N-H$ group always adopts a perpendicular orientation (designated as a wedge NH bond in Scheme 2) with respect to the approximate plane of the heavy atoms [42,43]. Apart from this, in the molecules adopting ketenimine tautomeric form, there are three further degrees of conformational freedom: (i) flip of the N–H bond in the $-C=N-H$ imine group, which can assume Z or E orientation with respect to the central C–C bond, (ii) torsion around the central C–C bond, which can assume *trans* or *cis* orientation with respect to the position of the $-NH_2$ and $=NH$ groups, (iii) torsional (or inversional) movements of hydrogen atoms in the $-NH_2$ group (see Scheme 2).

Different orientation with respect to the (i) and (ii) degrees of freedom can give rise to four different isomers/conformers of the molecule adopting the ketenimine tautomeric form (see Appendix B, Figure A2). In each of these four structures, an easy tunneling of light hydrogen atoms with respect to the (iii) degree of freedom should readily lead to collapse of the higher-energy formal conformer to the lower-energy structure differing by torsion (or inversion) of the hydrogen atoms in the $-NH_2$ group. Therefore, under the experimental conditions, the molecule in the ketenimine tautomeric form can adopt four different isomers. The infrared bands appearing at 2055, 2030, and 2019 cm^{-1} as satellites of the most intense band at 2026 cm^{-1} can be the spectral indications of different isomers/conformers of the molecule adopting the ketenimine tautomeric form. Alternatively, the multiplet structure of the ketenimine IR band appearing in the 2055–2019 cm^{-1} range may be attributed to the site-splitting. Similar split bands of conformationally rigid ketenimines were reported earlier [39,41,44].

Upon irradiation of an Ar matrix containing the DAMN monomers at wavelengths from the $270 < \lambda < 320$ nm range, a set of new IR bands emerged at 3528, 3488, 3430, 2219, 1622, 1574, 1458, 1439, 1375, 1247, 1184, and 1109 cm^{-1} . The spectral positions of these bands were compared with the positions of the bands observed in the spectrum of 4-amino-1*H*-imidazole-5-carbonitrile (AICN) monomers trapped (in a separate experiment) from the gas phase into an Ar matrix. Very good match (Figure 5) of wavenumbers of the IR bands observed in both experiments demonstrates that AICN was generated upon UV excitation of DAMN.

AICN may adopt two tautomeric forms differing in the position of the hydrogen atom attached to one of the imidazole ring nitrogen atoms. In the literature, there are discrepancies regarding the nature of the AICN tautomer resulting from photo-transformations of DAMN. In early and influential works of Ferris and co-authors [1,2,8–12,45], the AICN tautomer is graphically presented as having the labile H-atom attached to the ring N-atom vicinal to the amino group (see Figure 6c). In other works [46–48], the AICN tautomer is graphically presented as having the labile H-atom attached to the ring N-atom vicinal to the nitrile group (see Figure 6b). Therefore, it seemed to us instructive to verify the tautomeric structure of AICN in the context of the present study, both experimentally and computationally.

Comparison of the IR spectra theoretically computed for the two tautomeric forms of AICN with the experimental spectrum of AICN monomers isolated in an Ar matrix (Figure 6a) shows that the compound trapped from the gas phase adopts the lower-energy structure with the labile hydrogen atom attached to the nitrogen atom vicinal to the nitrile group. Thus, this tautomeric form was generated upon excitation of matrix-isolated DAMN with UV ($270 < \lambda < 320$ nm) light.

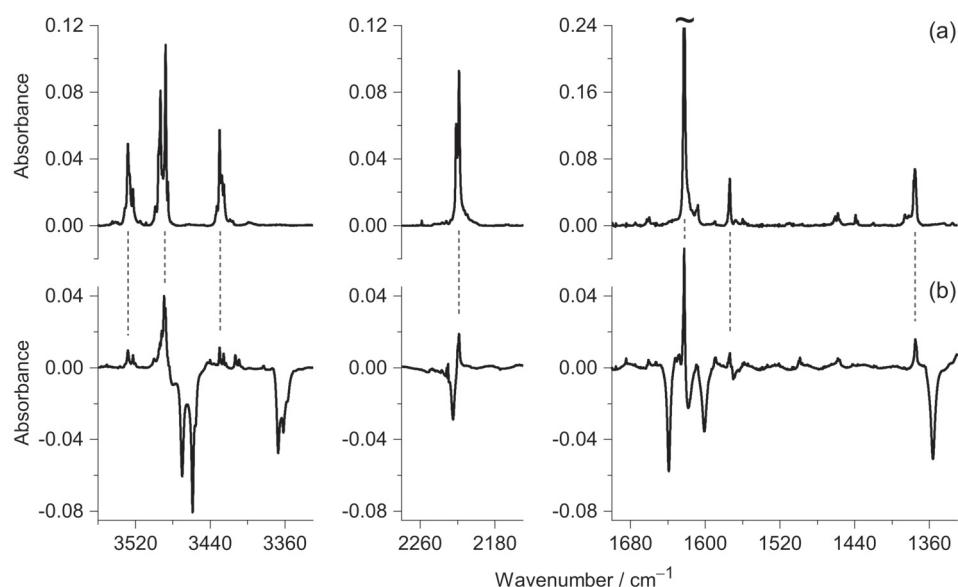


Figure 5. Experimental identification of AICN. (a) IR spectrum of AICN monomers trapped (in a separate experiment) from the gas phase into an Ar matrix; (b) Difference spectrum: the spectrum recorded after prolonged UV ($\lambda > 295$ nm) irradiation of matrix-isolated DAMN monomers minus the spectrum recorded before that irradiation. In this difference spectrum, the positive bands are due to photogenerated products and the negative bands are due to the consumed DAMN reactant. Dashed lines between the spectra in the top and bottom frames connect the strongest bands of AICN and their counterparts observed in the spectrum of products photogenerated from DAMN. Tilde (top-right frame) indicates that the strongest IR band of AICN is truncated.

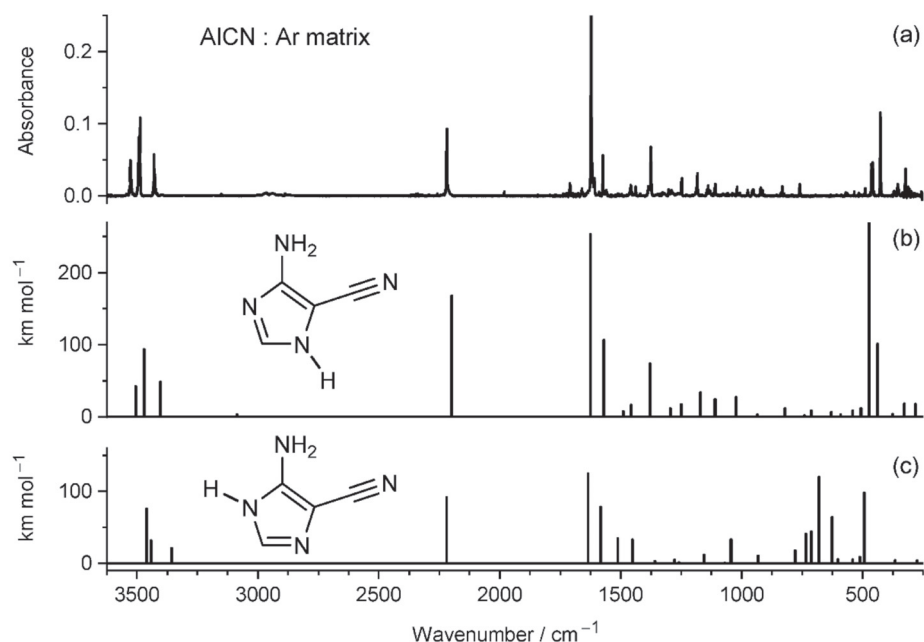
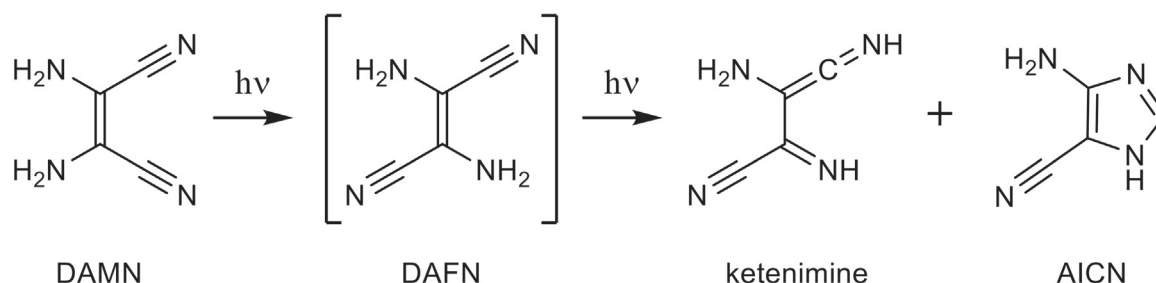


Figure 6. Comparison of (a) the experimental infrared spectrum of AICN monomers isolated in an Ar matrix at 12 K with theoretical infrared spectra of two tautomers of the compound computed at the DFT (B3LYP)/6-311++G(d,p) level: (b) 4-amino-1*H*-imidazole-5-carbonitrile, and (c) 5-amino-1*H*-imidazole-4-carbonitrile.

5. Discussion

The photochemical generation of ketenimine and AICN isomers was observed within the current work to occur upon UV excitation of DAMN. It looks quite probable that these photochemical processes should rely upon the generation of DAFN as an intermediate (see Scheme 3).



Scheme 3. Photoinduced transformations of matrix-isolated DAMN molecules.

The photoinduced isomerizations about double bonds have been of particular interest because they represent the simplest way of converting UV light into mechanical motion [49,50]. The *cis-trans* photoisomerizations were experimentally observed [51–55], and theoretically studied [55–58] for ethylene, stilbene, and azobenzene, where the isomers differ by orientation of the substituents about double bonds. The role of conical intersection of the ground and first excited states in the *cis-trans* photoisomerization is discussed in the works of Minezawa and Gordon [59,60]. In the particular case of the DAMN-to-DAFN transformation, the role of these conical intersections was theoretically studied by Szabla et al. [61]. Valiev et al. pointed out the importance of anharmonic effects for internal conversion between electronic states with the same spin multiplicity when the molecule contains accepting X–H stretching modes with a vibrational energy larger than 2000 cm^{-1} [62]. The alternative mechanism involving intersystem crossing to the triplet states is discussed for the *cis-trans* photoisomerizations in the works of Knuts et al. [63], Plachkevych et al. [64], and Szabla et al. [61].

Koch and Rodehorst [65] carried out a quantitative investigation of the photochemical conversion of DAMN into DAFN in methanol solution at $30\text{ }^\circ\text{C}$. Irradiation of DAMN with RPR-3000 Å lamps through Pyrex glass led to formation of a photostationary ratio of 80% of DAFN and 20% of DAMN [65]. However, it should be noted that under the matrix-isolation conditions of the present study, in the course of irradiations of DAMN, the formation of DAFN has not been verified. We previously studied UV-induced photochemical reactions of six-membered heterocycles, such as α -pyrone [66] or its sulfur analogues [67]. Upon UV irradiations of α -pyrone, we observed the ring-opening reactions leading to generation of the conjugated aldehyde-ketene, $\text{O}=\text{CH}-\text{CH}=\text{CH}-\text{CH}=\text{C}=\text{O}$. Subsequently, for the matrix-isolated conjugated aldehyde-ketene [66] as well as for its sulfur analogue [67], we observed the Z-E isomerizations around the central C=C bond. As it was demonstrated by using UV light filtered with different cut-off filters, the directions of the observed Z-E isomerization photoprocesses are dependent on the wavelength of the incident UV light. Here we should note that the molecules of aldehyde-ketene have a size similar to DAMN, DAFN, or AICN. Therefore, the lack of observation of DAFN in the present work should not be attributed to the spatial limitations induced by the cryogenic matrix, but rather to the different UV-absorptions of the involved species. With this idea in mind, we computed the lowest electronic singlet transitions of the relevant species and simulated their UV spectra, presented in Figure 7.

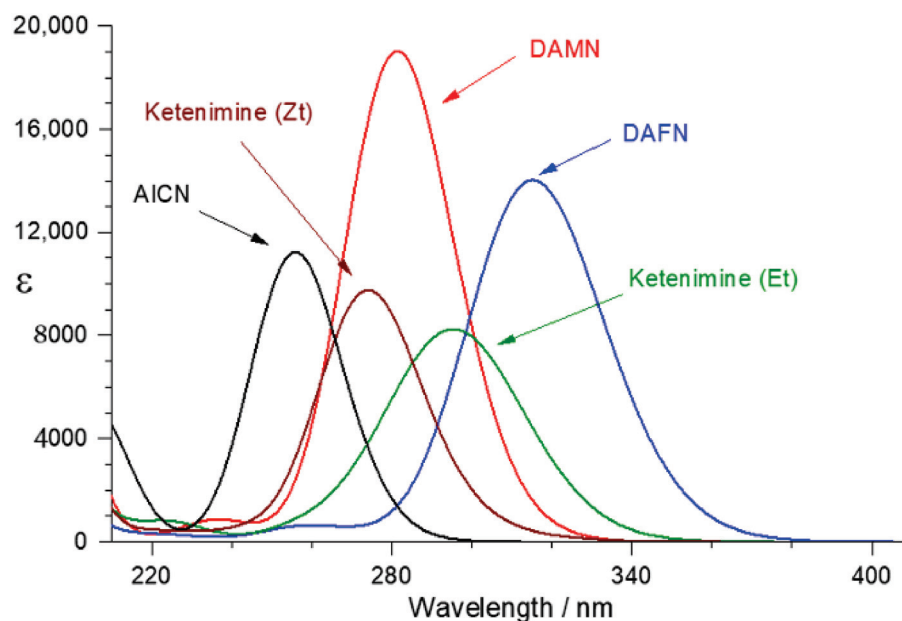


Figure 7. Simulated UV spectra of DAMN (red), DAFN (blue), ketenimine Zt and Et forms (brown and green, respectively), as well as 4-amino-1*H*-imidazole-5-carbonitrile (AICN, black), obtained from vertical transition energies determined by TD-DFT calculations at the B3LYP/6-311++G(d,p) level. Each computed transition was convoluted with a Lorentzian function having an hwhm of 0.248 eV (2000 cm^{-1}).

From the analysis of Figure 7, it immediately becomes clear why DAFN was not observed in the present work. This species has the longest wavelength absorption compared to any other isomer. Therefore, DAFN should be very photoreactive and will be consumed by the UV-light ($\lambda > 320$ nm or $\lambda > 295$ nm) which is used to promote DAMN or ketenimine to their electronically excited states. Analysis of Figure 7 also suggests that the ketenimine Zt isomer has higher probability of being accumulated in the cryomatrix (rather than the Et form, absorbing at longer wavelengths). In fact, it is the Zt isomer of ketenimine whose computed IR spectrum (Figure 4) best reproduces the observed experimental IR spectrum of the photoproducted ketenimine. The other isomer (Et) was not observed. Finally, the computed UV-spectra explain why the five-membered ring isomer (AICN) accumulated in the sample upon UV-irradiations at shorter wavelengths: it should be less affected by the filtered UV-irradiation ($\lambda > 295$ nm or $\lambda > 270$ nm) that consumes DAMN and also consumes the ketenimine at the more advanced stages of the experiment.

6. Conclusions

Experimental investigations carried out in the present work for matrix-isolated monomers of DAMN (2,3-diamino-2-butenedinitrile) led to identification of two products generated upon UV irradiation of the compound.

One of these photoproducts (the ketenimine tautomer of the compound, Scheme 3) was very reliably identified not only based on the characteristic ketenimine band appearing at 2026 cm^{-1} in the IR spectrum recorded after UV irradiation, but also on the basis of a good agreement between the whole IR spectrum of the photogenerated product and the theoretical spectrum predicted for the ketenimine tautomeric form. Moreover, the identification of the other photoproduct (4-amino-1*H*-imidazole-5-carbonitrile, AICN, Scheme 3) is unquestionable. All the strong and medium-strong bands present in the IR spectrum of AICN deposited from the gas phase into an Ar matrix have their counterparts in the spectrum recorded after UV irradiation of matrix-isolated sample containing DAMN and its isomeric ketenimine. The exact match of wavenumbers of the bands in the spectrum of the authentic AICN matrix sample and

the bands emerging upon UV irradiation of DAMN/ketenimine leaves no doubt about the correctness of the identification of the AICN photoproduct.

Author Contributions: Conceptualization, I.R.; investigation, I.R., H.R. and L.L.; writing—original draft preparation, L.L.; visualization, H.R. and I.R.; writing—review and editing, I.R., H.R. and L.L. All authors have read and agreed to the published version of the manuscript.

Funding: This work was supported by National Funds via the Portuguese Foundation for Science and Technology (FCT). The Chemical Process Engineering and Forest Products Research Centre (CIEPQPF) is supported by FCT through projects UIDB/EQU/00102/2020 and UIDP/EQU/00102/2020.

Institutional Review Board Statement: Not applicable.

Informed Consent Statement: Not applicable.

Conflicts of Interest: The authors declare no conflict of interest.

Appendix A. Structures of DAMN and DAFN

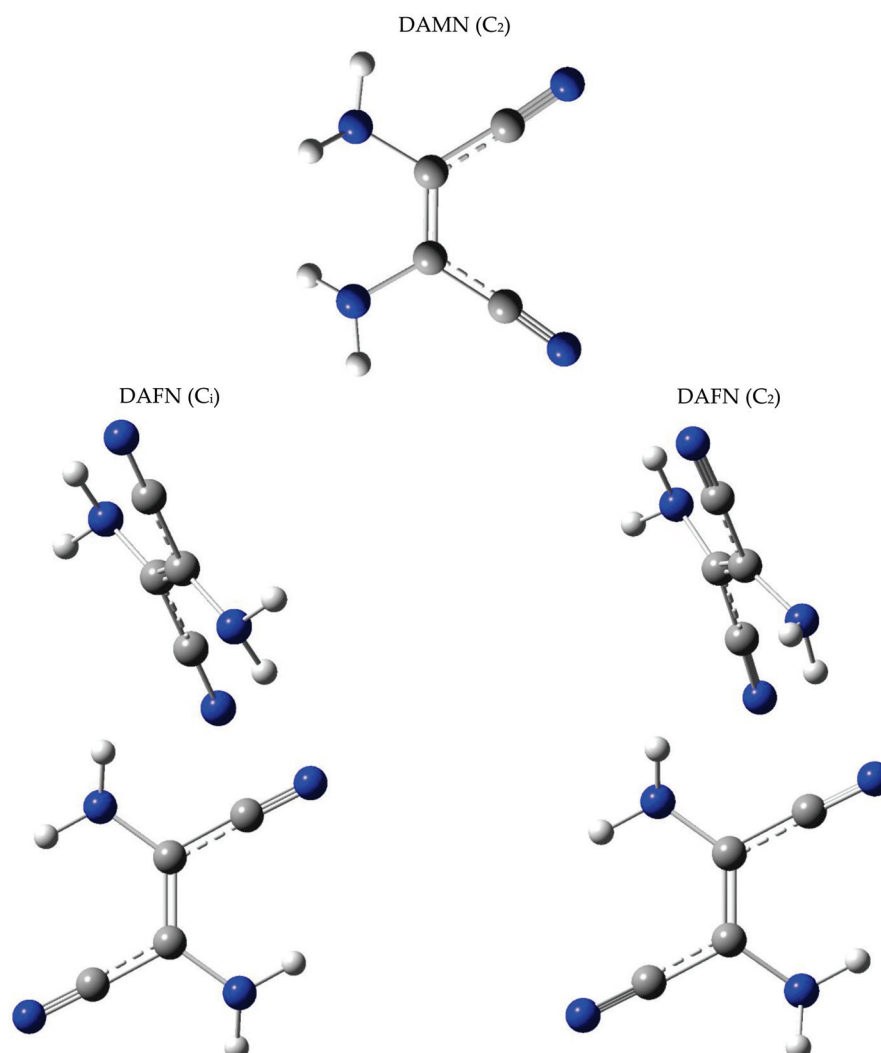


Figure A1. Optimized geometries of DAMN/DAFN. Top: DAMN (C_2 symmetry). Bottom left: DAFN (C_1 symmetry). Bottom right: DAFN (C_2 symmetry). Note: DAFN (C_1) differs from DAFN (C_2) only by a change in pyramidalization of one of the amino groups (see also Figure 2). Color codes: blue—nitrogen, gray—carbon, white—hydrogen.

Appendix B. Structures of the Ketenimine Tautomer of DAMN/DAFN

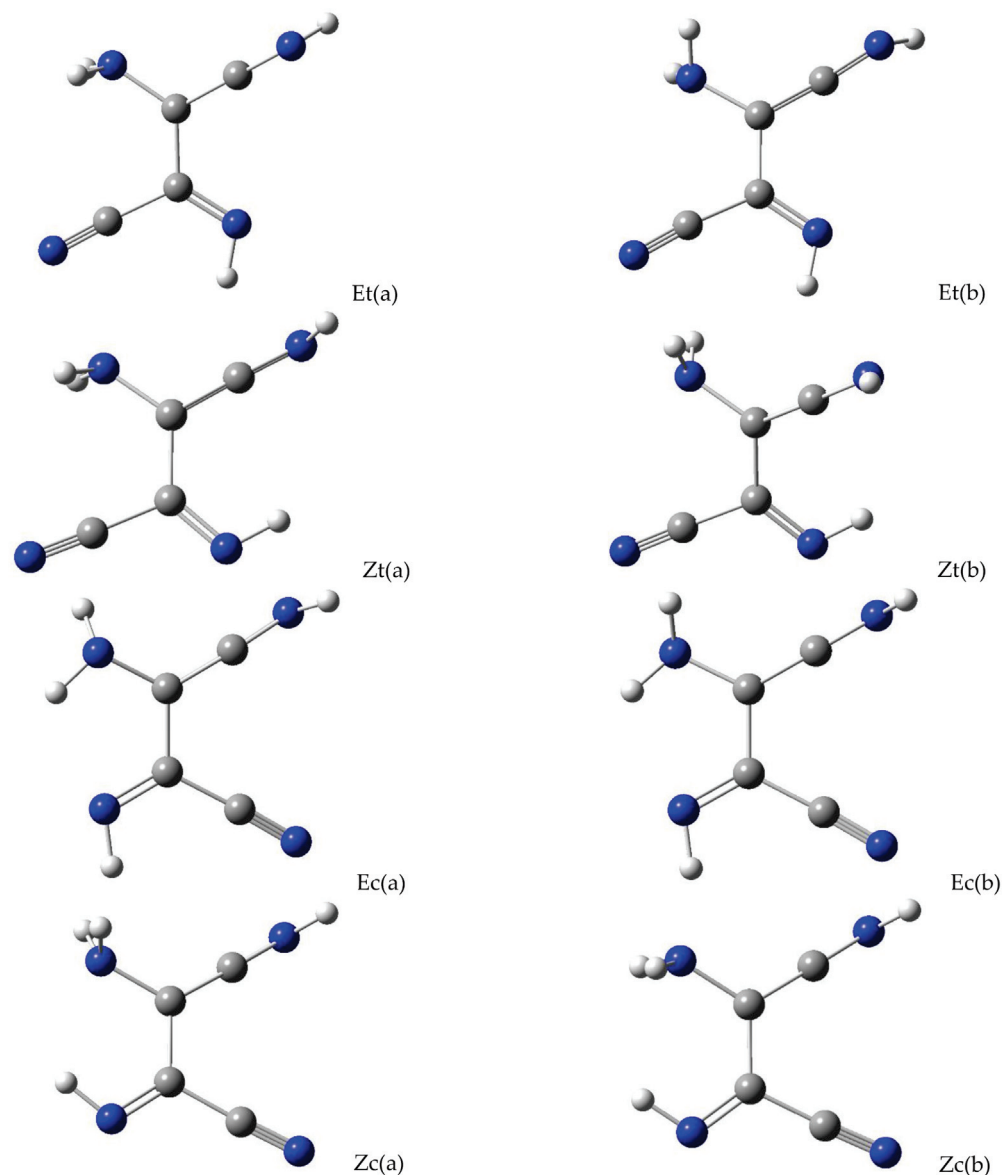


Figure A2. Optimized geometries of the ketenimine isomers. See Scheme 2 for the adopted E/Z and c/t naming system. Symbols (a,b) stand for different orientations of the NH₂ group, with all other conformational parameters equal. In the (a,b) pairs, the (a) orientation is more stable than (b). Color codes: blue—nitrogen, gray—carbon, white—hydrogen.

References

1. Sanchez, R.; Ferris, J.; Orgel, L.E. Conditions for Purine Synthesis: Did Prebiotic Synthesis Occur at Low Temperatures? *Science* **1966**, *153*, 72–73. [CrossRef] [PubMed]
2. Sanchez, R.A.; Ferris, J.P.; Orgel, L.E. Studies in Prebiotic Synthesis. II. Synthesis of Purine Precursors and Amino Acids from Aqueous Hydrogen Cyanide. *J. Mol. Biol.* **1967**, *30*, 223–253. [CrossRef] [PubMed]
3. Orgel, L.E.; Lohrmann, R. Prebiotic Chemistry and Nucleic Acid Replication. *Acc. Chem. Res.* **1974**, *7*, 368–377. [CrossRef]
4. Erian, A.W. The Chemistry of β -Enaminonitriles as Versatile Reagents in Heterocyclic Synthesis. *Chem. Rev.* **1993**, *93*, 1991–2005. [CrossRef]
5. Mamajanov, I.; Herzfeld, J. HCN polymers characterized by SSNMR: Solid state reaction of crystalline tetramer (diaminomaleonitrile). *J. Chem. Phys.* **2009**, *130*, 134504. [CrossRef]
6. Ruiz-Bermejo, M.; de la Fuente, J.L.; Pérez-Fernández, C.; Mateo-Martí, E. A Comprehensive Review of HCN-Derived Polymers. *Processes* **2021**, *9*, 597. [CrossRef]

7. Yamada, Y.; Nagashima, N.; Iwashita, Y.; Nakamura, A.; Kumashiro, I. Synthesis and Molecular Structure of Diaminofumaronitrile. *Tetrahedron Lett.* **1968**, *9*, 4529–4532. [CrossRef]
8. Ferris, J.P.; Orgel, L.E. An Unusual Photochemical Rearrangement in the Synthesis of Adenine from Hydrogen Cyanide. *J. Am. Chem. Soc.* **1966**, *88*, 1074. [CrossRef]
9. Ferris, J.P.; Kuder, J.E.; Catalano, A.W. Photochemical Reactions and Chemical Evolution of Purines and Nicotinamide Derivatives. *Science* **1969**, *166*, 765–766. [CrossRef]
10. Ferris, J.P.; Kuder, J.E. Chemical Evolution. III. The Photochemical Conversion of Enaminonitriles to Imidazoles. *J. Am. Chem. Soc.* **1970**, *92*, 2527–2533. [CrossRef]
11. Ferris, J.P.; Trimmer, R.W. Chemical Evolution. XXVIII. Photochemical Conversion of Enaminonitriles to Imidazoles. Scope and Mechanism. *J. Org. Chem.* **1976**, *41*, 19–24. [CrossRef]
12. Ferris, J.P.; Hagan, W.J., Jr. HCN and Chemical Evolution: The Possible Role of Cyano Compounds in Prebiotic Synthesis. *Tetrahedron* **1984**, *40*, 1093–1120. [CrossRef]
13. Boulanger, E.; Anoop, A.; Nachtigallova, D.; Thiel, W.; Barbatti, M. Photochemical Steps in the Prebiotic Synthesis of Purine Precursors from HCN. *Angew. Chem. Int. Edit.* **2013**, *52*, 8000–8003. [CrossRef] [PubMed]
14. Becke, A.D. Density-Functional Exchange-Energy Approximation with Correct Asymptotic Behavior. *Phys. Rev. A* **1988**, *38*, 3098–3100. [CrossRef]
15. Lee, C.T.; Yang, W.T.; Parr, R.G. Development of the Colle-Salvetti correlation-energy formula into a functional of the electron density. *Phys. Rev. B* **1988**, *37*, 785–789. [CrossRef]
16. Vosko, S.H.; Wilk, L.; Nusair, M. Accurate spin-dependent electron liquid correlation energies for local spin density calculations: A critical analysis. *Can. J. Phys.* **1980**, *58*, 1200–1211. [CrossRef]
17. Lapinski, L.; Reva, I.; Rostkowska, H.; Halasa, A.; Fausto, R.; Nowak, M.J. Conformational transformation in squaric acid induced by near-IR laser light. *J. Phys. Chem. A* **2013**, *117*, 5251–5259. [CrossRef]
18. Halasa, A.; Lapinski, L.; Reva, I.; Rostkowska, H.; Fausto, R.; Nowak, M.J. Three Conformers of 2-Furoic Acid: Structure Changes Induced with Near-IR Laser Light. *J. Phys. Chem. A* **2015**, *119*, 1037–1047. [CrossRef]
19. Zhurko, G.A. *Chemcraft—Graphical Program for Visualization of Quantum Chemistry Computations*, Version 1.8; 2016. Available online: <http://www.chemcraftprog.com> (accessed on 15 June 2022).
20. Frisch, M.J.; Trucks, G.W.; Schlegel, H.B.; Scuseria, G.E.; Robb, M.A.; Cheeseman, J.R.; Scalmani, G.; Barone, V.; Mennucci, B.; Petersson, G.A.; et al. *Gaussian 09*; Revision D.01; Gaussian, Inc.: Wallingford, CT, USA, 2013.
21. Krishnan, R.; Binkley, J.S.; Seeger, R.; Pople, J.A. Self-consistent molecular orbital methods. XX. A basis set for correlated wave functions. *J. Chem. Phys.* **1980**, *72*, 650–654. [CrossRef]
22. Clark, T.; Chandrasekhar, J.; Spitznagel, G.W.; Schleyer, P.V.R. Efficient Diffuse Function-Augmented Basis Sets for Anion Calculations. 3. The 3-21+G Basis Set for 1st Row Elements, Li-F. *J. Comput. Chem.* **1983**, *4*, 294–301. [CrossRef]
23. Frisch, M.J.; Pople, J.A.; Binkley, J.S. Self-consistent molecular orbital methods. 25. Supplementary functions for Gaussian basis sets. *J. Chem. Phys.* **1984**, *80*, 3265–3269. [CrossRef]
24. Peng, C.Y.; Schlegel, H.B. Combining Synchronous Transit and Quasi-Newton Methods to Find Transition States. *Isr. J. Chem.* **1993**, *33*, 449–454. [CrossRef]
25. Peng, C.Y.; Ayala, P.Y.; Schlegel, H.B.; Frisch, M.J. Using redundant internal coordinates to optimize equilibrium geometries and transition states. *J. Comput. Chem.* **1996**, *17*, 49–56. [CrossRef]
26. Fukui, K. The Path of Chemical Reactions—The IRC Approach. *Acc. Chem. Res.* **1981**, *14*, 363–368. [CrossRef]
27. Frisch, M.J.; Trucks, G.W.; Schlegel, H.B.; Scuseria, G.E.; Robb, M.A.; Cheeseman, J.R.; Scalmani, G.; Barone, V.; Petersson, G.A.; Nakatsuji, H.; et al. *Gaussian 16*; Revision C.01; Gaussian, Inc.: Wallingford, CT, USA, 2016.
28. Bauernschmitt, R.; Ahlrichs, R. Treatment of electronic excitations within the adiabatic approximation of time dependent density functional theory. *Chem. Phys. Lett.* **1996**, *256*, 454–464. [CrossRef]
29. Stratmann, R.E.; Scuseria, G.E.; Frisch, M.J. An efficient implementation of time-dependent density-functional theory for the calculation of excitation energies of large molecules. *J. Chem. Phys.* **1998**, *109*, 8218–8224. [CrossRef]
30. Nelson, D.D., Jr.; Fraser, G.T.; Klemperer, W. Ammonia dimer: A surprising structure. *J. Chem. Phys.* **1985**, *83*, 6201–6208. [CrossRef]
31. Nelson Jr., D. D.; Fraser, G.T.; Klemperer, W. Does Ammonia Hydrogen Bond? *Science* **1987**, *238*, 1670–1674. [CrossRef]
32. Tao, F.M.; Klemperer, W. Ab Initio Search for the Equilibrium Structure of the Ammonia Dimer. *J. Chem. Phys.* **1993**, *99*, 5976–5982. [CrossRef]
33. Jing, A.; Szalewicz, K.; van der Avoird, A. Ammonia dimer: Extremely fluxional but still hydrogen bonded. *Nat. Commun.* **2022**, *13*, 1470. [CrossRef]
34. Reva, I.D.; Stepanian, S.G.; Adamowicz, L.; Fausto, R. Conformational Behavior of Cyanoacetic Acid: A Combined Matrix Isolation Fourier Transform Infrared Spectroscopy and Theoretical Study. *J. Phys. Chem. A* **2003**, *107*, 6351–6359. [CrossRef]
35. Jacox, M.E.; Milligan, D.E. Infrared Study of the Reactions of CH₂ and NH with C₂H₂ and C₂H₄ in Solid Argon. *J. Am. Chem. Soc.* **1963**, *85*, 278–282. [CrossRef]
36. Jacox, M.E. Matrix Isolation Study of the Interaction of Excited Argon Atoms with Methyl Cyanide. Vibrational and Electronic Spectra of Ketenimine. *Chem. Phys.* **1979**, *43*, 157–172. [CrossRef]

37. Finnerty, J.; Mitschke, U.; Wentrup, C. Linear ketenimines. Variable structures of C,C-dicyanoketenimines and C,C-bis-sulfonylketenimines. *J. Org. Chem.* **2002**, *67*, 1084–1092. [CrossRef]
38. Inui, H.; Murata, S. Photochemistry of 2-(1-naphthyl)-2H-azirines in matrixes and in solutions: Wavelength-dependent C-C and C-N bond cleavage of the azirine ring. *J. Am. Chem. Soc.* **2005**, *127*, 2628–2636. [CrossRef]
39. Nunes, C.M.; Reva, I.; Pinho e Melo, T.M.V.D.; Fausto, R.; Šolomek, T.; Bally, T. The Pyrolysis of Isoxazole Revisited: A New Primary Product and the Pivotal Role of the Vinylnitrene. A Low-Temperature Matrix Isolation and Computational Study. *J. Am. Chem. Soc.* **2011**, *133*, 18911–18923. [CrossRef]
40. Nunes, C.M.; Reva, I.; Pinho e Melo, T.M.V.D.; Fausto, R. UV-Laser Photochemistry of Isoxazole Isolated in a Low-Temperature Matrix. *J. Org. Chem.* **2012**, *77*, 8723–8732. [CrossRef]
41. Nunes, C.M.; Pinto, S.M.V.; Reva, I.; Fausto, R. On the Photochemistry of 1,2-Benzisoxazole: Capture of Elusive Spiro-2H-azirine and Ketenimine Intermediates. *Eur. J. Org. Chem.* **2016**, *2016*, 4152–4158. [CrossRef]
42. Ito, F.; Nakanaga, T. Observation of the high-resolution spectrum of the N-H bending vibration of ketenimine CH₂CNH. *J. Mol. Spectrosc.* **2010**, *264*, 100–104. [CrossRef]
43. Tschöpe, M.; Schröder, B.; Erfort, S.; Rauhut, G. High-Level Rovibrational Calculations on Ketenimine. *Front. Chem.* **2021**, *8*, 623641. [CrossRef]
44. Reva, I.; Lopes Jesus, A.J.; Nunes, C.M.; Roque, J.P.L.; Fausto, R. UV-Induced Photochemistry of 1,3-Benzoxazole, 2-Isocyanophenol, and 2-Cyanophenol Isolated in Low-Temperature Ar Matrixes. *J. Org. Chem.* **2021**, *86*, 6126–6137. [CrossRef] [PubMed]
45. Ferris, J.P.; Narang, R.S.; Newton, T.A.; Rao, V.R. Mechanistic Studies on the Photochemical Conversion of Enaminonitriles to Imidazoles. *J. Org. Chem.* **1979**, *44*, 1273–1278. [CrossRef]
46. Becker, R.S.; Kolc, J.; Rothman, W. Spectroscopic and Photochemical Study of Diaminomaleonitrile and Diaminofumaronitrile. *J. Am. Chem. Soc.* **1973**, *95*, 1269–1273. [CrossRef]
47. Plese, M.; Jasien, P.G. The photochemical isomerization of DAMN to ACI: Stability of potential intermediates. *J. Mol. Struct. (Theochem)* **1996**, *364*, 121–130. [CrossRef]
48. Jeilani, Y.A.; Williams, P.N.; Walton, S.; Nguyen, M.T. Unified reaction pathways for the prebiotic formation of RNA and DNA nucleobases. *Phys. Chem. Chem. Phys.* **2016**, *18*, 20177–20188. [CrossRef]
49. Koumura, N.; Zijlstra, R.W.J.; van Delden, R.A.; Harada, N.; Feringa, B.L. Light-driven monodirectional molecular rotor. *Nature* **1999**, *401*, 152–155. [CrossRef]
50. Liu, F.Y.; Morokuma, K. Computational Study on the Working Mechanism of a Stilbene Light-Driven Molecular Rotary Motor: Sloped Minimal Energy Path and Unidirectional Nonadiabatic Photoisomerization. *J. Am. Chem. Soc.* **2012**, *134*, 4864–4876. [CrossRef]
51. Arai, T.; Tokumaru, K. Photochemical One-Way Adiabatic Isomerization of Aromatic Olefins. *Chem. Rev.* **1993**, *93*, 23–39. [CrossRef]
52. Duarte, L.; Fausto, R.; Reva, I. Structural and spectroscopic characterization of E- and Z-isomers of azobenzene. *Phys. Chem. Chem. Phys.* **2014**, *16*, 16919–16930. [CrossRef]
53. Duarte, L.; Khriachtchev, L.; Fausto, R.; Reva, I. Photoisomerization of azobenzenes isolated in cryogenic matrices. *Phys. Chem. Chem. Phys.* **2016**, *18*, 16802–16811. [CrossRef]
54. Mahimwalla, Z.; Yager, K.G.; Mamiya, J.-I.; Shishido, A.; Priimagi, A.; Barrett, C.J. Azobenzene photomechanics: Prospects and potential applications. *Polym. Bull.* **2012**, *69*, 967–1006. [CrossRef]
55. Quick, M.; Dobryakov, A.L.; Gerecke, M.; Richter, C.; Berndt, F.; Ioffe, I.N.; Granovsky, A.A.; Mahrwald, R.; Ernsting, N.P.; Kovalenko, S.A. Photoisomerization Dynamics and Pathways of trans- and cis- Azobenzene in Solution from Broadband Femtosecond Spectroscopies and Calculations. *J. Phys. Chem. B* **2014**, *118*, 8756–8771. [CrossRef] [PubMed]
56. Han, W.G.; Lovell, T.; Liu, T.Q.; Noodleman, L. Density functional studies of the ground- and excited-state potential-energy curves of stilbene cis-trans isomerization. *ChemPhysChem* **2002**, *3*, 167–178. [CrossRef]
57. Quenneville, J.; Martínez, T.J. Ab initio study of cis-trans photoisomerization in stilbene and ethylene. *J. Phys. Chem. A* **2003**, *107*, 829–837. [CrossRef]
58. Levine, B.G.; Martínez, T.J. Isomerization through conical intersections. *Annu. Rev. Phys. Chem.* **2007**, *58*, 613–634. [CrossRef]
59. Minezawa, N.; Gordon, M.S. Optimizing Conical Intersections by Spin-Flip Density Functional Theory: Application to Ethylene. *J. Phys. Chem. A* **2009**, *113*, 12749–12753. [CrossRef]
60. Minezawa, N.; Gordon, M.S. Photoisomerization of Stilbene: A Spin-Flip Density Functional Theory Approach. *J. Phys. Chem. A* **2011**, *115*, 7901–7911. [CrossRef]
61. Szabla, R.; Góra, R.W.; Šponer, J.; Šponer, J.E. Molecular Mechanism of Diaminomaleonitrile to Diaminofumaronitrile Photoisomerization: An Intermediate Step in the Prebiotic Formation of Purine Nucleobases. *Chem. Eur. J.* **2014**, *20*, 2515–2521. [CrossRef]
62. Valiev, R.R.; Nasibullin, R.T.; Cherepanov, V.N.; Baryshnikov, G.V.; Sundholm, D.; Ågren, H.; Minaev, B.F.; Kurtén, T. First-principles calculations of anharmonic and deuteration effects on the photophysical properties of polyacenes and porphyrinoids. *Phys. Chem. Chem. Phys.* **2020**, *22*, 22314–22323. [CrossRef]
63. Knuts, S.; Minaev, B.F.; Vahtras, O.; Ågren, H. Spin-Orbit Coupling in the Intersystem Crossing of the Ring-Opened Oxirane Biradical. *Int. J. Quantum Chem.* **1995**, *55*, 23–34. [CrossRef]

64. Plachkevych, O.; Minaev, B.; Ågren, H. Paramagnetic exchange spin-catalysis of the *cis-trans* isomerization of substituted ethylenes. *J. Phys. Chem.* **1996**, *100*, 8308–8315. [CrossRef]
65. Koch, T.H.; Rodehorst, R.M. A Quantitative Investigation of the Photochemical Conversion of Diaminomaleonitrile to Diaminofumaritrile and 4-Amino-5-Cyanoimidazole. *J. Am. Chem. Soc.* **1974**, *96*, 6707–6710. [CrossRef]
66. Breda, S.; Reva, I.; Lapinski, L.; Fausto, R. Matrix isolation FTIR and theoretical study of α -pyrone photochemistry. *Phys. Chem. Chem. Phys.* **2004**, *6*, 929–937. [CrossRef]
67. Breda, S.; Reva, I.; Lapinski, L.; Cristiano, M.L.S.; Frija, L.; Fausto, R. Photochemical Ring-Opening and Intramolecular Hydrogen Shift Reactions in Sulfur Analogues of α -Pyrone. *J. Phys. Chem. A* **2006**, *110*, 6415–6425. [CrossRef]

Article

Vibrational-Excitation-Induced and Spontaneous Conformational Changes in Solid *Para*-H₂—Diminished Matrix Effects

Sándor Góbi^{1,*}, Gopi Ragupathy¹, Gábor Bazsó² and György Tarczay^{1,3,4,*}

¹ MTA-ELTE Lendület Laboratory Astrochemistry Research Group, Institute of Chemistry, ELTE Eötvös Loránd University, P.O. Box 32, H-1518 Budapest, Hungary; gopir007@gmail.com

² Wigner Research Centre for Physics, P.O. Box 49, H-1525 Budapest, Hungary; bazso.gabor@wigner.mta.hu

³ Laboratory of Molecular Spectroscopy, Institute of Chemistry, ELTE Eötvös Loránd University, P.O. Box 32, H-1518 Budapest, Hungary

⁴ Centre for Astrophysics and Space Science, ELTE Eötvös Loránd University, P.O. Box 32, H-1518 Budapest, Hungary

* Correspondence: sandor.gobi@ttk.elte.hu (S.G.); gyorgy.tarczay@ttk.elte.hu (G.T.)

Abstract: Both vibrational-excitation-induced (by (N)IR laser) and spontaneous (by H atom tunneling) conformational changes are often investigated by matrix-isolation spectroscopy. It is well known that rigid hosts, such as solid noble gases, N₂, or *normal*-H₂, can largely affect both the quantum efficiency of the (N)IR photon-induced process and the tunneling rate. In the present study, the conformational changes of formic and acetic acids, as well as glycine, were investigated in a soft quantum host, solid *para*-H₂. It is shown that the tunneling rates in *para*-H₂ are orders of magnitude larger than those in rigid hosts. Furthermore, our results also suggest that the quantum efficiencies of some (N)IR-light-induced conformational changes are larger than in rigid matrices. These results can open a door for the applications of *para*-H₂ host in conformational and tunneling studies and can help understand the details of these complex processes.

Keywords: conformational switching; near-IR laser irradiation; quantum efficiency; hydrogen atom tunneling; formic acid; acetic acid; glycine; matrix isolation; *para*-H₂; IR spectroscopy

Citation: Góbi, S.; Ragupathy, G.;

Bazsó, G.; Tarczay, G.

Vibrational-Excitation-Induced and Spontaneous Conformational Changes in Solid

Para-H₂—Diminished Matrix Effects.

Photochem **2022**, *2*, 563–579. <https://doi.org/10.3390/photochem2030039>

Academic Editor: Frédéric Paul

Received: 20 June 2022

Accepted: 17 July 2022

Published: 26 July 2022

Publisher's Note: MDPI stays neutral with regard to jurisdictional claims in published maps and institutional affiliations.



Copyright: © 2022 by the authors. Licensee MDPI, Basel, Switzerland. This article is an open access article distributed under the terms and conditions of the Creative Commons Attribution (CC BY) license (<https://creativecommons.org/licenses/by/4.0/>).

1. Introduction

Matrix-isolation spectroscopy is a well-tried method to study light-induced and spontaneous conformational changes. UV irradiation is the simplest and a very frequently used method for isomerization. It can also be used to induce conformational changes, but usually, the UV absorption bands of different conformers overlap; therefore, in most cases, it is sufficient to shift the conformational ratio only to a limited extent. IR laser irradiation is a more selective method for conformational switching. In this case, a selected conformer is vibrationally excited, which can then convert into another one. When there is no spectral overlap between the excited vibrational band of the excited conformer and the bands of other conformer(s), and there is no rapid spontaneous back conversion, it allows high or complete depletion of the vibrationally excited conformer. Using this method, conformational switching was observed for many model systems, including formic [1–6], acetic [6–9], trifluoro- and tribromoacetic [10,11], propiolic [12], propionic and 2-chloropropionic [13,14], glycolic [15], α -ketocarboxylic [16], oxamic [17], dicarboxylic [18–20], (hetero)cyclic organic [21–23], and amino acids [24–29], as well as sulfur-containing compounds [30–34].

In the above examples, the conformational change was induced locally, i.e., in most of the cases, the first overtone of the OH stretching mode ($2\nu(\text{OH})$) of the carboxylic ($-\text{COOH}$) group was excited, which caused a *trans*-to-*cis* (or *Z* to *E*) conformational change of the $-\text{COOH}$ group. However, vibrational excitation can also trigger a conformational change farther from the absorbing oscillator. Among the first examples, it was shown that the

excitation of CH and C=O stretching overtones ($2\nu(\text{CH})$ and $2\nu(\text{C}=\text{O})$) could also induce a *cis-trans* conformational change in formic and acetic acid [5,9]. More recent examples include amino acids. The irradiation of the first overtone of the NH stretching mode ($2\nu(\text{NH})$) of glycine results in the *cis-trans* conversion of the $-\text{COOH}$ group [24], while the excitation of the $2\nu(\text{OH})$ mode of the carboxylic hydroxyl ($-\text{OH}$) group can induce a conformational change in the side chain in serine [29]. Other examples of this so-called remote switching include 2-thiocytosine, in which rotamerization of the thiol ($-\text{SH}$) moiety was induced by the excitation of the NH_2 stretching overtone ($2\nu(\text{NH}_2)$) [35]; in kojic acid, in which the phenolic $-\text{OH}$ group was irradiated, and the conformational change of the hydroxymethyl ($-\text{CH}_2\text{OH}$) group was observed [36]; in 6-methoxyindole, in which the excitation of the $2\nu(\text{NH})$ stretching overtone mode induced the conformational change of the methoxy ($-\text{OCH}_3$) group [37]; and in glycolamide, where pumping the NH_2 stretching overtone ($2\nu(\text{NH}_2)$) resulted in the rotation of the $-\text{CH}_2\text{OH}$ group [38]. The selective excitation of the OH stretching overtone of one of the $-\text{COOH}$ groups of an asymmetrical dicarboxylic acid, *E*-glutaconic acid, can induce the conformational change (*cis-trans*) of the other $-\text{COOH}$ moiety, located at the other end of the molecule [39]. Furthermore, it was also found that the $2\nu(\text{NH})$ mode of each imino-thiol isomer of thioacetamide changes the orientation of a remote $-\text{SH}$ group, while the orientation of the imino ($=\text{NH}$) group remains the same [40]. There are instances where the local excitation is only slightly more efficient than the remote one; a recent example is 2-fluoro-4-hydroxy benzoic acid [41]. When a high-energy conformer is prepared by the above method, it might convert to lower-energy conformers either via a low-energy classical barrier or by H atom tunneling. For several dozens of molecules the tunneling times were measured in rigid noble gas [2,7,9–11,13,14,16,17,22,24–26,31,32,34,40–47], *normal*- H_2 (*n*- H_2) [45–48], and N_2 matrices [6,10–12,15,25–29,49].

Upon studying the conformational changes in a rigid matrix, one has to keep in mind that the host may have a non-negligible effect on the quantum yields of the light-induced processes and the rate of the spontaneous ones. Not surprisingly, different quantum yields were observed for the $2\nu(\text{OH})$ excitation-induced *cis-trans* conformational change of acetic acid in different matrices [9]. For instance, photo-induced rotamerization was found to be more efficient in solid Xe than in Ar for multiple systems, whereas Kr lies between them [50]. This is likely due to the ability of the host to compensate for the energy gap between the intramolecular energy levels participating in the energy relaxation process through the conversion of the excess internal energy of the guest molecule into lattice phonons [51]. The local matrix morphology (matrix sites) is also expected to have an influence on the energy relaxation dynamics owing to its effect on the anharmonicity and intermode coupling constants [3]. It is a completely unexplored question how the host and the sites can influence the ratio of the local and remote conformational change. There might be examples when a local conformational change is sterically hindered by close packing of the host atoms while there is more space for the conformational change of a remote group.

The effect of the host is even more complicated for conformational changes by H atom tunneling. It can be expected that the tunneling rate should be principally determined by three factors. First is the dispersion interaction between the noble gas atom and the sample molecule. More precisely, the *cis* carboxylic acid becomes relatively more stable resulting from its higher permanent dipole moment compared to the *trans* form, which ensures a more intense interaction with the host environment [2]. Moreover, the stabilization is also controlled by the polarizability of the noble gas atoms; higher polarizability translates into a larger interaction [52]. Nevertheless, the extent of solvation cannot always explain everything about the tunneling behavior of carboxylic acids [53]. Secondly, the energy mismatch between the ground-state *cis* conformer and a vibrationally excited *trans* form can be overcome by the dissipation of the excess energy via a one- or multiphonon process [2,52]. Evidently, the probability of a one-phonon process is higher, resulting in a higher tunneling rate. Thirdly, reorganization of the matrix upon tunneling has been proposed to be a rate-determining step and may explain the temperature-dependence of the process as well

as the dependence on the quality of the matrix, where the latter can be explained by the different reorganization energies [54,55].

It is now well documented for several model molecules, including formic and acetic [6,56], as well as propionic acids [12], HOCO radical [49], glycine [25], alanine [26,27], cysteine [28], and serine [29], that N₂ can extremely stabilize the higher-energy conformer as compared to noble gas matrices. This stabilizing effect of the N₂ matrix as compared to the Ar matrix results in two and four orders of difference in tunneling rates for HOCO radical and formic acid, respectively [6,49,56]. This might be rationalized by the quadruple moment of N₂ [25]. The higher-energy conformer of these species has a larger dipole moment than the transition structure and the lower-energy conformer; therefore, the higher-energy form is stabilized by a dipole-quadrupole interaction. It is also important to note that in different sites, the tunneling rates can be largely different, and due to the presence of several similar but slightly different sites, often not exponential but dispersive decay kinetics is observed for the conformational change [31,57]. Finally, we can mention a very interesting phenomenon observed for tribromoacetic acid in a N₂ matrix [11]. The excitation of the 2ν(OH) mode of the *trans* conformer predominantly converts the molecules located in a specific matrix site into the *cis* form; then, upon tunneling back to the *trans* form populates almost exclusively another matrix site.

In the present study, we measure the quantum yields of the 2ν(OH) excitation induced *cis-trans* conformational change and the rates of the spontaneous conformational changes of formic and acetic acids and glycine in a quantum host, solid *para*-H₂ (*p*-H₂). Since in this host, the vibrational amplitude of the H₂ molecules is comparable with the volume of the molecule [58], it provides a soft environment in which the steric effect is a much less important, less determining factor than in rigid matrices. In addition, the intermolecular interactions between the studied and the host molecules are also considerably smaller for *p*-H₂ than for noble gas, *normal*-H₂ (*n*-H₂), or N₂ matrices. The comparison of the values measured in *p*-H₂ should allow us to understand the host effects in more detail and could result in a better match of theory and experiment.

2. Materials and Methods

The experiments were conducted on the VIZSLA setup, which consists of an ultrahigh-vacuum (UHV) compatible stainless steel chamber capable of being evacuated to a base pressure of a few 1×10^{-9} mbar when cooled [59]. For the matrix-isolation experiments, Ar (Messer, 99.9999%), *n*-H₂ (Messer, 99.999%), and *p*-H₂ were used. *p*-H₂ was prepared by flowing *n*-H₂ through porous Fe(III) oxide (Sigma-Aldrich, (St. Louis, MI, USA), hydrated, catalyst grade, 30–50 mesh) cooled down to 13.9 K wrapped around the upper cryostat of the setup. All gases were collected in the separate gas mixing line in a 1 L glass bulb for the preparation of the mixtures with the carboxylic acids or in a 0.5 L bulb for the matrix containing glycine afterwards.

On the gas mixing line, a few cm³ of formic acid (FA, Sigma-Aldrich >98%) or acetic acid (AA, Sigma-Aldrich >99%) were undergone three freeze-thaw cycles in a small glass vial in order to eliminate dissolved gases from them. The mixtures of the carboxylic acids with Ar, *n*-H₂, and *p*-H₂, respectively, were prepared by introducing a few mbar of the acid vapors into the 0.5 L glass bulb and then diluting it with the carrier gas in two steps. The mixtures were left for at least 45 min after the first dilution and for at least 30 min after the second one to obtain sufficiently homogeneous mixtures. The final sample-to-gas ratios were estimated to be 1:1000 (FA:Ar), 1:1100 (FA:*n*-H₂), 1:3700 (FA:*p*-H₂), 1:1000 (AA:Ar), 1:1100 (AA:*n*-H₂), and 1:1800 (AA:*p*-H₂), respectively. Subsequently, the mixtures were introduced into the main chamber through a copper tube with an inner diameter of 6 mm, a leak valve, and a stainless-steel capillary array ending approximately 3 cm from the substrate. The leak valves were open so that the inlet rates of the gas mixtures were 0.6–0.9 mbar L min⁻¹ when using *n*-H₂ or *p*-H₂ and 1.1–1.3 mbar L min⁻¹ when using Ar. Then, the depositions were carried out to a gold-plated silver substrate mounted on the cold finger of an RDK-415D2 cryostat (Sumitomo Heavy Industries Inc., Tokyo, Japan), which

can be ultimately cooled down to 3.1 K. The temperature of the substrate, independently of the sample material, was kept at 15 K when depositing Ar-containing matrices and at 3.1 K when the carrier gases were *n*-H₂ or *p*-H₂, respectively.

The glycine sample was prepared differently. Before evacuating the chamber, a small amount of glycine (Reanal, >99%) was inserted into a quartz sample holder tube (with a 0.5 cm diameter exit hole) inside a stainless-steel oven. The whole sample inlet system is directly attached to the vacuum chamber and can be moved horizontally through vacuum-compatible bellows. The oven temperature was measured by a K-type thermocouple and controlled by a Lakeshore Model 336 controller. The volatile impurities such as water had been removed by vacuum evaporation at 100 °C before the experiments. The matrix was prepared by co-depositing glycine and the carrier gas onto the substrate. For this, the temperature of the oven with the glycine was set to 138 °C during deposition. The matrix gases were introduced by the same stainless steel capillary array used to introduce the gas mixtures in the case of the experiments carried out with carboxylic acids, which are parallel to the oven. Inlet rates of the carrier gases were 0.8 mbar L min⁻¹ when using Ar and 0.7 mbar L min⁻¹ when using *n*-H₂ or *p*-H₂, respectively.

All near-IR (NIR) irradiations were carried out by an Optical Parametric Oscillator (OPO, GWU/Spectra-Physics VersaScan MB 240, FWHM ≈ 5 cm⁻¹) pumped by a pulsed Nd:YAG laser (Spectra-Physics Quanta Ray Lab 150, *P* ≈ 2.1–2.2 W, λ = 355 nm, *f* = 10 Hz, pulse duration = 2–3 ns). All irradiations were performed at 8 K in the case of Ar and at 3.1 K for the *n*-H₂ and *p*-H₂ experiments, respectively.

The mid-IR (MIR) spectra were taken by a Bruker Invenio FT-IR spectrometer equipped with a liquid N₂-cooled mid-band Mercury Cadmium Telluride (MCT) detector working in reflection-absorption mode. Each spectrum was collected in the spectral region of 4000–600 cm⁻¹ at a resolution of 1 cm⁻¹. For every measurement, a low-pass filter with a cutoff wavelength of 1830 cm⁻¹ was inserted between the spectrometer beam source and the substrate. For the experiments with glycine, a different filter was used that lets through light only in the 1900–1200 cm⁻¹ region. This was performed to eliminate the spectral changes (e.g., *cis-trans* conversion of the carboxylic acids) caused by the NIR photons originating from the spectrometer beam source. During deposition, 32 scans were averaged in each minute, whereas during and after irradiation, 8 scans were averaged, requiring approximately 8 s in the case of the FA-Ar experiment, and 2 scans were averaged (roughly every 2 s) for the remaining carboxylic acid matrix-isolation experiments. In the case of the glycine experiment, 32 scans were averaged each minute during deposition and irradiation as well. In order to prevent the appearance of spectral artifacts due to the scattering of the laser beam on the substrate, another low-pass filter with a cutoff wavelength of 3860 cm⁻¹ was placed between the substrate and the infrared detector during irradiation. For the glycine experiment, this filter was in the beam path during deposition as well. The near-IR (NIR) spectra were taken by the same FT-IR spectrometer after deposition and before irradiation to find the band positions used for the excitation of the sample molecule conformers. The spectra averaged 128 scans in the case of the AA experiments, the FA-*n*-H₂ experiment, as well as the glycine experiment, 32 scans during the FA-*p*-H₂ experiment, and 256 scans in the FA-Ar experiment. The resolution was set to 1 cm⁻¹ covering the spectral range of 8000–600 cm⁻¹. The cutoff filters were taken out for the NIR measurements waiting 15 min to purge the system properly after removing/reinserting the filters. The MIR background spectra were registered right before the deposition in every experiment with carboxylic acids at 1 cm⁻¹ resolution saved in the 16,000–0 cm⁻¹ spectral region averaging 512 scans. The MIR backgrounds were saved with and without the 3860 cm⁻¹ low-pass cutoff filter in the beam path, whereas the temperature was set to 15 K while collecting the MIR backgrounds for the Ar-matrix experiments and 3.1 K for the ones performed with *n*-H₂ and *p*-H₂, respectively. Background spectra of 512 scans were taken at 8 K before deposition for the glycine experiments using the resolution of 1 cm⁻¹ in the spectral region of 16000–0 cm⁻¹ with both filters in the beam path. One NIR background with the resolution of 1 cm⁻¹ averaging 512 scans was collected at 3.1 K and was used for

all the experiments performed with carboxylic acids. For the glycine experiments, NIR background spectra of 256 scans at the resolution of 0.5 cm^{-1} were collected right before deposition at 8 K (Ar matrix) and at 3.1 K (*n*-H₂ and *p*-H₂).

The assignment of the vibrational spectra was based on the findings of previous studies on FA, AA, and glycine made in Ar matrices [3,7,24]. In order to determine the column densities, the computed anharmonic vibrational intensities were used. For this, quantum-chemical DFT computations were performed utilizing the Gaussian 09 (Rev. D01) program package [60]. The optimization of the geometric structures belonging to the minima on the potential energy surface was performed at the B3LYP/cc-pVTZ level of theory. Then, anharmonic vibrational frequencies and intensities of the minima structures were computed by vibrational perturbation theory (VPT2) at the same level of theory. The optimized geometries and the calculated vibrational properties are listed in Tables S1–S12 in the Supplementary Material.

3. Results and Discussion

3.1. Determining the Column Densities and Quantum Efficiencies

Upon NIR irradiation, the conformational changes could be followed by monitoring the MIR spectra of the matrices. The column densities of the species ($N_t(\mathbf{X})$ for species \mathbf{X} in cm^{-2}) at timestep t (in s) were determined by using their most intense bands that do not overlap with other ones; when there was more than one good candidate (such as for FA and AA), the obtained $N_t^i(\mathbf{X})$ values obtained for the i^{th} vibrational mode were averaged, and an error estimation could be provided in such a case. Unfortunately, no error estimate could be given in the case of glycine since only one vibrational mode could be used to calculate the column density of the conformers. The bands that were used for the determination of the column densities and for the NIR excitations are summarized in Table S13 and Figures S1 and S2 in the Supplementary Material. The following equation could be used to calculate $N_t^i(\mathbf{X})$ of each species for a particular vibrational mode:

$$N_t^i(\mathbf{X}) = \ln(10) \left(A_t^i(\mathbf{X}) / c_{\text{abs}}^i \right) \cos(\alpha) / 2 \quad (1)$$

where $A_t^i(\mathbf{X})$ is the integrated band area of the vibrational mode i of species \mathbf{X} (in cm^{-1}), c_{abs}^i represents the absorption coefficient of the same vibrational mode approximated by the computed MIR anharmonic intensities (in cm), whereas α is the angle of incidence relative to the surface normal of the substrate. α is approximately 60° in *n*- and in *p*-H₂ and 42° in Ar due to its refractive index being different from 1.0 (practically 1.3). The temporal evolution of the column densities for the FA and glycine systems are visualized in Figures 1 and 2, whereas that of the AA-Ar sample can be found in the Supplementary Material (Figure S3). It is worth noting that due to the uncertainty of the theoretically obtained IR absorption coefficients, the column density profile of the decaying conformer may not perfectly match that of the forming one. In order to quantify the conversion rates, kinetic curves could be generated by fitting single-exponential functions on the column densities, where t is the time since the beginning of the laser excitation, and k (in s^{-1}) is the first-order rate constant of the conversion process.

$$N_t(\mathbf{X}) = N_{t=0}(\mathbf{X})e^{-kt} + N_{t=\infty}(\mathbf{X}) \quad (2)$$

For the growth profiles, a modified function can be used as an estimation:

$$N_t(\mathbf{X}) = N_{t=\infty}(\mathbf{X}) \left(1 - e^{-kt} \right) \quad (3)$$

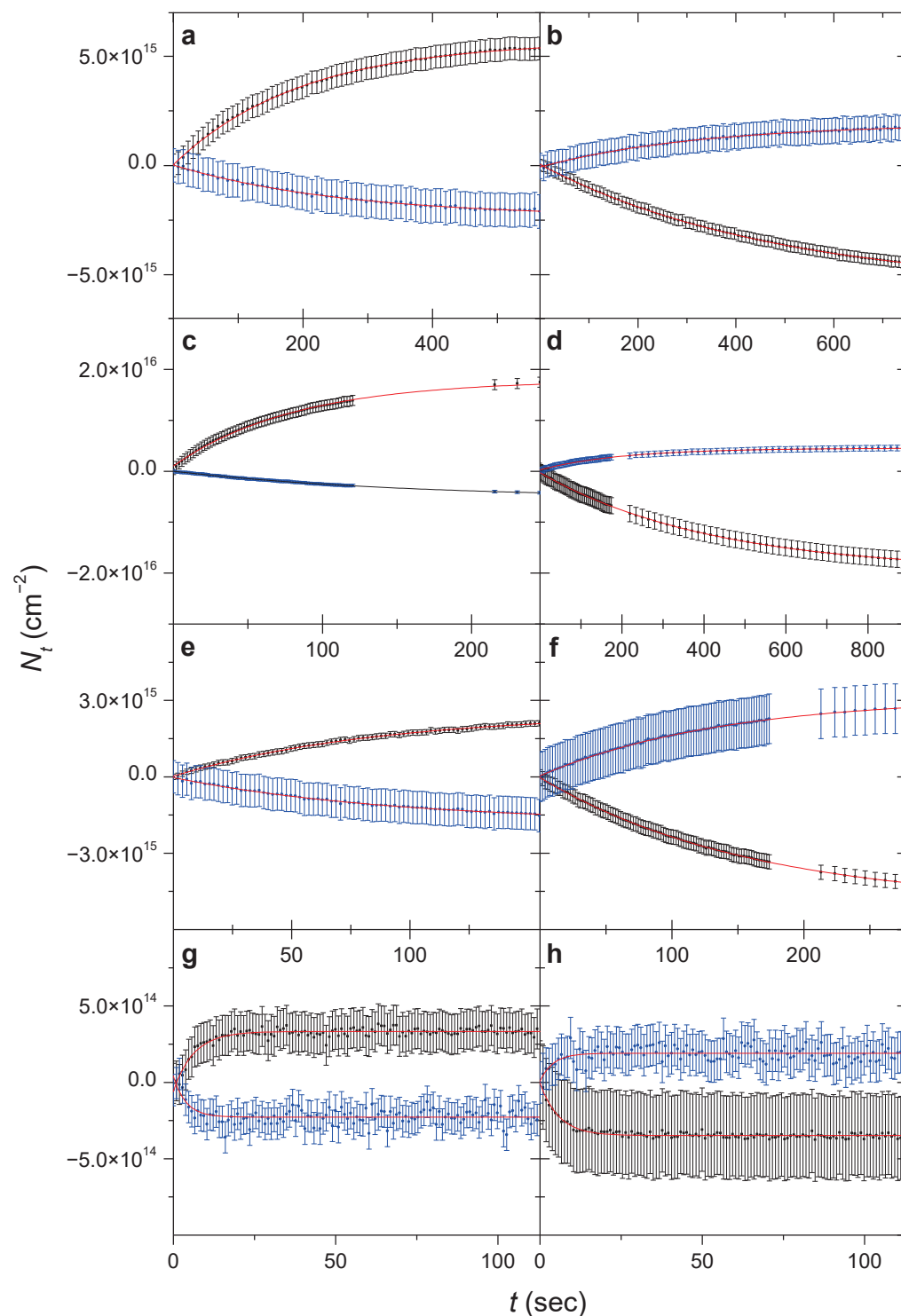


Figure 1. Kinetic plots of the FA-Ar system during (a) and after (b) the NIR laser excitation of 6929.9 cm^{-1} as well as during (c) and after (d) the NIR laser excitation of 6934.7 cm^{-1} , that of the FA-*n*-H₂ matrix during (e) and after (f) the NIR laser excitation of 6937.6 cm^{-1} , and the FA-*p*-H₂ sample during (g) and after (h) NIR laser excitation of 6940.0 cm^{-1} . Blue symbols show the column densities of the *trans*, the black ones display those of the *cis* isomers, whereas the red traces display the kinetic fit. Note the different scale for different species.

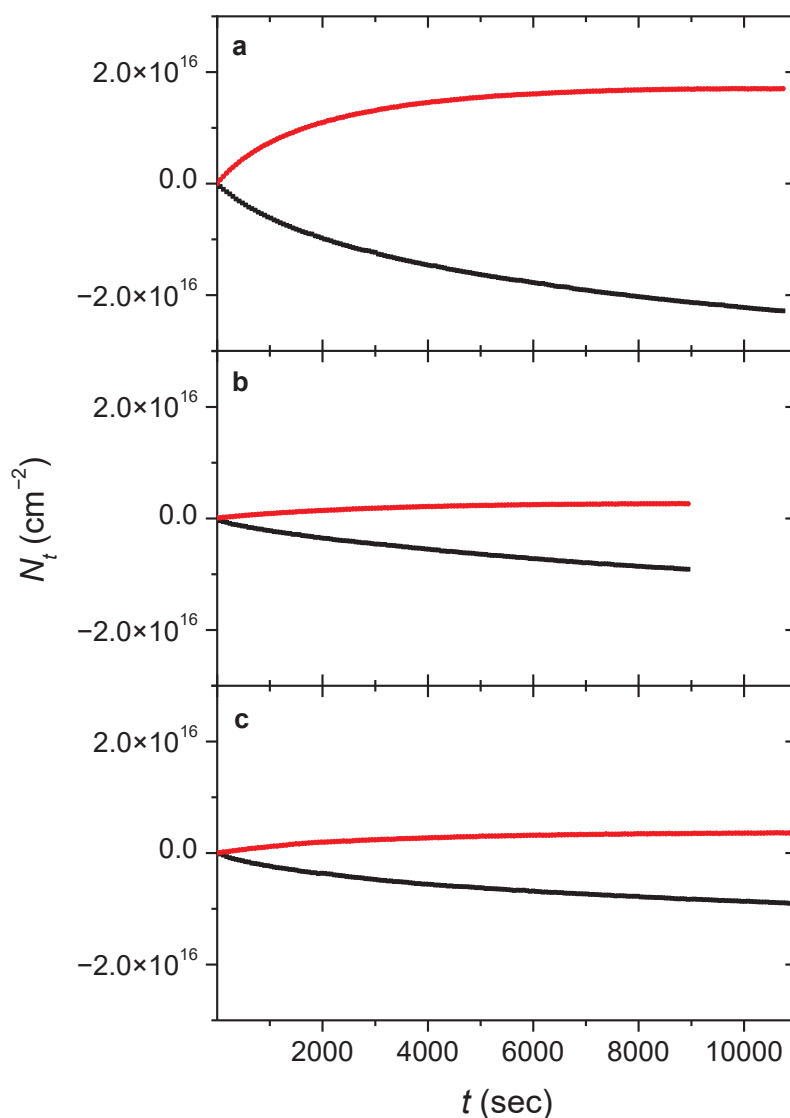


Figure 2. Kinetic plots of the glycine-Ar system during the NIR laser excitation of 6968.8 cm^{-1} (a), that of the glycine-*n*-H₂ matrix during the NIR laser excitation of 6963.2 cm^{-1} (b), and the glycine-*p*-H₂ sample during the NIR laser excitation of 6968.1 cm^{-1} (c). Red symbols show the column densities of conformer III, whereas the black ones display those of conformer I. All conformer III had to be converted to I in H₂ matrices before the actual irradiation experiments by exciting the $2\nu(\text{OH})$ mode the former at 6954.5 cm^{-1} (*n*-H₂) and 6959.3 cm^{-1} (*p*-H₂), respectively. The fitted curves are not visualized on this figure for the sake of clarity.

Once the conversion rates are known, they can be used to estimate the quantum efficiency (ϕ^i , a dimensionless value) of the processes when exciting the i^{th} NIR band of the conformer [5,9,61].

$$\phi^i = k_p^i / \sigma^i I \quad (4)$$

where k_p^i is the pumping rate in s^{-1} , whereas σ^i and I represent the absorption cross-section of the i^{th} vibrational mode in cm^2 and the average photon flux of the laser beam at that wavelength in $\text{cm}^2\text{ s}^{-1}$, respectively. σ^i can be calculated by dividing the absorbance of the excited NIR (overtone) band (A , dimensionless value) by the column density of the transforming conformer at the beginning of irradiation ($N_{t=0}(\text{X})$). One also needs to take into account that the apparent thickness of the sample (therefore the A value) is different for the NIR beam coming from the spectrometer for the laser beam (the latter closes at an

angle of approximately 23° with the surface normal. On the other hand, I is estimated by dividing the output power of the produced NIR laser light used for excitation (P , in W) by the photon energy (E_{photon} , in J) times the irradiated surface area S ($= 1 \text{ cm}^2$). It is important to point out that P was measured at the aperture of the OPO, thus neglecting the losses due to the optical elements such as the mirrors and the window of the vacuum chamber. As such, P (and therefore I) represents an upper estimate, meaning that the ϕ_i values presented here are lower estimates.

Alternatively, another estimation for ϕ^i can also be made by dividing the number of molecules converted (n_{conv}) by the number of photons absorbed per time unit (n_{abs} , both in s^{-1}), which can be obtained as follows:

$$n_{\text{conv}} = k_p^i N_{t=0}(\text{trans})S \quad (5)$$

$$n_{\text{abs}} = (1 - 10^{-A})IS \quad (6)$$

The ϕ_i values deduced by the two approaches can then be averaged; all the values discussed above are listed in Tables 1 and 2. It should also be noted that the overall uncertainty of ϕ^i appears to be at around 50%, according to the conclusions made previously [9,40,41,61].

Table 1. Calculated quantum efficiencies (ϕ^i) of the *trans-cis* conversion of FA and AA upon NIR laser excitation. The applied the excitation wavenumbers are in parentheses.

	FA				AA
	Ar (6929.9 cm^{-1})	Ar (6934.7 cm^{-1})	<i>n</i> -H ₂ (6937.6 cm^{-1})	<i>p</i> -H ₂ (6940.0 cm^{-1})	Ar (6957.9 cm^{-1})
$N_{t=\infty}(\text{trans})$ (cm^{-2})	$(2.6 \pm 0.4) \times 10^{16}$	$(1.7 \pm 0.5) \times 10^{16}$	$(1.8 \pm 0.3) \times 10^{16}$	$(1.7 \pm 0.1) \times 10^{16}$	$(5.8 \pm 0.9) \times 10^{16}$
$N_{t=\infty}(\text{cis})$ (cm^{-2})	$(5.7 \pm 0.3) \times 10^{15}$	$(1.9 \pm 0.1) \times 10^{16}$	$(2.5 \pm 0.1) \times 10^{15}$	$(3 \pm 1) \times 10^{14}$	$(5.1 \pm 0.4) \times 10^{15}$
k_p^i (s^{-1})	$(5.7 \pm 0.4) \times 10^{-4}$	$(3 \pm 1) \times 10^{-3}$	$(9.4 \pm 0.2) \times 10^{-4}$	$(4 \pm 4) \times 10^{-3}$	$(2.2 \pm 0.1) \times 10^{-3}$
$N_{t=0}(\text{I})$ (cm^{-2})	$(2.8 \pm 0.4) \times 10^{16}$	$(2.8 \pm 0.5) \times 10^{16}$	$(2.0 \pm 0.3) \times 10^{16}$	$(1.7 \pm 0.1) \times 10^{16}$	$(6.3 \pm 0.9) \times 10^{16}$
A	0.0108	0.0148	0.0025	0.0025	0.0183
σ^i (cm^2)	$(3.9 \pm 0.6) \times 10^{-19}$	$(5 \pm 1) \times 10^{-19}$	$(1.3 \pm 0.2) \times 10^{-19}$	$(1.5 \pm 0.1) \times 10^{-19}$	$(2.9 \pm 0.5) \times 10^{-19}$
P (W)	7.4×10^{-3} ^a	7.4×10^{-3} ^a	2.4×10^{-2}	2.4×10^{-2}	2.4×10^{-2}
E_{photon} (J)	1.4×10^{-19}	1.4×10^{-19}	1.4×10^{-19}	1.4×10^{-19}	1.4×10^{-19}
I ($\text{cm}^{-2} \text{ s}^{-1}$)	5.3×10^{16}	5.3×10^{16}	1.7×10^{17}	1.7×10^{17}	1.7×10^{17}
ϕ^i	2.8×10^{-2}	1.1×10^{-1}	4.3×10^{-2}	1.6×10^{-1}	4.5×10^{-2}
n_{conv} (s^{-1})	1.6×10^{13}	8.4×10^{13}	1.9×10^{13}	7.0×10^{13}	1.4×10^{14}
n_{abs} (s^{-1})	1.3×10^{15}	1.8×10^{15}	9.8×10^{14}	9.8×10^{14}	7.0×10^{15}
$\phi_{\text{alternative}}^i$	1.2×10^{-2}	4.7×10^{-2}	1.9×10^{-2}	7.1×10^{-2}	2.0×10^{-2}
ϕ_{average}	$(2.0 \pm 0.8) \times 10^{-2}$	$(8 \pm 3) \times 10^{-2}$	$(3 \pm 1) \times 10^{-2}$	$(1.2 \pm 0.5) \times 10^{-1}$	$(3 \pm 1) \times 10^{-2}$

^a With the effect of OPO bandwidth taken into account (measured value was 2.4×10^{-2} W).

Table 2. Calculated quantum efficiencies (ϕ^i) of the conversion of glycine conformer I→III upon NIR laser excitation. The applied the excitation wavenumbers are in parentheses.

	Glycine		
	Ar (6968.8 cm^{-1})	<i>n</i> -H ₂ (6963.2 cm^{-1}) ^a	<i>p</i> -H ₂ (6968.1 cm^{-1}) ^a
k_p^i (s^{-1})	$(4.8 \pm 0.1) \times 10^{-4}$	$(3.5 \pm 0.1) \times 10^{-4}$	$(3.4 \pm 0.1) \times 10^{-4}$
$N_{t=0}(\text{I})$ (cm^{-2})	6.0×10^{16}	5.8×10^{16}	5.8×10^{16}
A	0.0043	0.0056	0.0184
σ^i (cm^2)	7.2×10^{-20}	9.7×10^{-20}	3.2×10^{-19}
P (W)	0.021 ± 0.002	0.023 ± 0.001	0.021 ± 0.002
E_{photon} (J)	1.4×10^{-19}	1.4×10^{-19}	1.4×10^{-19}
I ($\text{cm}^{-2} \text{ s}^{-1}$)	$(1.5 \pm 0.1) \times 10^{17}$	$(1.6 \pm 0.1) \times 10^{17}$	$(1.5 \pm 0.1) \times 10^{17}$
ϕ^i	4.4×10^{-2}	2.3×10^{-2}	7.1×10^{-3}
n_{conv} (s^{-1})	2.9×10^{13}	2.0×10^{13}	2.0×10^{13}
n_{abs} (s^{-1})	1.5×10^{15}	2.0×10^{15}	6.2×10^{15}
$\phi_{\text{alternative}}^i$	1.9×10^{-2}	1.0×10^{-2}	3.2×10^{-3}
ϕ_{average}	$(3 \pm 1) \times 10^{-2}$	$(1.7 \pm 0.7) \times 10^{-2}$	$(5 \pm 3) \times 10^{-3}$

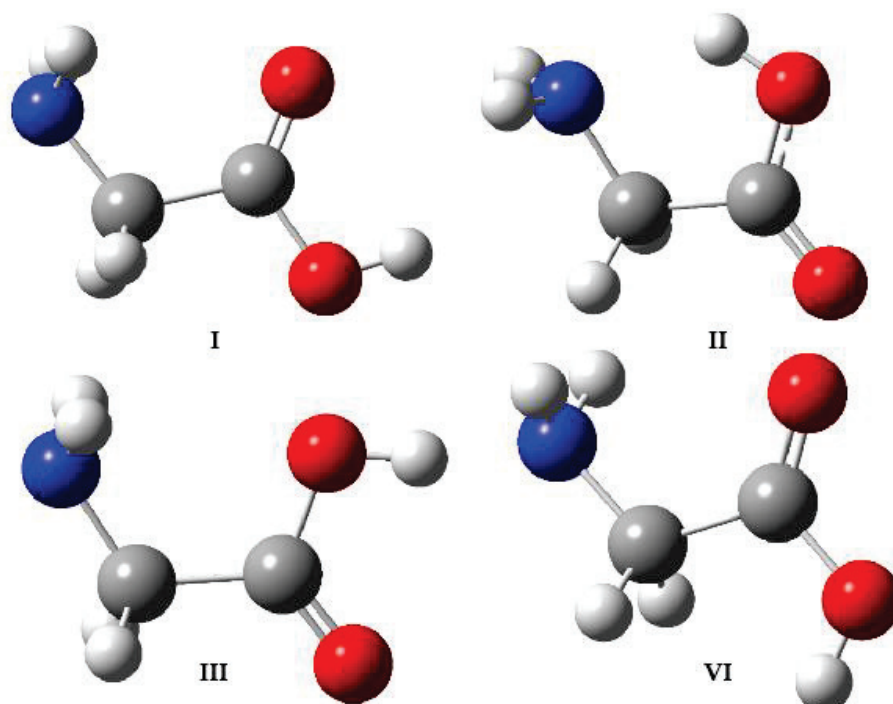
^a All conformer III had to be converted to I in H₂ matrices before the actual irradiation experiments, by exciting the $2\nu(\text{OH})$ mode the former at 6954.5 cm^{-1} (*n*-H₂) and 6959.3 cm^{-1} (*p*-H₂), respectively.

An important question is how k_p^i is calculated, which is of fundamental importance as it partially determines how quickly an equilibrium between the higher-energy *cis* (*E*) and the lower-energy *trans* (*Z*) conformers can be reached for the carboxylic acids when exciting the latter; thus, it has a fundamental influence on the ϕ^i values of the carboxylic acids. The same does not apply to glycine, as there was no observable tunneling of the III to I process on the experimental timescale (Scheme 1). Therefore for glycine, simply the growth rate of III was used since I follows a rather complicated (higher-order or dispersive) kinetics as a result of multiple (more and less stable) sites and also transforms into conformer II as a minor by-product, whose effects can never be perfectly eliminated. However, for the carboxylic acids, the effect of the relatively fast *cis-trans* back-conversion via hydrogen atom tunneling must also be considered [5,9,61]. This results in the rapid saturation of $N_t(cis)$ when pumping the *trans* form. Since the pumping and tunneling (k_t^i , also in s^{-1}) rates are identical in equilibrium, one can write that

$$k_p^i N_{t=\infty}(trans) = k_t^i N_{t=\infty}(cis) \quad (7)$$

which can be reformulated so that k_p^i can be obtained:

$$k_p^i = k_t^i N_{t=\infty}(cis) / N_{t=\infty}(trans) \quad (8)$$



Scheme 1. Experimentally observed conformers of glycine.

It is worth noting that $N_{t=\infty}(cis-FA)$ values are smaller for the higher k_t^i observed in hydrogen matrices, thus somewhat compensating the latter. Accordingly, less *trans* conformer can transform into *cis* before the rate of the reverse (tunneling) process becomes equal to the pumping rate, and thus, the equilibrium is reached earlier (Figure 1).

3.2. *Cis-Trans Tunneling Rates of the Carboxylic acids*

Although the NIR-induced conversion preceded the tunneling rate (k_t^i) measurements, as was discussed in the previous subsection, the rate of the back conversion via H atom tunneling must be determined first in order to be able to estimate the ϕ^i values of the

photon-induced processes in carboxylic acids; thus, we discuss the tunneling rates first. The spontaneous *cis* to *trans* conversion via H atom tunneling of carboxylic acids in low-temperature matrices, especially that of FA and AA, has been extensively investigated in the literature, studying the process in many different matrix environments. Thus, k_t^i of FA and AA obtained here can be directly compared with previous results (Table 3). We have found that k_t^i of *cis*-FA in Ar is $(2.6 \pm 0.5) \times 10^{-3} \text{ s}^{-1}$ (when the pumping wavelength was 6929.9 cm^{-1}), which agrees within error limits with the literature value of 2.3×10^{-3} (both values were obtained at the experimental temperature of 8 K) [2,5]. Interestingly, there seems to be no significant dependence of k_t^i values of *cis*-FA in Ar matrix on which of the two different sites of the $2\nu(\text{OH})$ mode of the *trans* form was previously pumped ($k_t^i = (2.4 \pm 0.1) \times 10^{-3} \text{ s}^{-1}$ after excitation at 6929.9 cm^{-1}).

Table 3. *Cis*-to-*trans* tunneling rates (k_t^i , in s^{-1}) and half-lives ($t_{1/2}^i(\text{cis})$, in s) of *cis*-FA and *cis*-AA after NIR laser excitation. Comparative data taken from the literature are in italics.

Species	Matrix	k_t^i	$t_{1/2}^i(\text{cis})$	Ref.
FA	Ne	-	$\approx 5 \pm 1^a$	[42]
	Ar	$(2.6 \pm 0.5) \times 10^{-3}$	270 ± 50^b	-
		$(2.4 \pm 0.1) \times 10^{-3}$	290 ± 10^c	-
		2.3×10^{-3}	-	[2,5]
	Kr	$\approx 1.5 \times 10^{-3}$	-	[2]
	Xe	$\approx 4 \times 10^{-4}$	-	[2]
AA	N ₂	$\approx 2 \times 10^{-5}$	-	[6]
	<i>n</i> -H ₂	$(6.8 \pm 0.5) \times 10^{-3}$	102 ± 8	-
		-	$\approx 140^a$	[48]
	<i>p</i> -H ₂	$(2.1 \pm 0.3) \times 10^{-1}$	3.3 ± 0.6	-
	Ar	$(2.5 \pm 0.3) \times 10^{-2}$	28 ± 3	-

^a determined at 4.2 K; ^b after exciting the *trans*-FA $2\nu(\text{OH})$ mode at 6929.9 cm^{-1} ; ^c after exciting the *trans*-FA $2\nu(\text{OH})$ mode at 6934.7 cm^{-1} .

It should be noted that the tunneling rate heavily depends on the noble gas used, which was explained by the stabilization of the *cis* form due to solvation, phonon-assisted tunneling [2], and matrix reorganization effects [54,55]. The extent of solvation (stabilization) is related to the increased dipole moment of the *cis* form, having an experimental dipole moment of 3.79 D vs. 1.42 D in the case of the *trans* conformer [62]. The theoretical values obtained at the used B3LYP/cc-pVTZ level of theory level should also be mentioned since they agree reasonably well with the experimental ones: 3.87 D (*cis*-FA) and 1.51 D (*trans*-FA), respectively. The computed dipole moment of the transition state lies between that of the two minima (2.77 D), suggesting an intermediate degree of solvation, thus a relatively lower stabilization than in the case of the *cis* form.

Moreover, the level of solvation also depends on the variation in the polarizability of the noble gas atoms; the higher the permanent dipole moment and the polarizability, the larger the dipole-induced dipole interaction is. As a consequence, the *cis* carboxylic acid in a matrix environment becomes more stable relative to the *trans* conformer. Regarding the polarizability of the medium, the respective values are 0.39, 0.80, and $1.64 \times 10^{-24} \text{ cm}^3$ for Ne, *n*-H₂, and Ar, respectively [63]. The difference between the observed tunneling rates of FA in *n*-H₂ and in Ar could then be explained by their different polarizabilities. Ne is an exception, though, where despite its low polarizability, the tunneling rate was found to be anomalously high, almost two orders of magnitude higher than in Ar. This finding was speculated to be caused by the small energy gap between the *cis* conformer and a vibrationally excited *trans* form. Accordingly, an efficient transformation of the former to the latter can be achieved because only one phonon is required for energy dissipation. A larger energy mismatch can undergo only through a multiphonon relaxation process, which evidently necessitates a longer period of time to proceed [42]. Similarly, in Ar, the energy gap between the ground-state *cis*-FA and the first excited state of the ν_8 (C–H out of

plane wagging) mode of the *trans*-FA is small enough for a relaxation process involving only one phonon (Debye frequency at 0 K: 93 cm^{-1} , that of Ne is 75 cm^{-1}) [64]. Therefore, the tunneling rate in Ar is expected to be relatively high [2]. In other matrices, such as in Xe, the energy mismatch is larger than the Debye frequency of that particular matrix (64 cm^{-1} at 0 K) [64], thus requiring a multiphonon process for the relaxation and resulting in the slowdown of the tunneling process by orders of magnitude [2]. The formation of complexes between FA and Xe was also proposed to account for the slower tunneling [65].

The effect of matrix reorganization on the temperature dependence of the tunneling rate has also been investigated by theoretical works [54,55]. The influence of the different matrices on the tunneling rate can be explained by the different reorganization energies; the highest value was found for Ar and lower ones for Kr, and especially for Xe, which may explain the differences in the observed tunneling rates [55].

The N_2 matrix behaves in a unique way in which a dipole-quadrupole interaction between the $-\text{OH}$ group of the guest and the host molecule is simulated by their 1:1 complex [53]; this complexation stabilizes the *cis* and *trans* conformers more than the transition state, thus effectively raising the barrier between the energy minima [6,56]. The relatively low Debye frequency of this matrix (69 cm^{-1}) [64] may also contribute to the inefficient relaxation, thus to the slowdown of the tunneling process.

The H atom tunneling process becomes faster in *n*- H_2 ($k_t^i = (6.8 \pm 0.5) \times 10^{-3}\text{ s}^{-1}$ at 3.1 K). Interestingly, the $t_{1/2}^i(\text{cis})$ value of the former found in the literature is ca. 140 s at 4.2 K [48], which still shows a reasonable agreement with our experimental result. This tunneling rate lies between those of *cis*-FA in Ne and in Ar, possibly likely due to the intermediate polarizability (thus solvation capability, see above) of *n*- H_2 compared to the two noble gases [48]. Moreover, *n*- H_2 has a nonzero quadrupole moment allowing for a small dipole-quadrupole interaction [66].

The tunneling rate is even higher in *p*- H_2 ($k_t^i = (2.1 \pm 0.3) \times 10^{-1}\text{ s}^{-1}$ at 3.1 K), which can be due to the fact that *p*- H_2 is considered a soft matrix even compared to *n*- H_2 ; therefore, relaxations may proceed virtually unhindered [58]. Furthermore, unlike *n*- H_2 , *p*- H_2 has zero quadrupole moment, excluding the possibility of such interactions with the isolated sample molecule [66]. Lastly, similarly to Ne, the Debye-frequencies of solid *n*- H_2 and *p*- H_2 are expected to be relatively high owing to their low masses (e.g., the derived value for *p*- H_2 is 88 cm^{-1}) [67], whereas the energy mismatch between *cis* and a vibrationally-excited *trans* form may be small. All the three effects listed above may contribute to the fast tunneling also by providing a possibility for a one-phonon relaxation mechanism rather than a multiphonon one.

In contrast, k_t^i of AA in Ar was found to be similar to that of FA in Ar or in *n*- H_2 and *p*- H_2 ($(2.5 \pm 0.3) \times 10^{-2}\text{ s}^{-1}$ at 8 K) and quite similar to the literature value ($(2.23 \pm 0.07) \times 10^{-2}\text{ s}^{-1}$ at 8 K) [9]. The higher rate found for AA compared to FA was explained by the presence of the methyl rotor providing efficient deactivation channels by its low-frequency vibrational modes [9]. It should be noted that k_t^i was determined to be similar in Kr ($(1.86 \pm 0.02) \times 10^{-2}\text{ s}^{-1}$ at 8 K) to that in Ar [9] and a couple of hundred times slower in N_2 ($\approx 3 \times 10^{-5}\text{ s}^{-1}$ at 8 K) [6], according to what is expected based on the findings discussed above for FA. However, unlike in the case of FA, k_t^i is some five times higher in Xe ($(1.04 \pm 0.05) \times 10^{-1}\text{ s}^{-1}$ at 8 K) than in Ar or Kr [9], implying that many different effects counterbalancing each other have to be taken into careful consideration [68]. Unfortunately, the tunneling rate of *cis*-AA becomes so high in the hydrogen matrices, that this conformer could not be observed and therefore k_t^i could not be determined. Nevertheless, a rough estimate can be given by making a few assumptions, which is detailed in the next subsection.

It is also important to point out that the glycine conformer VI could not be detected in *n*- H_2 and *p*- H_2 , either, also possibly due to its rapid tunneling back to conformer I. $t_{1/2}^i(\text{cis})$ of VI in Ar ($4 \pm 1\text{ s}$) is comparable to that of the *cis*-FA in *p*- H_2 , and it is expected to have even higher values in *n*- H_2 and in *p*- H_2 , most likely making the detection of VI in these matrix environments unfeasible.

3.3. Quantum Efficiency of the Processes

Before discussing the results, it must be highlighted that the spectral bandwidth of the laser light originating from our OPO device is larger than what was used previously in Ref. [5] (FWHM $\approx 5 \text{ cm}^{-1}$ vs. 0.1 cm^{-1} , respectively). Accordingly, the bandwidth of the laser beam is comparable to or even broader than that of the vibrational overtone band upon its excitation in the case of our setup. As a consequence, a considerable part of the incoming photons cannot be absorbed by the examined molecular system. Furthermore, the absorption efficiency of the photons having different wavelengths varies greatly for a particular process; thus, only an averaged, general ϕ_i value can be accessed when using a pumping source with a relatively large spectral bandwidth. These considerations also imply that our setup is less sensitive to the excitation wavelength used as long as it is chosen to be close enough to the absorption band selected for excitation. In contrast to this, having a laser beam with an appropriately small bandwidth allows for the precise determination of ϕ^i at a certain wavelength, for instance, exactly at the peak maximum. However, the latter is inherently more sensitive to the proper selection of the laser wavelength when exciting an absorption band. A wrongly wavelength-calibrated OPO may cause much more serious issues in this case.

While keeping this in mind, we chose to excite the $2\nu(\text{OH})$ mode of the samples to find out the ϕ_i values of the *trans-cis* (for FA and AA) and the I \rightarrow III (glycine) isomerization processes. The experiments with carboxylic acids were performed in Ar so that the quantum efficiencies of the processes made in this matrix environment may serve as references and thus can be directly compared with those obtained by earlier studies made on these systems [5,9]. For instance, the ϕ^i of FA was found to be $(2.0 \pm 0.8) \times 10^{-2}$ (excitation wavelength 6929.9 cm^{-1}), which is roughly an order of magnitude lower than that of the literature value of 1.7×10^{-1} [5]. In contrast, the σ^i value of FA in Ar is similar to the one discussed in the literature [61]. The discrepancy in ϕ^i may at least partially originate from the above-mentioned difference between the bandwidths of the OPO devices used; the excited overtone band of FA in Ar is about four times less broad (FWHM $\approx 1 \text{ cm}^{-1}$) than that of the laser light exiting our OPO device, resulting in the fact that only part of the incoming photons are actually absorbed by the vibrational overtone causing an apparently lower ϕ^i for our setup, and indeed, the ϕ^i of FA in Ar increases to $(6 \pm 3) \times 10^{-2}$ if a Gaussian laser spectrum is assumed and this effect is taken into account. Interestingly, if the other matrix site of the FA $2\nu(\text{OH})$ band at 6934.7 cm^{-1} is excited, the ϕ^i becomes larger equaling $(8 \pm 3) \times 10^{-1}$ (Table 1) being closer to the aforementioned literature value. However, this site was determined to have a ϕ^i of 7×10^{-2} previously [5], which agrees well with our data. The scaling of ϕ^i taking the bandwidth into account is not necessary for the results of other experiments (e.g., FA in hydrogen matrices or AA in Ar), where the bandwidths of the excited overtone bands were significantly larger and comparable to that of the NIR laser beam, therefore the latter is not expected to have a significant influence on the apparent ϕ^i value.

As far as the effect of different matrix environments is concerned, ϕ^i increases marginally (possibly within experimental uncertainty) when using different noble gases according to their increasing polarizability (c.f. 2.2×10^{-2} , 2.6×10^{-2} , and 3.5×10^{-2} for AA in Ar, Kr, and Xe, respectively) [9]. The relative ratio of the ϕ^i values in various cryogenic environments are directly related to the k_p^i values that can be observed in different matrices since the other two quantities that determine ϕ^i (σ^i and I , equation (4)) have a small variation. Moreover, it can be concluded that the efficiency of the process does not change significantly when using *n*-H₂ instead of Ar ($\phi^i = (3 \pm 1) \times 10^{-2}$). Interestingly, a so-called 'light-induced mobility' effect was observed by a previous work in the FA-*n*-H₂ system upon NIR laser irradiation, i.e., FA dimer formation was observed when exciting the monomeric form [48]. This phenomenon was completely absent in our case, and the lack of it in our experiments may be explained by the lower temperature achieved by our setup (4.2 vs. 3.1 K), making our matrix more rigid than in the earlier work. In contrast to what is observed in *n*-H₂, ϕ^i is evidently higher in *p*-H₂ ($(1.2 \pm 0.5) \times 10^{-1}$, Table 1) than in

the other two matrices. This finding indicates that a simple change in the relative amount of the nuclear spin isomers in solid H₂ may result in a significant increase in ϕ^i as well.

What can be summarized in general about AA is that the determined ϕ^i in Ar ($(3 \pm 1) \times 10^{-2}$) is similar to the previously obtained value (2.2×10^{-2}) [9,61] and is similar to that of FA when exciting the 6929.9 cm⁻¹ band ($(2.0 \pm 0.8) \times 10^{-2}$). Interestingly, earlier studies found that ϕ^i of FA was almost an order of magnitude higher compared to that of AA, which was explained by the presence of the methyl rotor enabling more energy relaxation channels thus allowing for a more efficient de-excitation [9]. Nevertheless, based on the findings with FA, the rotamerization process is expected to become even more efficient in *p*-H₂. However, $N_t(\text{cis-AA})$ becomes so small in hydrogen matrices due to the expectedly very quick reverse (H atom tunneling) process, that all of its vibrational bands (including its most intense ν (C=O) stretching band) are below the IR detection limit (even during the laser excitation), thus unfortunately preventing us from determining k_p^i in these environments. Nevertheless, a rough estimate for the low limit after a few assumptions is given below.

First, based on the findings of the experiments with FA, ϕ^i in Ar and in *n*-H₂ are similar, whereas σ^i in the latter is about one-third of that in Ar; therefore, the same can be assumed for AA as well. Accordingly, if we take the ϕ^i and σ^i values of the AA-Ar system, make a correction to the latter, and take into account that I was 1.5×10^{17} cm⁻² s⁻¹, k_p^i for the AA-*n*-H₂ can be estimated using Equation (4), which equals 5.1×10^{-3} s⁻¹. The alternative way can also be used to estimate k_p^i (3.5×10^{-3} s⁻¹); for this $\phi_{\text{alternative}}^i$ (presumed to be identical to that of the AA-Ar system), $N_{t=0}(\text{trans})$ (1.5×10^{16} cm⁻²), A (0.0068) are needed to be known utilizing Equations (5) and (6). Then, Equation (7) can be used to obtain k_t^i by knowing $N_{t=\infty}(\text{trans})$ (1.5×10^{16} cm⁻² by assuming that only a negligible portion of *trans*-AA transforms upon irradiation), $N_{t=\infty}(\text{cis})$ ($< 1.5 \times 10^{13}$ cm⁻² based on the assumption that the $\nu(\text{C=O})$ mode is below the detection limit; therefore, its integrated area is less than 0.001 cm⁻¹), and using the mean value of the two k_p^i values obtained by the two alternative methods (roughly 4.3×10^{-3} s⁻¹). This translates into a k_t^i value of $> 4.3 \times 10^0$ s⁻¹ (equaling $t_{1/2}^i(\text{cis}) \approx 0.16$ s). The same considerations can be applied to the AA-*p*-H₂ system, except that ϕ^i is expected to be approximately 3.4 times higher than in Ar (as deduced from the results with FA, equaling 2.0×10^{-1}); the same correction factor for $\phi_{\text{alternative}}^i$ (1.1×10^{-1}) was found to be 4.4, whereas $N_{t=0}(\text{trans}) = N_{t=\infty}(\text{trans})$, $N_{t=\infty}(\text{cis})$, A , and I are equal to 1.9×10^{16} cm⁻², $< 1.5 \times 10^{13}$ cm⁻², 00061, 1.6×10^{17} cm⁻² s⁻¹ and respectively. Consequently, the mean k_p^i value is 5.3×10^{-3} s⁻¹ yielding a k_t^i value of $> 6.7 \times 10^0$ s⁻¹ (i.e., $t_{1/2}^i(\text{cis}) \approx 0.10$ s).

Regarding glycine, we did not expect to see the rotamerization of I→VI involving the H atom of the -OH group of the molecule in hydrogen matrices owing to the expected extremely rapid back conversion via tunneling. Instead, the emphasis was put on the laser-induced conversion of I→III, resulting in the rotation of the whole -COOH moiety. The ϕ^i of the I→III conversion shows a weaker dependence on the matrix than that of the FA, and it ranges between 5×10^{-3} (in *p*-H₂) and 3×10^{-2} (in Ar). Importantly, these values are more than an order of magnitude higher than that of the I→VI process (determined to be 8×10^{-4} in Ar), according to what is expected [25]. Even though the value obtained in the *p*-H₂ matrix is some six times lower, it could be at least partially explained by the σ^i higher than in Ar or in *n*-H₂ matrices, which is expected to be some 3–4 times lower in hydrogen matrix compared to Ar based on the results with FA. Consequently, σ^i in the *p*-H₂ is probably overestimated, which causes the discrepancy between the results. The seemingly more or less independent nature of the I→III conversion on the chosen media is somewhat unexpected since the rotation of the -COOH group should be more hindered in rigid (Ar, *n*-H₂) matrices than in a soft matrix (*p*-H₂). In order to explain this finding, it could be speculated that in *p*-H₂, a fast forward-backward I⇌VI conversion takes place in parallel with the main I→III rotamerization, thus decreasing the apparent efficiency of the latter process. This hypothesis could be verified by a future study on model systems, where the rotation of the -OH group is hindered.

4. Conclusions

FA, AA, and glycine samples were investigated in Ar, *n*-H₂, and *p*-H₂ matrices. The tunneling rates were determined, and the one obtained for FA in Ar is in good agreement with the literature value ($(2.6 \pm 0.5) \times 10^{-3} \text{ s}^{-1}$ vs. $2.3 \times 10^{-3} \text{ s}^{-1}$) [2,5]. The half-life of *cis*-FA in *n*-H₂ is still not particularly different from the one found in the literature (102 ± 8 vs. 140 s) [48]. Most importantly, k_t^i of *cis*-FA has been determined in *p*-H₂ for the first time, and it was found to be $(2.1 \pm 0.3) \times 10^{-1} \text{ s}^{-1}$, i.e., almost two orders of magnitude higher than that in Ar or even in *n*-H₂. With regard to AA, its k_t^i in Ar was determined to be $(2.5 \pm 0.3) \times 10^{-2} \text{ s}^{-1}$ which, similarly to *cis*-FA, compares very well with the literature value ($(2.23 \pm 0.07) \times 10^{-2} \text{ s}^{-1}$) [9]. Unfortunately, due to the extremely rapid back conversion of *cis*-AA to its *trans* form via H atom tunneling, k_t^i could not be determined in hydrogen matrix although they are expected to be even higher than in Ar matrix and a low limit be given ($>4.3 \times 10^{-0} \text{ s}^{-1}$ and $>6.7 \times 10^{-0} \text{ s}^{-1}$ in *n*-H₂ and in *p*-H₂, respectively). These values signify a *cis*-AA half-life in these media in the order of a few tenths of seconds. No tunneling between the conformers could be detected in the experiments carried out with glycine.

As far as the quantum efficiencies of the NIR laser-induced *trans* to *cis* conversion are concerned, the ϕ^i value for FA in Ar was obtained to be $(2.0 \pm 0.8) \times 10^{-2}$ (i.e., 2%) when pumping the *trans*-FA overtone band 6929.9 cm^{-1} . This value is remarkably different from earlier results when the same pumping wavelength was used to generate the *cis* form (1.7×10^{-1}) [5]. However, the bandwidth of the laser beam was quite different in the two cases: our result shows more like an averaged value over the whole absorption peak, whereas the smaller bandwidth used in the earlier work allowed for the determination at a very precise wavelength (possibly nearby the maximum of the excited NIR band). Nonetheless, ϕ^i was also calculated for another NIR overtone band of *cis*-AA at 6934.7 cm^{-1} ($(8 \pm 3) \times 10^{-2}$), which shows a much better agreement with the literature value of 7×10^{-2} [5]. Regarding the behavior of this process in hydrogen matrices, ϕ^i does not differ much in *n*-H₂ ($3 \pm 1) \times 10^{-2}$ from that taken in Ar, however, the process proceeds more efficiently in *p*-H₂ ($1.2 \pm 0.5) \times 10^{-1}$. For AA, owing to the rapid tunneling in the hydrogen matrices, only ϕ^i in Ar could be determined ($3 \pm 1) \times 10^{-2}$, which is within error limits with the one found in the literature (2.2×10^{-2}) [9,61]. As for glycine, the ϕ^i values for the I→VI conversion were not determined, the ϕ^i values for the I→III conversion in the three environment (Ar, *n*-H₂, and *p*-H₂) are $(3 \pm 1) \times 10^{-2}$, $(1.7 \pm 0.7) \times 10^{-2}$, and $(5 \pm 3) \times 10^{-3}$, respectively. This result contradicts the intuition, where one would expect a more efficient process in the case of the softer *p*-H₂ matrix. The discrepancy could be resolved by assuming a fast forward-backward I⇌VI conversion occurring simultaneously with the main I→III conversion, which would decrease the observed efficiency of the latter process.

The present results imply that in the case of spontaneous conformational change in solid *p*-H₂, the matrix effects are diminished as compared to rigid hosts. This offers an excellent possibility for the comparison of the theoretical models with experimentally measured tunneling rates. The results also suggest that the quantum efficiencies of some (N)IR-light-induced conformational changes are larger in solid *p*-H₂ than in rigid hosts. The present study raises some new questions as well. Can conformational changes with large site rearrangements be induced by NIR laser radiation in *p*-H₂? How does the shift from a rigid to a soft matrix affect the ratio of the quantum efficiencies of local and remote conformational changes? We plan to address these and similar questions in subsequent studies.

Supplementary Materials: The following supporting information can be downloaded at: <https://www.mdpi.com/article/10.3390/photochem2030039/s1>, Tables S1–S12: optimized geometries as well as harmonic and anharmonic vibrational frequencies and their intensities of the *cis* and *trans* conformers of formic and acetic acid, as well as those of glycine; Table S13 and Figure S1: the vibrational band positions used to determine the column densities of each species; Figure S2: bands used for NIR excitation; Figure S3: kinetic plots of acetic acid in Ar matrix during and after the NIR laser excitation.

Author Contributions: Conceptualization, G.T.; Data curation, S.G.; Formal analysis, S.G.; Funding acquisition, G.T.; Investigation, S.G. and G.R.; Methodology, S.G. and G.T.; Project administration, G.T.; Resources, G.T.; Supervision, G.T.; Visualization, S.G.; Writing—original draft, S.G. and G.T.; Writing—review and editing, S.G., G.R., G.B. and G.T. All authors have read and agreed to the published version of the manuscript.

Funding: This research was funded by the Lendület program of the Hungarian Academy of Sciences and was also supported by the ELTE Institutional Excellence Program (TKP2020-IKA-05).

Institutional Review Board Statement: Not applicable.

Informed Consent Statement: Not applicable.

Data Availability Statement: The data are available from the authors upon request.

Conflicts of Interest: The authors declare no conflict of interest.

References

- Pettersson, M.; Lundell, J.; Khriachtchev, L.; Räsänen, M. IR Spectrum of the Other Rotamer of Formic Acid, *cis*-HCOOH. *J. Am. Chem. Soc.* **1997**, *119*, 11715–11716. [CrossRef]
- Pettersson, M.; Maçõas, E.M.S.; Khriachtchev, L.; Lundell, J.; Fausto, R.; Räsänen, M. *Cis* → *trans* conversion of formic acid by dissipative tunneling in solid rare gases: Influence of environment on the tunneling rate. *J. Chem. Phys.* **2002**, *117*, 9095–9098. [CrossRef]
- Maçõas, E.M.S.; Lundell, J.; Pettersson, M.; Khriachtchev, L.; Fausto, R.; Räsänen, M. Vibrational spectroscopy of *cis*- and *trans*-formic acid in solid argon. *J. Mol. Spectrosc.* **2003**, *219*, 70–80. [CrossRef]
- Pettersson, M.; Maçõas, E.M.S.; Khriachtchev, L.; Fausto, R.; Räsänen, M. Conformational Isomerization of Formic Acid by Vibrational Excitation at Energies below the Torsional Barrier. *J. Am. Chem. Soc.* **2003**, *125*, 4058–4059. [CrossRef] [PubMed]
- Maçõas, E.M.S.; Khriachtchev, L.; Pettersson, M.; Juselius, J.; Fausto, R.; Räsänen, M. Reactive vibrational excitation spectroscopy of formic acid in solid argon: Quantum yield for infrared induced *trans*→*cis* isomerization and solid state effects on the vibrational spectrum. *J. Chem. Phys.* **2003**, *119*, 11765–11772. [CrossRef]
- Lopes, S.; Domanskaya, A.V.; Fausto, R.; Räsänen, M.; Khriachtchev, L. Formic and acetic acids in a nitrogen matrix: Enhanced stability of the higher-energy conformer. *J. Chem. Phys.* **2010**, *133*, 144507. [CrossRef]
- Maçõas, E.M.S.; Khriachtchev, L.; Pettersson, M.; Fausto, R.; Räsänen, M. Rotational Isomerism in Acetic Acid: The First Experimental Observation of the High-Energy Conformer. *J. Am. Chem. Soc.* **2003**, *125*, 16188–16189. [CrossRef]
- Maçõas, E.M.S.; Khriachtchev, L.; Fausto, R.; Räsänen, M. Photochemistry and Vibrational Spectroscopy of the *Trans* and *Cis* Conformers of Acetic Acid in Solid Ar. *J. Phys. Chem. A* **2004**, *108*, 3380–3389. [CrossRef]
- Maçõas, E.M.S.; Khriachtchev, L.; Pettersson, M.; Fausto, R.; Räsänen, M. Rotational isomerism of acetic acid isolated in rare-gas matrices: Effect of medium and isotopic substitution on IR-induced isomerization quantum yield and *cis*→*trans* tunneling rate. *J. Chem. Phys.* **2004**, *121*, 1331–1338. [CrossRef]
- Apóstolo, R.F.G.F.G.; Bazsó, G.; Bento, R.R.F.R.F.; Tarczay, G.; Fausto, R. The first experimental observation of the higher-energy *trans* conformer of trifluoroacetic acid. *J. Mol. Struct.* **2016**, *1125*, 288–295. [CrossRef]
- Apóstolo, R.F.G.F.G.; Bazsó, G.; Ogruc-Ildiz, G.; Tarczay, G.; Fausto, R. Near-infrared in situ generation of the higher-energy *trans* conformer of tribromoacetic acid: Observation of a large-scale matrix-site changing mediated by conformational conversion. *J. Chem. Phys.* **2018**, *148*, 044303. [CrossRef] [PubMed]
- Lopes, S.; Nikitin, T.; Fausto, R. Propionic Acid in Solid Nitrogen: NIR- and UV-Induced *cis* → *trans* Isomerization and Matrix-Site-Dependent *trans* → *cis* Tunneling. *J. Phys. Chem. A* **2019**, *123*, 1581–1593. [CrossRef]
- Maçõas, E.M.S.; Khriachtchev, L.; Pettersson, M.; Fausto, R.; Räsänen, M.; Maças, E.M.S.; Khriachtchev, L.; Pettersson, M.; Fausto, R.; Räsänen, M. Internal rotation in propionic acid: Near-infrared-induced isomerization in solid Argon. *J. Phys. Chem. A* **2005**, *109*, 3617–3625. [CrossRef] [PubMed]
- Bazsó, G.; Góbi, S.; Tarczay, G. Near-Infrared Radiation Induced Conformational Change and Hydrogen Atom Tunneling of 2-Chloropropionic Acid in Low-Temperature Ar Matrix. *J. Phys. Chem. A* **2012**, *116*, 4823–4832. [CrossRef] [PubMed]
- Halasa, A.; Lapinski, L.; Reva, I.; Rostkowska, H.; Fausto, R.; Nowak, M.J. Near-Infrared Laser-Induced Generation of Three Rare Conformers of Glycolic Acid. *J. Phys. Chem. A* **2014**, *118*, 5626–5635. [CrossRef]

16. Reva, I.; Nunes, C.M.; Biczysko, M.; Fausto, R.; Nunes, C.M.; Biczysko, M.; Fausto, R. Conformational switching in pyruvic acid isolated in Ar and N₂ matrixes: Spectroscopic analysis, anharmonic simulation, and tunneling. *J. Phys. Chem. A* **2015**, *119*, 2614–2627. [CrossRef]
17. Halasa, A.; Lapinski, L.; Rostkowska, H.; Reva, I.; Nowak, M.J. Tunable Diode Lasers as a Tool for Conformational Control: The Case of Matrix-Isolated Oxamic Acid. *J. Phys. Chem. A* **2015**, *119*, 2203–2210. [CrossRef]
18. Maçôas, E.M.S.S.; Fausto, R.; Pettersson, M.; Khriachtchev, L.; Räsänen, M. Infrared-induced rotamerization of oxalic acid monomer in argon matrix. *J. Phys. Chem. A* **2000**, *104*, 6956–6961. [CrossRef]
19. Maçôas, E.M.S.S.; Fausto, R.; Lundell, J.; Pettersson, M.; Khriachtchev, L.; Räsänen, M. Conformational Analysis and Near-Infrared-Induced Rotamerization of Malonic Acid in an Argon Matrix. *J. Phys. Chem. A* **2000**, *104*, 11725–11732. [CrossRef]
20. Maçôas, E.M.S.S.; Fausto, R.; Lundell, J.; Pettersson, M.; Khriachtchev, L.; Räsänen, M. A matrix isolation spectroscopic and quantum chemical study of fumaric and maleic acid. *J. Phys. Chem. A* **2001**, *105*, 3922–3933. [CrossRef]
21. Lapinski, L.; Reva, I.; Rostkowska, H.; Halasa, A.; Fausto, R.; Nowak, M.J. Conformational transformation in squaric acid induced by near-IR laser light. *J. Phys. Chem. A* **2013**, *117*, 5251–5259. [CrossRef]
22. Halasa, A.; Lapinski, L.; Reva, I.; Rostkowska, H.; Fausto, R.; Nowak, M.J. Three Conformers of 2-Furoic Acid: Structure Changes Induced with Near-IR Laser Light. *J. Phys. Chem. A* **2015**, *119*, 1037–1047. [CrossRef]
23. Kuş, N.; Fausto, R. Effects of the matrix and intramolecular interactions on the stability of the higher-energy conformers of 2-fluorobenzoic acid. *J. Chem. Phys.* **2017**, *146*, 124305. [CrossRef]
24. Bazsó, G.; Magyarfalvi, G.; Tarczay, G. Near-infrared laser induced conformational change and UV laser photolysis of glycine in low-temperature matrices: Observation of a short-lived conformer. *J. Mol. Struct.* **2012**, *1025*, 33–42. [CrossRef]
25. Bazsó, G.; Magyarfalvi, G.; Tarczay, G. Tunneling Lifetime of the ttc /VIp Conformer of Glycine in Low-Temperature Matrices. *J. Phys. Chem. A* **2012**, *116*, 10539–10547. [CrossRef]
26. Bazsó, G.; Najbauer, E.E.; Magyarfalvi, G.; Tarczay, G. Near-Infrared Laser Induced Conformational Change of Alanine in Low-Temperature Matrixes and the Tunneling Lifetime of Its Conformer VI. *J. Phys. Chem. A* **2013**, *117*, 1952–1962. [CrossRef]
27. Nunes, C.M.; Lapinski, L.; Fausto, R.; Reva, I. Near-IR laser generation of a high-energy conformer of L-alanine and the mechanism of its decay in a low-temperature nitrogen matrix. *J. Chem. Phys.* **2013**, *138*, 125101. [CrossRef]
28. Najbauer, E.E.; Bazsó, G.; Góbi, S.; Magyarfalvi, G.; Tarczay, G. Exploring the Conformational Space of Cysteine by Matrix Isolation Spectroscopy Combined with Near-Infrared Laser Induced Conformational Change. *J. Phys. Chem. B* **2014**, *118*, 2093–2103. [CrossRef]
29. Najbauer, E.E.; Bazsó, G.; Apóstolo, R.; Fausto, R.; Biczysko, M.; Barone, V.; Tarczay, G. Identification of Serine Conformers by Matrix-Isolation IR Spectroscopy Aided by Near-Infrared Laser-Induced Conformational Change, 2D Correlation Analysis, and Quantum Mechanical Anharmonic Computations. *J. Phys. Chem. B* **2015**, *119*, 10496–10510. [CrossRef]
30. Lapinski, L.; Nowak, M.J.; Reva, I.; Rostkowska, H.; Fausto, R. NIR-laser-induced selective rotamerization of hydroxy conformers of cytosine. *Phys. Chem. Chem. Phys.* **2010**, *12*, 9615. [CrossRef]
31. Reva, I.; Nowak, M.J.; Lapinski, L.; Fausto, R. Spontaneous tunneling and near-infrared-induced interconversion between the amino-hydroxy conformers of cytosine. *J. Chem. Phys.* **2012**, *136*, 064511. [CrossRef]
32. Lapinski, L.; Reva, I.; Rostkowska, H.; Fausto, R.; Nowak, M.J. Near-IR-Induced, UV-Induced, and Spontaneous Isomerizations in 5-Methylcytosine and 5-Fluorocytosine. *J. Phys. Chem. B* **2014**, *118*, 2831–2841. [CrossRef]
33. Rostkowska, H.; Lapinski, L.; Kozankiewicz, B.; Nowak, M.J. Photochemical isomerizations of thiosemicarbazide, a matrix isolation study. *J. Phys. Chem. A* **2012**, *116*, 9863–9871. [CrossRef]
34. Halasa, A.; Reva, I.; Lapinski, L.; Nowak, M.J.; Fausto, R. Conformational Changes in Thiazole-2-carboxylic Acid Selectively Induced by Excitation with Narrowband Near-IR and UV Light. *J. Phys. Chem. A* **2016**, *120*, 2078–2088. [CrossRef]
35. Halasa, A.; Lapinski, L.; Rostkowska, H.; Nowak, M.J. Intramolecular Vibrational Energy Redistribution in 2-Thiocytosine: SH Rotamerization Induced by Near-IR Selective Excitation of NH₂ Stretching Overtone. *J. Phys. Chem. A* **2015**, *119*, 9262–9271. [CrossRef]
36. Halasa, A.; Reva, I.; Lapinski, L.; Rostkowska, H.; Fausto, R.; Nowak, M.J. Conformers of Kojic Acid and Their Near-IR-Induced Conversions: Long-Range Intramolecular Vibrational Energy Transfer. *J. Phys. Chem. A* **2016**, *120*, 2647–2656. [CrossRef]
37. Lopes Jesus, A.J.; Reva, I.; Araujo-Andrade, C.; Fausto, R. Conformational Switching by Vibrational Excitation of a Remote NH Bond. *J. Am. Chem. Soc.* **2015**, *137*, 14240–14243. [CrossRef]
38. Lapinski, L.; Reva, I.; Rostkowska, H.; Lopes Jesus, A.J.; Vieira Pinto, S.M.; Fausto, R.; Nowak, M.J. Conformational Isomerizations by Rotation around C–C or C–N Bonds: A Comparative Study on Matrix-Isolated Glycolamide and N-Hydroxyurea Excited with Near-IR Laser Light. *J. Phys. Chem. A* **2019**, *123*, 3831–3839. [CrossRef]
39. Kovács, B.; Kuş, N.; Tarczay, G.; Fausto, R. Experimental Evidence of Long-Range Intramolecular Vibrational Energy Redistribution through Eight Covalent Bonds: NIR Irradiation Induced Conformational Transformation of E-Glutaconic Acid. *J. Phys. Chem. A* **2017**, *121*, 3392–3400. [CrossRef]
40. Góbi, S.; Reva, I.; Csonka, I.P.; Nunes, C.M.; Tarczay, G.; Fausto, R. Selective conformational control by excitation of NH imino vibrational antennas. *Phys. Chem. Chem. Phys.* **2019**, *21*, 24935–24949. [CrossRef]
41. Góbi, S.; Balbisi, M.; Tarczay, G. Local and Remote Conformational Switching in 2-Fluoro-4-Hydroxy Benzoic Acid. *Photochem* **2022**, *2*, 102–121. [CrossRef]

42. Marushkevich, K.; Khriachtchev, L.; Räsänen, M. High-energy conformer of formic acid in solid neon: Giant difference between the proton tunneling rates of cis monomer and trans-cis dimer. *J. Chem. Phys.* **2007**, *126*, 241102. [CrossRef]
43. Góbi, S.; Nunes, C.M.; Reva, I.; Tarczay, G.; Fausto, R. S–H rotamerization via tunneling in a thiol form of thioacetamide. *Phys. Chem. Chem. Phys.* **2019**, *21*, 17063–17071. [CrossRef]
44. Rostkowska, H.; Lapinski, L.; Khvorostov, A.; Nowak, M.J. Proton-Transfer Processes in Thiourea: UV Induced Thione → Thiol Reaction and Ground State Thiol → Thione Tunneling. *J. Phys. Chem. A* **2003**, *107*, 6373–6380. [CrossRef]
45. Rostkowska, H.; Lapinski, L.; Nowak, M.J. Hydrogen-atom tunneling through a very high barrier; Spontaneous thiol → thione conversion in thiourea isolated in low-temperature Ar, Ne, H₂ and D₂ matrices. *Phys. Chem. Chem. Phys.* **2018**, *20*, 13994–14002. [CrossRef]
46. Rostkowska, H.; Lapinski, L.; Khvorostov, A.; Nowak, M.J. Proton transfer processes in selenourea: UV-induced selenone→selenol photoreaction and ground state selenol→selenone proton tunneling. *Chem. Phys.* **2004**, *298*, 223–232. [CrossRef]
47. Lapinski, L.; Rostkowska, H.; Khvorostov, A.; Yaman, M.; Fausto, R.; Nowak, M.J. Double-Proton-Transfer Processes in Dithiooxamide: UV-Induced Dithione → Dithiol Reaction and Ground-State Dithiol → Dithione Tunneling. *J. Phys. Chem. A* **2004**, *108*, 5551–5558. [CrossRef]
48. Marushkevich, K.; Khriachtchev, L.; Räsänen, M. High-energy conformer of formic acid in solid hydrogen: Conformational change promoted by host excitation. *Phys. Chem. Chem. Phys.* **2007**, *9*, 5748–5751. [CrossRef]
49. Ryazantsev, S.V.; Feldman, V.I.; Khriachtchev, L. Conformational Switching of HOCO Radical: Selective Vibrational Excitation and Hydrogen-Atom Tunneling. *J. Am. Chem. Soc.* **2017**, *139*, 9551–9557. [CrossRef]
50. Räsänen, M.; Kunttu, H.; Murto, J. Infrared Induced Conformer Interconversion Processes in Low-Temperature Matrices. *Laser Chem.* **1988**, *9*, 123–145. [CrossRef]
51. Bondybey, V.E. Relaxation and Vibrational Energy Redistribution Processes in Polyatomic Molecules. *Annu. Rev. Phys. Chem.* **1984**, *35*, 591–612. [CrossRef]
52. Domanskaya, A.; Marushkevich, K.; Khriachtchev, L.; Räsänen, M. Spectroscopic study of cis-to-trans tunneling reaction of HCOOD in rare gas matrices. *J. Chem. Phys.* **2009**, *130*, 154509. [CrossRef]
53. Tsuge, M.; Khriachtchev, L. Tunneling Isomerization of Small Carboxylic Acids and Their Complexes in Solid Matrixes: A Computational Insight. *J. Phys. Chem. A* **2015**, *119*, 2628–2635. [CrossRef] [PubMed]
54. Trakhtenberg, L.I.; Fokeyev, A.A.; Zyubin, A.S.; Mebel, A.M.; Lin, S.H. Matrix reorganization with intramolecular tunneling of H atom: Formic acid in Ar matrix. *J. Chem. Phys.* **2009**, *130*, 144502. [CrossRef]
55. Trakhtenberg, L.I.; Fokeyev, A.A.; Zyubin, A.S.; Mebel, A.M.; Lin, S.H. Effect of the Medium on Intramolecular H-Atom Tunneling: Cis–Trans Conversion of Formic Acid in Solid Matrixes of Noble Gases. *J. Phys. Chem. B* **2010**, *114*, 17102–17112. [CrossRef] [PubMed]
56. Marushkevich, K.; Räsänen, M.; Khriachtchev, L. Interaction of Formic Acid with Nitrogen: Stabilization of the Higher-Energy Conformer. *J. Phys. Chem. A* **2010**, *114*, 10584–10589. [CrossRef] [PubMed]
57. Schreiner, P.R.; Wagner, J.P.; Reisenauer, H.P.; Gerbig, D.; Ley, D.; Sarka, J.; Császár, A.G.; Vaughn, A.; Allen, W.D. Domino Tunneling. *J. Am. Chem. Soc.* **2015**, *137*, 7828–7834. [CrossRef]
58. Tsuge, M.; Lee, Y.-P. Spectroscopy of molecules confined in solid *para*-hydrogen. In *Molecular and Laser Spectroscopy*; Gupta, V.P., Ozaki, Y., Eds.; Elsevier: Amsterdam, The Netherlands, 2020; pp. 167–215. ISBN 978-0-12-818870-5.
59. Bazsó, G.; Csonka, I.P.; Góbi, S.; Tarczay, G. VIZSLA—Versatile Ice Zigzag Sublimation Setup for Laboratory Astrochemistry. *Rev. Sci. Instrum.* **2021**, *92*, 124104. [CrossRef]
60. Frisch, M.J.; Trucks, G.W.; Schlegel, H.B.; Scuseria, G.E.; Robb, M.A.; Cheeseman, J.R.; Scalmani, G.; Barone, V.; Mennucci, B.; Petersson, G.A.; et al. *Gaussian 09 Revision, D.01*; Gaussian, Inc.: Wallingford, CT, USA, 2013.
61. Maçôas, E.M.S.S.; Khriachtchev, L.; Pettersson, M.; Fausto, R.; Räsänen, M.M. Rotational isomerization of small carboxylic acids isolated in argon matrices: Tunneling and quantum yields for the photoinduced processes. *Phys. Chem. Chem. Phys.* **2005**, *7*, 743–749. [CrossRef]
62. Hocking, W.H. The Other Rotamer of Formic Acid, cis-HCOOH. *Zeitschrift fur Naturforsch. Sect. A J. Phys. Sci.* **1976**, *31*, 1113–1121. [CrossRef]
63. *CRC Handbook of Chemistry and Physics*; Lide, D.R. (Ed.) CRC Press: Boca Raton, FL, USA, 2005.
64. Jodl, H.J. Solid state aspects of matrices. In *Chemistry and Physics of Matrix-Isolated Species*; Andrews, L., Moskovits, M., Eds.; North-Holland: Amsterdam, The Netherlands, 1989; p. 430. ISBN 9780444705495.
65. Cao, Q.; Melavuori, M.; Lundell, J.; Räsänen, M.; Khriachtchev, L. Matrix-isolation and ab initio study of the complex between formic acid and xenon. *J. Mol. Struct.* **2012**, *1025*, 132–139. [CrossRef]
66. Ceponkus, J.; Nelander, B. A simple model for the water o-H₂ complex. *J. Chem. Phys.* **2006**, *124*, 2–6. [CrossRef]
67. Nucara, A.; Calvani, P.; Cunsolo, S.; Lupi, S.; Ruzicka, B. Translational and rotational spectra in the fundamental infrared band of liquid and solid parahydrogen. *Phys. Rev. B* **1993**, *47*, 2590–2595. [CrossRef]
68. Fausto, R.; Khriachtchev, L.; Hamm, P. Conformational changes in cryogenic matrices. In *Physics and Chemistry at Low Temperatures*; Jenny Stanford Publishing: New York, NY, USA, 2011; pp. 51–84. ISBN 9789814267519.

Article

Mass-Resolved Momentum Imaging of Three Dichloroethylene Isomers by Femtosecond Laser-Induced Coulomb Explosion

Yoriko Wada ¹, Hiroshi Akagi ¹, Takayuki Kumada ², Ryuji Itakura ¹ and Tomonari Wakabayashi ^{3,*}

¹ Kansai Photon Science Institute, National Institutes for Quantum Science and Technology, Kizugawa 619-0215, Japan

² Japan Atomic Energy Agency, Tokai-mura, Ibaraki 319-1195, Japan

³ Department of Chemistry, School of Science and Engineering, Kindai University, Higashi-Osaka 577-8502, Japan

* Correspondence: wakaba@chem.kindai.ac.jp; Tel.: +81-6-4307-3408

Abstract: Coulomb explosion experiments using linearly polarized intense 60 fs laser pulses were conducted for structural characterization of three dichloroethylene (DCE) isomers, 1,1-DCE, *cis*-1,2-DCE, and *trans*-1,2-DCE. Under relatively low laser intensity at 1.8×10^{14} W/cm², mass-resolved momentum imaging (MRMI) for selected fragment ions of ³⁵Cl⁺ and C²⁺ revealed different patterns for the three isomers. The C²⁺ ion fragmented from multiply charged *trans*-1,2-DCE was forced to leave perpendicularly to the direction of the laser polarization, due to recoil forces from adjacent cations. In contrast, the fast ions of C²⁺ from *cis*-1,2-DCE exhibited an isotropic distribution, whereas the fast ions of C²⁺ from 1,1-DCE recoiled along the laser polarization together with the slow C²⁺ ions, and thereby distinction of the three isomers was demonstrated. Coulomb explosion occurs predominantly at specific orientation, which is useful for potential applications of MRMI analysis to molecular structure assays.

Keywords: dichloroethylene isomers; femtosecond laser; coulomb explosion; mass-resolved momentum imaging; molecular structure assay

Citation: Wada, Y.; Akagi, H.; Kumada, T.; Itakura, R.; Wakabayashi, T. Mass-Resolved Momentum Imaging of Three Dichloroethylene Isomers by Femtosecond Laser-Induced Coulomb Explosion. *Photochem* **2022**, *2*, 798–809. <https://doi.org/10.3390/photochem2030051>

Academic Editors: Rui Fausto and Robert Koles

Received: 18 August 2022

Accepted: 13 September 2022

Published: 16 September 2022

Publisher's Note: MDPI stays neutral with regard to jurisdictional claims in published maps and institutional affiliations.



Copyright: © 2022 by the authors. Licensee MDPI, Basel, Switzerland. This article is an open access article distributed under the terms and conditions of the Creative Commons Attribution (CC BY) license (<https://creativecommons.org/licenses/by/4.0/>).

1. Introduction

Coulomb explosion is a molecular process in a multiply charged ion, resulting in explosive release of fragment ions by their Coulomb repulsion. Tracing back trajectories of the fragment ions, molecular structure of the nascent parent ion can be reconstructed to understand the structure and dynamics of the multiply charged ion. Coulomb explosion imaging (CEI) is a technique pioneered by Naaman and co-workers to study geometric structures of small molecules, where valence electrons are stripped off from a projectile ion by a thin foil of gold [1]. This technique has been developed to identify each of the chiral pair of epoxide molecules [2]. Momentum analysis of fragment ions by CEI has been applied by introducing intense ultrafast laser pulses for ionization [3–10]. Thus far, applications are found for small molecules such as water vapor molecules, H₂O [3] and D₂O [4], sulfur dioxide, SO₂ [4], carbon disulfide, CS₂ [5], dichloromethane, CH₂Cl₂ [6], and weakly bound clusters of N₂Ar, O₂Ar, and O₂Xe [7]. This has been extended to relatively large molecules of 3,5-dibromo-3',5'-difluoro-4'-cyanobiphenyl [8] and group-6 metal hexacarbonyls, Cr(CO)₆, Mo(CO)₆, and W(CO)₆ [9].

Structural characterization of reactive chemical species such as atomic clusters and reaction intermediates has long been a central subject in chemistry, where fragility and reactivity have thwarted attempts to make a crystalline form necessary for the X-ray diffraction analysis to identify definite molecular structures [11,12]. As a recent example, we refer to a series of photo-sensitive sp-conjugated polyene-iodine adducts, C_{2n}H₂I₆ (*n* = 5–9), which have been identified only in solutions by UV–VIS absorption, ¹³C-NMR, and infrared absorption (FTIR) spectroscopy [13–15]. Despite the analysis of chemical shifts [13] and vibrational-mode frequencies [14], positions of six iodine atoms in the molecular adduct,

namely, the molecular structure, could not be located unequivocally on the experimental bases. Recently, an sp-hybridized carbon molecule of diiododiacetylene, $I(C\equiv C)_2I$, has been studied by Coulomb explosion experiments to find anisotropic angular distribution of fragment ions [16]. The experimental results imply that Coulomb explosion experiments would be able to characterize the structure of such fragile or reactive molecules, if they could be introduced into a high vacuum. For the investigation of molecular structures in such complexes as organic halogen adducts, we focus herein on the gas phase experiment utilizing mass-resolved momentum imaging (MRMI) for fragment ions generated upon Coulomb explosion.

Characterization of isomeric forms in a molecular species is one of the challenging issues in Coulomb explosion experiments [17–25]. Thus far, distinction of enantiomers of $CHBrClF$ and $CF_3CHBrCl$ has been reported [17–19]. Instantaneous chirality induced by zero-point vibrations has been observed for a symmetric molecule of CD_4 [20]. For structural isomers, distinction of 2,6- and 3,5-difluoroiodobenzene isomers has been demonstrated [21]. Recently, laser-induced alignment has been combined with CEI for determination of enantiomeric state of an axially chiral molecule (3,5-dibromo-3',5'-difluoro-4'-cyanobiphenyl molecule) [22], and identification of difluoroiodobenzene isomers [23] and dihydroxybromobenzene isomers [23]. Yatsuhashi et al. conducted Coulomb explosion experiments on the isomers of dichloroethylene (DCE) $C_2H_2Cl_2$, namely, 1,1-DCE, *cis*-1,2-DCE, and *trans*-1,2-DCE, using linearly polarized intense femtosecond laser pulses [24]. From dissimilarity observed for angular distributions of fragment ions, e.g., $^{35}Cl^{y+}$ ($y = 1,2$), $^{12}C^{z+}$ ($z = 2,3$), and H^+ , the authors concluded that *trans*-1,2-DCE was clearly distinguishable from the other two [24]. Additionally, for a similar species of dibromoethylene $C_2H_2Br_2$, the *cis*-1,2 and *trans*-1,2 isomers have been identified with X-ray-induced Coulomb explosion, but the 1,1-isomer has not been treated [25]. In order to complete a protocol for discrimination of all the three isomers in DCE, an additional tool is necessary for distinction between the two isomers, *cis*-1,2-DCE and 1,1-DCE.

In this work, three isomers of DCE were examined by the momentum imaging for fragment ions, on the basis of new experimental data from laser-induced Coulomb explosion. In addition to a similar laser-intensity condition to the previous experiments [24], $1.7 \times 10^{15} \text{ W/cm}^2$ (1.7 PW/cm²), we studied a condition of an order-of-magnitude-lower intensity, $1.8 \times 10^{14} \text{ W/cm}^2$ (0.18 PW/cm²), where saturation of ionization is avoided whereas the high degree of geometrical alignment is maintained. MRMI, i.e., simultaneous mapping of angular and velocity distributions for fragment ions [26–28], is demonstrated to be a powerful tool for identification of the three isomers of DCE.

2. Experiment and Analysis

2.1. Measurement of Time-of-Flight (TOF) Spectra

Figure 1 shows a schematic diagram of the experimental setup. Linearly polarized femtosecond laser pulses (pulse width ~60 fs, wavelength ~795 nm, pulse energy ~3 mJ/pulse) from a Ti:sapphire laser system (Thales $\alpha 10US-A$, France) at a repetition rate of 10 Hz were led through the neutral density (ND) filter to adjust the pulse energy, and focused in a vacuum chamber by using a plano-convex lens ($f = 254 \text{ mm}$ at 785 nm). The laser intensity at the focus was estimated on the basis of drift momentum of D_2^+ produced by ionization of gaseous D_2 molecules in a circularly polarized laser field [29,30].

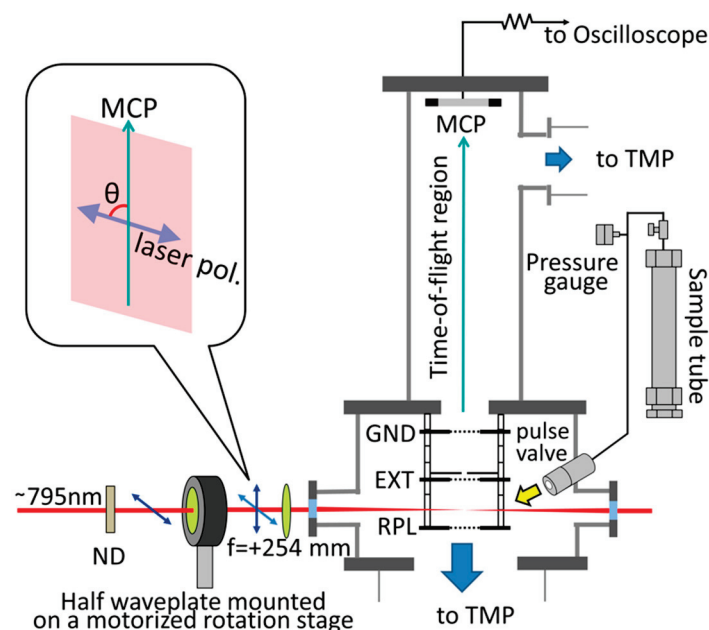


Figure 1. Schematic diagram of the experimental setup; MCP, micro-channel plate; GND, ground electrode; EXT, extracting electrode with a slit; RPL, repelling electrode; ND, neutral density filter; TMP, turbo molecular pump.

Commercially available reagents, 1,1-DCE (Aldrich, 99%, Tokyo, Japan), *cis*-1,2-DCE (Wako Chemicals, 99.0%, Tokyo, Japan), and *trans*-1,2-DCE (Aldrich, 98%, Tokyo, Japan), were degassed by repeated freeze–thaw cycles. The vapor molecules were introduced into the vacuum chamber through a pulsed valve (Parker High-Speed Pulse Valve, Series 9, USA). To avoid negative effects on the momentum images due to clustering and space charge effects, the backing pressure of the pulsed valve was kept below 1.3×10^3 Pa. The pressure in the vacuum chamber was below 8×10^{-5} Pa throughout the experiments. The present condition has no relevance to filamentation or plasma-induced terahertz radiation at relatively high pressure [31].

Photoinduced ions at the laser focus were extracted in an electric field of 0.2 kV/cm, then accelerated in the second electric field of 1.9 kV/cm with a standard Wiley–McLaren-type mass spectrometer [32]. In order to avoid concomitant detection of excess ions produced in front of and behind the laser focus, a slit of 0.5 mm was placed on the extraction electrode (EXT) [24]. The ions passing through the slit were mass-separated during the travel through a field-free region of 1.5 m, and detected by a micro-channel-plate detector (MCP, Jordan C-0701, φ 18 mm). The signal was averaged for 1000 laser shots by using a digitizing oscilloscope (LeCroy WaveRunner 104Xi-A, 1 GHz, USA).

For a limited surface area on the MCP detector, only a part of the ions exploding forward and backward to the detector was counted as signals. Taking the detection geometry into account, the ion intensity was plotted as a function of angle θ between the direction of the laser polarization and the direction of the flight axis toward the MCP detector (see the inset in Figure 1) to obtain the angular distribution of fragment ions.

2.2. Analysis

The polarization angle of the linearly polarized laser field was rotated from $\theta = 0^\circ$ to 90° by an interval of 5° using a zeroth-order half-wave plate mounted on a motorized rotary stage (Thorlabs PRM1/MZ8E, USA). A series of time-of-flight (TOF) spectra were recorded by changing the polarization angle, from which the angular distribution was deduced for two fragment ions of $^{35}\text{Cl}^+$ and C^{2+} .

Using the same set of TOF spectra, the momentum image (MRMI) was constructed [26–28]. Equation (1) represents the relation between the displacement of flight times, Δt , from

the central position of a peak in the TOF spectrum ($p_{//} = 0$) for a fragment ion and the momentum due to Coulomb explosion, $p_{//}$, in parallel with the flight axis. Transformation from the TOF spectrum to the momentum distribution was performed by Equation (1):

$$p_{//} = qF\Delta t, \quad (1)$$

where q denotes the charge of the fragment ion and F the strength of the extraction electric field [28]. Momentum distributions thus calculated were plotted as a function of the laser polarization angle to obtain a contour map, representing both the angular distribution and the velocity distribution in a single 2D image. To obtain better statistics, the distributions in the positive and negative momentum ranges are averaged and plotted in the first quadrant in the MRMI map. On the basis of the symmetry with respect to the laser polarization direction, the momentum distributions in the three other quadrants are the same as that in the first quadrant.

3. Results

3.1. TOF Spectra

Figure 2 shows TOF spectra for three isomers of DCE under the low-laser-intensity condition, $1.8 \times 10^{14} \text{ W/cm}^2$. Laser polarization is set perpendicular to the flight axis. Each spectrum is normalized to the peak intensity of the ion signal for $\text{C}_2\text{H}_2^{35}\text{Cl}_2^+$ (m/z 96). Major peaks commonly observed for the three isomers are $\text{C}_2\text{H}_2\text{Cl}_2^+$ (m/z 96, 98, 100), $\text{C}_2\text{H}_2\text{Cl}^+$ (m/z 61, 63), C_2HCl^+ (m/z 60, 62), $\text{C}_2\text{H}_2\text{Cl}_2^{2+}$ (m/z 48, 49, 50), and C_2H_2^+ (m/z 26). Minor but important peaks are noted for atomic ions of Cl^+ (m/z 35, 37), C^+ (m/z 12), C^{2+} (m/z 6), and H^+ (m/z 1).

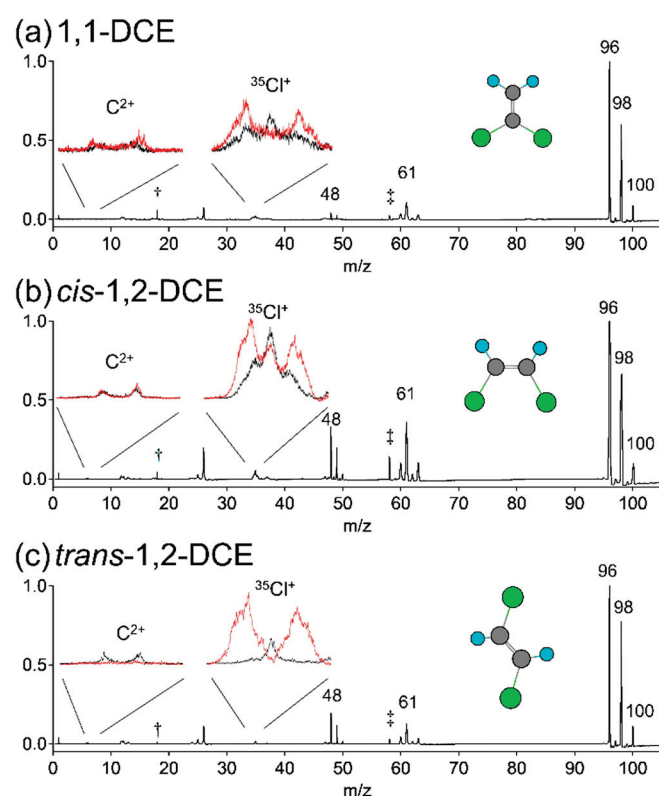


Figure 2. TOF mass spectra of dichloroethylene isomers obtained at the laser intensity of $1.8 \times 10^{14} \text{ W/cm}^2$. Inset spectra show detailed profiles for C^{2+} and $^{35}\text{Cl}^+$. Traces in black correspond to laser polarization perpendicular to the flight axis, while traces in red parallel to the flight axis. Peaks with daggers are due to impurities: water (m/z 18) and acetone (m/z 58). Molecular structures are depicted for the three dichloroethylene isomers; Carbon atoms in gray, hydrogen atoms in light blue, and chlorine atoms in green.

Inset spectra in Figure 2 depict split TOF profiles for C^{2+} and $^{35}Cl^+$ as a result of Coulomb explosion. In a multiply charged molecular ion, nascent ionic fragments recoil to each other by repulsive forces to leave the center of mass of the molecular framework, acquiring additional velocity components. Deviation, Δt , from the center of symmetry of the TOF peak profile is proportional to the magnitude of parallel momentum, $p_{//}$, forward or backward with respect to the direction toward the MCP detector (See Equation (1) for the relation between the magnitude of momentum and the splitting). Traces in red are the spectra with laser polarization parallel to the flight axis. A split pair of peaks for $^{35}Cl^+$ is commonly observed for the three isomers of DCE, as seen in traces in red in Figure 2a–c. Black traces of $^{35}Cl^+$, for which laser polarization is perpendicular to the extraction electric field show smaller splitting in Figure 2a,b or no split component in Figure 2c. The smaller the splitting, the slower the velocity acquired from the Coulomb explosion.

For two selected ion signals of $^{35}Cl^+$ (m/z 35) and C^{2+} (m/z 6), angular distributions are obtained from a series of the TOF data measured in the present work and compared with those in the preceding work [24]. Concerning the signal at m/z 12 mainly of C^+ , possibilities of overlapping signals of doubly charged carbon dimer ions of C_2^{2+} , and triply charged chlorine ions of $^{35}Cl^{3+}$ (m/z 11.7) and $^{37}Cl^{3+}$ (m/z 12.3) cannot be ruled out. Thus, we choose C^{2+} rather than C^+ .

3.2. Angular Distribution

$^{35}Cl^+$: Angular distributions of $^{35}Cl^+$ generated upon Coulomb explosion are shown in Figure 3 for three isomers of DCE. At a glance, *trans*-1,2-DCE can be easily identified by its little intensity in the direction of $\pm 90^\circ$ both under the high- (Figure 3c) and low- (Figure 3f) laser-intensity conditions. In contrast, it seems to be difficult to distinguish 1,1-DCE (Figure 3a,d) from *cis*-1,2-DCE (Figure 3b,e). At this point, the situation has not been very much improved for identification of the isomers. Our new experimental data on $^{35}Cl^+$ in Figure 3 merely reproduce the reported angular distributions [24].

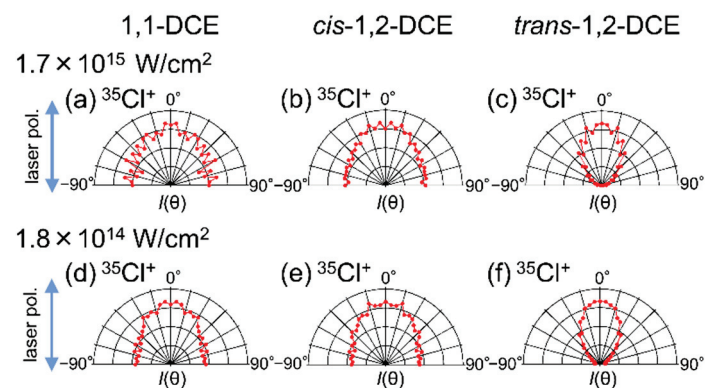


Figure 3. Angular distributions of $^{35}Cl^+$ generated from 1,1-DCE (a,d), *cis*-1,2-DCE (b,e), and *trans*-1,2-DCE (c,f). Laser intensities are $1.7 \times 10^{15} \text{ W/cm}^2$ for (a–c) and $1.8 \times 10^{14} \text{ W/cm}^2$ for (d–f). The vertical arrows represent the direction of laser polarization.

In more detail, under the high-laser-intensity condition in Figure 3a–c, 1,1-DCE (Figure 3a) exhibits non-vanishing components in all directions, larger by a factor of ~ 1.5 in 0° (parallel) than in $\pm 90^\circ$ (perpendicular). Similar distribution is observed for *cis*-1,2-DCE (3b). A qualitative difference is noted for *trans*-1,2-DCE (Figure 3c), exhibiting an anisotropic distribution with a strong parallel component at 0° and no perpendicular component at $\pm 90^\circ$, indicating that the $^{35}Cl^+$ ion in *trans*-1,2-DCE is ejected solely along the direction parallel to the laser polarization.

The characteristic feature under the high-laser-intensity condition is found also under the low-laser-intensity condition in Figure 3d–f. Two isomers, 1,1-DCE (Figure 3d) and *cis*-1,2-DCE (Figure 3e), exhibit oval distribution, having a slightly larger component in the parallel direction at 0° . In contrast, *trans*-1,2-DCE (Figure 3f) exhibits again a distinctly

different distribution from the other two isomers. The predominating distribution at 0° with little component at $\pm 90^\circ$ for $^{35}\text{Cl}^+$ (Figure 3f) is similar to that observed under the high-laser-intensity condition (Figure 3c). From the angular distribution of $^{35}\text{Cl}^+$, *trans*-1,2-DCE can be identified, but discrimination between 1,1-DCE and *cis*-1,2-DCE remains difficult.

C^{2+} : Under the high-laser-intensity condition at $1.7 \times 10^{15} \text{ W/cm}^2$ in Figure 4, angular distributions of C^{2+} for 1,1-DCE (Figure 4a) and *cis*-1,2-DCE (Figure 4b) resemble each other, i.e., a larger component in 0° (parallel), whereas isotropic distribution is noted for *trans*-1,2-DCE (Figure 4c). According to the preceding work, *trans*-1,2-DCE releases more C^{2+} ions into the direction perpendicular to the laser polarization under the moderate laser intensity at $1.3 \times 10^{15} \text{ W/cm}^2$, whereas an isotropic distribution is seen under the extremely high laser intensity at $2.2 \times 10^{15} \text{ W/cm}^2$ [24]. The present experimental condition, $1.7 \times 10^{15} \text{ W/cm}^2$, falls in-between the two conditions in the literature [24], and our result is close to the latter extremity, as shown in Figure 3c.

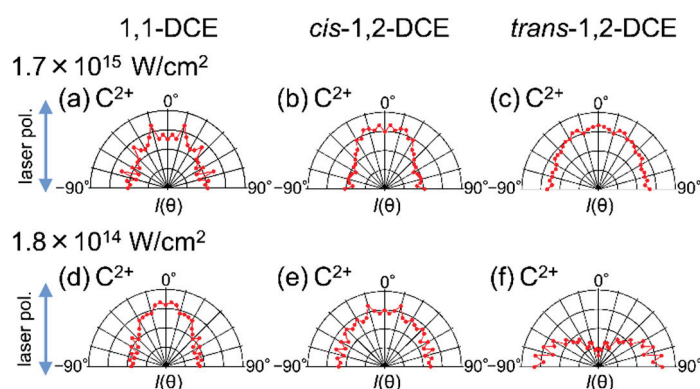


Figure 4. Angular distributions of C^{2+} generated from 1,1-DCE (a,d), *cis*-1,2-DCE (b,e), and *trans*-1,2-DCE (c,f). Laser intensities are $1.7 \times 10^{15} \text{ W/cm}^2$ for (a–c) and $1.8 \times 10^{14} \text{ W/cm}^2$ for (d–f). The vertical arrows represent the direction of laser polarization.

It is noted that the angular distribution of C^{2+} for *trans*-1,2-DCE changes dramatically by lowering the laser intensity to $1.8 \times 10^{14} \text{ W/cm}^2$. In Figure 4f, C^{2+} ions are emitted mostly in the direction perpendicular to the laser polarization at the angle of $\pm 90^\circ$ and little emission is seen in the parallel direction at 0° . Even under the condition at the low laser intensity, a difference is not noticeable in Figure 4d,e. Thus, discrimination of the isomers between 1,1-DCE and *cis*-1,2-DCE is impossible from the angular distribution of the C^{2+} fragment ion.

3.3. Momentum Image

$^{35}\text{Cl}^+$: Using the series of the TOF data used for Figures 3 and 4, MRMI analysis is performed for $^{35}\text{Cl}^+$ and C^{2+} . Since the TOF signals of $^{35}\text{Cl}^+$ and C^{2+} are well-separated from those of the other ionic species, clean momentum images are obtained. Momentum images of $^{35}\text{Cl}^+$ are presented in Figure 5. In addition to the angular distribution of momentum, the magnitude of momentum for the leaving ion is represented by distance from the origin, i.e., faster at the outer rim and slower around the center. The contour plot stands for the population of ions having a specific direction and a specific velocity. Independently on the laser intensity, two components are discernible in the momentum images for 1,1-DCE (Figure 5a,d) and *cis*-1,2-DCE (Figure 5b,e), i.e., one for the fast ions traveling forward or backward along the laser polarization, which appear as a split pair of spots at the upper and lower parts of the image, and the other for the slow ions spreading around the center of the image. Therefore, the momentum image of $^{35}\text{Cl}^+$ is not sufficient to distinguish 1,1-DCE and *cis*-1,2-DCE. In the momentum images for *trans*-1,2-DCE (Figure 5c,f), only the component of fast ions is discernible along the parallel laser polarization without any slow component.

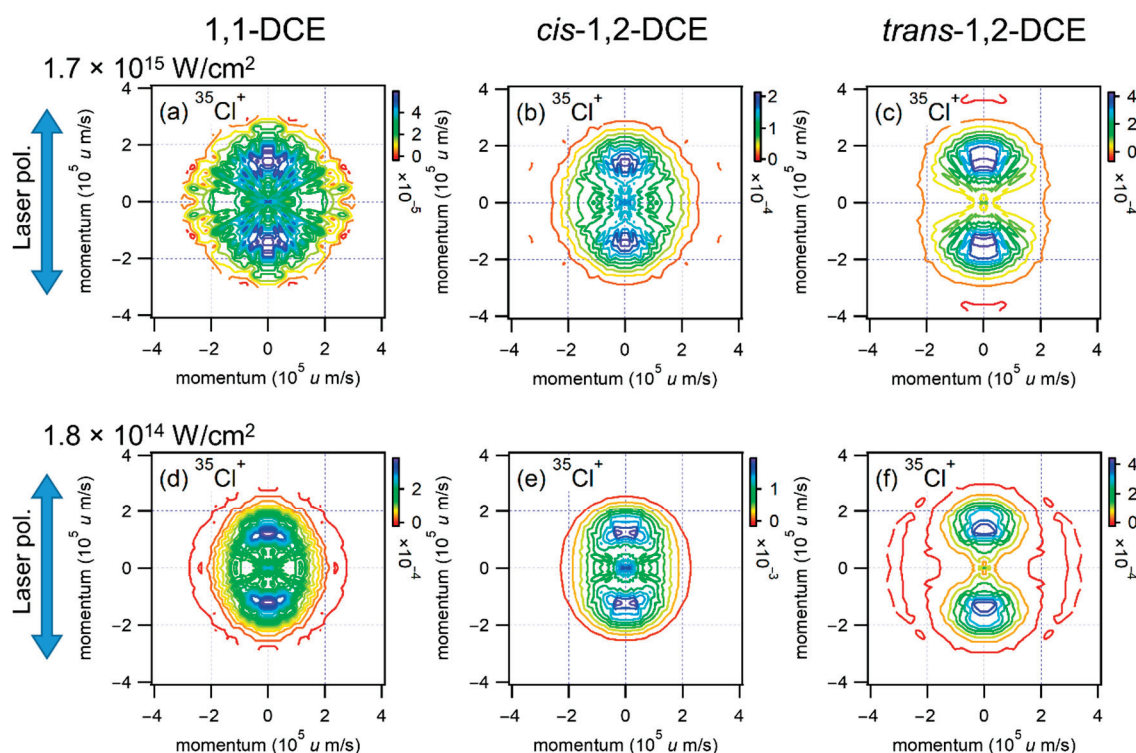


Figure 5. Momentum images of $^{35}\text{Cl}^+$ generated from 1,1-DCE (a,d), *cis*-1,2-DCE (b,e), and *trans*-1,2-DCE (c,f). Laser intensities are $1.7 \times 10^{15} \text{ W/cm}^2$ for (a–c) and $1.8 \times 10^{14} \text{ W/cm}^2$ for (d–f). The vertical arrows represent the direction of laser polarization.

C^{2+} : Using momentum images of C^{2+} in Figure 6, appreciable difference between two isomers of 1,1-DCE and *cis*-1,2-DCE is noticed. The image of C^{2+} for 1,1-DCE (Figure 6a) under the high-laser-intensity condition at $1.7 \times 10^{15} \text{ W/cm}^2$ contains at least two groups of ions, i.e., a group of fast ions slightly polarized in parallel with laser polarization and a group of slow ions locating near the center of the image, as is seen more clearly under the low laser intensity condition in Figure 6d. On the other hand, for *cis*-1,2-DCE (Figure 6b) and *trans*-1,2-DCE (Figure 6c), a single component of rather isotropic angular distribution is conspicuous, demonstrating a visible difference between 1,1-DCE (Figure 6a) and the *cis* (Figure 6b) and *trans* (Figure 6c) isomers of 1,2-DCE.

At the appropriately low laser intensity, namely, $1.8 \times 10^{14} \text{ W/cm}^2$, momentum images for the three isomers in DCE clearly show different patterns as shown in Figure 6d–f. First, the image of C^{2+} for 1,1-DCE (Figure 6d) shows again the groups of fast and slow ions. Second, the image for *cis*-1,2-DCE (Figure 6e) shows a single velocity component of fast ions whose angular distribution is almost isotropic and slightly polarized in the direction along the laser polarization. Finally, a drastic change is noted in the image of C^{2+} for *trans*-1,2-DCE (Figure 6f). The single velocity component of fast ions in Figure 6f directs perpendicularly to the laser polarization, exhibiting a sharp contrast to the observation of the isotropic distribution in the high laser-intensity counterpart in Figure 6c.

The magnitude of the momentum, $2.0 \times 10^5 \text{ u m/s}$, for *trans*-1,2-DCE at the pair of spots with maximum population in Figure 6f, is appreciably smaller than that in Figure 6c, $2.7 \times 10^5 \text{ u m/s}$. This implies that the total charge number of the cation is smaller and/or that enhanced ionization at a deformed molecular structure [33,34] takes place predominantly at the low-laser-intensity condition.

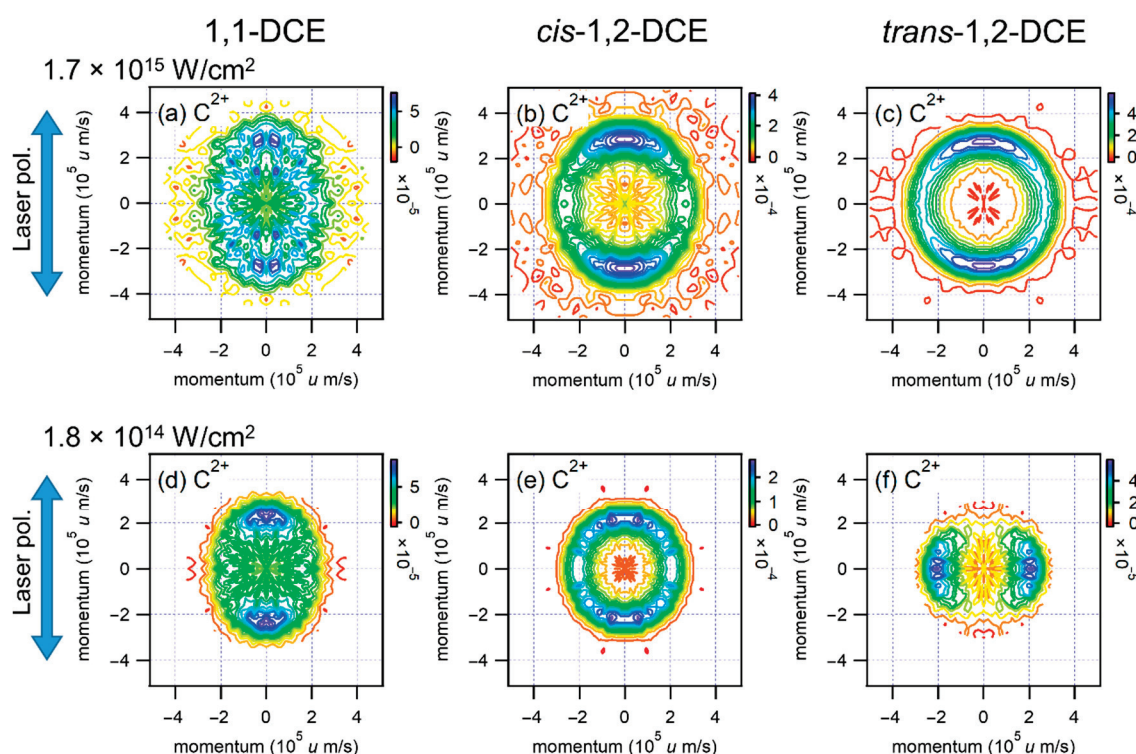


Figure 6. Momentum images of C^{2+} generated from 1,1-DCE (a,d), *cis*-1,2-DCE (b,e), and *trans*-1,2-DCE (c,f). Laser intensities are 1.7×10^{15} W/cm² for (a–c) and 1.8×10^{14} W/cm² for (d–f). The vertical arrows represent the direction of laser polarization.

Using the momentum image of the C^{2+} , it is possible to discern the structural isomer of 1,1-DCE from the *cis* and *trans* isomers of 1,2-DCE, even under the relatively high-laser-intensity condition. Furthermore, by lowering the laser intensity, in addition to the 1,1-DCE isomer, the pair of *cis* and *trans* isomers of 1,2-DCE can be distinguished by differently polarized emission of C^{2+} , i.e., isotropic but slightly polarized in parallel with the laser polarization for *cis*-1,2-DCE and perpendicularly polarized emission of C^{2+} from *trans*-1,2-DCE, as evidenced by the series of momentum images in Figure 6d–f. Under the laser intensity at 1.8×10^{14} W/cm², it is demonstrated that all the three isomers in DCE can be identified by the momentum images of the C^{2+} fragment ion.

4. Discussion

The laser polarization can select molecules at specific orientation upon ionization with a short laser pulse, whereby only a fraction of molecules is preferentially ionized into multiply charged ions for Coulomb explosion. In this case, the angular distribution of fragment ions reflects intrinsic anisotropy of the parent molecule. This selection of molecular *geometrical alignment*, or the idea of a preferential *ionization axis*, was proposed for DCE isomers [24,35,36]. Geometrical alignment is determined by orientation-dependent probability of ionization, which primarily depends on the shape of the outer edge of a molecular orbital with respect to the laser polarization [37,38]. However, in the case of multiple ionization, it is difficult to identify which orbitals are contributing. Furthermore, when the chemical bond can be elongated to possibly twice the bond length for the equilibrium geometry in the neutral ground state within the exposure time of an intense laser pulse, probability of multiple ionization is significantly enhanced at an alignment angle in which the chemical bond is parallel to the laser electric field [39]. In addition, dynamical alignment by the interaction between the induced dipole moment and the laser electric field influences significantly the angular distribution of the recoiled fragment ions [40–43].

Here, we discuss the momentum distribution of fragment ions of DCE isomers on the basis of the specific molecular orientation upon ionization. We simply assume that

the molecules whose most polarizable axis is oriented along the laser polarization are preferentially ionized into multiply charged ions. Anisotropic nature of polarizability of a molecule is represented by a tensor property. The six components of the polarizability tensor, α , are diagonalized to three orthogonal components along the principal axes of the ellipsoid. For a molecule of DCE isomers, two of them along the molecular plane, α_{xx} and α_{yy} , have characteristic values of 42–82 in the unit of cubic Bohr radius, a_0^3 , whereas the other component perpendicular to the molecular plane, α_{zz} , is smaller than the two, having a value of ~ 33.7 commonly for the three DCE isomers [44]. In this work, the principal axis of the largest polarizability among the three components is defined as the *most polarizable axis* of the target molecule, which is indicated by the solid red arrow in each of Figure 7a–c.

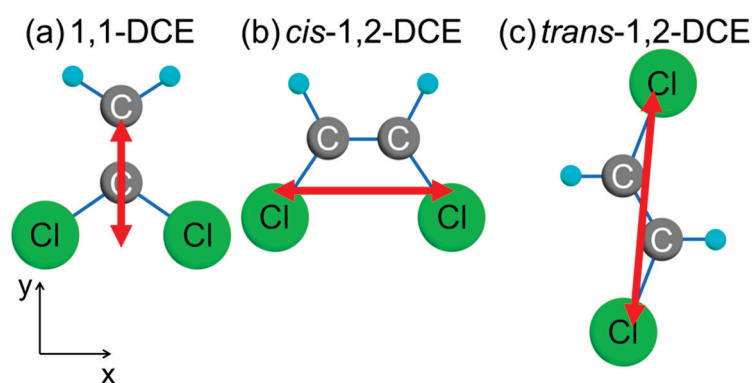


Figure 7. The largest component of polarizability along the principal axis (red arrow) evaluated for (a) 1,1-DCE, (b) *cis*-1,2-DCE, and (c) *trans*-1,2-DCE isomers by density functional theory calculations [44].

4.1. Momentum Distribution of $^{35}\text{Cl}^+$

Having the momentum parallel to the laser polarization, the fast component of the fragment ion, Cl^+ , commonly observed for the three isomers of DCE, is released upon ionization of the molecule aligned along the relevant C–Cl bond. Since the leaving Cl^+ ion is located at an edge of the molecular framework, the nascent molecular ion of minimum charges for Coulomb explosion is $\text{Cl}^+(\text{C}_2\text{H}_2\text{Cl})^+$. The slow component of the fragment ion, Cl^+ , observed for 1,1-DCE in Figure 5a,d and for *cis*-1,2-DCE in Figure 5b,e is possibly a superposition of Cl^+ signals from singly charged molecular ions, $\text{Cl}^+\text{C}_2\text{H}_2\text{Cl}$. The parallel release of the fast Cl^+ ions to the laser polarization might have relevance to the most polarizable axis for *cis*-1,2-DCE in Figure 7b and for *trans*-1,2-DCE in Figure 7c (solid arrows in red). However, the close resemblance of split patterns in Figure 5a–f rather indicates a common mechanism where the molecule aligned with its C–Cl bond axis parallel to the laser axis is preferentially ionized into the least multiply charged repulsive pair of ions, C^+ and Cl^+ , for Coulomb explosion. This molecular geometrical alignment along the C–Cl bond is compatible qualitatively with the ionization axis discussed previously [24].

4.2. Momentum Distribution of C^{2+}

For the doubly charged fragment ion, C^{2+} , more than three charges, $>+3e$, are expected for the molecular ion. The momentum images of C^{2+} show appreciable differences between 1,1-DCE (Figure 6a,d) and *cis*-1,2-DCE (Figure 6b,e), which are explainable by the difference in relative positions of carbon atoms in a molecule. In 1,1-DCE, one carbon atom is bonded to two chlorine atoms and the other is located away from the chlorine atoms. The former, locating close to the molecular center of mass, contributes to the isotropic low-velocity (slow) component, and the latter, located at the edge of a molecule, contributes to the anisotropic high-velocity (fast) component. As a result, two types of components emerge in the momentum image in Figure 6a,d. In *cis*-1,2-DCE, each of the two carbon atoms is bonded to one chlorine atom and both are equivalent in a molecule, and thus the majority of C^{2+} fragment ions from *cis*-1,2-DCE constitute a single-velocity component in Figure 6b,e.

The momentum image of C^{2+} for *trans*-1,2-DCE in Figure 6f at the low-laser-intensity condition shows a pattern extending in the direction perpendicular to the laser polarization. This makes a sharp contrast to those of C^{2+} for the other two isomers in Figure 6d,e, which extend more or less in parallel with the direction of laser polarization. To cause C^{2+} to be Coulomb-exploded, at least one counter cation, namely, a carbon or chlorine ion, is necessary. Regardless of which ion is the counterpart, the repulsive force will point in a direction rather parallel to the laser polarization, considering the stable structure shown in Figure 7c. However, heavy chlorine nuclei locating along the most polarizable axis force the C^{2+} ion to leave more or less perpendicularly to the axis of laser polarization. The Cl nuclei move slower than the C^{2+} ion because the mass of Cl ($m = 35$ or 37) is roughly three times heavier than that of ^{12}C . Thus, the Cl nuclei stay longer near the molecular center of mass, preventing the C^{2+} from leaving in the direction parallel to the laser polarization. The disturbance by Cl nuclei will cause the trajectory of C^{2+} to be bent, resulting in deviation from the expected momentum distribution on the basis of the initial geometrical structure. The structural deformation also causes deviated momentum distribution [33,34]. Nevertheless, the initial acceleration determines overall properties of the Coulomb explosion event.

4.3. Molecular Structure Assay

The momentum image of $^{35}Cl^+$ fragment ions obtained in the present work represents molecular geometrical alignment along the C–Cl bond of the molecule. Moreover, the momentum image of C^{2+} reflects the relative position of multiply charged fragment ions in a highly charged molecule. A key feature to be noted is to conduct experiments under the condition at the lowest possible laser intensity, as long as sufficient signal counts of fragment ions formed by Coulomb explosion are detectable, where the number of ionization channels is reduced and the intrinsic anisotropy is maximized in MRMI. Ultra-short laser pulses, <10 fs, would be advantageous to surmise a molecular structure from MRMI by avoiding extensive deformation [3–6,33,34], enhanced ionization [39], and dynamical alignment [40–43] of molecules prior to Coulomb explosion. A combination of MRMI with laser-induced alignment might be helpful for applying this method for other molecules and/or to determine molecular structure more precisely, as shown previously [22,23]. Although one should relent on locating the position of hydrogen atoms in a molecule because of their migration being inevitably large [45–47], it will not be a serious problem as it can be reasonably guessed from the position of heavier atoms.

5. Conclusions

According to the different momentum distributions of $^{35}Cl^+$, *trans*-1,2-DCE was easily discriminated from the other two. Moreover, the momentum image of C^{2+} enabled us to identify all the three isomers by intensifying the difference in anisotropic distributions between the pair of structural isomers, *cis*-1,2-DCE and 1,1-DCE. Mass-resolved momentum imaging, MRMI, was demonstrated to reflect the difference in the location of constituent atoms in a molecule. This, in turn, implies a potential application of MRMI to acquiring information that enables one to reconstruct the relative position of constituent atoms in a molecule, namely, the molecular structure. The analysis of MRMI can be exploited to guess unknown structures of molecular species as long as their chemical compositions are known.

Author Contributions: Conceptualization, R.I. and T.W.; investigation, Y.W., H.A. and T.K.; data curation, Y.W.; visualization, Y.W.; writing—original draft preparation, Y.W. and T.W.; writing—review and editing, H.A. and R.I.; funding acquisition, R.I. and T.W. All authors have read and agreed to the published version of the manuscript.

Funding: This study is partly supported by JSPS KAKENHI (Grant No. JP26288013) and MEXT—Supported Program for the Strategic Research Foundation at Private Universities.

Institutional Review Board Statement: Not applicable.

Informed Consent Statement: Not applicable.

Data Availability Statement: The data presented in this study are available upon request from the corresponding author.

Acknowledgments: The authors are grateful to Y. Hagihara for support in data analysis. The authors thank M. Nishikino and N. Hasegawa for the support in laser operation. Y.W. acknowledges Grant-in-Aid for JSPS Research Fellow (Grant No. JP24-10606).

Conflicts of Interest: The authors declare no conflict of interest.

References

- Vager, Z.; Naaman, R.; Kanter, E.P. Coulomb explosion imaging of small molecules. *Science* **1989**, *244*, 426–431. [CrossRef]
- Herwig, P.; Zawatzky, K.; Grieser, M.; Heber, O.; Jordan-Thaden, B.; Krantz, C.; Novotný, O.; Repnow, R.; Schurig, V.; Schwalm, D.; et al. Imaging the absolute configuration of a chiral epoxide in the gas phase. *Science* **2013**, *342*, 1084–1086. [CrossRef] [PubMed]
- Sanderson, J.H.; El-Zein, A.; Bryan, W.A.; Newell, W.R.; Langley, A.J.; Taday, P.E. Geometry modifications and alignment of H₂O in an intense femtosecond laser pulse. *Phys. Rev. A* **1999**, *59*, R2567–R2570. [CrossRef]
- Légaré, F.; Lee, K.F.; Litvinyuk, I.V.; Dooley, P.W.; Wesolowski, S.S.; Bunker, P.R.; Dombi, P.; Krausz, F.; Badrauk, A.D.; Villeneuve, D.M.; et al. Laser Coulomb explosion imaging of small molecules. *Phys. Rev. A* **2005**, *71*, 013415. [CrossRef]
- Hasegawa, H.; Hishikawa, A.; Yamanouchi, K. Coincidence imaging of Coulomb explosion of CS₂ in intense laser fields. *Chem. Phys. Lett.* **2001**, *349*, 57–63. [CrossRef]
- Gagnon, J.; Lee, K.F.; Rayner, D.M.; Corkum, P.B.; Bhardwaj, V.R. Coincidence imaging of polyatomic molecules via laser-induced Coulomb explosion. *J. Phys. B At. Mol. Opt. Phys.* **2008**, *41*, 215104. [CrossRef]
- Wu, J.; Kunitski, M.; Schmidt, L.P.H.; Jahnke, T.; Dörner, R. Structures of N₂Ar, O₂Ar, and O₂Xe dimers studied by Coulomb explosion imaging. *J. Chem. Phys.* **2012**, *137*, 104308. [CrossRef]
- Slater, C.S.; Blake, S.; Brouard, M.; Lauer, A.; Vallance, C.; John, J.J.; Turchetta, R.; Nomerotski, A.; Christensen, L.; Nielsen, J.H.; et al. Covariance imaging experiments using a pixel-imaging mass-spectrometry camera. *Phys. Rev. A* **2014**, *89*, 11401. [CrossRef]
- Tanaka, H.; Nakashima, N.; Yatsushashi, T. Anisotropic Coulomb explosion of CO ligands in group 6 metal hexacarbonyls: Cr(CO)₆, Mo(CO)₆, W(CO)₆. *J. Phys. Chem. A* **2016**, *120*, 6917–6928. [CrossRef]
- Mathur, D. Structure and dynamics of molecules in high charge states. *Phys. Rep.* **2004**, *391*, 1–118. [CrossRef]
- Castleman, A.W.; Bowen, K.H. Clusters: Structures, energies, and dynamics of intermediate states of matter. *J. Phys. Chem.* **1996**, *100*, 12911–12944.
- Wakabayashi, T.; Ong, A.-L.; Strelnikov, D.; Krättschmer, W. Flashing carbon on cold surfaces. *J. Phys. Chem. B* **2004**, *108*, 3686–3690. [CrossRef]
- Wada, Y.; Wakabayashi, T.; Kato, T. Photoinduced reaction of hydrogen-end-capped polyynes with iodine molecules. *J. Phys. Chem. B* **2011**, *115*, 8439–8445. [CrossRef] [PubMed]
- Wada, Y.; Morisawa, Y.; Wakabayashi, T. Spectroscopic characterization of a series of polyyne-iodine molecular complexes of H(C≡C)_nH(I₂) *n*=5–9. *Chem. Phys. Lett.* **2012**, *541*, 54–59. [CrossRef]
- Wada, Y.; Koma, K.; Ohnishi, Y.; Sasaki, Y.; Wakabayashi, T. Photoinduced reaction of methylpolyynes H(C≡C)_nCH₃ (*n*=5–7) and H(C≡C)_nH with I₂ molecules. *Eur. J. Phys. D* **2012**, *66*, 322. [CrossRef]
- Mitsubayashi, N.; Yatsushashi, T.; Tanaka, H.; Furukawa, S.; Kozai, M.; Okada, K.; Nakashima, N. Anisotropic Coulomb explosion of acetylene and diacetylene derivatives. *Int. J. Mass Spectrom.* **2016**, *403*, 43–52. [CrossRef]
- Pitzer, M.; Kunitski, M.; Johnson, A.S.; Jahnke, T.; Sann, H.; Sturm, F.; Schmidt, L.P.H.; Schmidt-Böcking, H.; Dörner, R.; Stohner, J.; et al. Direct determination of absolute molecular stereochemistry in gas phase Coulomb explosion imaging. *Science* **2013**, *341*, 1096–1100. [CrossRef]
- Pitzer, M.; Kastirke, G.; Burzynski, P.; Weller, M.; Metz, D.; Neff, J.; Waitz, M.; Trinter, F.; Schmidt, L.P.H.; Williams, J.B.; et al. Stereochemical configuration and selective excitation of the chiral molecule halothane. *J. Phys. B At. Mol. Opt. Phys.* **2016**, *49*, 234001. [CrossRef]
- Pitzer, M.; Kastirke, G.; Kunitski, M.; Jahnke, T.; Bauer, T.; Goihl, C.; Trinter, F.; Schober, C.; Henrichs, K.; Becht, J.; et al. Absolute configuration from different multifragmentation pathways in light-induced Coulomb explosion imaging. *ChemPhysChem* **2016**, *17*, 2465–2472. [CrossRef]
- Kitamura, T.; Nishide, T.; Shiromaru, H.; Achiba, Y.; Kobayashi, N. Direct observation of “dynamic” chirality by Coulomb explosion imaging. *J. Chem. Phys.* **2001**, *115*, 5–6. [CrossRef]
- Ablitim, U.; Bomme, C.; Savelyev, E.; Xiong, H.; Kushawaha, R.; Boll, R.; Amini, K.; Osipov, T.; Kilcoyne, D.; Rudenko, A.; et al. Isomer-dependent fragmentation dynamics of inner-shell photoionized difluoroiodobenzene. *Phys. Chem. Chem. Phys.* **2017**, *19*, 13419–13431. [CrossRef] [PubMed]
- Christensen, L.; Nielsen, J.H.; Slater, C.S.; Lauer, A.; Brouard, M.; Stapelfeldt, H. Using laser-induced Coulomb explosion of aligned chiral molecules to determine their absolute configuration. *Phys. Rev. A* **2015**, *92*, 033411. [CrossRef]

23. Burt, M.; Amini, K.; Lee, J.W.L.; Christiansen, L.; Johansen, R.R.; Kobayashi, Y.; Pickering, J.D.; Vallance, C.; Brouard, M.; Stapelfeldt, H. Communication: Gas-phase structural isomer identification by Coulomb explosion of aligned molecules. *J. Chem. Phys.* **2018**, *148*, 091102. [CrossRef]
24. Yatsunami, T.; Nakashima, N.; Azuma, J. Coulomb explosion of dichloroethylene geometric isomers at 1 PW cm⁻². *J. Phys. Chem. A* **2013**, *117*, 1393–1399. [CrossRef]
25. Ablikim, U.; Bomme, C.; Xiong, H.; Savelyev, E.; Obaid, R.; Kaderiya, B.; Augustin, S.; Schnorr, K.; Dumitriu, I.; Osipov, T.; et al. Identification of absolute geometries of cis and trans molecular isomers by Coulomb explosion imaging. *Sci. Rep.* **2016**, *6*, 38202. [CrossRef]
26. Hishikawa, A.; Iwamae, A.; Hoshina, K.; Kono, M.; Yamanouchi, K. Mass-resolved two-dimensional momentum imaging of the Coulomb explosion of N₂ and SO₂ in an intense laser field. *Chem. Phys. Lett.* **1998**, *282*, 283–291. [CrossRef]
27. Hishikawa, A.; Iwamae, A.; Hoshina, K.; Kono, M.; Yamanouchi, K. Coulomb explosion dynamics of N₂ in intense laser field by mass-resolved momentum imaging. *Chem. Phys.* **1998**, *231*, 315–329. [CrossRef]
28. Iwamae, A.; Hishikawa, A.; Yamanouchi, K. Extraction of molecular dynamics in intense laser fields from mass-resolved momentum imaging maps: Application to Coulomb explosion of NO. *J. Phys. B At. Mol. Opt. Phys.* **2000**, *33*, 223–240. [CrossRef]
29. Litvinyuk, I.V.; Lee, K.F.; Dooley, P.W.; Rayner, D.M.; Villeneuve, D.M.; Corkum, P.B. Alignment-dependent strong field ionization of molecules. *Phys. Rev. Lett.* **2003**, *90*, 233003. [CrossRef]
30. Alnaser, A.S.; Tong, X.M.; Osipov, T.; Voss, S.; Maharjan, C.M.; Shan, B.; Chang, Z.; Cocke, C.L. Laser-peak-intensity calibration using recoil-ion momentum imaging. *Phys. Rev. A* **2004**, *70*, 023413. [CrossRef]
31. Jahangri, F.; Hashida, M.; Tokita, S.; Nagashima, T.; Hangyo, M.; Sakabe, S. Enhancing the energy of terahertz radiation from plasma-produced by intense femtosecond laser pulses. *Appl. Phys. Lett.* **2013**, *102*, 191106. [CrossRef]
32. Wiley, W.C.; McLaren, I.H. Time-of-flight mass spectrometer with improved resolution. *Rev. Sci. Instrum.* **1955**, *26*, 1150. [CrossRef]
33. Hishikawa, A.; Iwamae, A.; Yamanouchi, K. Ultrafast deformation of the geometrical structure of CO₂ induced in intense laser fields. *Phys. Rev. Lett.* **1999**, *83*, 1127–1130. [CrossRef]
34. Hishikawa, A.; Iwamae, A.; Yamanouchi, K. Ultrafast structural deformation of NO₂ in intense laser fields studied by mass-resolved momentum imaging. *J. Chem. Phys.* **1999**, *111*, 8871–8878. [CrossRef]
35. Wong, M.C.H.; Brichta, J.-P.; Spanner, M.; Patchkovskii, S.; Bhardwaj, V.R. High-harmonic spectroscopy of molecular isomers. *Phys. Rev. A* **2011**, *84*, 051403, Erratum in *Phys. Rev. A* **2012**, *85*, 049901. [CrossRef]
36. Le, A.-T.; Lucchese, R.R.; Lin, C.D. High-order harmonic generation from molecular isomers with midinfrared intense laser pulses. *Phys. Rev. A* **2013**, *88*, 021402. [CrossRef]
37. Tong, X.M.; Zhao, Z.X.; Lin, C.D. Theory of molecular tunneling ionization. *Phys. Rev. A* **2002**, *66*, 033402. [CrossRef]
38. Alnaser, A.S.; Voss, S.; Tong, X.M.; Maharjan, C.M.; Ranitovic, P.; Ulrich, B.; Osipov, T.; Shan, B.; Chang, Z.; Cocke, C.L. Effect of molecular structure on ion disintegration patterns in ionization of O₂ and N₂ by short laser pulses. *Phys. Rev. Lett.* **2004**, *93*, 113003. [CrossRef]
39. Posthumus, J.H.; Giles, A.J.; Thompson, M.R.; Codling, K. Field-ionization, Coulomb explosion of diatomic molecules in intense laser fields. *J. Phys. B* **1996**, *29*, 5811–5829. [CrossRef]
40. Rosca-Pruna, F.; Vrakking, M.J.J. Experimental observation of revival structures in picosecond laser-induced alignment of I₂. *Phys. Rev. Lett.* **2001**, *87*, 153902. [CrossRef]
41. Stapelfeldt, H.; Seideman, T. Colloquium: Aligning molecules with strong laser pulses. *Rev. Mod. Phys.* **2003**, *75*, 543–557. [CrossRef]
42. Tong, X.M.; Zhao, Z.X.; Alnaser, A.S.; Voss, S.; Cocke, C.L.; Lin, C.D. Post ionization alignment of the fragmentation of molecules in an ultrashort intense laser field. *J. Phys. B* **2005**, *38*, 333–341. [CrossRef]
43. Koch, C.P.; Lemeshko, M.; Sugny, D. Quantum control of molecular rotation. *Rev. Mod. Phys.* **2019**, *91*, 035005. [CrossRef]
44. Frisch, M.J.; Trucks, G.W.; Schlegel, H.B.; Scuseria, G.E.; Robb, M.A.; Cheeseman, J.R.; Scalmani, G.; Barone, V.; Petersson, G.A.; Nakatsuji, H.; et al. *B3LYP/6-311++G(2d,p) Optimized Molecular Geometries and Polarizability Tensors for DCE Isomers*, Gaussian 16; Revision A.03; Gaussian, Inc.: Wallingford, CT, USA, 2016.
45. Hishikawa, A.; Matsuda, A.; Fushitani, M.; Takahashi, E. Visualizing recurrently migrating hydrogen in acetylene dication by intense ultrashort laser pulses. *Phys. Rev. Lett.* **2007**, *99*, 258302. [CrossRef]
46. Itakura, R.; Liu, P.; Furukawa, Y.; Okino, T.; Yamanouchi, K.; Nakano, H. Two-body Coulomb explosion and hydrogen migration in methanol induced by intense 7 and 21 fs laser pulses. *J. Chem. Phys.* **2007**, *127*, 104306. [CrossRef] [PubMed]
47. Ibrahim, H.; Wales, B.; Beaulieu, S.; Schmidt, B.E.; Thiré, N.; Fowe, E.P.; Bisson, É.; Hebeisen, C.T.; Wanie, V.; Giguère, M.; et al. Tabletop imaging of structural evolutions in chemical reactions demonstrated for the acetylene cation. *Nat. Commun.* **2014**, *5*, 4422. [CrossRef] [PubMed]

Article

Phosphorescence of C_5N^- in Rare Gas Solids

Urszula Szczepaniak^{1,2,†}, Robert Kołos^{2,*}, Jean-Claude Guillemin³ and Claudine Crépin^{1,*}

¹ Institut des Sciences Moléculaires d'Orsay (ISMO), CNRS, Université Paris-Saclay, F-91405 Orsay, France; u.szczepaniak@obvotec.com

² Institute of Physical Chemistry, Polish Academy of Sciences, Kasprzaka 44/52, PL-01-224 Warsaw, Poland

³ Ecole Nationale Supérieure de Chimie de Rennes, CNRS, Univ. Rennes, ISCR-UMR6226, F-35000 Rennes, France; jean-claude.guillemin@ensc-rennes.fr

* Correspondence: rkolos@ichf.edu.pl (R.K.); claudine.crepin-gilbert@universite-paris-saclay.fr (C.C.); Tel.: +48-22-343-32-18 (R.K.); +33-1-69-15-75-39 (C.C.)

† Current address: obvioTec AG, Garstligweg 8, 8634 Hombrechtikon, Switzerland.

Abstract: Phosphorescence of C_5N^- was discovered following the ArF-laser (193 nm) photolysis of cyanodiacetylene (HC_5N) isolated in cryogenic argon, krypton, and xenon matrices. This visible emission, with an origin around 460 nm, is vibrationally resolved, permitting the measurement of frequencies for eight ground-state fundamental vibrational modes, including the three known from previous IR absorption studies. Phosphorescence lifetime amounts to tens or even hundreds of ms depending on the matrix host; it is five times longer than in the case of HC_5N .

Keywords: anion; cyanopolyynes; luminescence; matrix isolation

1. Introduction

Cyanopolyynes ($HC_{2n+1}N$) constitute the most prominent homologous series of astrochemically-relevant molecules. They have been detected via microwave rotational transitions in many extraterrestrial sources, up to $n = 5$ [1–7]. Cyanopolyynes radicals $C_{2n+1}N$ and the corresponding anions $C_{2n+1}N^-$ ($n = 1, 2$) have also been identified in the interstellar medium [8,9]. The first detection of C_5N^- , in microwave emission from the shell of a carbon star IRC +10216, was based solely on theoretical spectroscopic predictions, as no laboratory data existed. The anion may also be present in Titan's atmosphere [10].

Vibrational spectroscopy of C_3N^- and C_5N^- generated from HC_3N and HC_5N in rare gas solids was studied via IR absorption [11,12]. IR photodissociation spectroscopy provided information on certain stretching modes for gas-phase $C_{2n+1}N^-$ ($n = 1$ to 5) species [13]. Ultraviolet and visible absorption was studied for these anions ($n = 3$ to 6) in solid neon [14].

Photoelectron spectroscopy of C_3N^- and C_5N^- supplied the adiabatic electron detachment energies as high as 4.305 ± 0.001 and 4.45 ± 0.03 eV, respectively [15]. These values, measured for gas-phase species, are expected to be even higher for anions isolated in rare-gas cryogenic matrices, given that polarizable media better stabilize a charged species than a neutral one. For C_3^- and C_6^- , in solid Ar, the measured photodetachment thresholds were, respectively, 0.24 and 0.48 eV higher than in the gas phase [16]. For C_8H^- in Ne, absorption to a valence state located 0.39 eV above the gas-phase photodetachment energy was reported [14].

The most extensive theoretical study dealing with the ground electronic state characteristics of $C_{2n+1}N^-$ species (including the vertical electron detachment energies) was published by Botschwina and Oswald in 2008 [17]. More recently, Skomorowski et al. [18] provided reliable (EOM-CCSD) predictions for the energies of vertical excitations to the bound electronic states of $n = 0$ to 3 species, and for the resonances embedded in continua above the ground states of the corresponding neutral radicals.

Citation: Szczepaniak, U.; Kołos, R.; Guillemin, J.-C.; Crépin, C. Phosphorescence of C_5N^- in Rare Gas Solids. *Photochem* **2022**, *2*, 263–271. <https://doi.org/10.3390/photochem2020019>

Academic Editor: Elena Cariati

Received: 14 February 2022

Accepted: 22 March 2022

Published: 28 March 2022

Publisher's Note: MDPI stays neutral with regard to jurisdictional claims in published maps and institutional affiliations.



Copyright: © 2022 by the authors. Licensee MDPI, Basel, Switzerland. This article is an open access article distributed under the terms and conditions of the Creative Commons Attribution (CC BY) license (<https://creativecommons.org/licenses/by/4.0/>).

Phosphorescence has already been observed for C_3N^- anion produced by UV irradiation of Ar, Kr, and Xe matrices doped with HC_3N [19]. Here we report on similar experiments aimed at C_5N^- , carried out with HC_5N -doped rare gas matrices.

2. Experimental

The precursor molecule, HC_5N , was synthesized using the method developed by Trolez and Guillemin [20] and purified before each experiment by exposing to vacuum at $T \approx 200$ K.

Noble gas (hereafter: NG; Ar 4.5, Kr 4.0 or Xe 4.8 from Messer) was mixed with precursor molecules at a ratio of approx. 500:1, using standard manometric techniques. The mixture was subsequently trapped inside the closed-cycle helium refrigerator (Air Products Displex DE202FF, CaF_2 windows) onto a sapphire plate at 22 K (Ar), 30 K (Kr), or 14 K (Xe) as measured and regulated with a Scientific Instruments Inc. 9620-1 temperature controller. The typical amount of deposited gas was 6–8 mmol. All spectroscopic measurements were carried out at the lowest attainable temperature, 7–8 K. Composition of the samples was verified with a Nicolet FTIR spectrometer, either Nexus 670/870 or iS50 (resolution of 0.125 cm^{-1}), equipped with liquid nitrogen-cooled MCT detectors. The use of a sapphire substrate plate imposed the low-frequency detection limit of approx. 1350 cm^{-1} . Cryogenic samples were photolyzed with a 193 nm ArF excimer laser (Coherent Compex Pro), during or after the sample deposition. The laser typically operated at a repetition rate of 10 Hz, the energy delivered to the sample surface did not exceed 5 mJ/cm^2 per pulse, and the usual irradiation time was several hours (at least 4 h in Ar, 3 h in Kr and 1 h in Xe).

A Continuum Surelite II + OPO Horizon pulse laser system operating at 10 Hz in the 192–400 nm range was used for the excitation of luminescence. That latter was dispersed with a 0.6 m Jobin-Yvon grating monochromator and detected either with a photomultiplier (Hamamatsu H3177-50) connected to the exit slit or with a gated CCD camera (Andor iStar DH720), both featuring a detection range of 200–850 nm. Time synchronization between excitation pulses and luminescence detection was provided by a home-made triggering device. Tunable excitation permitted us to separate the new emission features from those of the already known phosphorescence of the parent molecule [21] or of the chain-growth products [22].

In luminescence decay time measurements, phosphorescence light, selected with the grating monochromator, was detected by the photomultiplier. Photons arriving after the excitation laser pulse were counted in successive time gates using a National Instrument acquisition card (PCIe-6251) and a homemade LabView-based software.

3. Results and Discussion

Strong phosphorescence of HC_5N in NG solids was discovered and analyzed in the course of our previous studies [21]. The UV photolysis of that compound trapped in Ar led to the isoelectronic anion C_5N^- detected via its IR spectrum [12]. On the other hand, phosphorescence of C_3N^- was found in photolyzed NG matrices doped with HC_3N [19]. We therefore sought to find phosphorescence of C_5N^- by photolyzing HC_5N . The ArF laser radiation (193 nm) was applied. The choice of optimal conditions to photoexcite the anion was crucial, given that the parent species phosphoresces and that the presence of an intensely emitting photoproduct (dicyanoocatetrayne, $NC_{10}N$) in irradiated HC_5N/NG samples was previously reported [22].

Four major new luminescence bands appeared in a correlated way after UV irradiation in all three applied noble gas matrices. Their frequencies are listed in Table 1. This vibrationally structured emission was distinctly different from the phosphorescence of either the precursor molecule [21] or of $NC_{10}N$ [22]. It is recognized as the phosphorescence of C_5N^- based on the following arguments: (i) analysis of its vibronic structure reveals three stretching fundamental frequencies of C_5N^- that were independently measured via IR absorption (see Table 1); (ii) it is long-lived, in the millisecond time range; and (iii) its

origin (2.68–2.69 eV) conforms to the vertical singlet-triplet excitation energy (3.03 eV) theoretically predicted for C_5N^- [18].

Table 1. Vibronic band wavenumbers ($\tilde{\nu}$) of C_5N^- phosphorescence, as measured in noble gas matrices. Resultant distances from the vibrationless phosphorescence origin ($\Delta\tilde{\nu}$) are juxtaposed with IR absorption data ($\tilde{\nu}_{IR}$), when available. All values in cm^{-1} ; the estimated error of ($\Delta\tilde{\nu}$) is 8 cm^{-1} .

Ar			Kr		Xe			Involved Mode
$\tilde{\nu}$	$\Delta\tilde{\nu}$	$\tilde{\nu}_{IR}^1$	$\tilde{\nu}$	$\Delta\tilde{\nu}$	$\tilde{\nu}$	$\Delta\tilde{\nu}$	$\tilde{\nu}_{IR}$	
21,720			21,721/21,697		21,614			
~19,800	1920	1923.2	19,798/19,767	1923/1930	19,692	1922	1925.4	ν_1
19,610	2110	2111.3	19,610/19,577	2111/2120	19,505	2109	2119.1	ν_2
19,540	2180	2183.8	19,543/19,510	2178/2187	19,428	2186	2191.2	ν_3

¹ Ref. [12].

Said emission could be detected, with varying intensity, following the excitation in a large spectral range (370–220 nm). Phosphorescence intensity depended also on the matrix material, being the highest in solid Xe and the lowest in solid Ar. Photon energies in the vicinity of 3.6 eV were chosen for efficient luminescence excitation in Kr and Xe. Such radiation should excite only the C_5N^- emission (via $1^1\Sigma^-$ or $1^1\Delta$ states) [18] and guaranteed the avoidance of electron detachment. In Ar, phosphorescence of C_5N^- was difficult to detect; it was better seen with more energetic excitation (e.g., 287 nm (4.32 eV)).

Figure 1 shows the main emission bands assigned to C_5N^- , observed in various NG matrices. The spectral features detected in Ar were very weak and broad. The highest energy one, with a structure due to multiple trapping sites, can be seen as the dotted line in Figure 1. In Kr (bottom panel of Figure 1), the origin band appeared as a doublet around $21,700\text{ cm}^{-1}$ and two dominant components were also observed in the remaining bands, the anion therefore seems to be trapped in two main matrix sites. Conversely, phosphorescence detected in Xe (top panel) exhibited single, narrow bands, which allowed for clear assignments of the vibronic structure.

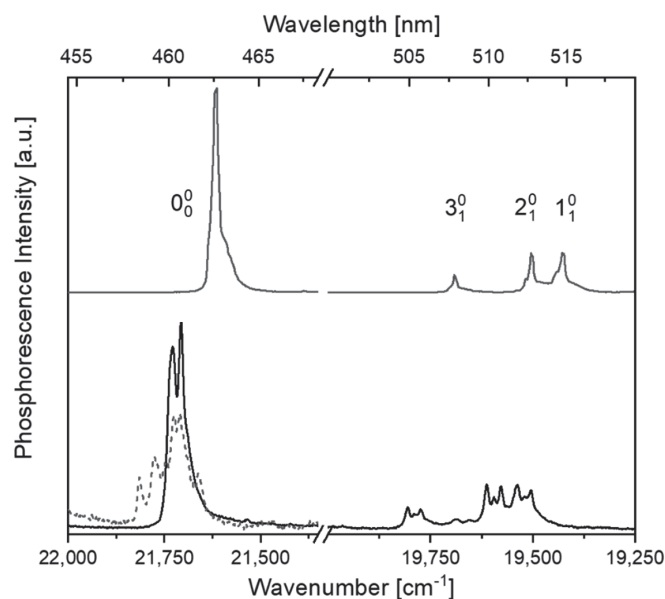


Figure 1. Laser-excited phosphorescence of C_5N^- , as detected in photolyzed (193 nm) NG matrices doped with HC_5N , $T = 8\text{ K}$. Top: Xe matrix, excitation 349.5 nm (3.55 eV, $28,610\text{ cm}^{-1}$). Bottom, continuous line: Kr matrix, excitation 347.1 nm (3.57 eV, $28,810\text{ cm}^{-1}$). Dotted line: in Ar matrix, excitation 287 nm (4.32 eV, $34,840\text{ cm}^{-1}$).

A thorough vibronic analysis of phosphorescence was possible in solid Xe, where the high signal-to-noise ratio gave access to a multitude of weak emission lines. Figure 2 shows the full phosphorescence spectrum (the origin band appears as saturated in order to reveal the weakest features). The assignment of observed bands, reported in Table 2, was assisted with theoretical predictions [12,17]. A comparison of the vibrational frequencies deduced from the phosphorescence spectrum and those theoretically predicted is reported in Table 3.

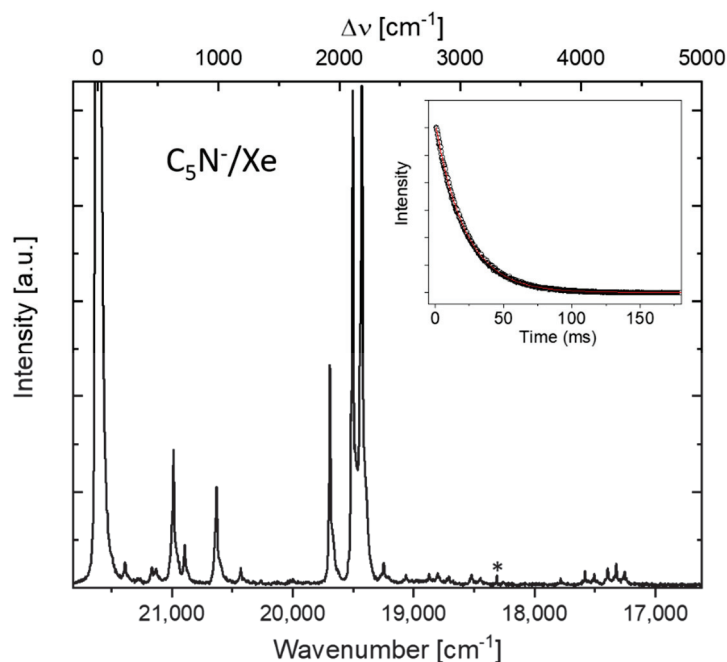


Figure 2. Laser-excited (349.5 nm) phosphorescence of C_5N^- , as detected in a photolyzed (193 nm) HC_5N/Xe matrix, $T = 8$ K (vertical expansion of the top trace of Figure 1). Asterisk marks an Hg line used for wavelength calibration. Inset: C_5N^- phosphorescence decay in Xe; emission detected at $21,615\text{ cm}^{-1}$. Red trace shows the monoexponential fitting curve with a time constant of 21.94 ± 0.03 ms.

Table 2. Wavelengths (λ , nm), wavenumbers ($\tilde{\nu}$, cm^{-1}), and assignments of vibronic bands for the $a^3\Sigma-X^1\Sigma^+$ system of C_5N^- anion isolated in solid Xe. Relative values ($\Delta\tilde{\nu}$, cm^{-1}) give distances from the vibrationless origin.

λ	$\tilde{\nu}$	$\Delta\tilde{\nu}$	Intensity ¹	Assignment
462.7	21,614	0	<i>vs</i>	0_0^0
467.5	21,388	226	<i>v</i> <i>w</i>	8_1^0 (or 9_2^0)
470.4	21,279	335	<i>vs</i> <i>w</i>	$8_1^0 9_1^0$
472.5	21,164	450	<i>v</i> <i>w</i>	8_2^0 (or 9_4^0)
473.3	21,130	484	<i>v</i> <i>w</i>	7_1^0
476.5	20,985	629	<i>m</i>	5_1^0
478.6	20,893	721	<i>w</i>	$7_1^0 8_1^0$
484.8	20,629	985	<i>m</i>	7_2^0
489.5	20,429	1184	<i>v</i> <i>w</i>	4_1^0
507.8	19,692	1922	<i>s</i>	3_1^0
512.7	19,505	2109	<i>vs</i>	2_1^0
514.7	19,428	2185	<i>vs</i>	1_1^0
519.6	19,246	2368	<i>v</i> <i>w</i>	4_2^0
524.6	19,063	2551	<i>vs</i> <i>w</i>	$3_1^0 5_1^0$
530.0	18,869	2744	<i>vs</i> <i>w</i>	$2_1^0 5_1^0$
531.9	18,799	2815	<i>vs</i> <i>w</i>	$1_1^0 5_1^0$
534.5	18,707	2906	<i>vs</i> <i>w</i>	$3_1^0 7_2^0$

Table 2. Cont.

λ	$\tilde{\nu}$	$\Delta\tilde{\nu}$	Intensity ¹	Assignment
540.0	18,520	3094	<i>vvw</i>	2 ⁰ 7 ⁰ ₁ 2 ⁰
542.1	18,447	3167	<i>vvw</i>	1 ⁰ 7 ⁰ ₁ 2 ⁰
562.3	17,784	3830	<i>vvw</i>	3 ⁰ ₂
568.8	17,582	4032	<i>vw</i>	2 ⁰ 3 ⁰ ₁
571.3	17,505	4109	<i>vw</i>	1 ⁰ 3 ⁰ ₁ 1 ⁰
574.9	17,394	4220	<i>vw</i>	2 ⁰ ₂
577.2	17,324	4290	<i>vw</i>	1 ⁰ 2 ⁰ ₁ 1 ⁰
579.6	17,252	4361	<i>vw</i>	1 ⁰ ₂

¹ s: strong, m: medium, w: weak, v: very.

Table 3. Wavenumbers of fundamental vibrational modes for C₅N[−] anion. All values in cm^{−1}.

Mode, Symmetry	Theory		Experiment	
	DFT ¹	CCSD(T) ²	Ar Matrix ³	Xe Matrix ⁴
ν_1 σ	2184	2202.6	2183.8	2186
ν_2 σ	2116	2128.6	2111.3	2109
ν_3 σ	1921	1927.2	1923.2	1922
ν_4 σ	1166	1167.7		1184
ν_5 σ	612	614.4		629
ν_6 π	529	503.0		
ν_7 π	500	493.7		484
ν_8 π	242	227.4		226
ν_9 π	102	96.5		109 ⁵

¹ Harmonic values scaled by 0.96, basis set aug-cc-pVTZ (Ref. [12]). ² Basis set cc-pVQZ+, anharmonic calculations of stretching modes and harmonic calculations of bending modes (Ref. [17]). ³ IR absorption measurement (Ref. [12]). ⁴ This work, derived from electronic phosphorescence. ⁵ Tentative, based on a combination mode $8_1^0 9_1^0$.

The most intense vibronic bands in C₅N[−] phosphorescence are those due to the fundamental modes associated with triple bonds, namely ν_1 , ν_2 , and ν_3 (it should be noted that the shorter chain of C₃N[−] has just two alike modes with frequencies around 2000 cm^{−1}; both were shown to dominate in its triplet-singlet emission [19]). In phosphorescence of other previously studied mono- [21,23–25] and dicyanopolyne [22,26–28] molecules, the vibronic bands produced by the triple bonds were also prominent. The mode contributing especially strongly to the vibronic structure of these emissions was a stretching, either a quasi-centrosymmetric one for the C_{2n+1}N backbone [24] or fully symmetric for NC_{2n}N [22], which caused, along the chain, shrinking of the consecutive interatomic distances alternated with their expansion (i.e., an in-phase oscillation of the three triple bonds) [29]. Distortion patterns of that type qualitatively resembled the geometry changes predicted to accompany the a³Σ⁺–X¹Σ⁺ transitions of cyanopolyne-family molecules, including C₅N[−] [29]. For the latter species, however, there is no vibrational mode around 2000 cm^{−1} that would produce the unison expansion or the unison shrinking of all triple bonds. Still, such an in-phase distortion of two triple bonds is the characteristic shared by the crucial modes ν_1 , ν_2 , and ν_3 .

The two remaining stretching fundamentals ν_4 and ν_5 (influenced mostly by distortions of the single C–C bonds), are also clearly visible in the vibronic structure (at 1184 cm^{−1} and 629 cm^{−1}, respectively; see Figure 2, Table 2). The quasi-symmetric mode ν_5 is similar to the C–C stretch-related bands observed in phosphorescence of HC₅N (ν_6) [21] or C₄N₂ (ν_3 , *gerade* symmetry) [26]. The band due to ν_4 is weak but unambiguously assigned. It is noteworthy that its analogues were revealed only as overtones in phosphorescence of C₄N₂ and HC₅N. Bending (π -symmetry) modes appear weakly in phosphorescence due to its Σ⁺–Σ⁺ orbital character. The ν_8 band at 226 cm^{−1} is easily assigned by comparison with theoretical values (Table 3) and taking into account that similar modes were identified in phosphorescence spectra of HC₅N [21] and C₄N₂ [26]. A frequency of 109 cm^{−1} can

be deduced for the lowest-energy bending (ν_9) based on a very weak feature tentatively recognized as a combination band. Another bending-related band appears at 484 cm^{-1} . It is assigned to ν_7 based on theoretical predictions (Table 3). The highest-energy bending (*zig-zag* type, ν_6) does not seem to produce a detectable vibronic band. Nonetheless, such a mode appeared, albeit weakly, in phosphorescence of HC_5N [21], C_4N_2 [26] and C_3N^- [19]. Considering the closeness of ν_6 and ν_7 (separation of 9 cm^{-1} derived with harmonic CCSD(T) calculations) [17], a possibility exists, however, that the band at 484 cm^{-1} represents the said *zig-zag* mode and ν_7 is not detected.

Present non-detection of IR absorption bands for C_5N^- generated in Ar or Kr matrices indicates that 193 nm laser radiation was not as effective in producing this anion as the broadband far-UV irradiation applied by Coupeaud et al. [12]. In solid Xe, however, IR bands due to ν_1 , ν_2 , and ν_3 stretching fundamentals of C_5N^- could be discerned (see Table 1). Some mismatch between $\Delta\tilde{\nu}$ and $\tilde{\nu}_{\text{IR}}$ values listed in Table 1 may stem, on the one hand, from the experimental error inherent to $\Delta\tilde{\nu}$ ($5\text{--}8\text{ cm}^{-1}$) and, on the other hand, from the coupling of the electronic transition with phonons. That last issue is mode-specific and may slightly deviate the maximum of the measured phosphorescence bands from the true zero-phonon transition frequencies.

Influence of the NG environment is manifested by a red-shift of phosphorescence in Xe, with respect to Kr. It is usual for the transitions involving valence electrons and originates from an increase of the host polarizability. Furthermore, the size of C_5N^- is obviously bigger than the distance between the nearest NG atoms forming the lattice, which may induce the trapping of HC_5N and C_5N^- in multiple sites. This is indeed observed in Ar and Kr, but not in Xe, where the lattice parameter is the largest.

A very long luminescence decay time was evident even to the naked eye. As reported for numerous instances of triplet-singlet transitions in NG matrices (see e.g., Ref. [30]), the heavier the host, the shorter the phosphorescence decay (we observed the same pattern for the related, matrix-isolated molecules HC_5N [21] and C_4N_2 [26]). This is a consequence of the spin-orbit coupling enhancement by external heavy atoms [31–33]. The values presently measured in Kr and Xe matrices are, respectively, $\sim 250\text{ ms}$ and $\sim 22\text{ ms}$ (see the insert of Figure 2). These are ca. five times higher than those of the isoelectronic species HC_5N ($\sim 50\text{ ms}$ in Kr and $\sim 4.8\text{ ms}$ in Xe, as presently measured in the same samples). It indicates a much lower nonradiative $T_1 \rightarrow S_0$ conversion efficiency for C_5N^- than for HC_5N , in possible relation to an intersystem crossing channel enhanced by the presence of large CH stretching mode energy quanta. Phosphorescence lifetime reported for the shorter analogue, C_3N^- , was twice as long ($\sim 0.5\text{ s}$ in Kr) [19], likely due to a smaller number of internal degrees of freedom, leading to less efficient non-radiative relaxation. Such a decrease in the phosphorescence lifetime with the increase of polyynic chain length was pointed out in our previous reports on mono- and dicyanopolyynes [22,29].

The detection of photoproducts in UV-irradiated $\text{HC}_5\text{N}/\text{NG}$ samples, including cyanodiacetylene isomers [12], intermolecular coupling products (HC_9N [24], C_{10}N_2 [22]), and noble gas insertion species H-NG- C_5N [34], is already well documented. While we do not provide here any in-depth discussion of the energetics of C_5N^- formation from HC_5N , it should be noted that a gas-phase process leading from that precursor to H^+ and C_5N^- would require an overall energy input by far higher than that provided with a single quantum of 193 nm radiation. However, one should consider that (i) C_5N radicals are being formed in the sample (as elucidated from the kinetics of the parallel production of NC_{10}N [22]), (ii) electron attachment to these radicals is obviously exothermic, and (iii) protons, when bound as NG-H-NG $^+$ cations, can be stabilized in NG matrices [35]. The latter species could not be traced in the present experiments, due to the use of a sapphire substrate plate (see Experimental). However, Ar_2H^+ cations were shown to accompany C_5N^- in a correlated manner when HC_5N was photolyzed in solid argon [12]. Importantly, we did not observe any trace of C_5N^- in a sample deprived of noble gas atoms, i.e., when dinitrogen was used as a host material for HC_5N photolysis.

The $a^3\Sigma^+-X^1\Sigma^+$ system of C_5N^- could be induced with wavelengths from a broad range, approx. 370–200 nm. A detailed study of phosphorescence excitation spectra is in progress, together with the relevant theoretical support. Especially interesting are the relaxation pathways leading to the observed emission when excitation energy exceeds the C_5N^- photodetachment threshold.

4. Conclusions

Phosphorescence of C_5N^- was observed here for the first time. Lifetime of the involved lowest triplet state is five times longer than for the parent HC_5N molecule. Positions of the main vibronic bands of the $a^3\Sigma^+-X^1\Sigma^+$ system are consistent with the frequencies of the three vibrational modes previously observed [12] in IR absorption spectra. Matrix material, either Ar, Kr, or Xe, was shown to influence both the intensity of phosphorescence and its band structure. In particular, the presence of two main matrix sites (types of microenvironments) is suggested by the doubling of bands observed in Kr, whereas the Xe-matrix spectra seem to originate in a single site. Phosphorescence characteristics, influenced by the external heavy atom effect, did not show any measurable site-dependence in Kr, while the host dependence (Xe vs. Kr) was obvious in terms of both emission intensity and decay time. Emission from the Xe matrix sample, intense and rich in detail, allowed for the first measurement of the previously unreachable ground-state vibrational frequencies ν_4 , ν_5 , ν_7 , ν_8 , and (tentatively) ν_9 .

Author Contributions: Conceptualization, R.K. and C.C.; methodology, R.K. and C.C.; formal analysis, U.S., R.K. and C.C.; investigation, U.S. and R.K.; resources, J.-C.G. and C.C.; writing—original draft preparation, U.S., R.K. and C.C.; writing—review and editing, U.S., R.K., J.-C.G. and C.C.; supervision, R.K. and C.C.; funding acquisition, U.S., R.K., J.-C.G. and C.C. All authors have read and agreed to the published version of the manuscript.

Funding: This work was financially supported by the Polish National Science Centre, project no. 2011/03/B/ST4/02763, French-Polish scientific cooperation programs Partenariat Hubert-Curie Polonium (2012–2013) and PICS (2014–2016). U.S. is a beneficiary of the French Government scholarship Bourse Eiffel, managed by Campus France, and of the project “Scholarships for PhD students of Podlaskie Voivodeship”. The project is co-financed by European Social Fund, Polish Government and Podlaskie Voivodeship. J.-C.G. thanks for the financial support received from Centre National d’Etudes Spatiales (CNES) and the French program Physique et Chimie du Milieu Interstellaire (PCMI) funded by the Centre National de la Recherche Scientifique and CNES.

Institutional Review Board Statement: Not applicable.

Data Availability Statement: The data presented in this study are available within the article.

Acknowledgments: We thank Michèle Chevalier for assistance in experiments and Marcin Gronowski for the discussion of theoretical issues.

Conflicts of Interest: The authors declare no conflict of interest.

References

1. Turner, B.E. Detection of Interstellar Cyanoacetylene. *Astrophys. J. Lett.* **1971**, *163*, L35–L39. [CrossRef]
2. Mauersberger, R.; Henkel, C.; Sage, L.J. Dense Gas in Nearby Galaxies. III-HC₃N as an Extragalactic Density Probe. *Astron. Astrophys.* **1990**, *236*, 63–68.
3. Kunde, V.G.; Aikin, A.C.; Hanel, R.A.; Jennings, D.E.; Maguire, W.C.; Samuelson, R.E. C₄H₂, HC₃N and C₂N₂ in Titan’s Atmosphere. *Nature* **1981**, *292*, 686–688. [CrossRef]
4. Bockelée-Morvan, D.; Lis, D.C.; Wink, J.E.; Despois, D.; Crovisier, J.; Bachiller, R.; Benford, D.J.; Biver, N.; Colom, P.; Davies, J.K.; et al. New Molecules Found in Comet C/1995 O1 (Hale-Bopp): Investigating the Link between Cometary and Interstellar Material. *Astron. Astrophys.* **2000**, *353*, 1101–1114.
5. Snell, R.L.; Schloerb, F.P.; Young, J.S.; Hjalmarsen, A.; Friberg, P. Observations of HC₃N, HC₅N, and HC₇N in Molecular Clouds. *Astrophys. J.* **1981**, *244*, 45. [CrossRef]
6. Broten, N.W.; Oka, T.; Avery, L.W.; MacLeod, J.M.; Kroto, H.W. The Detection of HC₉N in Interstellar Space. *Astrophys. J.* **1978**, *223*, L105–L107. [CrossRef]

7. Loomis, R.A.; Burkhardt, A.M.; Shingledecker, C.N.; Charnley, S.B.; Cordiner, M.A.; Herbst, E.; Kalenskii, S.; Lee, K.L.K.; Willis, E.R.; Xue, C.; et al. An Investigation of Spectral Line Stacking Techniques and Application to the Detection of HC₁₁N. *Nat. Astron.* **2021**, *5*, 188–196. [CrossRef]
8. Thaddeus, P.; Gottlieb, C.A.; Gupta, H.; Brünken, S.; McCarthy, M.C.; Agúndez, M.; Guélin, M.; Cernicharo, J. Laboratory and Astronomical Detection of the Negative Molecular Ion C₃N[−]. *Astrophys. J.* **2008**, *677*, 1132–1139. [CrossRef]
9. Cernicharo, J.; Guélin, M.; Agúndez, M.; McCarthy, M.C.; Thaddeus, P. Detection of C₅N[−] and Vibrationally Excited C₆H in IRC +10216. *Astrophys. J.* **2008**, *688*, L83–L86. [CrossRef]
10. Vuitton, V.; Lavvas, P.; Yelle, R.V.; Galand, M.; Wellbrock, A.; Lewis, G.R.; Coates, A.J.; Wahlund, J.E. Negative Ion Chemistry in Titan’s Upper Atmosphere. *Planet. Space Sci.* **2009**, *57*, 1558–1572. [CrossRef]
11. Kołos, R.; Gronowski, M.; Botschwina, P. Matrix Isolation IR Spectroscopic and Ab Initio Studies of C₃N[−] and Related Species. *J. Chem. Phys.* **2008**, *128*, 154305. [CrossRef] [PubMed]
12. Coupeaud, A.; Turowski, M.; Gronowski, M.; Piétri, N.; Couturier-Tamburelli, I.; Kołos, R.; Aycard, J.P. C₅N[−] Anion and New Carbenic Isomers of Cyanodiacetylene: A Matrix Isolation IR Study. *J. Chem. Phys.* **2008**, *128*, 154303. [CrossRef] [PubMed]
13. Stanca-Kaposta, E.C.; Schwaneberg, F.; Fagiani, M.R.; Wende, T.; Hagemann, F.; Wünschmann, A.; Wöste, L.; Asmis, K.R. Infrared Photodissociation Spectroscopy of C_{2n+1}N[−] Anions with n = 1–5. *Z. Phys. Chem.* **2014**, *228*, 351–367. [CrossRef]
14. Grutter, M.; Wyss, M.; Maier, J.P. Electronic Absorption Spectra of C_{2n}H[−], C_{2n−1}N[−] (n = 4–7), and C_{2n−1}N (n = 3–7) Chains in Neon Matrices. *J. Chem. Phys.* **1999**, *110*, 1492–1496. [CrossRef]
15. Yen, T.A.; Garand, E.; Shreve, A.T.; Neumark, D.M. Anion Photoelectron Spectroscopy of C₃N[−] and C₅N[−]. *J. Phys. Chem. A* **2010**, *114*, 3215–3220. [CrossRef] [PubMed]
16. Szczepanski, J.; Ekern, S.; Vala, M. Vibrational Spectroscopy of Small Matrix-Isolated Linear Carbon Cluster Anions. *J. Phys. Chem. A* **1997**, *101*, 1841–1847. [CrossRef]
17. Botschwina, P.; Oswald, R. Carbon Chains of Type C_{2n+1}N[−] (N = 2–6): A Theoretical Study of Potential Interstellar Anions. *J. Chem. Phys.* **2008**, *129*, 044305. [CrossRef]
18. Skomorowski, W.; Gulania, S.; Krylov, A.I. Bound and Continuum-Embedded States of Cyanopolyynes Anions. *Phys. Chem. Chem. Phys.* **2018**, *20*, 4805–4817. [CrossRef]
19. Turowski, M.; Gronowski, M.; Boyé-Péronne, S.; Douin, S.; Moneron, L.; Crépin, C.; Kołos, R. The C₃N[−] Anion: First Detection of Its Electronic Luminescence in Rare Gas Solids. *J. Chem. Phys.* **2008**, *128*, 164304. [CrossRef] [PubMed]
20. Trolez, Y.; Guillemin, J.-C. Synthesis and Characterization of 2,4-Pentadienenitrile—A Key Compound in Space Science. *Angew. Chem. Int. Ed.* **2005**, *44*, 7224–7226. [CrossRef] [PubMed]
21. Turowski, M.; Crépin, C.; Gronowski, M.; Guillemin, J.C.; Coupeaud, A.; Couturier-Tamburelli, I.; Pietri, N.; Kołos, R. Electronic Absorption and Phosphorescence of Cyanodiacetylene. *J. Chem. Phys.* **2010**, *133*, 074310. [CrossRef]
22. Szczepaniak, U.; Kołos, R.; Gronowski, M.; Chevalier, M.; Guillemin, J.C.; Crépin, C. Synthesis and Electronic Phosphorescence of Dicyanoacetate (NC₁₀N) in Cryogenic Matrices. *J. Phys. Chem. A* **2018**, *122*, 5580–5588. [CrossRef]
23. Couturier-Tamburelli, I.; Piétri, N.; Crépin, C.; Turowski, M.; Guillemin, J.C.; Kołos, R. Synthesis and Spectroscopy of Cyanotriacetylene (HC₇N) in Solid Argon. *J. Chem. Phys.* **2014**, *140*, 044329. [CrossRef] [PubMed]
24. Szczepaniak, U.; Kołos, R.; Gronowski, M.; Chevalier, M.; Guillemin, J.-C.; Turowski, M.; Custer, T.; Crépin, C. Cryogenic Photochemical Synthesis and Electronic Spectroscopy of Cyanotetracetylene. *J. Phys. Chem. A* **2017**, *121*, 7374–7384. [CrossRef] [PubMed]
25. Szczepaniak, U.; Ozaki, K.; Tanaka, K.; Ohnishi, Y.; Wada, Y.; Guillemin, J.C.; Crépin, C.; Kołos, R.; Morisawa, Y.; Suzuki, H.; et al. Phosphorescence Excitation Mapping and Vibrational Spectroscopy of HC₉N and HC₁₁N Cyanopolyynes in Organic Solvents. *J. Mol. Struct.* **2020**, *1214*, 128201. [CrossRef]
26. Turowski, M.; Crépin, C.; Couturier-Tamburelli, I.; Pietri, N.; Kołos, R. Low-Temperature Phosphorescence of Dicyanoacetylene in Rare Gas Solids. *Low Temp. Phys.* **2012**, *38*, 723–726. [CrossRef]
27. Crépin, C.; Turowski, M.; Cepenkus, J.; Douin, S.; Boyé-Péronne, S.; Gronowski, M.; Kołos, R. UV-Induced Growth of Cyanopolyynes Chains in Cryogenic Solids. *Phys. Chem. Chem. Phys.* **2011**, *13*, 16780–16785. [CrossRef]
28. Turowski, M.; Crépin, C.; Douin, S.; Kołos, R. Formation and Spectroscopy of Dicyanotriacetylene (NC₈N) in Solid Kr. *J. Phys. Chem. A* **2015**, *119*, 2701–2708. [CrossRef]
29. Szczepaniak, U. Spectroscopy and Photochemistry of Astrophysically-Relevant Molecules of the Cyanoacetylene Family. Ph.D. Thesis, Institute of Physical Chemistry, Polish Academy of Sciences, Warsaw, Poland, Université Paris-Saclay, Université Paris-Sud-Paris XI, Orsay, France, 2017. Available online: <https://tel.archives-ouvertes.fr/tel-01562041/> (accessed on 1 February 2022).
30. Wright, M.R.; Frosch, R.P.; Robinson, G.W. Phosphorescence Lifetime of Benzene. an Intermolecular Heavy-Atom Effect, a Deuterium Effect, and a Temperature Effect. *J. Chem. Phys.* **1960**, *33*, 934–935. [CrossRef]
31. Minaev, B.F. External Heavy-Atom Effects on Radiative Singlet-Triplet Transitions. *J. Appl. Spectrosc.* **1985**, *43*, 887–890. [CrossRef]
32. Minaev, B. Theoretical Study of the External Heavy Atom Effect on Phosphorescence of Free-Base Porphin Molecule. *Spectrochim. Acta-Part A Mol. Biomol. Spectrosc.* **2004**, *60*, 3213–3224. [CrossRef] [PubMed]
33. Baryshnikov, G.; Minaev, B.; Ågren, H. Theory and Calculation of the Phosphorescence Phenomenon. *Chem. Rev.* **2017**, *117*, 6500–6537. [CrossRef] [PubMed]

34. Turowski, M.; Gronowski, M.; Guillemin, J.C.; Kołos, R. Generation of H-Kr-C₅N and H-Xe-C₅N Molecules. *J. Mol. Struct.* **2012**, *1025*, 140–146. [CrossRef]
35. Kunttu, H.M.; Seetula, J.A. Photogeneration of Ionic Species in Ar, Kr and Xe Matrices Doped with HCl, HBr and HI. *Chem. Phys.* **1994**, *189*, 273–292. [CrossRef]

Article

Energy Relaxation of Porphycene in Atomic and Molecular Cryogenic Matrices

Jacek Dobkowski ¹, Igor V. Sazanovich ^{1,†}, Aleksander Gorski ¹ and Jacek Waluk ^{1,2,*}

¹ Institute of Physical Chemistry, Polish Academy of Sciences, Kasprzaka 44/52, 01-224 Warsaw, Poland; jdobkowski@ichf.edu.pl (J.D.); igor.sazanovich@stfc.ac.uk (I.V.S.); agorski@ichf.edu.pl (A.G.)

² Faculty of Mathematics and Science, Cardinal Stefan Wyszyński University, Dewajtis 5, 01-815 Warsaw, Poland

* Correspondence: jwaluk@ichf.edu.pl

† Present address: Central Laser Facility, Research Complex at Harwell, STFC Rutherford Appleton Laboratory, Harwell Science and Innovation Campus, Chilton, Oxfordshire OX11 0QX, UK.

Abstract: The kinetics of relaxation of high-lying electronic states of porphycene (porphyrin isomer) embedded in different cryogenic matrices were studied using picosecond time-resolved fluorescence (TRF) and transient absorption (TA) techniques. The molecule was excited into the Soret band, i.e., with a large energy excess compared to that of the lowest (Q) excited state. The TRF and TA time profiles obtained for porphycene embedded in argon and methane matrices were remarkably different: the overall relaxation in argon occurred in 64 ps, whereas the corresponding value for methane matrix was 18 ps. Analysis of the evolution over time of different spectral ranges of TRF spectra indicates the multidimensional character of relaxation kinetics.

Keywords: vibrational relaxation; time-resolved spectra; picosecond transient absorption

Citation: Dobkowski, J.; Sazanovich, I.V.; Gorski, A.; Waluk, J. Energy Relaxation of Porphycene in Atomic and Molecular Cryogenic Matrices. *Photochem* **2022**, *2*, 299–307. <https://doi.org/10.3390/photochem2020021>

Academic Editors: Rui Fausto and Robert Kotos

Received: 1 March 2022

Accepted: 26 March 2022

Published: 6 April 2022

Publisher's Note: MDPI stays neutral with regard to jurisdictional claims in published maps and institutional affiliations.



Copyright: © 2022 by the authors. Licensee MDPI, Basel, Switzerland. This article is an open access article distributed under the terms and conditions of the Creative Commons Attribution (CC BY) license (<https://creativecommons.org/licenses/by/4.0/>).

1. Introduction

When a molecule is electronically excited into a higher-lying state, it undergoes complicated dynamic processes before reaching the thermally equilibrated S_1 level. Energy relaxation involves several intramolecular and intermolecular steps: (i) internal conversion (IC), potentially including intermediate electronic states between the initially excited and the emitting one; (ii) intramolecular vibrational redistribution (IVR); and (iii) thermalization of S_1 , with outflow of energy from the molecule into the environment. These processes usually occur over different timescales. Relaxation dynamics has been intensely studied for porphyrins, which are molecules of biological relevance [1–21]. Excitation into the high-energy Soret band is followed by ultrafast IC (tens to hundreds of femtoseconds), IVR (subpicosecond to single picosecond regime), and cooling (10–20 ps). The relaxation kinetics depends on various factors, such as the structure of the chromophore (e.g., planar vs. nonplanar) or the excess energy acquired via photoexcitation.

Intermolecular relaxation channels are usually slower than intramolecular ones, occurring on the time scale of single to tens of picoseconds in solutions or glasses. However, relaxation can take even longer when the molecule is located in a specific environment, such as cryogenic matrices [22–24]. Under these conditions, relaxation times of several hundred picoseconds have been observed. We have previously demonstrated this by coupling time-resolved fluorescence and transient absorption techniques with matrix isolation. The investigated chromophores included a series of porphyrin isomers—porphycene (Pc, Scheme 1) and its derivatives—embedded in rare gas and nitrogen matrices [25–28]. A large difference in the time-resolved fluorescence profiles was observed for different excitation wavelengths. When the sample was excited using the 355 nm laser line into the Soret band, i.e., with high excess energy (about 11000 cm^{-1} above S_1), fluorescence relaxation occurred

on the time scale of 100 ps. In contrast, for low-energy excitation (593 nm, Q band), the emission was fully relaxed less than 40 picoseconds after photoexcitation [25].



Scheme 1. (Left) porphyrin (porphine); (right) porphycene.

The purpose of the present work is to check to what extent the rate of energy flow from an excited chromophore to the environment can be affected by the structure of the latter. For that purpose, we compared the relaxation kinetics obtained for porphycene in matrices consisting of atoms (Ar) and molecules (CH₄). We observe a clear difference between the relaxation times in the two media. Moreover, the kinetic profiles of the fluorescence evolution strongly depend on the probed spectral range, demonstrating the multidimensional character of the energy relaxation.

2. Materials and Methods

Solid gas matrices were obtained after depositing a stream of gas containing vapors of the investigated compound onto a sapphire window held at 5–30 K in a closed-cycle helium cryostat (Advanced Research Systems Inc., Macungie, PA, USA).

To record the transient absorption (TA) spectra, a home-built pump-probe picosecond spectrometer was used. Pulses with a duration of 1.5 ps (1055 nm) and an energy of 4 mJ, with a repetition of 33 Hz, are provided by a Light Conversion (Vilnius, Lithuania) Nd:glass laser. The third harmonic (352 nm) is used as the pump, whereas the probe, optically delayed with respect to excitation, is the picosecond continuum (400–800 nm) generated in D₂O. The detection unit consists of a Jasný polychromator, containing a Jobin Yvon grating with a flat focusing field, where a CCD matrix is fixed (Hamamatsu S7031, one stage TE-cooled, back-thinned CCD, 1024 × 128 pixels). The temporal resolution of the spectrometer is 2.5 ps.

Time-resolved fluorescence (TRF) spectra were recorded by means of a home-made picosecond spectrofluorimeter, described in detail elsewhere [29]. In short, the first beam (352 nm, 1.5 ps) is used for excitation. The second beam passes through an optical Kerr shutter and opens it. The fluorescence can be transmitted by the shutter only for the time period in which the opening pulse penetrates the Kerr medium. The opening pulse is delayed with respect to the excitation by an optical delay line (maximum delay of 3000 ps, 0.1 ps/step). The delay time is calculated with respect to the maximum of the excitation pulse. The fluorescence is transmitted by a quartz fiber to the detection system consisting of a polychromator (Acton SpectraPro-275, Acton Research Corporation, Acton, MA, USA) and a CCD detector (Princeton Instruments, Inc., Trenton, NJ, USA). The temporal resolution of the spectrofluorimeter is 6.5 ps. The spectra were corrected for the instrumental response.

Time-dependent evolution of TRF spectra can contain artefacts generated by light velocity dispersion (LVD). To check that our results are free from such effects, TRF spectra were recorded for the solution of anthracene in cyclohexane at 294 K. These spectra did not exhibit any differences in the spectral distribution with different delay times. The normalized kinetic curves describing the increased integrated TRF intensity evaluated for spectral intervals of 21,500–25,500, 240,00–25,500, and 21,500–22,700 cm⁻¹ were identical within the margin of experimental error. The increase in the kinetic curves was strictly associated with the temporal resolution of the apparatus.

3. Results and Discussion

3.1. Time-Resolved Fluorescence

The time-resolved fluorescence spectra of porphycene in an Ar matrix are shown in Figure 1. The evolution of the shape of the emission can be clearly observed. Initially (6 ps delay), the spectrum consists of a broad band with the maximum at about $15,600\text{ cm}^{-1}$. At 36 ps delay, it blue shifts by ca. 300 cm^{-1} ; traces of a vibrational structure appear, which become clearly visible after 76 ps. Then, these vibronic features shift to higher energies and become narrower. The fully relaxed spectrum is observed for delay times longer than ca. 150 ps.

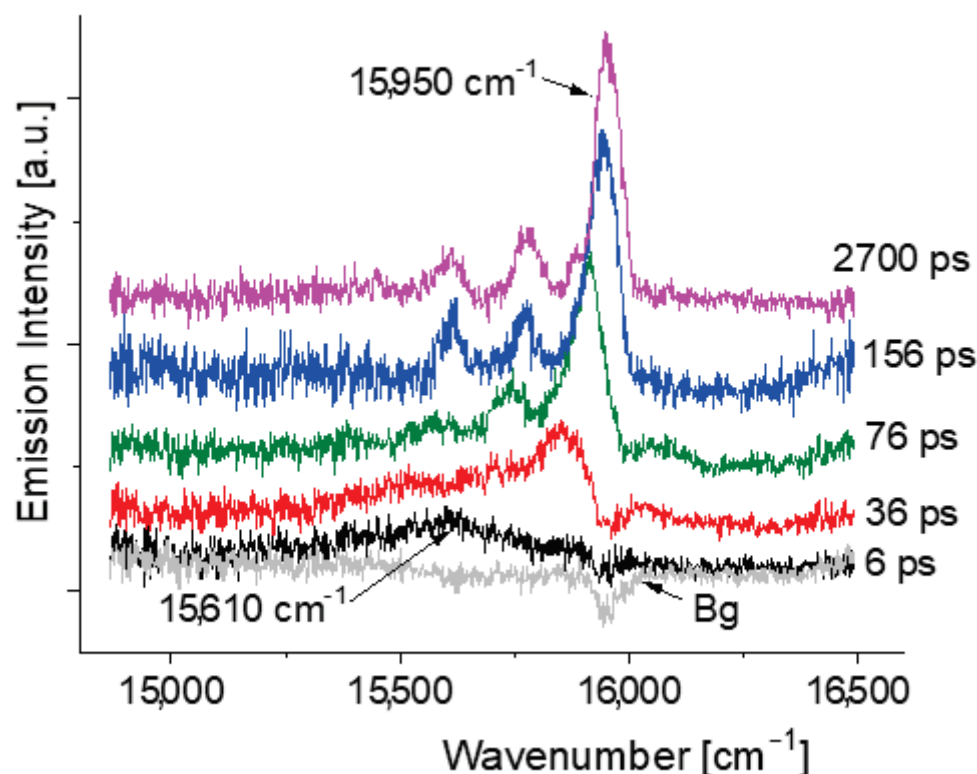


Figure 1. TRF spectra of Pc in argon at 6 K recorded as a function of the delay time: 6, 36, 76, 156, and 2700 ps. The spectra offset was shifted vertically for better visualization. Bg indicates the background.

In our former work [25], time-resolved spectra of the same system at 15 K were recorded, with a time resolution of 30 ps. The present improvement (to 6.5 ps) made it possible to observe changes in the spectral profile occurring during the initial several tens of picoseconds. As shown below, this was crucial for the methane matrices.

We analyzed the kinetic profiles of the spectral changes in emission using two approaches. First, the evolution of the mass center (MC) of the TRF spectra was plotted versus delay time (Figure 2). It could be fitted well with a single exponential risetime of 64 ± 2 ps. In the next step, the evolutions of individual bands were considered separately (Figure 3 and Table 1). The spectral range encompassing the whole emission is labeled P0. P1 corresponds to the 0–0 transition, whereas P2 and P3 denote the features due to the 3Ag and 4Ag vibrational modes, respectively [30–32]. These totally symmetric modes involve in-plane bending of the pyrrole units. The observed kinetic profiles of integrated intensity are completely different: a biexponential rise is obtained for the integration of the whole emission (P0). In contrast, the low-energy portion (P3) exhibits a rapid rise, followed by a long decay before reaching a plateau (most probably, corresponding to the fluorescence lifetime of about 15 ns). The profile associated with the (0–0) transition (P1) is even more complex, showing an initial delay before the rise, with a time constant similar to

that obtained for the whole emission. These results reflect the multidimensional movement of the initially launched wavepacket.

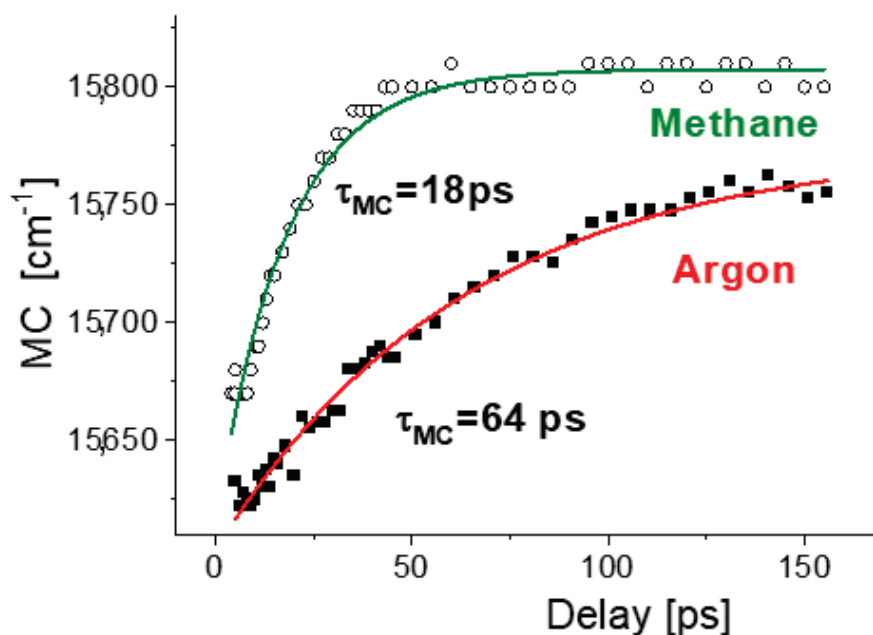


Figure 2. The position of the mass center (MC) of the TRF spectra versus delay time obtained for Pc in argon (squares) and methane (circles) matrices at 6 K and 8 K, respectively. The lines show the results of monoexponential fits: $\tau_{MC} = 64 \pm 2 \text{ ps}$ (argon) and $\tau_{MC} = 18 \pm 2 \text{ ps}$ (methane).

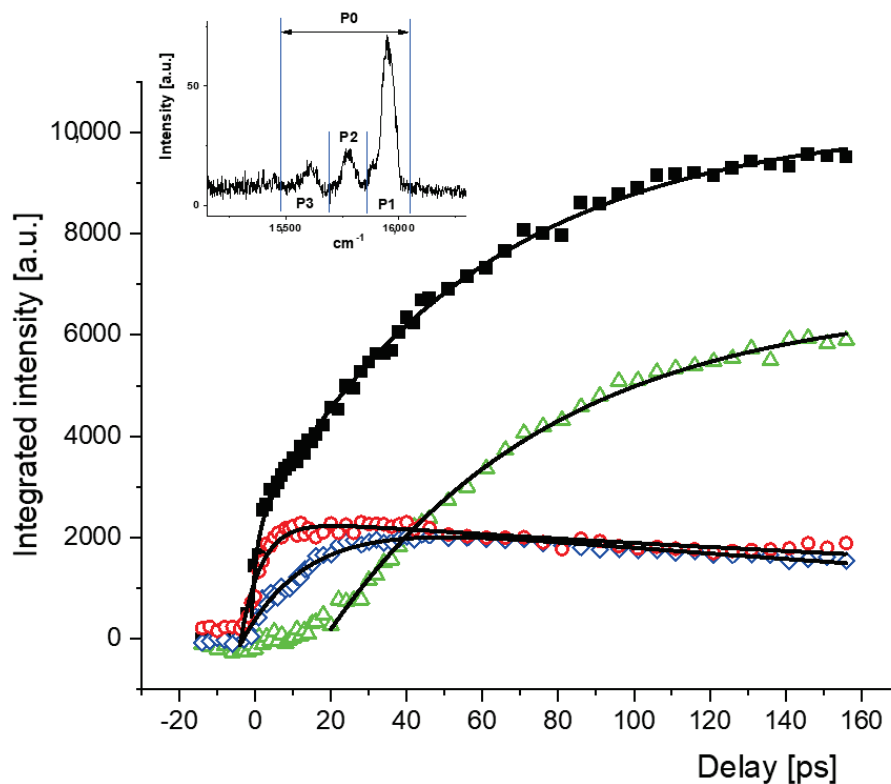


Figure 3. Pc incorporated in argon matrix 6 K. Kinetic profiles of integrated intensity obtained for different integration limits: 15,486–16,029 cm^{-1} (P0, squares), 15,834–16,029 cm^{-1} (P1, triangles), 15,700–15,834 (P2, rhombs), 15,486–15,700 (P3, circles).

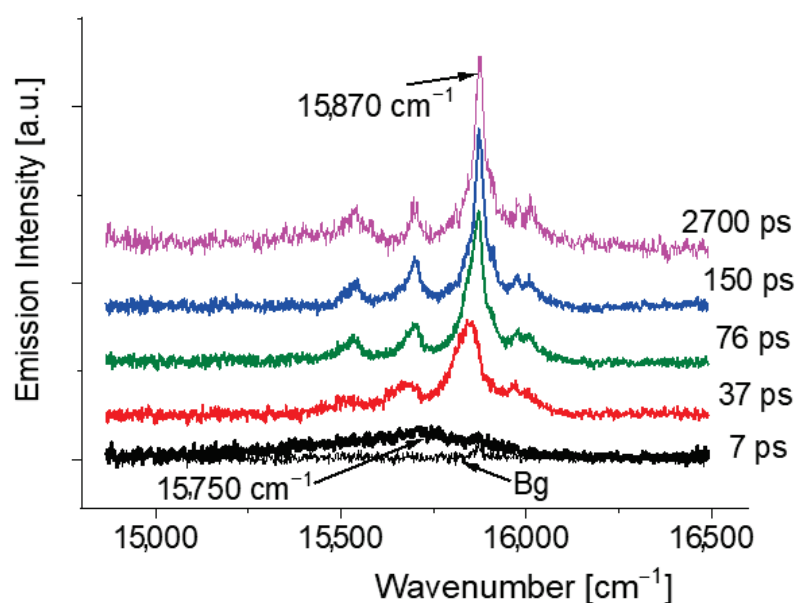
Table 1. Kinetic parameters for Pc incorporated in argon matrix at 6 K, evaluated from the experimental kinetic curves (see Figure 3). D: decay, R: rise.

<Spectral Region>\cm ⁻¹	τ \ps	Amplitude	τ \ps	Amplitude
P0 15,486–16,029	58 ± 2 (R)	8123 ± 80	5 ± 3 (R)	1660 ± 150
P1 15,834–16,029	63 ± 3 (R)	6500 ± 120	-	-
P2 15,700–15,834	18 ± 1 (R)	2680 ± 90	300 ± 31 (D)	2540 ± 100
P3 15,486–15,700	6 ± 0.5 (R)	2474 ± 94	400 ± 45 (D)	2187 ± 47

The same procedures were repeated to analyze the fluorescence of Pc in methane. A shorter relaxation time is evident: the initially (7 ps) broad emission already becomes structured after 37 ps delay, and reaches its final shape at 76 ps (Figure 4). The spectrum recorded after 37 ps delay resembles that in argon obtained after 76 ps. One should also note that the maximum of the broad band observed just after the excitation is separated from the maximum of the relaxed fluorescence by 120 cm⁻¹, whereas the corresponding value for argon was 340 cm⁻¹ (Figure 1). This may be explained by the faster relaxation in CH₄, so that the “initial” spectrum in this matrix is in fact more relaxed than the corresponding spectrum in argon. The evolution of different bands (Figure 5, Table 2) exhibits a pattern similar to that observed for argon: the risetimes increase in the order P3 < P2 < P1; however, the values are definitely shorter for methane. Both P2 and P3 exhibit a decay before reaching a plateau. These decays are about 10 times shorter than in argon.

Table 2. Kinetic parameters for Pc incorporated in methane matrix at 8 K, evaluated from the experimental kinetic curves (see Figure 5). D: decay, R: rise.

<Spectral Region>\cm ⁻¹	τ \ps	Amplitude	τ \ps	Amplitude
P0 15,432–15,952	12 ± 0.4 (R)	10,430 ± 152	1653 ± 321 (D)	10,980 ± 132
P1 15,760–15,952	28 ± 2 (R)	8854 ± 585	380 ± 75 (D)	9072 ± 611
P2 15,606–15,760	8 ± 0.4 (R)	5200 ± 100	24 ± 1 (D)	2761 ± 30
P3 15,432–15,606	5 ± 1 (R)	2560 ± 600	20 ± 7 (D)	1213 ± 640

**Figure 4.** TRF spectra of Pc in methane matrix at 8 K, recorded for different delay times (τ): 7, 37, 76, 150, and 2700 ps. For ease of visualization, the intensity of the spectrum recorded for the delay of 2700 ps was normalized to that of the spectrum recorded for 150 ps. Bg indicates the background.

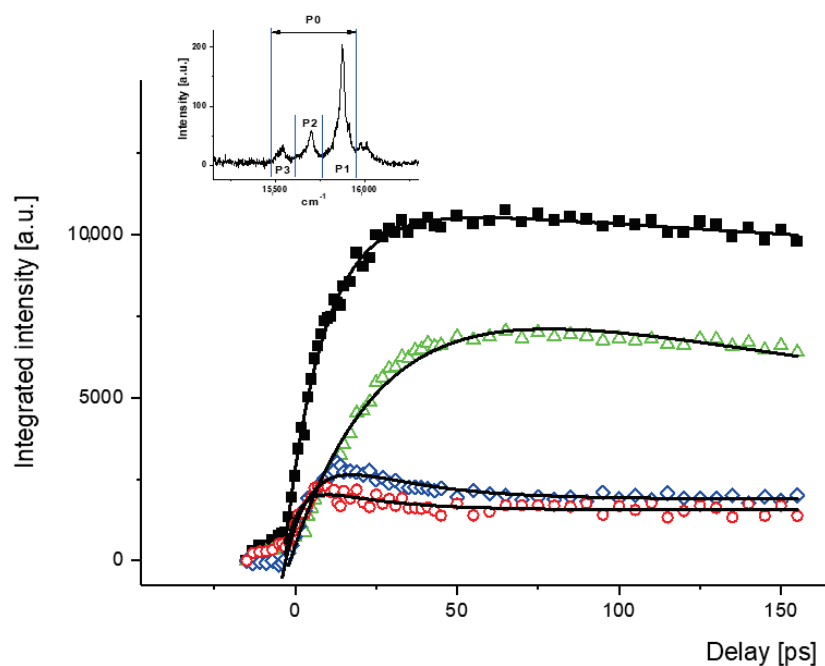


Figure 5. Pc incorporated in methane at 8 K. Kinetics profiles of integrated intensity obtained for different integration limits: (1) 15,432–15,952 cm⁻¹ (P0, squares), 15,760–15,952 cm⁻¹ (P1, triangles), 15,606–15,760 cm⁻¹ (P2, rhombs), and 15,432–15,606 (P3, circles).

3.2. Transient Absorption

An alternative way of probing the relaxation kinetics is to use transient absorption (Figures 6–8). The signal is dominated by ground state bleaching. However, the features P2 and P3, corresponding to 3Ag and 4Ag vibrational modes, appear in the stimulated emission. The kinetic profiles of these bands, indicated by arrows in Figure 6, are in agreement with the data obtained from TRF analysis. Thus, in argon matrix, they are barely visible at a pump-probe delay of 76 ps and become well-structured after 176 ps. In methane, the spectral evolution is faster, so that fully relaxed vibronic features are observed at 76 ps.

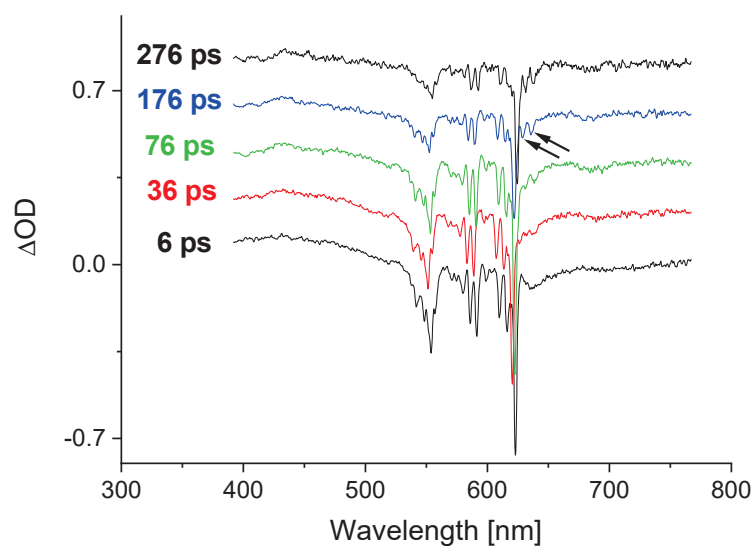


Figure 6. TA spectra of Pc in argon at 6 K recorded as a function of the delay time. The arrows show the vibronic feature of stimulated fluorescence. For ease of visualization, each consecutive spectrum was shifted vertically by 0.2 ΔOD units.

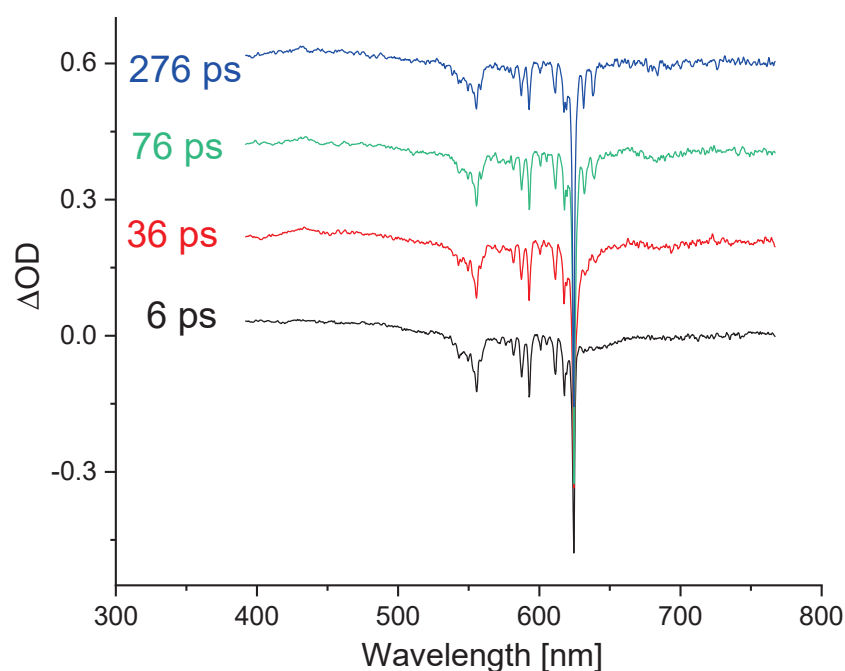


Figure 7. TA spectra of Pc in methane at 30 K recorded as a function of the delay time.

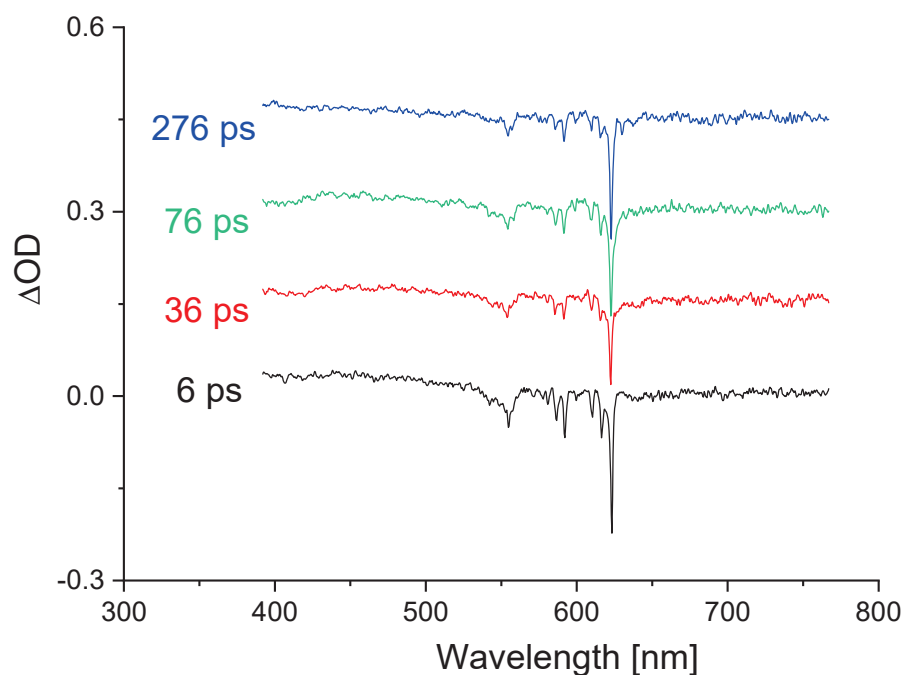


Figure 8. TA spectra of Pc in krypton at 5.2 K recorded as a function of the delay time.

TA spectra were also obtained for Pc embedded in solid krypton (Figure 8). Here, the situation is different: the stimulated emission is practically not observed, except perhaps for very weak signals at 276 ps delay. We attribute the lack of the signal to the heavy atom effect of the matrix, leading to enhanced intersystem crossing to the triplet state, which results in the efficient quenching of fluorescence. Our unpublished data for Pc in xenon reveal nearly 100% triplet formation efficiency.

4. Summary

The time-resolved fluorescence and transient absorption spectra obtained for porphycene embedded in low-temperature argon and methane matrices indicated that S_1

relaxation, involving the outflow of energy from a chromophore photoexcited to high above S_1 , can be as slow as tens or even more than a hundred picoseconds. The relaxation kinetics is significantly dependent on the type of matrix, being considerably faster in solid methane than in argon. At least two factors may be responsible for this difference: (i) the presence of molecular vibrations in methane that can act as energy accepting modes; (ii) the different phonon characteristics of the two matrices. The relaxation kinetics is different for different spectral regions, reflecting the complicated nature of relaxation dynamics. We believe that these experimental data may provide a good starting point for theoretical simulations of intra- and intermolecular energy relaxation processes. What makes porphycene a good candidate for such studies is the fact that the vibrational structure of this molecule is well known for both S_0 and S_1 electronic states [31–33].

Author Contributions: Conceptualization, J.D. and J.W.; investigation, J.D., I.V.S. and A.G.; writing—original draft preparation, J.W.; writing—review and editing, J.D. and A.G. All authors have read and agreed to the published version of the manuscript.

Funding: This work was supported by the Polish National Science Center (grant 2016/22/A/ST4/00029).

Data Availability Statement: Data are contained within the article.

Conflicts of Interest: The authors declare no conflict of interest.

References

- Baskin, J.S.; Yu, H.Z.; Zewail, A.H. Ultrafast Dynamics of Porphyrins in the Condensed Phase: I. Free Base Tetraphenylporphyrin. *J. Phys. Chem. A* **2002**, *106*, 9837–9844. [CrossRef]
- Yu, H.Z.; Baskin, J.S.; Zewail, A.H. Ultrafast Dynamics of Porphyrins in the Condensed Phase: II. Zinc Tetraphenylporphyrin. *J. Phys. Chem. A* **2002**, *106*, 9845–9854. [CrossRef]
- Li, X.; Gong, C.; Gurzadyan, G.G.; Gelin, M.F.; Liu, J.; Sun, L. Ultrafast Relaxation Dynamics in Zinc Tetraphenylporphyrin Surface-Mounted Metal Organic Framework. *J. Phys. Chem. C* **2018**, *122*, 50–61. [CrossRef]
- Gurzadyan, G.G.; Tran-Thi, T.H.; Gustavsson, T. Time-Resolved Fluorescence Spectroscopy of High-Lying Electronic States of Zn-Tetraphenylporphyrin. *J. Chem. Phys.* **1998**, *108*, 385–388. [CrossRef]
- Akimoto, S.; Yamazaki, T.; Yamazaki, I.; Osuka, A. Excitation Relaxation of Zinc and Free-Base Porphyrin Probed by Femtosecond Fluorescence Spectroscopy. *Chem. Phys. Lett.* **1999**, *309*, 177–182. [CrossRef]
- Ghosh, M.; Mora, A.K.; Nath, S.; Chandra, A.K.; Hajra, A.; Sinha, S. Photophysics of Soret-Excited Free Base Tetraphenylporphyrin and Its Zinc Analog in Solution. *Spectrochim. Acta A Mol. Biomol. Spectrosc.* **2013**, *116*, 466–472. [CrossRef]
- Enescu, M.; Steenkeste, K.; Tfibel, F.; Fontaine-Aupart, M.-P. Femtosecond Relaxation Processes from Upper Excited States of Tetrakis(N-Methyl-4-Pyridyl)Porphyrins Studied by Transient Absorption Spectroscopy. *Phys. Chem. Chem. Phys.* **2002**, *4*, 6092–6099. [CrossRef]
- Karolczak, J.; Kowalska, D.; Lukaszewicz, A.; Maciejewski, A.; Steer, R.P. Photophysical Studies of Porphyrins and Metalloporphyrins: Accurate Measurements of Fluorescence Spectra and Fluorescence Quantum Yields for Soret Band Excitation of Zinc Tetraphenylporphyrin. *J. Phys. Chem. A* **2004**, *108*, 4570–4575. [CrossRef]
- Lukaszewicz, A.; Karolczak, J.; Kowalska, D.; Maciejewski, A.; Ziolk, M.; Steer, R.P. Photophysical Processes in Electronic States of Zinc Tetraphenyl Porphyrin Accessed on One- and Two-Photon Excitation in the Soret Region. *Chem. Phys.* **2007**, *331*, 359–372. [CrossRef]
- Mataga, N.; Shibata, Y.; Chosrowjan, H.; Yoshida, N.; Osuka, A. Internal Conversion and Vibronic Relaxation from Higher Excited Electronic State of Porphyrins: Femtosecond Fluorescence Dynamics Studies. *J. Phys. Chem. B* **2000**, *104*, 4001–4004. [CrossRef]
- Liu, X.; Yeow, E.K.L.; Velate, S.; Steer, R.P. Photophysics and Spectroscopy of the Higher Electronic States of Zinc Metalloporphyrins: A Theoretical and Experimental Study. *Phys. Chem. Chem. Phys.* **2006**, *8*, 1298–1309. [CrossRef] [PubMed]
- Venkatesh, Y.; Venkatesan, M.; Ramakrishna, B.; Bangal, P.R. Ultrafast Time-Resolved Emission and Absorption Spectra of Meso-Pyridyl Porphyrins Upon Soret Band Excitation Studied by Fluorescence up-Conversion and Transient Absorption Spectroscopy. *J. Phys. Chem. B* **2016**, *120*, 9410–9421. [CrossRef] [PubMed]
- Rodriguez, J.; Holten, D. Ultrafast Vibrational Dynamics of a Photoexcited Metalloporphyrin. *J. Chem. Phys.* **1989**, *91*, 3525–3531. [CrossRef]
- Rodriguez, J.; Kirmaier, C.; Holten, D. Time-Resolved and Static Optical Properties of Vibrationally Excited Porphyrins. *J. Chem. Phys.* **1991**, *94*, 6020–6029. [CrossRef]
- Kumble, R.; Palese, S.; Lin, V.S.Y.; Therien, M.J.; Hochstrasser, R.M. Ultrafast Dynamics of Highly Conjugated Porphyrin Arrays. *J. Am. Chem. Soc.* **1998**, *120*, 11489–11498. [CrossRef]
- Abraham, B.; Nieto-Pescador, J.; Gundlach, L. Ultrafast Relaxation Dynamics of Photoexcited Zinc-Porphyrin: Electronic-Vibrational Coupling. *J. Phys. Chem. Lett.* **2016**, *7*, 3151–3156. [CrossRef]

17. Morandeira, A.; Vauthey, E.; Schuwey, A.; Gossauer, A. Ultrafast Excited State Dynamics of Tri- and Hexaporphyrin Arrays. *J. Phys. Chem. A* **2004**, *108*, 5741–5751. [CrossRef]
18. Kullmann, M.; Hipke, A.; Nuernberger, P.; Bruhn, T.; Götz, D.C.G.; Sekita, M.; Guldi, D.M.; Bringmann, G.; Brixner, T. Ultrafast Exciton Dynamics after Soret- or Q-Band Excitation of a Directly B,B'-Linked Bisporphyrin. *Phys. Chem. Chem. Phys.* **2012**, *14*, 8038–8050. [CrossRef]
19. Shi, Y.; Liu, J.-Y.; Han, K.-L. Investigation of the Internal Conversion Time of the Chlorophyll a from S_3, S_2 to S_1 . *Chem. Phys. Lett.* **2005**, *410*, 260–263. [CrossRef]
20. Białkowski, B.; Stepanenko, Y.; Nejbauer, M.; Radzewicz, C.; Waluk, J. The Dynamics and Origin of the Unrelaxed Fluorescence of Free-Base Tetraphenylporphyrin. *J. Photochem. Photobiol. A* **2012**, *234*, 100–106. [CrossRef]
21. Marcelli, A.; Foggi, P.; Moroni, L.; Gellini, C.; Salvi, P.R. Excited-State Absorption and Ultrafast Relaxation Dynamics of Porphyrin, Diprotonated Porphyrin, and Tetraoxaporphyrin Dication. *J. Phys. Chem. A* **2008**, *112*, 1864–1872. [CrossRef]
22. Bondybey, V.E.; Milton, S.V.; English, J.H.; Rentzepis, P.M. Spectroscopic and Picosecond Time-Resolved Studies of Vibrational Relaxation in Naphthazarine in Solid Neon. *Chem. Phys. Lett.* **1983**, *97*, 130–134. [CrossRef]
23. Bondybey, V.E.; Haddon, R.C.; English, J.H. Fluorescence and Phosphorescence of 9-Hydroxyphenalenone in Solid Neon and Its Hydrogen Tunneling Potential Function. *J. Chem. Phys.* **1984**, *80*, 5432–5437. [CrossRef]
24. Huppert, D.; Bondybey, V.E.; Rentzepis, P.M. Single Excited Vibrational Level Lifetimes and Energy Dissipation Channels of Large Molecules in Inert Matrixes. *J. Phys. Chem.* **1985**, *89*, 5811–5815. [CrossRef]
25. Dobkowski, J.; Galievsky, V.; Gil, M.; Waluk, J. Time-Resolved Fluorescence Studies of Porphycene Isolated in Low-Temperature Gas Matrices. *Chem. Phys. Lett.* **2004**, *394*, 410–414. [CrossRef]
26. Dobkowski, J.; Galievsky, V.; Waluk, J. Relaxation in Excited States of Porphycene in Low-Temperature Argon and Nitrogen Matrices. *Chem. Phys. Lett.* **2000**, *318*, 79–84. [CrossRef]
27. Dobkowski, J.; Lobko, Y.; Gawinkowski, S.; Waluk, J. Energy Relaxation Paths in Matrix-Isolated Excited Molecules: Comparison of Porphycene with Dibenzoporphycenes. *Chem. Phys. Lett.* **2005**, *416*, 128–132. [CrossRef]
28. Dobkowski, J.; Galievsky, V.; Starukhin, A.; Vogel, E.; Waluk, J. Spectroscopy and Photophysics of Tetraalkyldibenzoporphycenes. *J. Phys. Chem. A* **1998**, *102*, 4966–4971. [CrossRef]
29. Dobkowski, J.; Galievsky, V.A.; Jasny, J.; Sazanovich, I.V. Time-Resolved Emission Spectroscopy of Pyrene Derivatives. *Pol. J. Chem.* **2004**, *78*, 961–972.
30. Gil, M.; Gorski, A.; Starukhin, A.; Waluk, J. Fluorescence Studies of Porphycene in Various Cryogenic Environments. *Low Temp. Phys.* **2019**, *45*, 656–662. [CrossRef]
31. Starukhin, A.; Vogel, E.; Waluk, J. Electronic Spectra in Porphycenes in Rare Gas and Nitrogen Matrices. *J. Phys. Chem. A* **1998**, *102*, 9999–10006. [CrossRef]
32. Gawinkowski, S.; Walewski, Ł.; Vdovin, A.; Slenczka, A.; Rols, S.; Johnson, M.R.; Lesyng, B.; Waluk, J. Vibrations and Hydrogen Bonding in Porphycene. *Phys. Chem. Chem. Phys.* **2012**, *14*, 5489–5503. [CrossRef] [PubMed]
33. Mengesha, E.T.; Sepioł, J.; Borowicz, P.; Waluk, J. Vibrations of Porphycene in the S_0 and S_1 Electronic States: Single Vibronic Level Dispersed Fluorescence Study in a Supersonic Jet. *J. Chem. Phys.* **2013**, *138*, 174201. [CrossRef] [PubMed]

Article

Water Clusters in Interaction with Corannulene in a Rare Gas Matrix: Structures, Stability and IR Spectra

Heloïse Leboucher¹, Joëlle Mascetti², Christian Aupetit², Jennifer A. Noble³ and Aude Simon^{1,*}

¹ Laboratoire de Chimie et Physique Quantiques (LCPQ), Fédération FeRMI, UMR5626, Université de Toulouse [UT3] & CNRS, University Paul Sabatier, 118 Route de Narbonne, 31062 Toulouse, France; heloise.leboucher@irsamc.ups-tlse.fr

² Institut des Sciences Moléculaires (ISM), Université de Bordeaux, UMR5255 CNRS, 351 Cours de la Libération, CEDEX, 33405 Talence, France; joelle.mascetti@u-bordeaux.fr (J.M.); christian.aupetit@u-bordeaux.fr (C.A.)

³ Laboratoire Physique des Interactions Ioniques et Moléculaires (PIIM), UMR7345, CNRS, Aix-Marseille Université, 13013 Marseille, France; jennifer.noble@univ-amu.fr

* Correspondence: aude.simon@irsamc.ups-tlse.fr

Abstract: The interaction of polycyclic aromatic hydrocarbons (PAHs) with water is of paramount importance in atmospheric and astrophysical contexts. We report here a combined theoretical and experimental study of corannulene-water interactions in low temperature matrices and of the matrix's influence on the photoreactivity of corannulene with water. The theoretical study was performed using a mixed density functional based tight binding/force field approach to describe the corannulene-water clusters trapped in an argon matrix, together with Born-Oppenheimer molecular dynamics to determine finite-temperature IR spectra. The results are discussed in the light of experimental matrix isolation FTIR spectroscopic data. We show that in the solid phase, π isomers of $(C_{20}H_{10})(H_2O)_n$, with $n = 2$ or 3, are energetically favored. These π complexes are characterized by small shifts in corannulene vibrational modes and large shifts in water bands. These π structures, particularly stable in the case of the water trimer where the water cluster is trapped "inside" the corannulene bowl, may account for the difference in photoreactivity of non-planar—compared to planar—PAHs with water. Indeed, planar PAHs such as pyrene and coronene embedded in $H_2O:Ar$ matrices form σ isomers and react with water to form alcohols and quinones under low energy UV irradiation, whereas no photoreactivity was observed for corannulene under the same experimental conditions.

Keywords: PAHs; astrochemistry; matrix isolation FTIR spectroscopy; water clusters; corannulene; DFTB; BOMD

Citation: Leboucher, H.; Mascetti, J.; Aupetit, C.; Noble, J.A.; Simon, A. Water Clusters in Interaction with Corannulene in a Rare Gas Matrix: Structures, Stability and IR Spectra. *Photochem* **2022**, *2*, 237–262. <https://doi.org/10.3390/photochem2020018>

Received: 1 March 2022

Accepted: 23 March 2022

Published: 25 March 2022

Publisher's Note: MDPI stays neutral with regard to jurisdictional claims in published maps and institutional affiliations.



Copyright: © 2022 by the authors. Licensee MDPI, Basel, Switzerland. This article is an open access article distributed under the terms and conditions of the Creative Commons Attribution (CC BY) license (<https://creativecommons.org/licenses/by/4.0/>).

1. Introduction

The interaction of polycyclic aromatic hydrocarbons (PAHs) with water is of paramount importance in a large number of fields, such as the petroleum industry [1], atmospheric science [2,3], astrophysics and astrochemistry. Due to its allotropy, a large fraction of interstellar carbon is expected to be included in large molecules or in dust grains with various degrees of organization and aromaticity, including fullerenes, diamondoids, PAHs, clusters of PAHs, or amorphous carbon grains, possibly hydrogenated [4]. AstroPAHs in particular are believed to be present in the interstellar medium (ISM), where they account for up to 20% of the total carbon [5,6]. PAHs have been of significant interest since the proposal in the eighties that they were the carriers of the Aromatic Infrared Bands (AIBs), a set of mid-IR emission bands observed in many regions of the ISM [7,8]. This proposal led to many experimental and theoretical spectroscopic studies in order to identify a specific PAH molecule [6]. However, it is only very recently that specific PAH molecules, the two isomers of cyano-naphthalene, have been successfully detected based on their rotational spectra [9].

In interstellar cold dense molecular clouds, where the temperature ranges from 10 to 50 K, PAHs are expected to be frozen on or in icy mantles of dust grains [10]. These ice

mantles are mainly composed of amorphous solid water (ASW), and allow chemical reactions to occur after heating or irradiation [11]. It has been shown that PAHs embedded in ASW, when irradiated by VUV light, undergo erosion processes and lead to oxidation products such as alcohols and ketones [12] via the formation of cationic intermediates. Interestingly, the formation of oxygenated PAHs is also observed in ASW when using low energy UV-visible irradiation [13–16]. It has also been shown that small complexes of coronene and water isolated in cryogenic argon matrices exhibit photochemical reactions similar to those observed in ASW [17]. We have previously demonstrated that, when embedded in a solid matrix, coronene forms σ complexes with water molecules arranged in interaction with the edge of the planar PAH [18]. Such σ interaction is expected to favor photochemical reaction through better H/charge transfer to form oxidation products from planar PAHs [17,19]. These results suggest that a relatively easy formation of oxygenated PAH photoproducts could account for shifts observed in the AIBs.

In this work, we present some experimental and theoretical results concerning corannulene $C_{20}H_{10}$ in interaction with water clusters embedded in a rare gas matrix. Corannulene is a fully aromatic non-planar PAH [20] of C_{5v} symmetry, consisting of a five membered carbon cycle surrounded by five six-membered carbon cycles that can be described as a bowl-like molecule with two faces: convex and concave (see Figure 1).

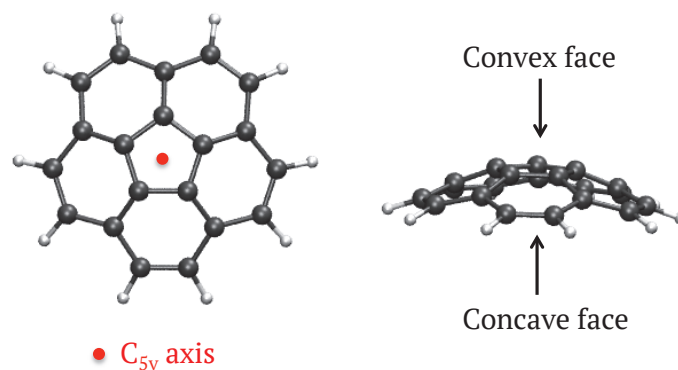


Figure 1. Scheme of corannulene $C_{20}H_{10}$, a hydrogenated cap of buckminsterfullerene of C_{5v} symmetry, top and side views.

Corannulene can be regarded as a cap of buckminsterfullerene C_{60} —a molecule that was identified in Space more than 10 years ago [21,22]—saturated with H atoms. It can thus reasonably be considered as a possible intermediate in “top-down” or “bottom-up” routes leading to C_{60} formation. The mechanism for the formation of buckminsterfullerene C_{60} is still under debate. Following its discovery, observational studies suggested that fullerenes could be produced by photochemical dehydrogenation and isomerisation of amorphous carbon grains [23–26], but the composition of such grains remains elusive. Among current hypotheses, buckminsterfullerene could be formed following decay and rearrangement of dehydrogenated PAHs [27] under the action of UV photons [28] or by collisions with energetic particles [29]. Such a “top-down” mechanism is expected to prevail in low-density environments such as interstellar clouds [30] and the corannulene molecule can be regarded as a possible intermediate in such a sequence. Alternatively, a “bottom-up” mechanism, consisting of the successive growth from smaller carbon chain building blocks, known as the closed network growth mechanism [31], would prevail in the hot, dense envelopes of evolved stars [30]. The need to characterize the structural diversity of carbon clusters, possibly hydrogenated and with amorphous character, that could play a role in the formation of buckminsterfullerene, motivated the development of dedicated experimental and theoretical approaches in order to obtain their spectral features in the UV-visible [32,33] and IR domains [34–37].

Because of its bowl shape, corannulene could be detected in astrophysical environments by radioastronomy, as put forward by Pilleri et al. [38]. The astrophysical interest of corannulene has also motivated experimental and theoretical spectroscopic studies in the IR, Raman and UV-visible domains [39], both in the solid phase and, in particular, in rare

gas matrices [39], in order to propose spectroscopic characteristics that should be searched for in space. Recently, its formation in the gas phase was achieved by Zhao et al. [40] using a “bottom-up” approach involving the reaction of 7-fluoranthenyl ($C_{16}H_9$) and benzo[ghi]fluoranthen-5-yl ($C_{18}H_9$) radicals with acetylene (C_2H_2) in conditions mimicking those of carbon-rich circumstellar envelopes. Interestingly, due to its bowl shape that can invert and form host-guest complexes, corannulene also presents a particularly interesting building block in materials chemistry [41].

Studies on the structures, energetics and spectroscopic signatures of corannulene-water complexes are, to the best of our knowledge, scarce. Theoretical studies of water clusters $(H_2O)_n$ in interaction with $[C_{20}H_{10}]^+$ were performed by Hernández-Rojas et al. [42]. Global optimization using a force field approach was used to determine the geometries of the larger clusters. They showed that, for $n = 1$ and 2, the water cluster preferentially binds to the side of $[C_{20}H_{10}]^+$, whereas larger sized water clusters interact preferentially with the concave face of cationic corannulene. Gas phase neutral corannulene-water complexes have been studied by Pérez et al. [43] using rotational spectroscopy complemented by *ab initio* calculations. They have shown that in $(C_{20}H_{10})(H_2O)$, the water molecule resides inside the bowl-like structure of corannulene, where it rotates freely around the C_5 axis and that dispersion interactions represent the main contribution to the binding. We have decided to investigate $(C_{20}H_{10})(H_2O)_n$ complexes isolated in argon matrices at 10 K. Our results are compared to those obtained in the gas phase [43] and to our previous study on coronene:water complexes. We detail our theoretical and experimental approaches in Section 2, report our results in Section 3, and discuss the experimental results in light of the calculations in Section 4.

2. Materials and Methods

2.1. Computational Methods

In order to determine the structures, energetics and IR spectra of $(C_{20}H_{10})(H_2O)_n$ ($n = 1-3$) embedded in an argon matrix, (hereafter quoted as: Ar) we used the same approach as that previously applied to coronene-water clusters $(C_{24}H_{12})(H_2O)_n$ ($n = 1, 2$) [18]. All calculations were performed with the deMonNano code [44].

The electronic structure of $(C_{20}H_{10})(H_2O)_n$ is described at the self consistent charge density functional based tight binding (SCC-DFTB) level of theory [45] using the Hamiltonian that we modified so as to obtain a good description of PAH-water interactions and used to describe coronene:water aggregates in an Ar matrix [18]. Briefly, an empirical dispersion term was added and the Mulliken charges were replaced by Truhlar Charge Model 3 (CM3) charges [46] in order to improve the description of the polarisation of the bonds. The latter modification revealed important for the description of long range electrostatic interactions [47,48] and for IR spectra [49,50]. This modified SCC-DFTB scheme (denoted hereafter simply as DFTB) was benchmarked against wavefunction and DFT calculations [48,51]. It was shown to provide a good description of the structures and energetics of water clusters and PAHs in interaction with water clusters [48,51,52]. The values of the DFTB shifts induced by the adsorption of PAHs determined for the IR bands of water-ice dangling OH were shown to be in good agreement with experimental data [53]. Focusing more specifically on corannulene:water, when optimising the structure of $(C_{20}H_{10})(H_2O)$ at the DFTB level, we found that the most stable structure was similar to that found by Pérez et al. [43] in the gas phase, i.e., with the water molecule interacting with the concave face of corannulene. We computed a DFTB intermolecular binding energy of $-21 \text{ kJ}\cdot\text{mol}^{-1}$ (without zero-point energy) which is in very good agreement with the binding energy of $-22.40 \text{ kJ}\cdot\text{mol}^{-1}$ determined using symmetry adapted perturbation theory (SAPT) analysis [43]. Besides, additional comparison between gas phase DFTB and DFT structures, energetics and IR spectra for isolated corannulene:water clusters was made (see data base associated to the present paper), revealing similar trends as for benzene:water and coronene:water clusters [48].

The argon-argon interaction is described at the force field (FF) level using the Aziz potential [54]. The DFTB/FF coupling is incorporated via a scheme close to first order degenerate perturbation theory and developed to describe clusters of hydrocarbons and water

trapped inside a rare gas matrix [55,56]. This DFTB/FF scheme was carefully benchmarked for PAH:H₂O:Ar systems, i.e., involving the same interactions as in this work, regarding structures, energetics and IR spectra [18,55,56]. In this work, the Ar matrix is modeled by a large cluster (1139 Ar atoms for the total pure Ar matrix) organised in a face cubic centered (fcc) crystalline structure at the center of which the impurity ((C₂₀H₁₀)(H₂O)_n) is inserted after removing a minimal number *x* of Ar atoms (*x* is the vacancy size). In the rest of the manuscript, the total system will be referred to as (C₂₀H₁₀)(H₂O)_n:Ar.

To obtain the initial geometries, several symmetry planes were considered for inserting the corannulene molecule into the matrix. After determining the most stable situation for the embedded corannulene, all the possible interaction sites of the water molecule with C₂₀H₁₀ were considered. For *n* = 1, the substitution of one Ar atom by one water molecule was considered for all Ar atoms interacting with the concave and convex faces of corannulene as well as in the [111] insertion layer of corannulene when Ar atoms interact with the H atoms of corannulene. Once the most stable geometries for the three situations are determined, the substitution of all possible Ar atoms interacting with the water monomer in the most stable (C₂₀H₁₀)(H₂O)_n:Ar systems by another water molecule are considered. The most stable situations where the dimer interacts with the concave face, convex face, and “in plane” H atoms of corannulene are retained and the interaction of a third water molecule with the existing dimer is considered. Local geometry optimisations are then performed and the relative stabilities of the determined isomers are estimated by comparison of their substitution energy values (*E_{sub}*, defined in ref. [18]) determined as follows: *E_{sub}* is equal to the energy of the optimised total system (*E*(C₂₀H₁₀)(H₂O)_n:Ar) plus the energy of the vacancy (*E*(Ar_{*x*})) minus the energy of the optimised total matrix (*E*(:Ar)) minus the energy of the isolated monomers (*E*(C₂₀H₁₀) + *nE*(H₂O)), i.e.,

$$E_{sub} = E((C_{20}H_{10})(H_2O)_n : Ar) + E(Ar_x) - E(: Ar) - E(C_{20}H_{10}) - nE(H_2O) \quad (1)$$

The IR spectra of the most stable (lowest value of *E_{sub}*) energy structures for all water cluster sizes in all three configurations in which the water cluster interacts with the concave face, convex face and “in plane” H atoms were first computed in the harmonic approximation. However, finite-temperature effects due to the anharmonicity of the PES may be expected even at low temperature. In this case, an *a priori* more suitable approach is to derive IR spectra from molecular dynamics (MD) simulations computing the Fourier transform of the dipole moment μ autocorrelation function

$$\alpha(\omega) \propto \omega^2 \int_0^{+\infty} dt \langle \mu(0) \cdot \mu(t) \rangle e^{i\omega t} \quad (2)$$

Therefore we used the same approach as in the work by Simon et al. [18], consisting in performing Born-Oppenheimer MD (BOMD) simulations in the microcanonical ensemble, computing the electronic structure on-the-fly with the DFTB/FF method. The IR absorption cross sections are determined using Equation (2) with the electrostatic dipole moment computed using the CM3 charges of the corannulene:water clusters, the Ar atoms remaining neutral. The positions of the Ar atoms at the surface of the cluster are frozen to ensure the absence of surface Ar atom motions in the molecular dynamics. The system was first thermalised at the desired temperature (10 K) by means of short simulations (10 ps) in the canonical ensemble using a Nose-Hoover chain of thermostats. These first (NVT) simulations allow the generation of the initial conditions for MD simulations performed in the microcanonical ensemble (NVE). For each corannulene-water cluster, 7 MD simulations of 100 ps in the (NVE) ensemble were run, using a time step of 0.1 fs. The IR spectra were computed for each simulation and averaged. In such conditions (low temperature), convergence is expected on positions but not necessarily on intensities [18], which was checked for the specific systems studied in the present work (see Appendix B, Figure A1). In addition, the quality of the dynamic IR spectra inside the Ar matrix was checked for the water monomer and dimer which, as will be discussed in Section 3.1.2, rotate in the matrix,

increasing the simulation time from 100 ps to 500 ps (see Appendix B, Figure A2). Due to the large number of large systems to be investigated consistently, we used the systematic procedure described hereabove (7×100 ps) for all of them.

2.2. Experimental Methods

Experiments were performed in a high vacuum experimental setup consisting of a stainless steel chamber with a base pressure of 10^{-7} mbar, containing a CsBr substrate cooled to 10 K by a closed-cycle He cryostat (Cryophysics Cryodine). The sample temperature was monitored by a Si diode thermometer positioned on the copper substrate holder in proximity to the CsBr window. Deionised ultrapure water was subjected to multiple freeze-pump-thaw cycles under vacuum to remove dissolved gases. Argon and water were premixed in a dosing line with concentrations of water in argon varying from 1:10 to 1:1 and injected into the chamber at a rate of 1 mL min^{-1} in order to form different mixtures containing H_2O monomers, dimers, trimers, and larger clusters up to hexamers. Corannulene (TCI, 97%, used without purification) was sublimated by heating the powder to 120°C in an oven within the high vacuum chamber and co-deposited with the argon:water mixture which was introduced as a diffusion jet flow via a gas nozzle inlet located 2 cm from the CsBr substrate. Depositions lasted for between one and two hours. Infrared spectra of corannulene: H_2O :Ar samples were recorded in transmission mode using a Bruker 70 V FTIR spectrometer with a DTGS detector from 4000 to 400 cm^{-1} at a 0.5 cm^{-1} resolution, with each spectrum averaged over 200 scans. Reference spectra of corannulene:Ar and H_2O :Ar at different concentrations were also recorded for comparison. All spectra were recorded at 10 K. Depositions were irradiated at 10 K with a mercury lamp ($\lambda > 235 \text{ nm}$, average power 150 mW, total fluence 0.72 J m^{-2}), and IR spectra measured after a series of irradiations (from 1 to 120 min).

3. Results

3.1. Computational Results: Influence of the Matrix

3.1.1. Structures and Energetics

Corannulene was inserted in different symmetry planes of the Ar matrix represented by a finite size fcc cluster initially of 1139 Ar atoms. After removing the minimum number of Ar atoms we found that the most stable situation corresponded to an insertion of the corannulene molecule in the [111] plane with a vacancy of 7 Ar atoms (see Figure 2, $E_{\text{sub}} = -2470 \text{ cm}^{-1}$, also see Appendix A, Table A1 for the results of the other symmetry planes). We obtained the same result as for coronene [18] and other PAHs such as naphthalene [57]. The substitution energy is smaller than that computed for coronene using the same model ($E_{\text{sub}} = -4810 \text{ cm}^{-1}$ [18]) which can be understood as the non planarity of corannulene leads to more perturbation of the Ar layers close to corannulene.

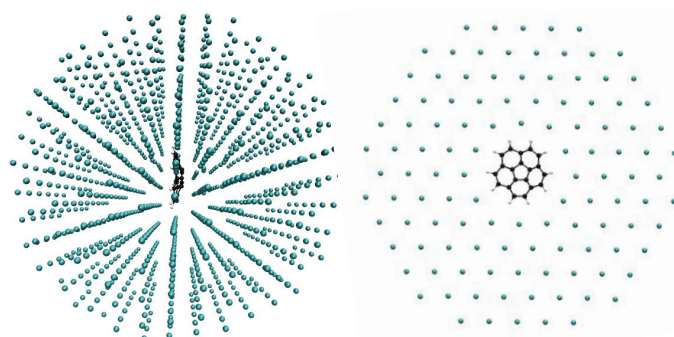


Figure 2. Optimised structure of $\text{C}_{20}\text{H}_{10}:\text{Ar}$ obtained at the DFTB/FF level of theory. The total system is reported on the left hand side, the selection of the [111] plane where corannulene is inserted is represented on the right hand side.

In Table 1 are reported the substitution energies obtained using Equation (1) for the most stable isomers of $(\text{C}_{20}\text{H}_{10})(\text{H}_2\text{O})_n:\text{Ar}$ ($n = 1-3$) of different types i.e., depending

whether the water molecules interact with the concave or convex faces of corannulene or with its H atoms. The geometries of the most stable isomers are reported in Figures 3–5 for $n = 1, 2$ and 3 respectively.

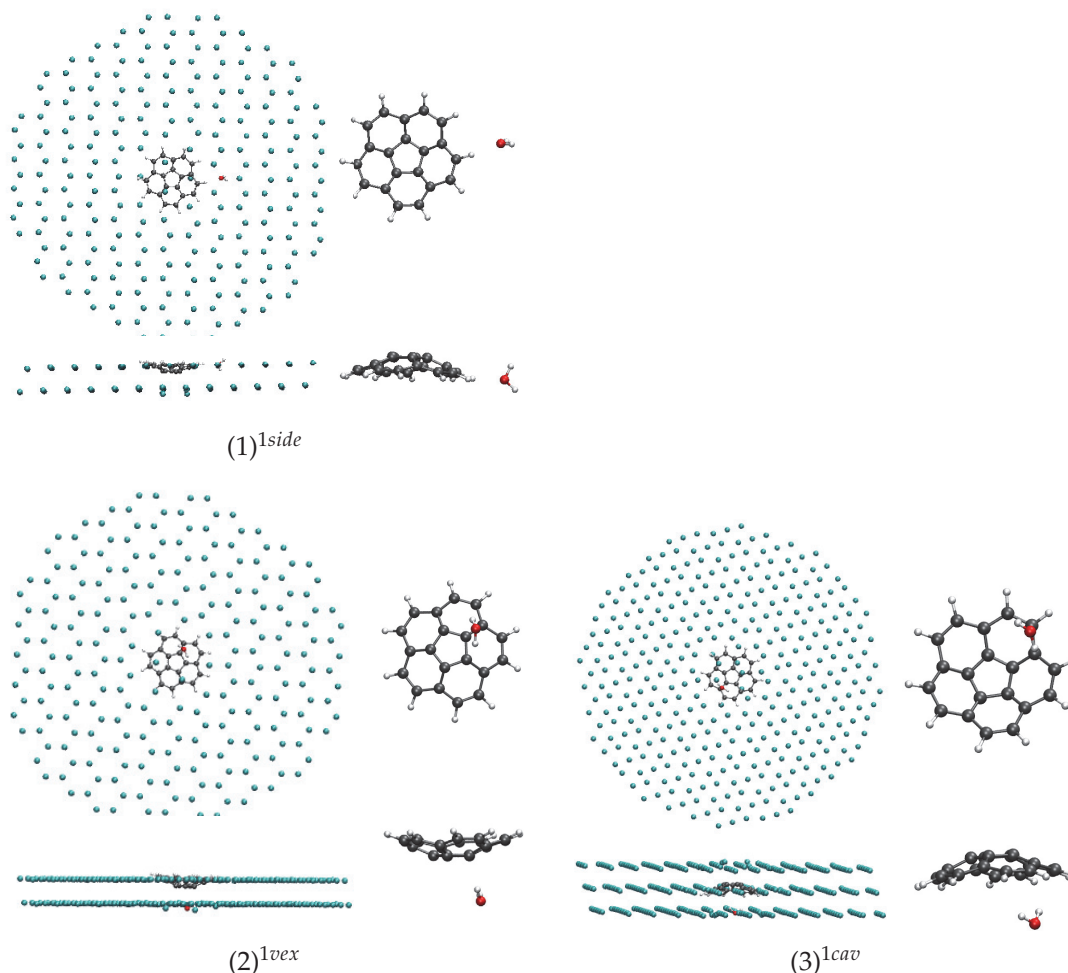


Figure 3. Most stable structures for $(C_{20}H_{10})(H_2O):Ar$ obtained at the DFTB/FF level of theory (selection of layers).

In the case of $n = 1$, the three conformers (1)^{1side}, (2)^{1vex} and (3)^{1cav} lie in an energy range of 150 cm^{-1} ($1.8\text{ kJ}\cdot\text{mol}^{-1}$), the most stable one corresponding to the water molecule interacting with an H atom of corannulene in the [111] symmetry plane ((1)^{1side}). Interestingly, the conformer in which the water molecule interacts with the concave face, known to be the most stable isomer in the gas phase [43], is the highest energy one ((3)^{1cav}), although the energy difference is small. These subtle differences from the gas phase originate from the constraints of the fcc lattice. For instance, in the (3)^{1cav} isomer, the water molecule substitutes an Ar atom whose position is not aligned with the C_{5V} axis of corannulene, and this prevents the water molecule from having the most stabilizing interaction with the corannulene as in the gas phase. When relaxing the geometry of this isomer after removing the matrix environment, the water molecule migrates towards the center of the “cup” and becomes the lowest energy isomer (see last column of Table 1).

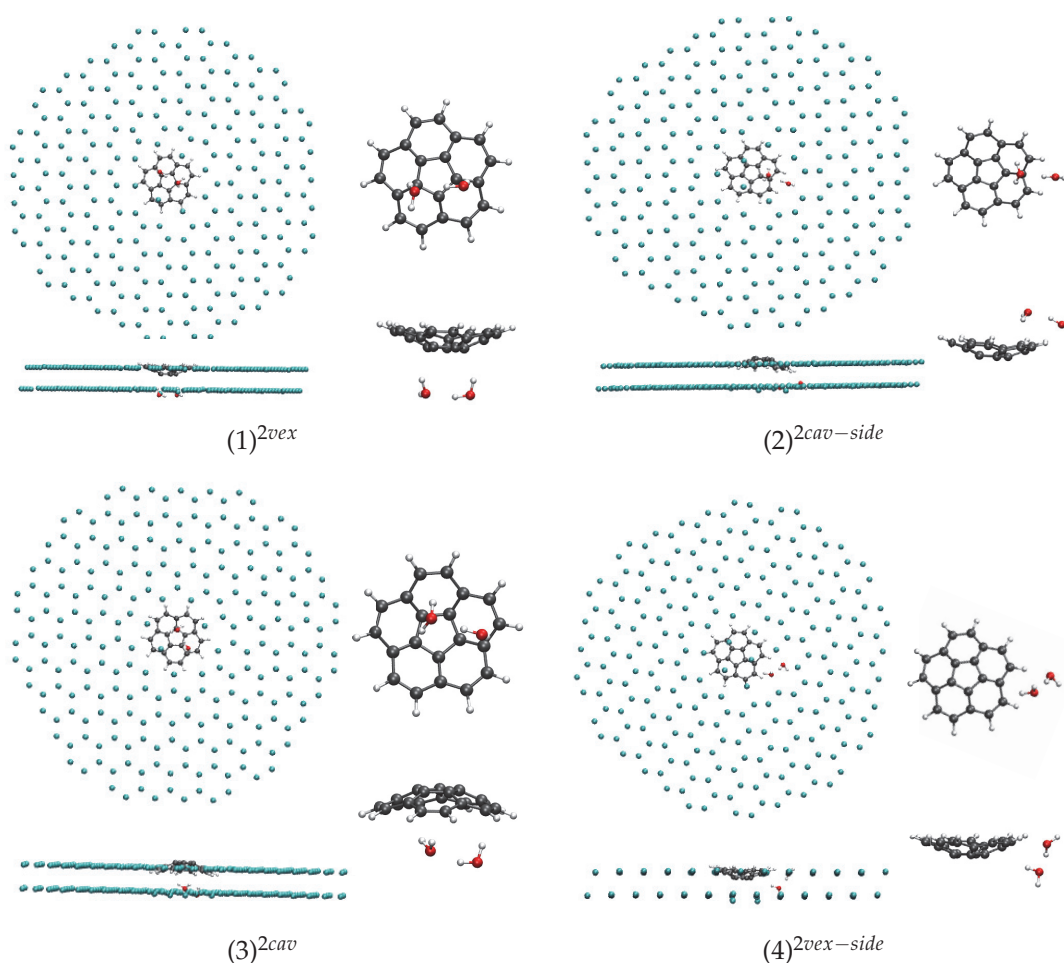


Figure 4. Most stable structures for $(C_{20}H_{10})(H_2O)_2:Ar$ obtained at the DFTB/FF level of theory (selection of layers).

The perturbation of the [111] Ar layers adjacent to that containing corannulene due to the presence of the impurity can be visualized on the side views of the systems in Figures 3–5, a few Ar atoms being moved out of their original plane. Now comparing with the results obtained for coronene ($C_{24}H_{12}$, planar PAH) inside an Ar matrix using the same computational approach, the isomer similar to the $(1)^{1side}$ isomer of the present work, designated as σ isomer in Simon et al. [18], was found more stable than the π isomer by $\sim 800\text{ cm}^{-1}$ in the case of coronene. This means that the stabilization of the “side” (or “ σ ”) isomer is enhanced in the case of a planar PAH with respect to the case of corannulene where it appears in competition with the two “ π ” isomers $(2)^{1vex}$ and $(3)^{1cav}$.

In the case of $n = 2$, the most stable isomer corresponds to the water dimer interacting through two H atoms with the convex face of corannulene ($(1)^{2vex}$, see Figure 4), the two H atoms pointing towards two central C atoms of corannulene. The corresponding isomer in which the water dimer interacts with the concave face of corannulene ($(3)^{2conv}$) is found 210 cm^{-1} (or $2.5\text{ kJ}\cdot\text{mol}^{-1}$) higher in energy. The isomer in which the water dimer interacts with both the concave (resp. convex) face and side H of corannulene is found 190 cm^{-1} or $2.3\text{ kJ}\cdot\text{mol}^{-1}$ (resp. 240 cm^{-1} or $2.9\text{ kJ}\cdot\text{mol}^{-1}$) higher in energy. As in the case of $n = 1$, when the geometries of $(C_{20}H_{10})(H_2O)_2$ are further relaxed after removal of the Ar matrix, the water dimer tends to move towards the center of the cup when it interacts with the concave face of corannulene and it leads to the stabilisation of such conformers (see last column of Table 1).

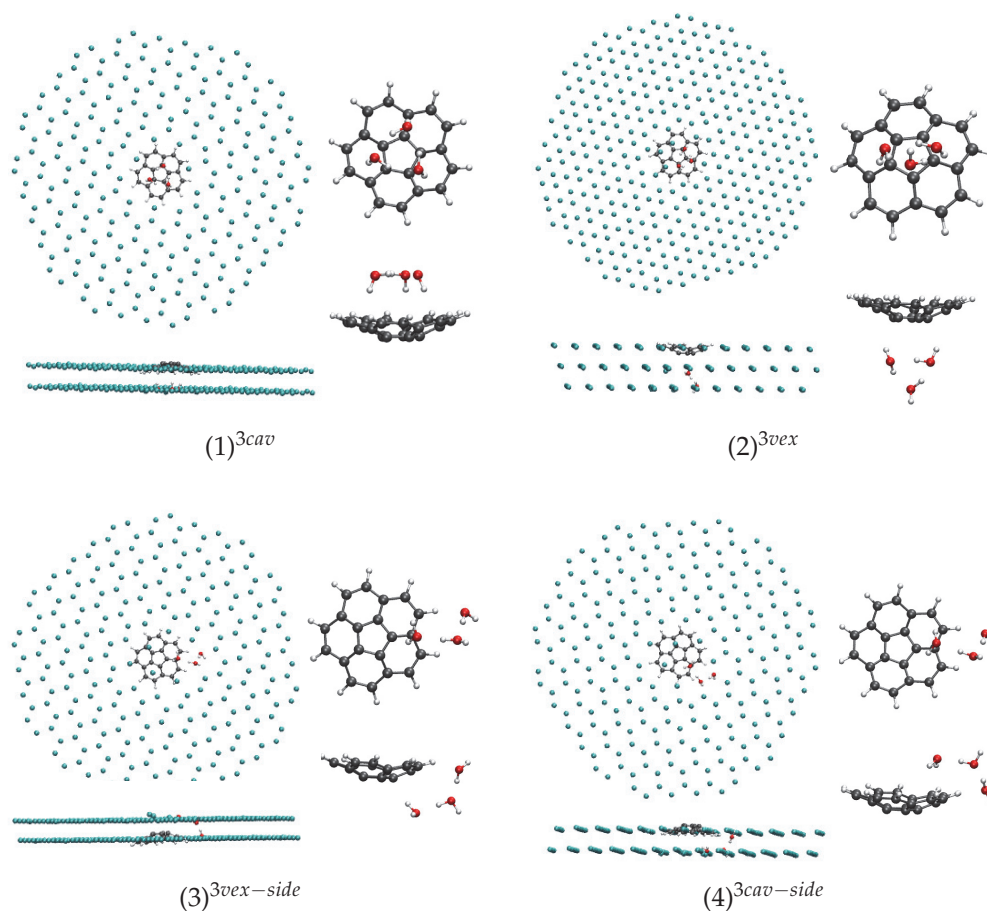


Figure 5. Most stable structures for $(C_{20}H_{10})(H_2O)_3:Ar$ obtained at the DFTB/FF level of theory (selection of layers).

Table 1. Substitution energies of the $(C_{20}H_{10})(H_2O)_n$ complexes ($n \leq 3$) and, for a given stoichiometry, relative energy with respect to the most stable system. In parenthesis are added the relative energy of the corresponding isolated $(C_{20}H_{10})(H_2O)_n$ aggregate (after removing the Ar matrix) after local DFTB geometry optimisation.

n_{H_2O}	Number of Atoms	Isomer	E_{sub} (cm^{-1})	ΔE ($kJ \cdot mol^{-1}$)
1	1164	(1) ^{1side}	−3590	0.0 (+10.3)
		(2) ^{1vex}	−3550	+0.5 (+7.5)
		(3) ^{1cav}	−3440	+1.8 (0.0)
2	1166	(1) ^{2vex}	−5890	0.0 (+16.5)
		(2) ^{2cav-side}	−5700	+2.3 (0.0)
		(3) ^{2cav}	−5680	+2.5 (+3.4)
		(4) ^{2vex-side}	−5650	+12.9 (+9.5)
3	1168	(1) ^{3cav}	−9200	0.0 (0.0)
		(2) ^{3vex}	−8860	+4.1 (+10.5)
		(3) ^{3vex-side}	−8610	+7.1 (+12.3)
		(4) ^{3cav-side}	−8420	+9.3 (+0.4)

In the case of $n = 3$, the isomer in which the water cyclic trimer, located in the [111] plane adjacent to that of corannulene, with its center approximately on the C_{5V} axis of corannulene, interacts with the concave face of corannulene through three H atoms ((1)^{3cav}, see Figure 5), is shown to be particularly stable with our model. Contrary to the smaller clusters ($n = 1, 2$), it is also the case after relaxation of the cluster after removing the Ar matrix as this conformer remains the most stable one in the gas phase. Next isomer, (2)^{3vex},

in which the cyclic trimer interacts with the convex face of corannulene through two H atoms, is found 340 cm^{-1} higher in energy. The next two isomers in which the water trimer adopts a “linear form” interacting with both one face (convex or concave) and an H atom of corannulene, namely the $(3)^{3vex-side}$ and $(4)^{3cav-side}$ are found respectively 590 and 780 cm^{-1} (7.1 and $9.3\text{ kJ}\cdot\text{mol}^{-1}$) higher in energy than the stable $(1)^{3cav}$ isomer.

3.1.2. IR Spectra

This section reports the computed IR spectra of all the $(\text{C}_{20}\text{H}_{10})(\text{H}_2\text{O})_n:\text{Ar}$ isomers for $n = 1-3$ and the comparison with those of $\text{C}_{20}\text{H}_{10}$ and of the corresponding $(\text{H}_2\text{O})_n$ clusters determined at the same level of theory. These simulations aim at getting insights into the influence of the coordination site (concave, convex or side) and of the geometry of the water cluster (linear or cycle)—in the case of the trimer—on the IR spectrum of the water molecule/cluster and corannulene upon coordination. The values of the positions and the shifts of the bands of interest upon coordination are reported in Tables A2–A4 for the harmonic spectra ($n = 1$ to 3 respectively), whereas Tables 2–4 report the data for finite-temperature (10 K) spectra. For the latter, the maxima were determined using the full width at half maximum (FWHM). Due to the fluctuations of the simulated IR cross sections and the significant broadening and merge of bands in some cases, we can estimate a human error of $\pm 5\text{ cm}^{-1}$ on the reported wavenumbers. The 10 K dynamic spectra of all the isomers reported in Figures 3–5 are displayed in Figures 6–8.

First of all, we found that, for all clusters, the bands of corannulene were hardly affected upon coordination, and it is in line with the experimental results. This is clearly the case of the ν_{CH} (C-H stretch) bands, and for the $\delta(\text{CH}) + \nu(\text{CC})$ bands (combination of in plane C-H bending and C-C stretches) that have very weak intensities in the computed spectra. Regarding the γ_{CH} (C-H out-of-plane) most modes, their energy can be slightly blue-shifted for the “side” isomers all the more as the cluster size increases. The most intense γ_{CH} band is shifted by $+5\text{ cm}^{-1}$ for $(1)^{1-side}$, $+9\text{ cm}^{-1}$ for $(2)^{2cav-side}$, $+8$ and $+14\text{ cm}^{-1}$ for $(3)^{3vex-side}$ and $(4)^{3cav-side}$ respectively using the harmonic data. This small blue shift was also observed for the σ isomer the coronene-water complex [18]. The computed dynamic shifts were found similar to the harmonic ones. Therefore a side isomer may be distinguished from a convex or concave isomer through the position of the γ_{CH} band as in the case of coronene [18]. It should be noticed that these shift values are small with respect to the accuracy of the computed absolute positions. However, the description of intermolecular interactions has been carefully benchmarked against wavefunction results, insuring their accuracy [48].

In the following, we focus on the influence of the interaction with corannulene on the IR spectra of $(\text{H}_2\text{O})_n:\text{Ar}$ ($n = 1-3$).

Regarding the dynamic spectra of the isomers with one water molecule (Figure 6), the first striking feature is the narrowing of the water bands upon coordination. Indeed, in our simulations of $\text{H}_2\text{O}:\text{Ar}$ at 10 K, the water molecule vibrates and rotates in the matrix, leading to the broadening of the resonant symmetric and asymmetric stretching modes (ν_1 and ν_3) as well as the bending mode (ν_2). Besides, the stretching modes are significantly redshifted with respect to the harmonic ones, as we reported in our previous work focusing on the IR spectra of the water molecules and clusters inside a rare gas matrix [56]. As can be seen in Tables A2 and 2, the shifts are quite variable depending on the isomer. For the $(1)^{1side}$ isomer, the ν_1 and ν_3 modes are blueshifted upon coordination, the blue shift being more pronounced in the anharmonic spectrum ($+38$ and $+35$ vs. $+4$ and $+2\text{ cm}^{-1}$ for the anharmonic and harmonic ν_1 and ν_3 modes respectively). On the opposite, in the case of the $(2)^{1vex}$ isomer, the ν_1 and ν_3 bands are redshifted, the shifts being less pronounced in the dynamic spectra (-36 and -43 cm^{-1} vs. -17 and -1 cm^{-1}). The case of $(3)^{1cav}$ is intermediate as the ν_1 and ν_3 modes are redshifted at the harmonic level and become slightly blueshifted in the 10 K dynamic spectra (Figure 6). Regarding the ν_2 mode, it is blueshifted (except in the $(1)^{1side}$ harmonic spectrum) increasing from the side to convex and concave isomers. However, the significant narrowing of the water bands upon coordination may lead to the impossibility to detect the $(\text{C}_{20}\text{H}_{10})(\text{H}_2\text{O})_n:\text{Ar}$ clusters in the matrix as they can be hindered by the bands of the water molecule.

For larger clusters, only the dynamic spectra will be discussed. Regarding $(C_{20}H_{10})_{0,1}(H_2O)_2:Ar$, let us just specify that, regarding the 10 K spectrum of the water dimer, the ν_1 and ν_3 modes are redshifted with respect to the harmonic spectra. The shifts obtained for the O-H modes for the H atoms interacting with the Ar atoms of the matrix (the ν_1 and ν_3 most energetic modes, usually designated as ν_{1a} and ν_{3a} , “a” standing for “acceptor”) are the most shifted (both by 48 cm^{-1}) whereas the lowest energetic ones (ν_{1d} and ν_{3d} , “d” standing for “donor”) are only shifted by 7 and 9 cm^{-1} respectively. It can be understood as the former interact with the Ar atoms of the matrix and therefore are more sensitive to the loose interaction with Ar expected to lead to anharmonic effects at low temperature. Extremely weak intensity bands also accompany the intense ones, to a lesser extent than for the water monomer because the motion is more hindered by the matrix environment. The water dimer vibrates around its equilibrium position with the possible occurrence of the rotation of the H-acceptor water monomer around the OO axis. Interestingly, the water dimer motion in our simulations appears similar to the experimental evidence of the “acceptor switching and rotation of the water dimer around its O-O axis” by Ceponkus et al. [58].

Table 2. Positions (cm^{-1}) of the IR anharmonic bands in matrix of the corannulene, water monomer and the corresponding $(C_{20}H_{10})(H_2O)$ isomers. For the latter, the shifts of the water modes induced by the adsorption on corannulene are also reported (/). For H_2O , the numbers in parenthesis are the positions determined for the longer simulations (see Appendix B and Figure A2). Experimental data are mentioned for comparison. ^a this work, ^b [59] ^c [60].

	Mode	This Work	Expt.	(1) ^{1side}	(2) ^{1vex}	(3) ^{1cav}
$C_{20}H_{10}$	$\gamma(CH)$	811	837 ^a	816	812	813
	$\delta(CH)$	1171	1139 ^a	1180	1175	1174
		1270		1270	1269	1269
	$\delta(CH) + \nu(CC)$	1640	1316 ^a	1639	1641	1640
	$\delta(CH) + \nu(CC)$	1849	1441 ^a	1852	1849	1851
	$\nu(CH)$	3013	3050 ^a	2996	3015	3017
(H_2O)	ν_1	3756 (3760)	3638.5 ^b , 3639.2 ^c	3794 /+38	3739 /−17	3763 /+7
	ν_2	1561 (1563)	1589 ^b , 1589.1 ^c	1568 /+7	1582 /+21	1593 /+32
	ν_3	4021 (4021)	3733.5 ^b , 3737.2 ^c	4056 /+35	4020 /−1	4028 /+7

Table 3. Positions (cm^{-1}) of the IR anharmonic bands in matrix of the corannulene, water dimer and the corresponding $(C_{20}H_{10})(H_2O)_2$. For the latter, the shifts of the water modes induced by the adsorption on corannulene are also reported (/). Experimental data are mentioned for comparison. ^a this work, ^b [58].

	Mode	This Work	Expt.	(1) ^{2vex}	(2) ^{2cav−side}	(3) ^{2cav}	(4) ^{2vex−side}
$C_{20}H_{10}$	$\gamma(CH)$	811	837 ^a	813	820	814	818
	$\delta(CH)$	1176	1139 ^a	1176	1174	1175	1178
		1270		1269	1267	1268	1261
	$\delta(CH) + \nu(CC)$	1640	1316 ^a	1641	1639	1640	1639
	$\delta(CH) + \nu(CC)$	1849	1441 ^a	1850	1852	1849	1852
	$\nu(CH)$	3013	3050 ^a	3020	3017	3022	2995
$(H_2O)_2$	ν_1	3658	3574 ^b	3630 /−28	3593 /−65	3624 /−34	3627 /−31
		3760	3633 ^b	3748 /−12	3745 /−15	3742 /−18	3754 /−6
	ν_2	1562	1597 ^b	1568 /+6	1570 /+8	1585 /+23	1569 /+7
		1587	1610 ^b	1597 /+10	1586 /−1	1608 /+21	1580 /−7
	ν_3	3982	3708 ^b	3926 /−56	3956 /−26	3924 /−58	3982 /0
		4024	3730 ^b	4031 /+7	4013 /−11	4008 /−16	4028 /+4

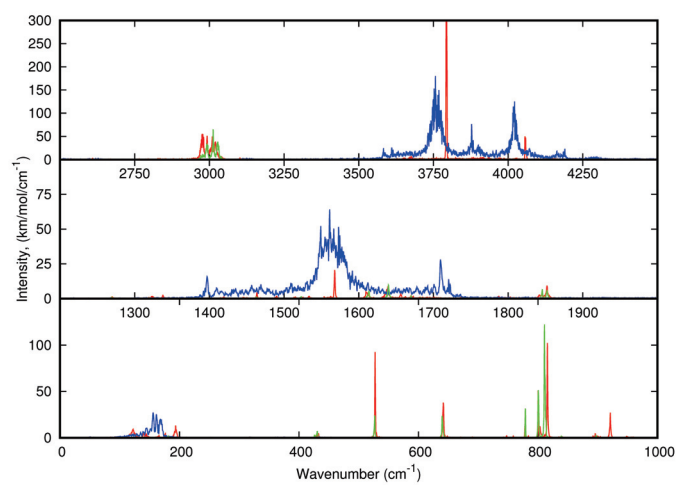
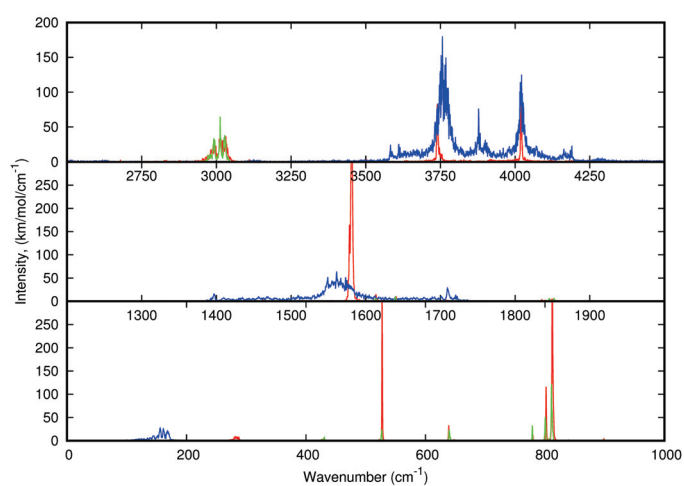
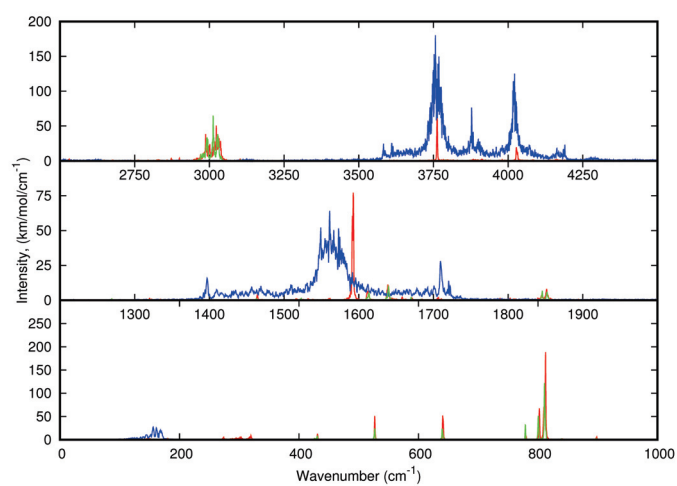
(1) 1_{side} (2) 1_{vex} (3) 1_{cav}

Figure 6. IR spectra derived from MD/DFTB-FF simulations at 10 K of the three lowest energy isomers of $(\text{C}_{20}\text{H}_{10})(\text{H}_2\text{O})\text{:Ar}$ (red), $\text{H}_2\text{O}\text{:Ar}$ (blue), and $\text{C}_{20}\text{H}_{10}\text{:Ar}$ (green).

Table 4. Positions (cm^{-1}) of the IR anharmonic bands in matrix of the corannulene, water trimer and the corresponding $(\text{C}_{20}\text{H}_{10})(\text{H}_2\text{O})_3$ isomers. In the case of the presence of broad bands, the maxima were determined using the FWHM, which is indicated in parenthesis. The shifts of the water modes induced by the adsorption on corannulene are also reported (/). * The shift was determined using a maximum position of 1579 cm^{-1} for the ν_2 band of $(\text{H}_2\text{O})_3$ estimated considering the structured broad band with a FWHM of 30 cm^{-1} . Experimental data are mentioned for comparison. ^a this work, ^b [61].

	Mode	This Work	Expt.	(1) ^{3cav}	(2) ^{3vex}	(3) ^{3vex-side}	(4) ^{3cav-side}
$\text{C}_{20}\text{H}_{10}$	$\gamma(\text{CH})$	811	837 ^a	815	813	819	825
	$\delta(\text{CH})$	1176	1139 ^a	1175	1175	1180	1176
	$\delta(\text{CH}) + \nu(\text{CC})$	1270	1269	1269	1273	1272	1271
	$\delta(\text{CH}) + \nu(\text{CC})$	1640	1316 ^a	1639	1639	1639	1638
	$\nu(\text{CH})$	1849	1441 ^a	1851	1849	1851	1852
		3013	3050 ^a	3008	3017	3012	3005
$(\text{H}_2\text{O})_3$	ν_1	3596 (50)	3514 ^b	3591 (12) / -5	3605 (49) / +9	3554 (12) / -42 3595 (10) / -1 3721 (10) / +125	3537 (11) / -59 3584 (10) / -12 3741 (8) / +145
	ν_2	1566		1566 (0)	1548 / -18		1577 / +11
		1570	1601 ^b	1571 / +1	1581 / +11	1586 (20) / +7 *	1592 / +22
		1591		1599 / +8	1600 / +9		1594 / +3
	ν_3	3948 (26)	3699 ^b	3902 (13) / -46	3950 (76) / +3	3944 / -4 3960 / +12 4012 / +64	3940 / -8 3954 / +6 4001 / +53

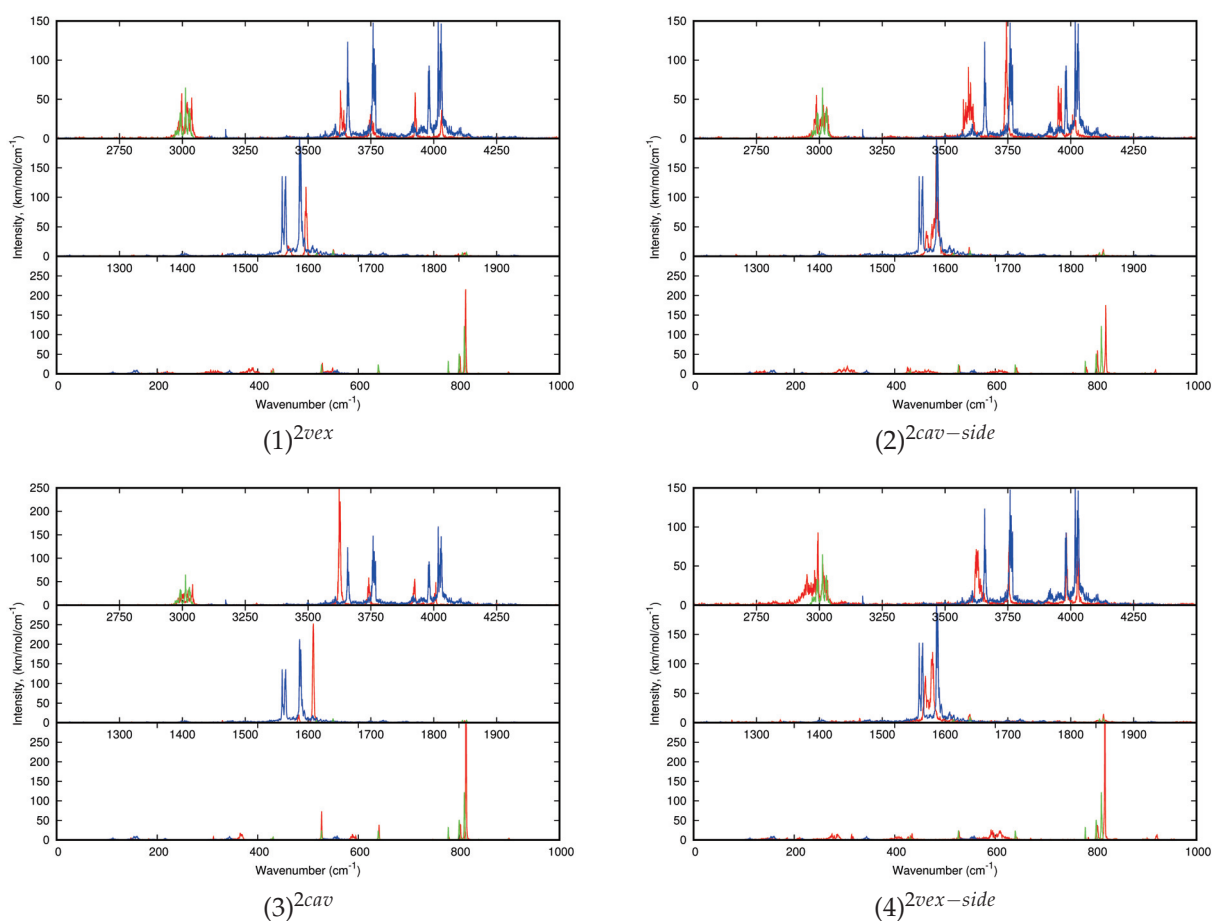


Figure 7. IR spectra derived from MD/DFTB-FF simulations at 10 K of the four lowest energy isomers of $(\text{C}_{20}\text{H}_{10})(\text{H}_2\text{O})_2:\text{Ar}$ (red), $(\text{H}_2\text{O})_2:\text{Ar}$ (blue), and $\text{C}_{20}\text{H}_{10}:\text{Ar}$ (green).

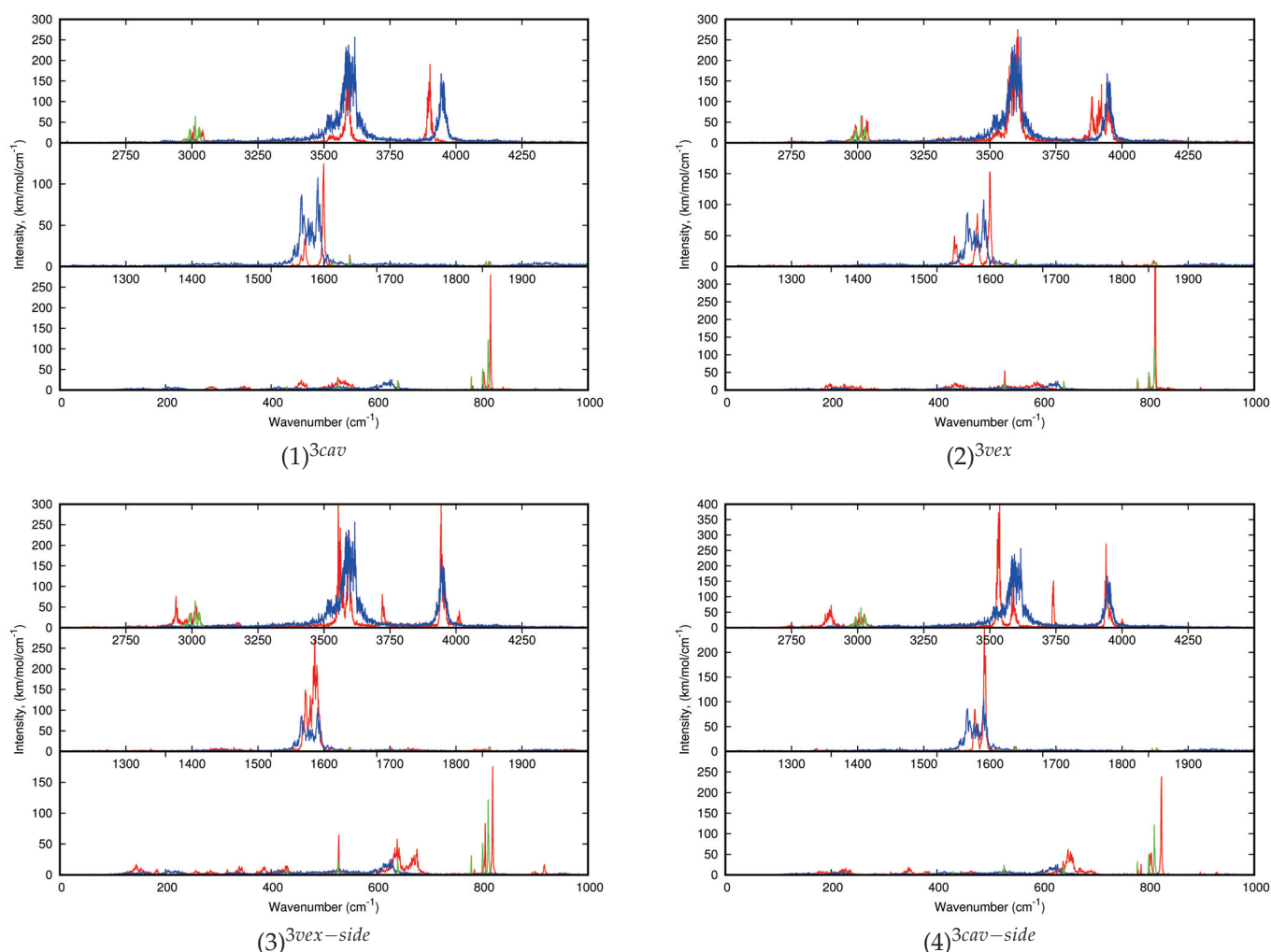


Figure 8. IR spectra derived from MD/DFTB-FF simulations at 10 K of the four lowest energy isomers of $(C_{20}H_{10})(H_2O)_3:Ar$ (red), $(H_2O)_3:Ar$ (blue), and $C_{20}H_{10}:Ar$ (green).

Regarding the spectra of all $C_{20}H_{10})(H_2O)_2:Ar$ isomers reported Figure 7, the differences in the shifts of the bands with respect to those of the bare water dimer might help identifying the type of isomer (cav, vex, cav-side or vex-side) formed in the experiments. Upon interaction with corannulene, the $(H_2O)_2$ ν_1 modes are globally redshifted and the shifts values are smaller in the 10 K spectra than in the harmonic ones. The shifts values are dependent on the isomer being smaller for the $(1)^{2vex}$ and $(4)^{2vex-side}$ isomers (see Table 3). The ν_3 bands are redshifted for $(2)^{2cav-side}$ and $(3)^{2cav}$, but it is not the case for the two other isomers for which the higher energy ν_3 band is blueshifted. Finally, a difference between the shifts of the ν_2 bands between the different isomers is noticeable. For instance, those for $(1)^{2vex}$ and $(3)^{2cav}$ are both blueshifted, the blue shift being larger for the latter.

Finally, the dynamic spectra of $(C_{20}H_{10})_{0,1}(H_2O)_{0,3}:Ar$ are reported in Figure 8. Regarding the water modes of $(H_2O)_3$, each type of mode leads to three broad bands more or less structured centered at 3596, 1569 and 3948 cm^{-1} for ν_1 to ν_3 . During the simulation, the water trimer vibrates around its equilibrium position with occasional flipping of the O-H bonds- not involved in intermolecular O-H bonds- from one side of the plane of the OOO cycle to the other side. As in the case of one and two water molecules, the water IR bands become narrower due to a hindrance of their motion upon interaction with corannulene, although it is not as relevant in the case of $(2)^{3vex}$ where the water trimer globally maintains its structure. It is all the more verified for the “cav” isomers $(1)^{3cav}$ and $(4)^{3cav-side}$, reflecting

stronger corannulene-water interactions than for the “vex” isomers. A significant difference is noticeable between the “side” isomers and the others. In the former, a band can be found at ~ 3720 and 3740 cm^{-1} , that was assigned to the O-H stretching mode for the bond interacting with the PAH [51]. In contrast with the other stoichiometries, the stretching modes do not appear systematically reshifted. The ν_1 mode is hardly redshifted in the case of the most stable (1)^{3cav} isomers whereas it is slightly blueshifted in the (2)^{3vex} spectrum. The ν_3 mode is redshifted for (1)^{3cav} but leads to mostly blueshifted bands for the three other isomers. The ν_2 modes are also globally blueshifted for all isomers, the amplitude of the shifts being dependent on the isomer. As in the case of the other stoichiometries, the differences in the spectra may allow us to distinguish specific isomers formed in the experiment.

3.2. Experiments

In this section, we present the FTIR spectra of water, corannulene, and water:corannulene mixtures recorded in argon matrices at 10 K, where water is present in the form of monomers, dimers, trimers and larger aggregates, depending on the H₂O:Ar ratio. The data will be compared to the computational results presented in the above section and discussed in the next section.

The IR spectra of water in solid argon have been previously studied in detail by several authors (see, for example, refs. [59–67]). Our experimental spectra agree with literature spectra and our assignments are based on them. The assignments of water monomers and water aggregates formed in our deposits will allow us to identify perturbed bands (shifts) and/or additional bands induced by the presence of corannulene. Figure A3 (a reproduction of Figure 3 in ref. [18]) presents the FTIR spectra of different H₂O:Ar deposits at 10 K with increasing concentrations of water: (a) H₂O:Ar = 1:500, where only monomers and dimers are present; (b) H₂O:Ar = 1:50, where larger aggregates (from trimers to hexamers) appear; and (c) H₂O:Ar = 1:25, where a mixture of water aggregates and water ice (ASW) is observed. These spectra have been discussed in detail in our previous paper [18] and Table A5 lists the main band positions of water aggregates (H₂O)_{*n*}, with *n* = 1–6, as well as those of some water complexes H₂O:CO₂, H₂O:N₂ and (H₂O)₂:N₂.

Although corannulene and coronene are both aromatic, they present marked differences in structure and reactivity [20]. Due to its C_{5v} symmetry, and its bowl-like non-planar structure, the corannulene molecule exhibits a richer IR spectrum than coronene, with more active modes and larger intensities. Table A6 lists the vibrational modes observed and calculated in this work, compared to experimental data from the NASA Ames PAH IR spectral database [68–70] and previous study by Rouillé et al. [39]. A summary of the main experimental bands is reported in Tables 2–4 where the frequencies are compared to the IR anharmonic band positions calculated in this work.

Figure 9 presents the FTIR spectra of corannulene in Ar and in H₂O:Ar (1:50) in two spectral regions of interest: 2000–400 cm^{−1}, where we can observe the main corannulene bands plus the deformation modes ν_2 of water; and 4000–2800 cm^{−1}, where we can observe all OH stretching modes of water monomers and aggregates plus the CH stretching bands of corannulene. Despite several attempts, it was impossible to obtain a pure corannulene:Ar spectrum without any traces of water; a small amount of water monomer (lines at 3756 and 3778 cm^{−1}) and trace of (H₂O)₂ (line at 3708 cm^{−1}) are always present in the experimental corannulene:Ar spectra. No change is observed in water monomer lines, nor in corannulene lines in this spectrum, so we consider that the trace amount of water in the matrix is not interacting with the corannulene.

If we now consider depositions with intentionally added water H₂O:Ar 1:50 (Figure 9, red traces labelled c), we can see that, apart from a minor broadening, the vibrational bands of corannulene remain almost unchanged in frequency compared to corannulene in argon. Contrary to what was observed in the case of coronene [17], where the most intense out-of-plane $\gamma(\text{CH})$ mode was blue-shifted by up to 12 cm^{−1} upon interaction with water aggregates, no or very small blue shifts (a few cm^{−1} i.e., within the spectral resolution) are observed for the $\gamma(\text{CH})$ mode of corannulene at 837 cm^{−1}. The main changes in the FTIR

spectrum appear in the OH stretching modes of water, especially in the bands assigned to water dimers and trimers. Small blue shifts and broadenings are observed for the bands located at 3700 (trimer), 3706 (dimer) and 3712 (monomer) cm^{-1} . No change is detected below 3500 cm^{-1} , in the region of the stretching modes of $(\text{H}_2\text{O})_n$ with $n = 4-6$.

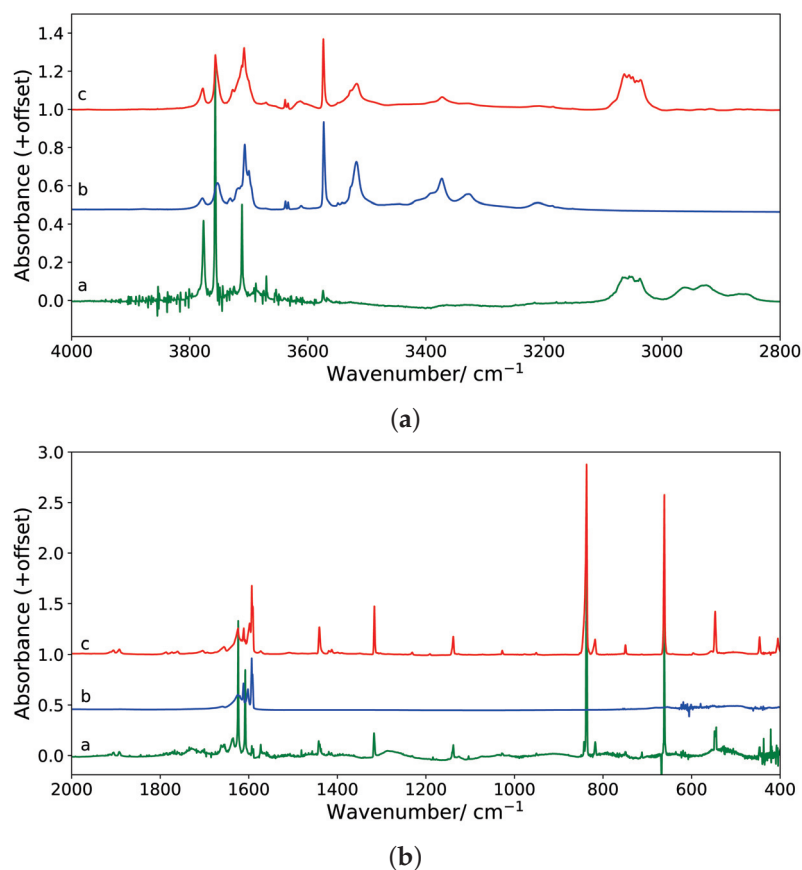


Figure 9. Experimental spectra measured in the wavelength ranges (a) 4000–2800 cm^{-1} and (b) 2000–400 cm^{-1} . Spectra in both panels are as follows: a—Corannulene in argon (green trace), b—water in argon (blue trace), and c—corannulene and water in argon (red trace).

Figure 10 presents the difference spectrum between the corannulene: H_2O :Ar deposition minus the H_2O :Ar deposition at 10 K in the 3800–3200 cm^{-1} and 1800–1500 cm^{-1} ranges, where stretching and bending water modes are, respectively, located. A new band appears at 3727 cm^{-1} , as well as two broad, weak bands at 3603 and 3613 cm^{-1} . These features are in proximity to a weak band in the H_2O :Ar spectrum assigned to a symmetric stretching mode of the water trimer at 3611 cm^{-1} . A weak band is also observed at 3536 cm^{-1} , in the region of the symmetric stretching modes of water dimers (3574 cm^{-1}) and trimers (3518 cm^{-1}). Additionally, a new band clearly appears at 1598 cm^{-1} , in the HOH bending region of water dimers at 1593 cm^{-1} and water trimers at 1602 cm^{-1} . We can thus conclude that molecular interaction between water dimers and/or trimers with corannulene are observed in the FTIR spectra.

Energy was introduced into the corannulene: H_2O :Ar samples via photons. Low energy UV irradiations of our deposition did not induce any change in the spectrum, contrary to what was previously observed for coronene: H_2O :Ar matrices at 10 K, where the interaction of coronene with water aggregates $(\text{H}_2\text{O})_n$ with n up to 3 led to the formation of oxygenated products [17].

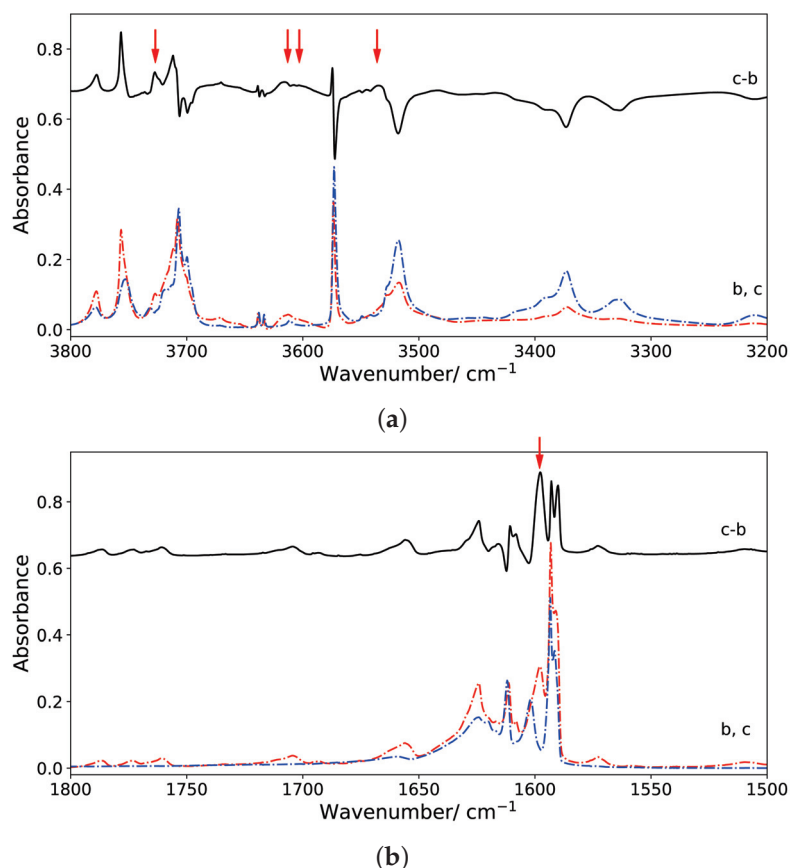


Figure 10. Experimental difference spectra in the wavelength ranges (a) 3800–3200 cm^{-1} and (b) 1800–1500 cm^{-1} . Spectra b (water, blue) and c (corannulene plus water, red) of Figure 9 are reproduced in dot-dashed lines, while the solid black line represents their difference spectrum (i.e., spectrum c minus spectrum b). New bands discussed in the text are indicated with red arrows at the following frequencies: 3727, 3613, 3603, 3536, and 1598 cm^{-1} .

4. Discussion

In this section, we discuss the assignment of the experimental spectra in the light of the calculated finite-temperature spectra (Tables 2–4 for corannulene in interaction with, respectively, water monomers, dimers and trimers). As the absolute positions of the calculated frequencies are not strictly accurate, we will use the calculated shifts to identify the $(\text{C}_{10}\text{H}_{20})(\text{H}_2\text{O})_n$ complexes formed in our experiments. Indeed, regarding the computed absolute positions, we are aware that they are not accurate. It is due to several reasons: (i) the DFTB method is a DFT-based approximate method (truncated hamiltonian, minimal valence basis set...). However, the DFTB/FF method used in the present work, quite unique to our knowledge, is mandatory to be able to perform on-the-fly BOMD simulations taking explicitly into account all atoms (including the atoms of the rare gas matrix). The possible presence of defaults is not taken into account. (ii) 0 K vibrational anharmonicities and nuclear quantum effects, expected to be significant in the case of water clusters, are not taken into account, and it is a major drawback of our computational studies. However, given the size of the systems and the presence of highly symmetric corannulene, an approach such as vibrational perturbational theory using a wavefunction method to describe the electronic structure in conjunction with a large basis set, which would allow to obtain accurate 0 K IR spectra for such systems, is prohibited. In our approach however, as specified in Section 3.1.2, intermolecular interactions are expected to be better described than intramolecular bonds as they have been carefully benchmarked against wavefunction results [48].

The new band observed at 3727 cm^{-1} may be due to a blue shift of 15 cm^{-1} of the ν_3 mode of the water monomer (3712 cm^{-1}) in $(\text{C}_{10}\text{H}_{20})(\text{H}_2\text{O})$ “side” or “cav” geometries

(see Table 2), or to a blue shift of 21 cm^{-1} of the ν_3 mode of the water dimer (3706 cm^{-1}) in $(\text{C}_{10}\text{H}_{20})(\text{H}_2\text{O})_2^{\text{vex}}$ (see Table 3). These two values being located between those calculated for these two complexes (7 to 35 cm^{-1}), it is impossible to conclude at this stage. However, it seems unlikely that $(\text{C}_{10}\text{H}_{20})(\text{H}_2\text{O})$ with “side” structure has been formed, as no large red shift has been observed on the $\nu(\text{CH})$ of corannulene, whereas $(\text{C}_{10}\text{H}_{20})(\text{H}_2\text{O})$ in the “cav” form, calculated to induce only a small blue shift in the $\nu(\text{CH})$ modes, could be a possible candidate (see Table 2).

If we now consider the new bands observed at 3603 and 3613 cm^{-1} , they may be red-shifted from the ν_3 modes of the water dimer (3706 cm^{-1} , shift of 93 cm^{-1}) or trimer (3700 cm^{-1} , shift of 87 cm^{-1}), or blueshifted from the ν_1 mode of the water dimer (3574 cm^{-1} , shifts of 29 and 39 cm^{-1}). From Tables 3 and 4, it appears that no blue shifts are calculated for the ν_1 modes of any $(\text{C}_{10}\text{H}_{20})(\text{H}_2\text{O})_2$ structures nor for $(\text{C}_{10}\text{H}_{20})(\text{H}_2\text{O})_3^{\text{cav}}$, whereas large red shifts are expected for the ν_3 modes of these complexes (from 46 to 58 cm^{-1}). So, the more likely assignment for these two new bands is to $(\text{C}_{10}\text{H}_{20})(\text{H}_2\text{O})_2$ “vex” or “cav” forms and to $(\text{C}_{10}\text{H}_{20})(\text{H}_2\text{O})_3^{\text{cav}}$. For the same reasons, the weak band observed at 3536 cm^{-1} must be red shifted from the ν_1 mode of the water dimer (3574 cm^{-1} , shift 38 cm^{-1}) in the $(\text{C}_{10}\text{H}_{20})(\text{H}_2\text{O})_2$ “vex” or “cav” forms, as only a small blue shift (5 cm^{-1} , see Table 4) is expected from the ν_1 mode of the water trimer observed at 3518 cm^{-1} .

Finally, the new band at 1598 cm^{-1} could be due to a blue shift of 6 or 5 cm^{-1} of the ν_2 mode of, respectively, the water monomer observed at 1592 cm^{-1} or of the dimer at 1593 cm^{-1} , or could be due to a red shift of 4 cm^{-1} of the ν_2 mode of the water trimer at 1602 cm^{-1} . Comparison with calculated shifts in Tables 3 and 4 shows that only blue shifts are expected for all ν_2 modes in all complexes, whatever the stoichiometry and structures. However, this blue shift is calculated to be 7 cm^{-1} in $(\text{C}_{10}\text{H}_{20})(\text{H}_2\text{O})^{\text{side}}$, but more than 30 cm^{-1} in $(\text{C}_{10}\text{H}_{20})(\text{H}_2\text{O})^{\text{cav}}$. As we have already eliminated $(\text{C}_{10}\text{H}_{20})(\text{H}_2\text{O})^{\text{side}}$ due to the absence of shifts in the $\nu(\text{CH})$ bands of corannulene, we thus assign this new band to $(\text{C}_{10}\text{H}_{20})(\text{H}_2\text{O})_2^{\text{vex}}$.

From the analysis of our experimental spectra—which is complicated by the presence of excess corannulene and water aggregates ($n = 1$ to 6)—and thanks to our calculations, we can conclude that: (1) no $(\text{C}_{10}\text{H}_{20})(\text{H}_2\text{O})$ complex has been detected in our experimental conditions. This can be due to the effect of argon environment, or to a better reactivity of corannulene with small aggregates (dimer, trimer) compared to the water monomer, (2) the $(\text{C}_{10}\text{H}_{20})(\text{H}_2\text{O})_3$ complex with the water trimer interacting with the concave face of corannulene has been identified, which is in line with the fact that it is the most stable calculated structure, and (3) the $(\text{C}_{10}\text{H}_{20})(\text{H}_2\text{O})_2$ complex is also formed, but it is impossible to firmly characterize its structure, which may be “vex” or “cav”. We have not seen any experimental evidence for the formation of complexes with larger aggregates ($n = 4$ to 6) on the difference spectra. Even if their formation cannot be completely excluded, it is hardly probable that they could be formed, because the water tetramer and larger cluster spectra are quite different from those of water dimer and trimer and located lower in energy.

5. Conclusions

Our study has shown that the weak PAH-water complexes formed in rare gas matrices may be different from those obtained in the gas phase. Our prior computations have shown that embedding in the matrix stabilises σ isomers in the case of planar aromatics [18], while for the clusters involving the non-planar corannulene studied in this work, π isomers remain favored in the cases of the water dimer and trimer. Such geometrical differences may account for the differences in photo-reactivity of these systems: indeed, pyrene and coronene react with water molecules to form alcohols and quinones under low energy irradiation [13,14] while corannulene does not, even when embedded in ASW (private comm. from J. Mascetti). The photoreactivity in planar PAHs could occur through the population of low energy charge transfer $\text{PAH}^+ - \text{H}_2\text{O}^-$ electronic excited states that are present when the water molecules interact through their oxygen atoms with the H atoms of the PAH [17,19]. Therefore, from the modeling reported in the present work, the most stable form of $(\text{C}_{20}\text{H}_{10})(\text{H}_2\text{O})_3$ in an argon matrix does not appear favorable to the presence

of such low energy excited states. The investigation of the electronic excited states of $(C_{20}H_{10})(H_2O)_n \cdot Ar$ systems ($n = 1-3$) will be the object of future work. Our studies illustrate the dependence of the mutual orientation of the reactants on the nature of bimolecular photo-redox reactions as evoked in a recent review [71]. The differentiation between flat and curved PAHs may be of importance in UV absorption and electron transfer reactions in PAH:water molecular systems. From an astrophysical point of view, even if it is still premature to project these results directly to PAHs of astro-relevant sizes embedded in water ice, there is probably no difference in the photoreactivity between flat and curved PAHs when using high energy UV photons that lead to PAH ionization, but the influence of geometry should be taken into account when using low energy UV photons that induce charge transfer reactions.

Author Contributions: All authors contributed to the work. H.L. and A.S. performed calculations; C.A. and J.M. ran experiments. All authors have discussed the results. Draft preparation and writing were done by H.L., A.S., J.A.N. and J.M. All authors have read and agreed to the submitted version of the manuscript.

Funding: This research was funded by the French National Agency for Research (ANR PARCS project ANR-13-BS008-0005) and supported by the Programme National Physique et Chimie du Milieu Interstellaire (PCMI) of CNRS/INSU with INC/INP co-funded by CEA and CNES, and by the French research network EMIE (Edifices Moléculaires Isolés et Environnés, GDR 3533).

Institutional Review Board Statement: Not applicable.

Informed Consent Statement: Not applicable.

Data Availability Statement: The data published in the present paper are made public in the archived datasets on the Zenodo website (<https://doi.org/10.5281/zenodo.6368179>) published on 18 March 2022.

Acknowledgments: H.L. and A.S. thank the computing mesocenter CALMIP (UMS CNRS 3667) for generous allocation of computer resources (p17002). J.M. and C.A. acknowledge the participation of internship students Maxime Gerbeaud-Lassau and Francisco Salvador in the experimental part of this study.

Conflicts of Interest: The authors declare no conflict of interest.

Abbreviations

AIBs	aromatic infrared bands
ASW	amorphous solid water
BOMD	Born-Oppenheimer molecular dynamics
DFTB	density functional based tight binding
FF	force field
IR	infrared
FTIR	Fourier transform infrared
ISM	interstellar medium
PAH	polycyclic aromatic hydrocarbon
UV	ultraviolet

Appendix A. Energetics: Insertion of Corannulene in the Matrix

Different insertion planes for corannulene inside the Ar matrix were tried. The substitution energies are reported in Table A1.

Table A1. Substitution energies for the insertion of the corannulene in different cristallographic planes.

Plane	Number of Ar Removed	E_{sub} (cm ⁻¹)
(100)	9	1400
(110)	5	3910
(111)	7	-2470
Cavity	13	3080

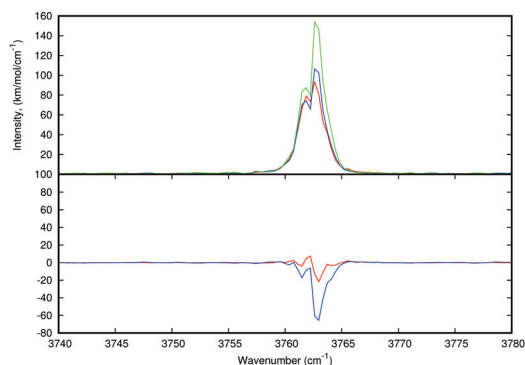
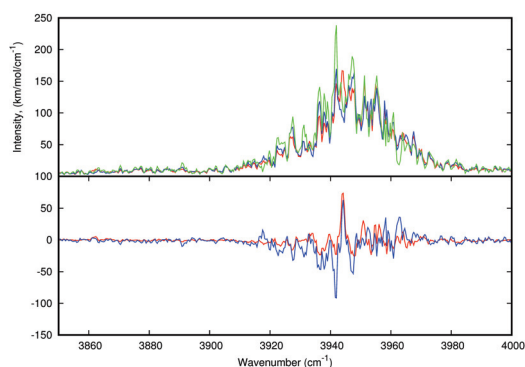
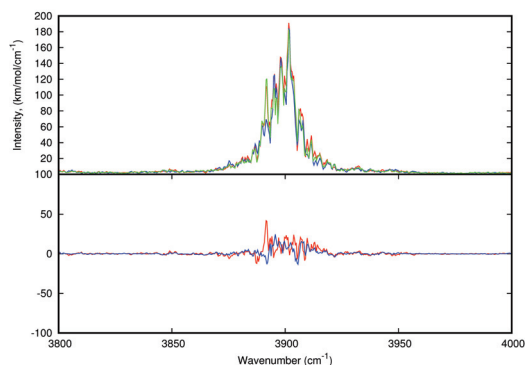
Appendix B. Convergence of IR Dynamic Spectra**(a)** ν_1 mode for $(3)^{1cav}$ **(b)** ν_3 mode for $(H_2O)_3$ **(c)** ν_3 mode for $(1)^{3cav}$

Figure A1. IR dynamic spectra at 10K obtained following the procedure described in Section 2.1 for $(3)^{1cav}$ (a), $(H_2O)_3$ (b) and $(1)^{3cav}$ (c). Zooms on the ν_1 (a) and ν_3 (b,c) modes are presented as an illustration of the convergence. In the upper panel of each plot we present the spectra averaged over 7×100 ps (red), 5×100 ps (blue) and 3×100 ps (green). In the lower panel of each plot we show the difference spectra between 7×100 ps and 5×100 ps dynamics (red) and between 7×100 ps and 3×100 ps MDs (blue). The resolution of all spectra is 0.4 cm^{-1} .

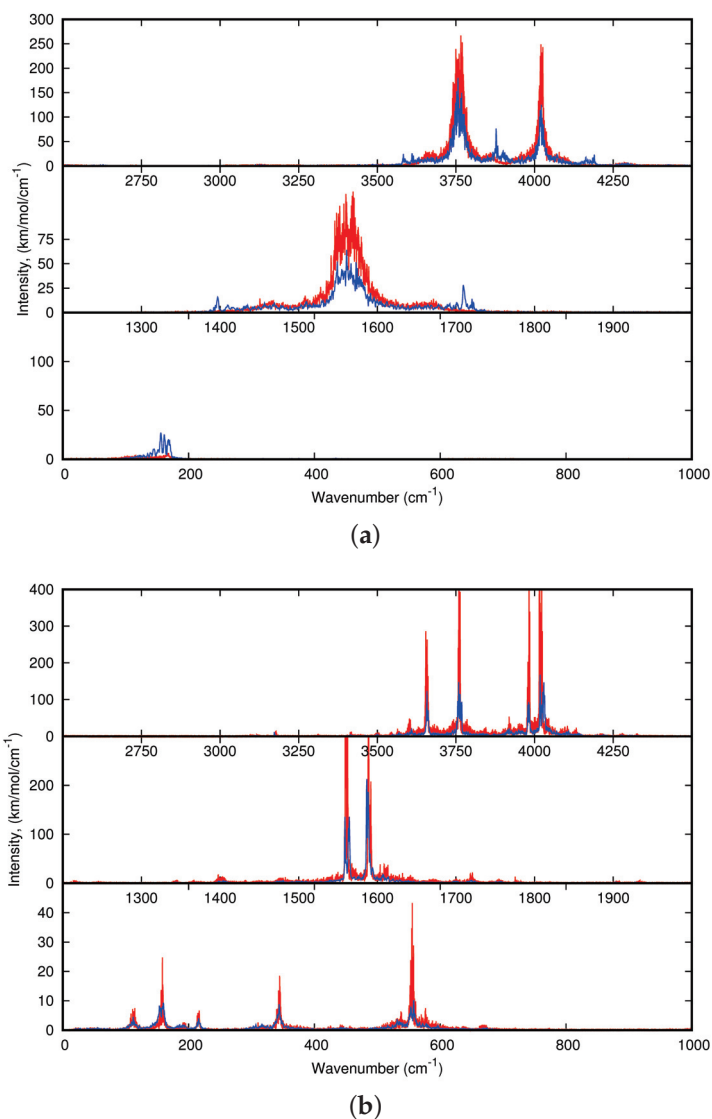


Figure A2. IR dynamic spectra at 10K for H₂O:Ar (a) and (H₂O)₂:Ar (b). The spectra of Figures 6 and 7, resulting from 7 × 100 ps MDs, are reported in blue. Those resulting from longer simulations, 7 × 500 ps for H₂O:Ar and 3 × 500 ps for (H₂O)₂:Ar, are reported in red.

Appendix C. Harmonic Data

Table A2. Positions (cm⁻¹) of the IR harmonic bands in matrix of the corannulene, water monomer and the corresponding (C₂₀H₁₀)(H₂O)₁ isomers. Harmonic IR intensities are reported in parenthesis, as well as shift values (/). Experimental data are also reported for comparison. ^a this work, ^b [59], ^c [60].

	Mode	This Work	Expt.	(1) ^{1side}	(2) ^{1vex}	(3) ^{1cav}
C ₂₀ H ₁₀	γ(CH)	812 (147)	837 ^a	817 (135)	814 (149)	813 (153)
	δ(CH)	1175 (2)	1139 ^a	1178 (3)	1177 (3)	1176 (3)
		1271 (<1)		1271(<1)	1271(<1)	1271 (<1)
	δ(CH) + ν(CC)	1646 (6)	1316 ^a	1644 (6)	1646 (3)	1645 (4)
	δ(CH) + ν(CC)	1857 (3)	1441 ^a	1856 (3)	1855 (3)	1856 (2)
	ν(CH)	2999* (60)	3050 ^a	2999 (62)	3002 (55)	3007 (45)
(H ₂ O)	ν ₁	3807 (39)	3638.5 ^b , 3639.2 ^c	3811 (138) /+4	3771 (52) /-36	3765 (57) /-42
	ν ₂	1571 (140)	1589 ^b , 1589.1 ^c	1568 (289) /-3	1588 (241) /+17	1594 (178) /+23
	ν ₃	4081 (33)	3733.5 ^b , 3737.2 ^c	4083 (83) /+2	4038 (21) /-43	4030 (10) /-51

Table A3. Positions (cm^{-1}) of the IR harmonic bands in matrix of the corannulene, water dimer and the corresponding $(\text{C}_{20}\text{H}_{10})(\text{H}_2\text{O})_2$ isomers. The shifts of the water modes upon interaction with corannulene are also reported (/). Experimental data are mentioned for comparison. ^a this work, ^b [58].

	Mode	This work	Expt.	(1) ^{2vex}	(2) ^{2cav-side}	(3) ^{2cav}	(4) ^{2vex-side}
$\text{C}_{20}\text{H}_{10}$	$\gamma(\text{CH})$	812	837 ^a	815	821	816	819
	$\delta(\text{CH})$	1175	1139 ^a	1174	1173	1175	1179
	$\delta(\text{CH}) + \nu(\text{CC})$	1271		1271	1271	1270	1271
	$\delta(\text{CH}) + \nu(\text{CC})$	1646	1316 ^a	1646	1644	1645	1644
	$\delta(\text{CH}) + \nu(\text{CC})$	1857	1441 ^a	1853	1855	1854	1856
	$\nu(\text{CH})$	2999	3050 ^a	3020	3022	3028	3019
$(\text{H}_2\text{O})_2$	ν_1	3665	3574 ^b	3628 / -37	3585 / -80	3639 / -26	3613 / -52
		3802	3633 ^b	3745 / -57	3757 / -45	3757 / -45	3752 / -50
	ν_2	1568	1597 ^b	1566 / -2	1573 / +5	1586 / +18	1570 / +2
		1593	1610 ^b	1597 / +4	1593 (0)	1609 / +16	1581 / -12
	ν_3	3991	3708 ^b	3925 / -66	3962 / -29	3941 / -50	3983 / -8
		4072	3730 ^b	4029 / -43	4018 / -54	4021 / -51	4028 / -44

Table A4. Positions (cm^{-1}) of the IR harmonic bands in matrix of the corannulene, water trimer and the corresponding $(\text{C}_{20}\text{H}_{10})(\text{H}_2\text{O})_3$. The shifts of the water modes upon interaction with corannulene are also reported (/). Experimental data are mentioned for comparison. ^a this work, ^b [61].

	Mode	This Work	Expt.	(1) ^{3cav}	(2) ^{3vex}	(3) ^{3vex-side}	(4) ^{3cav-side}
$\text{C}_{20}\text{H}_{10}$	$\gamma(\text{CH})$	812	837 ^a	816	814	820	826
	$\delta(\text{CH})$	1175	1139 ^a	1174	1174	1178	1177
	$\delta(\text{CH}) + \nu(\text{CC})$	1271		1269	1271	1271	1273
	$\delta(\text{CH}) + \nu(\text{CC})$	1646	1316 ^a	1645	1645	1644	1642
	$\delta(\text{CH}) + \nu(\text{CC})$	1857	1441 ^a	1854	1853	1855	1856
	$\nu(\text{CH})$	2999	3050 ^a	3013	3023	3021 (+2933)	3011 (+2888)
$(\text{H}_2\text{O})_3$	ν_1	3540		3514 / -26	3518 / -22	3563 / +23	3536 / -4
		3597	3514 ^b	3580 / -17	3576 / -21	3602 / +5	3595 / -2
		3621		3581 / -40	3599 / -22	3737 / +116	3748 / +127
	ν_2	1568		1564 / -4	1546 / -22	1579 / +11	1577 / +9
		1575	1601 ^b	1569 / -6	1580 / +5	1587 / +12	1581 / +6
		1595		1600 / +5	1602 / +7	1592 / -3	1595 (0)
ν_3	3960		3900 / -60	3894 / -66	3959 / -1	3951 / -9	
	3964	3699 ^b	3904 / -60	3925 / -39	3972 / +8	3965 / +1	
	3971		3913 / -58	3959 / -12	4017 / +46	4008 / +37	

Appendix D. Ftir Bands of Water Monomers, Dimers, Trimers and Larger Aggregates in Argon Matrices at 10 K

Table A5. From ref. [18] Band positions, in cm^{-1} , of $(\text{H}_2\text{O})_n$ water species with $n = 1$ to 6. Attributions are based on previous works [59–62,64–67].

n	Rovibrational Mode	Our Results (cm^{-1})	Exp Values (cm^{-1}) from Litt.	Refs.
1	$\nu_2 + \nu_3$	5346.1, 5325.5	5345.9, 5325.4	[59,60,62]
		5293.2, 5280.5	5295.4, 5280.6	
	ν_3	3776.9, 3756.5	3776.4, 3756.6	
		3724.8, 3711.4	3724.9, 3711.3	
	ν_1	3669.9, 3653.6	3669.7, 3653.5	
		ν_2 RTC	1662.5, 1657.7	
	ν_2	1636.3, 1624.2	1636.5, 1623.8	
		1608.1, 1573.3	1607.9, 1573.1	
		1556.9	1556.7	
	ν_2 NRM	1590.7	1589.2	

Table A5. Cont.

<i>n</i>	Rovibrational Mode	Our Results (cm ⁻¹)	Exp Values (cm ⁻¹) from Litt.	Refs.
2	ν_3 PD	3707.9	3708	
	ν_3 PA	3736.1	3737.8	
	ν_1 PA	3633.1	3633.1	
	ν_1 PD	3573.8	3574	
	ν_2 PD	1611.9	1610.6	
	ν_2 PA	1593.2	1593.1	
3	ν_3 PD	3699.8	3700	[59,61,64,65]
	ν_1 PA	3611.1	3612	
	ν_1 PD	3527.9	3528	
	ν_1 PD	3517.4	3516	
	ν_2 PA	1601.9	1602	
4		3372.9	3374	
5		3326.7	3327	
6		3541.3	3540	[64,67]
		3444.4	3445	
		3392.2	3391	
		3210.3	3212	
		3186.2	3195.2	
		3151.5	3150	
H ₂ O-CO ₂	ν_1	3638.4	3638	[60]
	ν_2	1589.5	1589.5	
H ₂ O-N ₂	ν_3	3730.3	3729.6	
(H ₂ O) ₂ -N ₂	ν_1	3640.2	3640.2	[66]
	ν_1 PD	3566.8	3566.6	
	ν_1 PD	3563.1	3563.5	

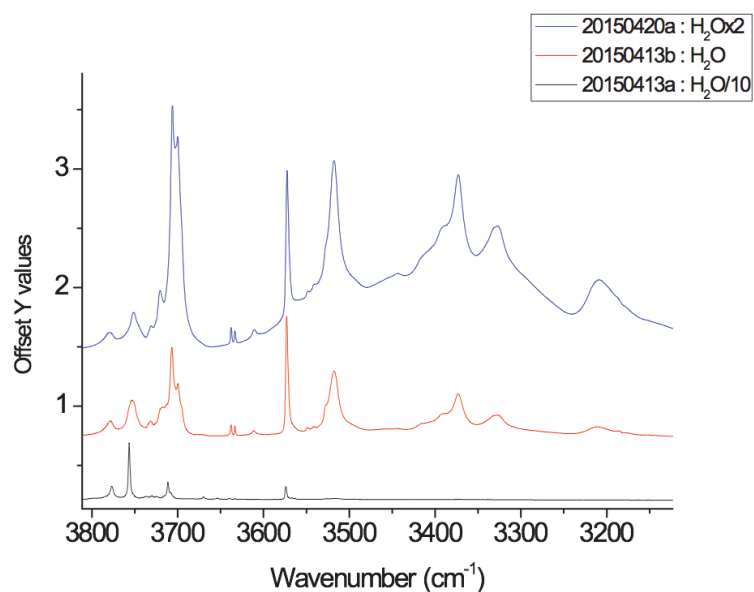


Figure A3. From ref. [18] Experimental FTIR spectra of H₂O:Ar depositions at 10 K (a) 1:500 (black, only water monomers and dimers are present); (b) 1:50 (red, larger water aggregates appear (trimers, tetramers, pentamers and hexamers); and (c) 1:25 (blue, a mixture of water aggregates and ASW).

Appendix E. FTIR Bands of Corannulene in Argon Matrices at 10 K

Table A6. Observed bands positions (cm^{-1}) and relative intensities (vs: very strong, s: strong, ms: medium strong, m: medium, mw: medium weak, w: weak) of corannulene isolated in argon matrices at 10 K and comparison with results by Rouillé et al. [39] in an argon matrix at 12 K Note that spectra of Rouillé et al. [39] also contained small amounts of water.

Vib. Modes	Wavenumbers (cm^{-1} , This Work)	from Ref. [39]
$\nu(\text{C-H})$	3064.5 m	
	3056.1 m	
	3050.5 m	
	3043.0 m	
	3037.4 m	
Combination modes	1906 w	
	1893 w	
$\nu(\text{C-C})$ and $\delta(\text{C-H})$ in-plane bending	1441.0 m	1442.7
		1428.8
	1316.3 m	1316.9
		1239.3
	1138.8 mw	1138.6
Out-of-plane bending $\gamma(\text{C-H})$		1025.2
	837.1 vs	837.2
	818.3 w	817.5
	749.8 w	748.7
	661.8 s	661.5
	547.4 m	
	446.8 w	
	405.9 w	

References

- Ghosh, A.K.; Chaudhuri, P.; Kumar, B.; Panja, S.S. Review on aggregation of asphaltene vis-a-vis spectroscopic studies *Fuel* **2016**, *185*, 541. [CrossRef]
- Callén, M.; de la Cruz, M.; López, J.; Murillo, R.; Navarro, M.; Mastral, A. Some inferences on the mechanism of atmospheric gas/particle partitioning of polycyclic aromatic hydrocarbons (PAH) at Zaragoza (Spain). *Chemosphere* **2008**, *73*, 1357–1365. [CrossRef] [PubMed]
- Vione, D.; Maurino, V.; Minero, C.; Pelizzetti, E.; Harrison, M.A.J.; Olariu, R.I.; Arsene, C. Photochemical reactions in the tropospheric aqueous phase and on particulate matter. *Chem. Soc. Rev.* **2006**, *35*, 441–453. [CrossRef] [PubMed]
- Dartois, E. Interstellar Carbon Dust. *C* **2019**, *5*, 80. [CrossRef]
- Allamandola, L.J.; Tielens, A.G.; Barker, J.R. Interstellar polycyclic aromatic hydrocarbons: The infrared emission bands, the excitation/emission mechanism, and the astrophysical implications. *Astrophys. J. Suppl. Ser.* **1989**, *71*, 733–775. [CrossRef] [PubMed]
- Tielens, A. Interstellar Polycyclic Aromatic Hydrocarbon Molecules. *Ann. Rev. Astron. Astrophys.* **2008**, *46*, 289–337. [CrossRef]
- Allamandola, L.J.; Tielens, A.G.G.M.; Barker, J.R. Polycyclic Aromatic-Hydrocarbons and the Unidentified Infrared-Emission Bands-Auto Exhaust Along the Milky-Way. *Astrophys. J.* **1985**, *290*, L25–L28. [CrossRef]
- Léger, A.; Puget, J.L. Identification of the ‘unidentified’ IR emission features of interstellar dust? *Astron. Astrophys.* **1984**, *137*, L5–L8.
- McGuire, B.A.; Loomis, R.A.; Burkhardt, A.M.; Lee, K.L.K.; Shingledecker, C.N.; Charnley, S.B.; Cooke, I.R.; Cordiner, M.A.; Herbst, E.; Kalenskii, S.; et al. Detection of two interstellar polycyclic aromatic hydrocarbons via spectral matched filtering. *Science* **2021**, *371*, 1265–1269. [CrossRef]
- Hardegree-Ullman, E.E.; Gudipati, M.S.; Boogert, A.C.A.; Lignell, H.; Allamandola, L.J.; Stapelfeldt, K.R.; Werner, M. Laboratory determination of the infrared band strengths of pyrene frozen in water ice: Implications for the composition of interstellar ices. *Astrophys. J.* **2014**, *784*, 172. [CrossRef]
- Tielens, A.G.G.M. *The Physics and Chemistry of the Interstellar Medium*; Cambridge University Press: Cambridge, UK, 2005.
- Cook, A.M.; Ricca, A.; Mattioda, A.L.; Bouwman, J.; Roser, J.; Linnartz, H.; Bregman, J.; Allamandola, L.J. Photochemistry of polycyclic aromatic hydrocarbons in cosmic water ice: The role of ionization and concentration. *Astrophys. J.* **2015**, *799*, 14. [CrossRef]

13. Guennoun, Z.; Aupetit, C.; Mascetti, J. Photochemistry of coronene with water at 10 K: First tentative identification by infrared spectroscopy of oxygen containing coronene products. *Phys. Chem. Chem. Phys.* **2011**, *13*, 7340–7347. [CrossRef] [PubMed]
14. Guennoun, Z.; Aupetit, C.; Mascetti, J. Photochemistry of Pyrene with Water at Low Temperature: Study of Atmospheric and Astrochemical Interest. *J. Phys. Chem. A* **2011**, *115*, 1844–1852. [CrossRef] [PubMed]
15. Noble, J.A.; Michoulier, E.; Aupetit, C.; Mascetti, J. Influence of ice structure on the soft UV photochemistry of PAHs embedded in solid water. *Astron. Astrophys.* **2020**, *644*, A22. [CrossRef]
16. Lignell, A.; Tenelanda-Osorio, L.I.; Gudipati, M.S. Visible-light photoionization of aromatic molecules in water-ice: Organic chemistry across the universe with less energy. *Chem. Phys. Lett.* **2021**, *778*, 138814. [CrossRef]
17. Noble, J.A.; Jouvet, C.; Aupetit, C.; Moudens, A.; Mascetti, J. Efficient photochemistry of coronene:water complexes. *Astron. Astrophys.* **2017**, *599*, A124. [CrossRef]
18. Simon, A.; Noble, J.A.; Rouaut, G.; Moudens, A.; Aupetit, C.; Iftner, C.; Mascetti, J. Formation of coronene: Water complexes: FTIR study in argon matrices and theoretical characterisation. *Phys. Chem. Chem. Phys.* **2017**, *19*, 8516–8529. [CrossRef]
19. Amor, N.B.; Michoulier, E.; Simon, A. Electronic excited states of benzene in interaction with water clusters: Influence of structure and size. *Theor. Chem. Accounts* **2021**, *140*, 70. [CrossRef]
20. Deng, Y.; Yu, D.; Cao, X.; Liu, L.; Rong, C.; Lu, T.; Liu, S. Structure, aromaticity and reactivity of corannulene and its analogues: A conceptual density functional theory and density functional reactivity theory study. *Mol. Phys.* **2018**, *116*, 956–968. [CrossRef]
21. Cami, J.; Bernard-Salas, J.; Peeters, E.; Malek, S.E. Detection of C₆₀ and C₇₀ in a Young Planetary Nebula. *Science* **2010**, *329*, 1180–1182. [CrossRef]
22. Sellgren, K.; Werner, M.W.; Ingalls, J.G.; Smith, J.D.T.; Carleton, T.M.; Joblin, C. C₆₀ in Reflection Nebulae. *Astrophys. J. Lett.* **2010**, *722*, L54. [CrossRef]
23. García-Hernández, D.A.; Manchado, A.; García-Lario, P.; Stanghellini, L.; Villaver, E.; Shaw, R.A.; Szczerba, R.; Perea-Calderon, J.V. Formation of fullerenes in H-containing planetary nebulae. *Astrophys. J. Lett.* **2010**, *724*, L39. [CrossRef]
24. García-Hernández, D.A.; Kameswara Rao, N.; Lambert, D.L. Are C-60 molecules detectable in circumstellar shells of R coronae berae stars? *Astrophys. J.* **2011**, *729*, 126. [CrossRef]
25. García-Hernández, D.A.; Iglesias-Groth, S.; Acosta-Pulido, J.A.; Manchado, A.; García-Lario, P.; Stanghellini, L.; Villaver, E.; Shaw, R.A.; Cataldo, F. The formation of fullerenes: Clues from new C-60, C-70, and (possible) planar C-24 detections in magellanic cloud planetary nebulae. *Astrophys. J. Lett.* **2011**, *737*, L30. [CrossRef]
26. García-Hernández, D.A.; Villaver, E.; García-Lario, P.; Acosta-Pulido, J.A.; Manchado, A.; Stanghellini, L.; Shaw, R.A.; Cataldo, F. Infrared study of fullerene planetary nebulae. *Astrophys. J.* **2012**, *760*, 107. [CrossRef]
27. Berné, O.; Montillaud, J.; Joblin, C. Top-down formation of fullerenes in the interstellar medium. *Astron. Astrophys.* **2015**, *577*, A133. [CrossRef]
28. Zhen, J.; Castellanos, P.; Paardekooper, D.M.; Linnartz, H.; Tielens, A.G.G.M. Laboratory formation of fullerenes from PAHs: Top-down interstellar chemistry. *Astrophys. J.* **2014**, *797*, L30. [CrossRef]
29. Omont, A. Interstellar fullerene compounds and diffuse interstellar bands. *Astron. Astrophys.* **2016**, *590*, A52. [CrossRef]
30. Berné, O.; Tielens, A.G.G.M. Formation of buckminsterfullerene (C-60) in interstellar space. *Proc. Natl. Acad. Sci. USA* **2012**, *109*, 401. [CrossRef]
31. Dunk, P.W.; Kaiser, N.K.; Hendrickson, C.L.; Quinn, J.P.; Ewels, C.P.; Nakanishi, Y.; Sasaki, Y.; Shinohara, H.; Marshall, A.G.; Kroto, H.W. Closed network growth of fullerenes. *Nat. Comm.* **2012**, *3*, 855. [CrossRef]
32. Gavilan, L.; Alata, I.; Le, K.; Pino, T.; Giuliani, A.; Dartois, E. VUV spectroscopy of carbon dust analogs: Contribution to interstellar extinction. *Astron. Astrophys.* **2016**, *586*, A106. [CrossRef]
33. Dubosq, C.; Calvo, F.; Rapacioli, M.; Dartois, E.; Pino, T.; Falvo, C.; Simon, A. Quantum modeling of the optical spectra of carbon clusters structural families and relation to the interstellar extinction UV-bump. *Astron. Astrophys.* **2020**, *634*, A62. [CrossRef]
34. Carpentier, Y.; Feraud, G.; Dartois, E.; Brunetto, R.; Charon, E.; Cao, A.T.; d'Hendecourt, L.; Brechignac, P.; Rouzaud, J.N.; Pino, T. Nanostructuring of carbonaceous dust as seen through the positions of the 6.2 and 7.7 μm AIBs. *Astron. Astrophys.* **2012**, *548*, A40. [CrossRef]
35. Gavilan, L.; Le, K.C.; Pino, T.; Alata, I.; Giuliani, A.; Dartois, E. Polyaromatic disordered carbon grains as carriers of the UV bump: Far-UV to mid-IR spectroscopy of laboratory analogs. *Astron. Astrophys.* **2017**, *607*, A73. [CrossRef]
36. Dubosq, C.; Falvo, C.; Calvo, F.; Rapacioli, M.; Parneix, P.; Pino, T.; Simon, A. Mapping the structural diversity of C₆₀ carbon clusters and their infrared response. *Astron. Astrophys.* **2019**, *625*, L11. [CrossRef]
37. Calvo, F.; Simon, A.; Parneix, P.; Falvo, C.; Dubosq, C. Infrared Spectroscopy of Chemically Diverse Carbon Clusters: A Data-Driven Approach. *J. Phys. Chem. A* **2021**, *125*, 5509–5518. [CrossRef]
38. Pilleri, P.; Herberth, D.; Giesen, T.F.; Gerin, M.; Joblin, C.; Mulas, G.; Mallocci, G.; Grabow, J.U.; Brünken, S.; Surin, L.; et al. Search for corannulene (C₂₀H₁₀) in the Red Rectangle. *Mon. Not. R. Astron. Soc.* **2009**, *397*, 1053–1060. [CrossRef]
39. Rouillé, G.; Jäger, C.; Steglich, M.; Huisken, F.; Henning, T.; Theumer, G.; Bauer, I.; Knölker, H.J. IR, Raman, and UV/Vis Spectra of Corannulene for Use in Possible Interstellar Identification. *ChemPhysChem* **2008**, *9*, 2085–2091. [CrossRef]
40. Zhao, L.; Doddipatla, S.; Kaiser, R.I.; Lu, W.; Kostko, O.; Ahmed, M.; Tuli, L.B.; Morozov, A.N.; Howlader, A.H.; Wnuk, S.F.; et al. Gas-phase synthesis of corannulene—A molecular building block of fullerenes. *Phys. Chem. Chem. Phys.* **2021**, *23*, 5740–5749. [CrossRef]

41. Stuparu, M.C. Corannulene: A Curved Polyarene Building Block for the Construction of Functional Materials. *Acc. Chem. Res.* **2021**, *54*, 2858–2870. [CrossRef]
42. Hernández-Rojas, J.; Calvo, F.; Rabilloud, F.; Bretón, J.; Gomez Llorente, J.M. Modeling Water Clusters on Cationic Carbonaceous Seeds. *J. Phys. Chem. A* **2010**, *114*, 7267–7274. [CrossRef] [PubMed]
43. Pérez, C.; Steber, A.L.; Rijs, A.M.; Temelso, B.; Shields, G.C.; Lopez, J.C.; Kisiel, Z.; Schnell, M. Corannulene and its complex with water: A tiny cup of water. *Phys. Chem. Chem. Phys.* **2017**, *19*, 14214–14223. [CrossRef] [PubMed]
44. Heine, T.; Rapacioli, M.; Patchkovskii, S.; Frenzel, J.; Koster, A.; Calaminici, P.; Duarte, H.A.; Escalante, S.; Flores-Moreno, R.; Goursot, A.; et al. deMonNano. 2009. Available online: <http://demon-nano.ups-tlse.fr/> (accessed on 27 February 2022).
45. Elstner, M.; Porezag, D.; Jungnickel, G.; Elsner, J.; Haugk, M.; Frauenheim, T.; Suhai, S.; Seifert, G. Self-consistent-charge density-functional tight-binding method for simulations of complex material properties. *Phys. Rev. B* **1998**, *58*, 7260–7268. [CrossRef]
46. Li, J.; Zhu, T.; Cramer, C.; Truhlar, D. New Class IV Charge Model for Extracting Accurate Partial Charges from Wave Functions. *J. Phys. Chem. A* **1998**, *102*, 1820–1831. [CrossRef]
47. Rapacioli, M.; Spiegelman, F.; Talbi, D.; Mineva, T.; Goursot, A.; Heine, T.; Seifert, G. Correction for dispersion and Coulombic interactions in molecular clusters with density functional derived methods: Application to polycyclic aromatic hydrocarbon clusters. *J. Chem. Phys.* **2009**, *130*, 244304. [CrossRef]
48. Simon, A.; Rapacioli, M.; Mascetti, J.; Spiegelman, F. Vibrational spectroscopy and molecular dynamics of water monomers and dimers adsorbed on polycyclic aromatic hydrocarbons. *Phys. Chem. Chem. Phys.* **2012**, *14*, 6771–6786. [CrossRef]
49. Kalinowski, J.; Lesyng, B.; Thompson, J.; Cramer, C.; Truhlar, D. Class IV Charge Model for the Self-Consistent Charge Density-Functional Tight-Binding Method. *J. Phys. Chem. A* **2004**, *108*, 2545–2549. [CrossRef]
50. Joalland, B.; Rapacioli, M.; Simon, A.; Joblin, C.; Marsden, C.J.; Spiegelman, F. Molecular Dynamics Simulations of Anharmonic Infrared Spectra of [SiPAH](+) pi-Complexes. *J. Phys. Chem. A* **2010**, *114*, 5846–5854. [CrossRef]
51. Simon, A.; Spiegelman, F. Water clusters adsorbed on polycyclic aromatic hydrocarbons: Energetics and conformational dynamics. *J. Chem. Phys.* **2013**, *138*, 194309. [CrossRef]
52. Simon, A.; Spiegelman, F. Conformational dynamics and finite-temperature infrared spectra of the water octamer adsorbed on coronene. *Comput. Theor. Chem.* **2013**, *1021*, 54–61. [CrossRef]
53. Michoulier, E.; Toubin, C.; Simon, A.; Mascetti, J.; Aupetit, C.; Noble, J.A. Perturbation of the Surface of Amorphous Solid Water by the Adsorption of Polycyclic Aromatic Hydrocarbons. *J. Phys. Chem. C* **2020**, *124*, 2994–3001. [CrossRef]
54. Aziz, R.A. A highly accurate interatomic potential for argon. *J. Chem. Phys.* **1993**, *99*, 4518–4525. [CrossRef]
55. Iftner, C.; Simon, A.; Korchagina, K.; Rapacioli, M.; Spiegelman, F. A density functional tight binding/force field approach to the interaction of molecules with rare gas clusters: Application to (C₆H₆)⁺⁰Ar_n clusters. *J. Chem. Phys.* **2014**, *140*, 034301. [CrossRef] [PubMed]
56. Simon, A.; Iftner, C.; Mascetti, J.; Spiegelman, F. Water Clusters in an Argon Matrix: Infrared Spectra from Molecular Dynamics Simulations with a Self-Consistent Charge Density Functional-Based Tight Binding/Force-Field Potential. *J. Phys. Chem. A* **2015**, *119*, 2449. [CrossRef]
57. Crépin, C.; Pujó, P.d.; Bouvier, B.; Brenner, V.; Millié, P. A simulation of naphthalene matrix isolation: Comparison with experiments. *Chem. Phys.* **2001**, *272*, 243–258. [CrossRef]
58. Ceponkus, J.; Uvdal, P.; Nelander, B. Acceptor Switching and Axial Rotation of the Water Dimer in Matrices, observed by Infrared Spectroscopy. *J. Chem. Phys.* **2010**, *133*, 074301. [CrossRef]
59. Perchard, J. Anharmonicity and Hydrogen Bonding. III. Analysis of the Near Infrared Spectrum of Water Trapped in Argon Matrix. *Chem. Phys.* **2001**, *273*, 217–233. [CrossRef]
60. Michaut, X.; Vasserot, A.M.; Abouaf-Marguin, L. Temperature and Time Effects on the Rovibrational Structure of Fundamentals of H₂O Trapped in Solid Argon: Hindered Rotation and RTC Satellite. *Vib. Spec.* **2004**, *34*, 83–93. [CrossRef]
61. Ceponkus, J.; Karlstro, G.; Nelander, B. Intermolecular Vibrations of the Water Trimer, a Matrix Isolation Study. *J. Chem. Phys. A* **2005**, *109*, 7859–7864. [CrossRef]
62. Bentwood, R.; Barnes, A.; Orville-Thomas, W. Studies of intermolecular interactions by matrix isolation vibrational spectroscopy: Self-association of water. *J. Mol. Spectrosc.* **1980**, *84*, 391–404. [CrossRef]
63. Buck, U.; Huisken, F. Infrared Spectroscopy of Size-Selected Water and Methanol Clusters. *Chem. Rev.* **2000**, *100*, 3863–3890. [CrossRef]
64. Ceponkus, J.; Uvdal, P.; Nelander, B. Water Tetramer, Pentamer, and Hexamer in Inert Matrices. *J. Phys. Chem. A* **2012**, *116*, 4842–4850. [CrossRef]
65. Ceponkus, J.; Engdahl, A.; Uvdal, P.; Nelander, B. Structure and Dynamics of Small Water Clusters, Trapped in Inert Matrices. *Chem. Phys. Lett.* **2013**, *581*, 1–9. [CrossRef]
66. Coussan, S.; Loutellier, A.; Perchard, J.; Racine, S.; Bouteiller, Y. Matrix isolation infrared spectroscopy and DFT calculations of complexes between water and nitrogen. *J. Mol. Struct.* **1998**, *471*, 37–47. [CrossRef]
67. Hirabayashi, S.; Yamada, K.M. Infrared Spectra and Structure of Water Clusters Trapped in Argon and Krypton Matrices. *J. Mol. Struct.* **2006**, *795*, 78–83. [CrossRef]

68. Bauschlicher, C.W.; Ricca, A.; Boersma, C.; Allamandola, L.J. The NASA Ames PAH IR Spectroscopic Database: Computational Version 3.00 with Updated Content and the Introduction of Multiple Scaling Factors. *Astrophys. J. Suppl. Ser.* **2018**, *234*, 32. [CrossRef]
69. Boersma, C.; Bauschlicher, C.W.; Ricca, A.; Mattioda, A.L.; Cami, J.; Peeters, E.; de Armas, F.S.; Saborido, G.P.; Hudgins, D.M.; Allamandola, L.J. The NASA AMES PAH spectroscopic database version 2.00: Updated content, web site and on off line tools. *Astrophys. J. Suppl. Ser.* **2014**, *211*, 8. [CrossRef]
70. Mattioda, A.L.; Hudgins, D.M.; Boersma, C.; Bauschlicher, C.W.; Ricca, A.; Cami, J.; Peeters, E.; de Armas, F.S.; Saborido, G.P.; Allamandola, L.J. The NASA Ames PAH IR Spectroscopic Database: The Laboratory Spectra. *Astrophys. J. Suppl. Ser.* **2020**, *251*, 22. [CrossRef]
71. Vauthey, E. Elucidating the Mechanism of Bimolecular Photoinduced Electron Transfer Reactions. *J. Phys. Chem. B* **2022**, *126*, 778–788. [CrossRef]

Article

Phosphorescence of Hydrogen-Capped Linear Polyynes Molecules C_8H_2 , $C_{10}H_2$ and $C_{12}H_2$ in Solid Hexane Matrices at 20 K

Tomonari Wakabayashi ^{1,*}, Urszula Szczepaniak ², Kaito Tanaka ¹, Satomi Saito ¹, Keisuke Fukumoto ¹, Riku Ohnishi ¹, Kazunori Ozaki ¹, Taro Yamamoto ¹, Hal Suzuki ¹, Jean-Claude Guillemin ³, Haruo Shiromaru ⁴, Takeshi Kodama ⁵ and Miho Hatanaka ⁶

¹ Department of Chemistry, School of Science and Engineering, Kindai University, Kowakae 3-4-1, Higashi-Osaka 577-8502, Japan; tomioka.baseball26@gmail.com (K.T.); osatomi.0430@gmail.com (S.S.); f.keisuke.0218@icloud.com (K.F.); 2133310144u@kindai.ac.jp (R.O.); 1410320657g@kindai.ac.jp (K.O.); kooraa00132357@gmail.com (T.Y.); h_suzuki@chem.kindai.ac.jp (H.S.)

² obvioTec AG, Garstligweg 8, 8634 Hombrechtikon, Switzerland; urszulka.szczepaniak@gmail.com

³ Univ Rennes, Ecole Nationale Supérieure de Chimie de Rennes, CNRS, ISCR—UMR6226, F-35000 Rennes, France; jean-claude.guillemin@ensc-rennes.fr

⁴ Department of Chemistry, Graduate School of Science, Tokyo Metropolitan University, Minami-Osawa 1-1, Hachioji 192-0364, Japan; shiromaru-haruo@tmu.ac.jp

⁵ Center for Basic Education and Integrated Learning, Kanagawa Institute of Technology, Shimo-Ogino 1030, Atsugi 243-0292, Japan; kodama-takeshi@gen.kanagawa-it.ac.jp

⁶ Department of Chemistry, Faculty of Science and Technology, Keio University, Hiyoshi 3-14-1, Yokohama 223-8522, Japan; hatanaka@chem.keio.ac.jp

* Correspondence: wakaba@chem.kindai.ac.jp; Tel.: +81-6-4307-3408

Citation: Wakabayashi, T.; Szczepaniak, U.; Tanaka, K.; Saito, S.; Fukumoto, K.; Ohnishi, R.; Ozaki, K.; Yamamoto, T.; Suzuki, H.; Guillemin, J.-C.; et al. Phosphorescence of Hydrogen-Capped Linear Polyynes Molecules C_8H_2 , $C_{10}H_2$ and $C_{12}H_2$ in Solid Hexane Matrices at 20 K. *Photochem* **2022**, *2*, 181–201. <https://doi.org/10.3390/photochem2010014>

Academic Editors: Rui Fausto and Robert Koles

Received: 2 February 2022

Accepted: 23 February 2022

Published: 28 February 2022

Publisher's Note: MDPI stays neutral with regard to jurisdictional claims in published maps and institutional affiliations.



Copyright: © 2022 by the authors. Licensee MDPI, Basel, Switzerland. This article is an open access article distributed under the terms and conditions of the Creative Commons Attribution (CC BY) license (<https://creativecommons.org/licenses/by/4.0/>).

Abstract: Laser-ablated polyynes molecules, $H(C\equiv C)_nH$, were separated by size in solutions and co-condensed with excess hexane molecules at a cryogenic temperature of 20 K in a vacuum system. The solid matrix samples containing C_8H_2 , $C_{10}H_2$, and $C_{12}H_2$ molecules were irradiated with UV laser pulses and the phosphorescence 0–0 band was observed at 532, 605, and 659 nm, respectively. Vibrational progression was observed for the symmetric stretching mode of the carbon chain in the ground state with increments of $\sim 2190\text{ cm}^{-1}$ for C_8H_2 , $\sim 2120\text{ cm}^{-1}$ for $C_{10}H_2$, and $\sim 2090\text{ cm}^{-1}$ for $C_{12}H_2$. Temporal decay analysis of the phosphorescence intensity revealed the lifetimes of the triplet state as $\sim 30\text{ ms}$ for C_8H_2 , $\sim 8\text{ ms}$ for $C_{10}H_2$, and $\sim 4\text{ ms}$ for $C_{12}H_2$. The phosphorescence excitation spectrum reproduces UV absorption spectra in the hexane solution and in the gas phase at ambient temperature, although the excitation energy was redshifted. The symmetry-forbidden vibronic transitions were observed for $C_{10}H_2$ by lower excitation energies of 25,500–31,000 cm^{-1} (320–390 nm). Detailed phosphorescence excitation patterns are discussed along the interaction of the polyynes molecule and solvent molecules of hexane.

Keywords: polyynes; phosphorescence; matrix isolation; electronic transition; molecular vibration

1. Introduction

Hydrogen-end-capped linear polyynes molecules, $H(C\equiv C)_nH$ or $C_{2n}H_2$ ($n \geq 2$), constitute a series of model compounds for *sp*-hybridized carbon species [1,2]. Since the discovery of cyanopolyynes, $H(C\equiv C)_nC\equiv N$ or $HC_{2n+1}N$ ($n \geq 2$), in the molecular clouds and circumstellar shells of a red giant (a carbon star in AGB) by radio astronomical observations [3–7], they have been thought of as candidates for interstellar molecules [8]. Laboratory experiments revealed UV absorption spectra of $C_{2n}H_2$ up to $n = 12$, thanks to the organic synthesis in the early 1970s [9,10]. Infrared absorption spectra, as well as the UV spectra, were measured for C_6H_2 and C_8H_2 in the gas phase [11,12]. Recently, cyanopolyynes of molecular formulae, $HC_{2n+1}N$, have been synthesized in the laboratory

up to $n = 2$ and reacted in cryogenic matrices into larger derivatives to identify their phosphorescence spectra [13–21]. Very recently, photosyntheses were conducted using polyynic precursors of HC_5N and C_4H_2 co-condensed in solid rare gas matrices, and the detection of phosphorescence of HC_9N was successful [18]. Using laser-ablated cyanopolyynes, the phosphorescence measurement was extended to HC_9N and HC_{11}N in solid organic molecules at 20 K as matrix hosts [22].

Polyynes were formed by the laser ablation of carbon particles [23,24] as well as by the arc discharge of graphite in organic solvents [1]. The formation of hydrogen-capped polyynes was confirmed up to C_{26}H_2 by the laser ablation in decalin [25]. Spectroscopic characterization has so far been performed by UV absorption [9,10], IR absorption [11,12,19,22,26], Raman [17,24], and resonance Raman spectroscopy [27,28]. In relation to the formation mechanism, $^1\text{H-NMR}$ and $^{13}\text{C-NMR}$ were applied to polyynes, C_{10}H_2 and C_{12}H_2 [28], and cyanopolyynes, HC_7N and HC_9N [29]. Using the size-separated polyynes of C_{2n}H_2 ($n = 5\text{--}8$), optical emission spectra were observed in solutions of hexane at ambient temperature [30]. Since the spectral range of the emission spanning from near-UV to visible [30] differs to that for the phosphorescence of cyanopolyynes of a relevant size [16,18], the emission was attributed to the fluorescence of polyynes. To obtain evidence for the assignment, we planned to observe the phosphorescence of C_{2n}H_2 ($n = 4\text{--}6$) in this work.

For the measurement of phosphorescence, it is crucial to keep the molecular samples at cryogenic temperature in a condensed phase. However, the unsaturated polyynes are highly reactive, leaving polymerized materials at high concentration. In solutions, the molecules are stable only under the dilute condition of less than ~ 1 mg/mL. We decided to allow the solution to be condensed directly on a cold surface under vacuum, where laser-induced phosphorescence measurements were performed. Dispersed phosphorescence spectra were recorded for C_8H_2 , C_{10}H_2 , and C_{12}H_2 within a range of 500–1000 nm by scanning the excitation wavelength in the ranges of UV, 213–302 nm, and near-UV, 302–409 nm, and converted to phosphorescence excitation spectra. Phosphorescence lifetimes were also measured and compared along the difference in size, n .

2. Materials and Methods

Polyynes were produced by the laser ablation of graphite particles in liquid hexane by irradiation with the 1064 nm output at ~ 0.5 J/pulse from a Nd:YAG laser system operated at 10 Hz (Continuum, Santa Clara, CA, USA, Powerlite 8010). The solution after laser irradiation was filtrated to remove solid particles to obtain a yellow solution, which is subjected to high-performance liquid chromatography (HPLC, Shimadzu, Kyoto, Japan, LC-10) using a polymeric ODS column (Wako Chemicals, Tokyo, Japan, Wakosil 5C-18AR, i.d. 10 mm \times 250 mm) eluted with hexane to separate the molecules of C_8H_2 , C_{10}H_2 , and C_{12}H_2 [24,28–30]. The concentration and purity of polyynes, C_{2n}H_2 , in the solution were estimated by the measurement of UV absorption spectra.

The C_8H_2 molecules isolated in a solution of hexane were condensed by using a rotary evaporator to a volume of ~ 1 mL at a concentration of ~ 1 mg/mL. Having similar molecular weights, 98 for C_8H_2 and 84 for hexane, the order of molecular number ratio of C_8H_2 to hexane is 1:1000, corresponding to the condition in which ten solvent molecules lie between two neighboring C_8H_2 molecules on average, though a fraction of C_8H_2 vaporizes together with hexane to reduce the efficiency of concentration. The concentrated solution was conducted into the vacuum system through a tubing of 0.10 mm in inner diameter. Reaching the exit of the tubing, the solution was sprayed onto a nearby copper slab cooled at 20 K using a closed-cycle helium refrigerator (Daikin, Osaka, Japan, V202CL), where the C_8H_2 molecules and the excess hexane molecules were co-condensed as an opaque, milky white, solid matrix sample. By the rapid introduction of the solution within several seconds, even droplets were directly condensed on the cold surface. The dimerization of C_8H_2 molecules was minimized and the C_8H_2 /hexane ratio in the solid matrix sample was more or less the same as the precursory condensed solution. The introduction of the room

temperature solution results in the instantaneous warming of the cold surface to ~60 K. The measurement was performed after waiting for the cold surface to be cooled down to 20 K.

The solid matrix sample at 20 K was irradiated with UV laser pulses of the second harmonic of an OPO output excited with nanosecond 355 nm laser pulses (Spectra Physics, Santa Clara, CA, USA, VersaScan-MB/INDI40). Emitted photons from the surface of the UV-irradiated matrix sample were collected through an optical-fiber bundle and dispersed by a polychromator (Acton Research Corporation, Acton, MA, USA, Model 320i) and recorded on a liquid-nitrogen-cooled CCD array detector (Princeton Instruments, Trenton, NJ, USA, PyLoN:256-OE) in a spectral range of 500–1000 nm. A long-pass glass filter having an appropriate cut-off wavelength was used to reduce stray light. The excitation wavelength was slowly scanned in a range of 213–302 nm and a series of dispersed emission spectra were recorded redundantly. Spectral resolution was ~0.1 nm for dispersed phosphorescence and 0.2–0.5 nm for the excitation spectrum.

Lifetime measurement was performed for selected bands of phosphorescence by using a photomultiplier detector (Hamamatsu Photonics, Hamamatsu, Japan, R928) and a digitizing oscilloscope (LeCroy, Chestnut Ridge, NY, USA, WavePro 954). The waveform of amplified phosphorescence signals was summed over 1000 laser pulses and transferred to a PC. The same experimental procedures of the spectral measurement and the lifetime measurement for C_8H_2 were applied also to $C_{10}H_2$ and $C_{12}H_2$. For the longer wavelength excitation in 302–409 nm for $C_{10}H_2$, the sum-frequency mixing (SFM) of the OPO system was exploited.

3. Results

3.1. Phosphorescence Spectra and Excitation Spectra

Figure 1 shows a dispersed phosphorescence spectrum of C_8H_2 embedded in a solid hexane matrix at 20 K, observed at the excitation of 231.8 nm. Peaks are conspicuous at 532.3, 602.4, 693.2, 815.1, and 986.9 nm for the 0–0, 0–1, 0–2, 0–3, and 0–4 bands, respectively. Adjacent peaks in the series of transitions from the $v = 0$ level in the upper electronic state to $v = 0, 1, 2, 3,$ and 4 levels in the lower electronic state are separated by successive increments of 2190, 2172, 2157, and 2136 cm^{-1} , which are attributable to the member of a vibrational progression of the symmetric stretching σ_g mode of the sp -carbon chain in the electronic ground state, $X^1\Sigma_g^+$. The upper state of the phosphorescence is the lowest triplet state, $a^3\Sigma_u^+$. Smaller peaks are discernible between the high-intensity peaks. Appearing in a similar pattern repeatedly in the gaps, these tiny peaks are attributable to combination bands of some symmetric vibrational species with the symmetric stretching σ_g mode.

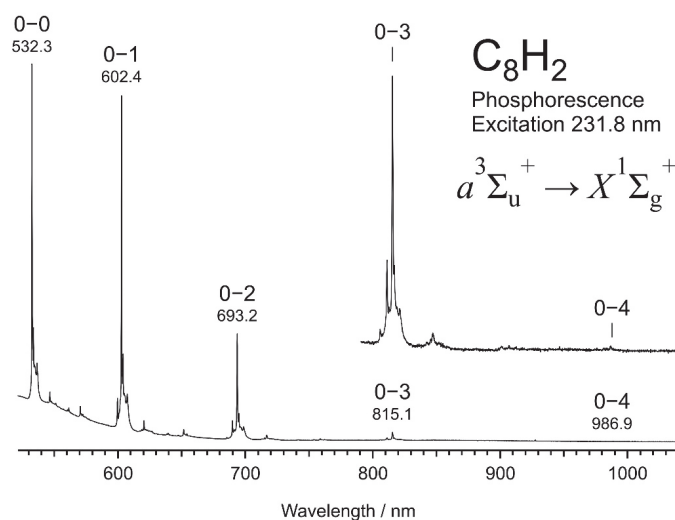


Figure 1. Dispersed phosphorescence spectrum of C_8H_2 , $a^3\Sigma_u^+ \rightarrow X^1\Sigma_g^+$, in solid hexane at 20 K induced by the excitation with UV photons at 231.8 nm.

Figure 2 illustrates the phosphorescence excitation mapping for the 0–1 band of C_8H_2 at 602.5 nm. Relatively strong emission was observed when the excitation wavelength was set at 232 nm and 221 nm. The trace in white at the bottom of the panel represents the intensity of the horizontal cross section at the excitation of 232 nm. The peak at 602.5 nm is again the 0–1 band of the phosphorescence. Small peaks near 620 and 640 nm are the combinations. A few satellite peaks accompany the foot of the main peak at 602.5 nm, which are signals belonging to the same σ_g mode, but their photons of phosphorescence are emitted from molecules in different environments in the matrix sample. A less intense but almost identical phosphorescence spectrum is obtained at the excitation of 221 nm. The series of spots corresponding to the phosphorescence peaks are discernible along the horizontal line at 221 nm in the mapping. As a result, the strong phosphorescence peak at 602.5 nm appears twice, at excitation wavelengths of 232 and 221 nm. When the intensity of phosphorescence at 602.5 nm is plotted as a function of the excitation wavelength, we obtain another spectrum in yellow in the left of the panel. This action spectrum primarily represents the strength of absorption at relevant UV wavelength and is called an excitation spectrum. The upper electronic state is designated as $^1\Sigma_u^+$, to which the UV photon lifts the molecule to be excited from the ground state, $X^1\Sigma_g^+$.

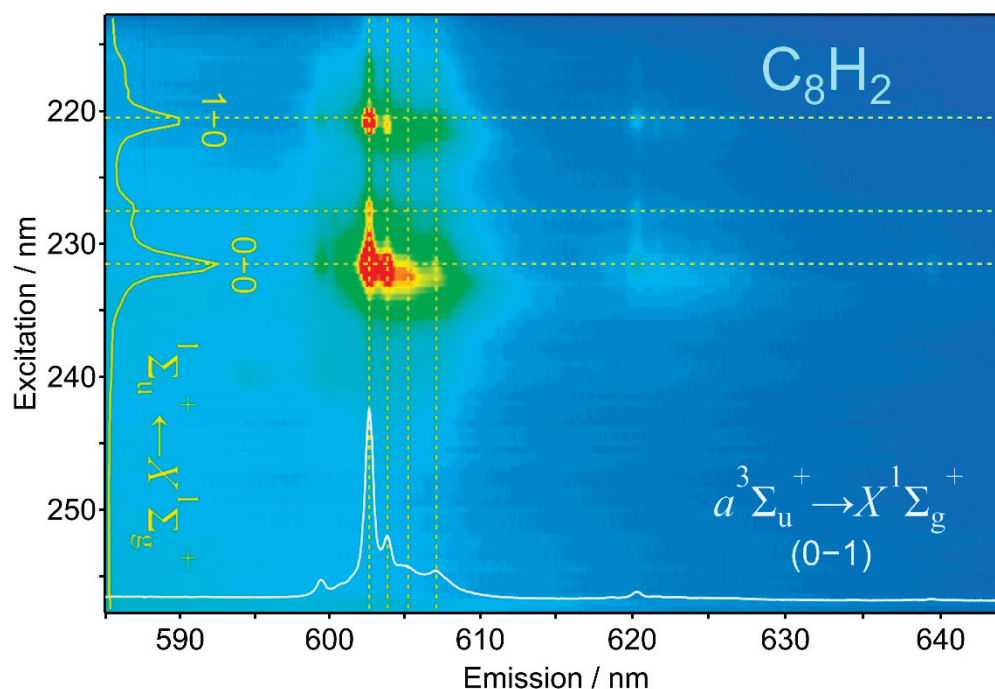


Figure 2. Phosphorescence excitation mapping of C_8H_2 in solid hexane at 20 K probed by the emission intensity of the 0–1 band peaking at 602.5 nm.

Figure 3 shows the excitation spectrum for the 0–1 band in the phosphorescence at 603 nm of C_8H_2 , plotted as a function of energy. The intensity is scaled according to the conversion from wavelength to energy. Two major bands, namely the 0–0 band at $43,113\text{ cm}^{-1}$ and the 1–0 band at $45,243\text{ cm}^{-1}$, constitute the vibrational progression of the symmetric stretching σ_g mode in the excited state, $^1\Sigma_u^+$. The increment of 2130 cm^{-1} is smaller than the phosphorescence counterpart of 2190 cm^{-1} , indicating a slightly shallow potential with a lower harmonic frequency in the excited state, $^1\Sigma_u^+$. The overall shape of the excitation spectrum and the vibrational frequency in the upper state are explainable by the absorption of a UV photon via the fully allowed electric dipole transition, $^1\Sigma_u^+ \leftarrow X^1\Sigma_g^+$. When the transition energy of the 0–0 band is compared with that observed at $43,960\text{ cm}^{-1}$ by UV absorption in the solution of hexane, the peak in the solid matrix is redshifted by 847 cm^{-1} . Weaker bands or shoulders at the higher energy side of the major bands in Figure 3 are

rather close to the bands in the UV absorption spectrum in the solution of hexane, i.e., at 227 nm ($44,050\text{ cm}^{-1}$) for the 0–0 band and 216 nm ($46,300\text{ cm}^{-1}$) for the 1–0 band. The band with a shoulder in the phosphorescence excitation curve is fitted with three Gaussian functions to provide two narrow bands and a broad component for the base line. Among the two sets of the narrow-band features, one is the major component of high intensity, and the other is the minor component at the shoulder located close to the position of peaks in the solution at ambient temperature.

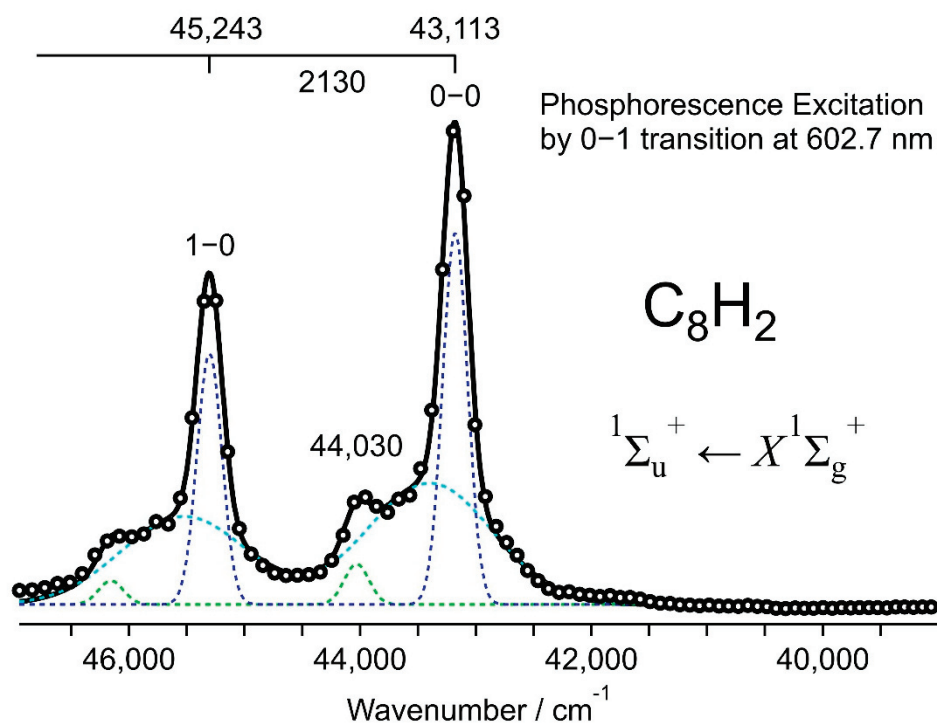


Figure 3. Phosphorescence excitation spectrum of C_8H_2 in solid hexane at 20 K plotted by the emission intensity at 602.7 nm for the 0–1 band of the $a^3\Sigma_u^+ \rightarrow X^1\Sigma_g^+$ transition (open circles). The spectral features correspond to the absorption spectrum for the fully allowed electronic transition in the UV, ${}^1\Sigma_u^+ \leftarrow X^1\Sigma_g^+$.

Figure 4 compares the dispersed phosphorescence spectra of C_8H_2 , C_{10}H_2 and C_{12}H_2 with the excitation at 231.8, 259.0, and 282.0 nm, respectively, where the phosphorescence intensity is maximum for each size. As is expected for a particle-in-a-box model, the phosphorescence wavelength, as well as the excitation wavelength, shifts to a longer wavelength as the size of the carbon chain increases. The 0–0 band of phosphorescence appears at 532.3 nm for C_8H_2 , 605.1 nm for C_{10}H_2 , and 658.8 nm for C_{12}H_2 . The vibrational progression is conspicuous for the symmetric stretching σ_g mode for each polyynes, exhibiting an increment of ~ 2190 , ~ 2120 , and $\sim 2090\text{ cm}^{-1}$ for C_{2n}H_2 of $n = 4, 5$, and 6 , respectively. The bands of C_{10}H_2 and C_{12}H_2 are relatively broad compared with those of C_8H_2 , probably because of the lack of uniformity in the packing patterns of molecules surrounding the C_{2n}H_2 molecule. As is seen in the dashed line for C_{10}H_2 in Figure 4, a slightly different excitation wavelength at 261.7 nm provides a different band shape with a sharp phosphorescence peak at 599.4 nm, and with a broad distribution of satellites up to 605 nm. The detailed matrix effect is discussed in the latter Section 4.4. Despite the broadness of bands, peaks are discernible for major features: (1) the σ_g vibrational progression with three bands and (2) the combination bands between the major bands of σ_g .

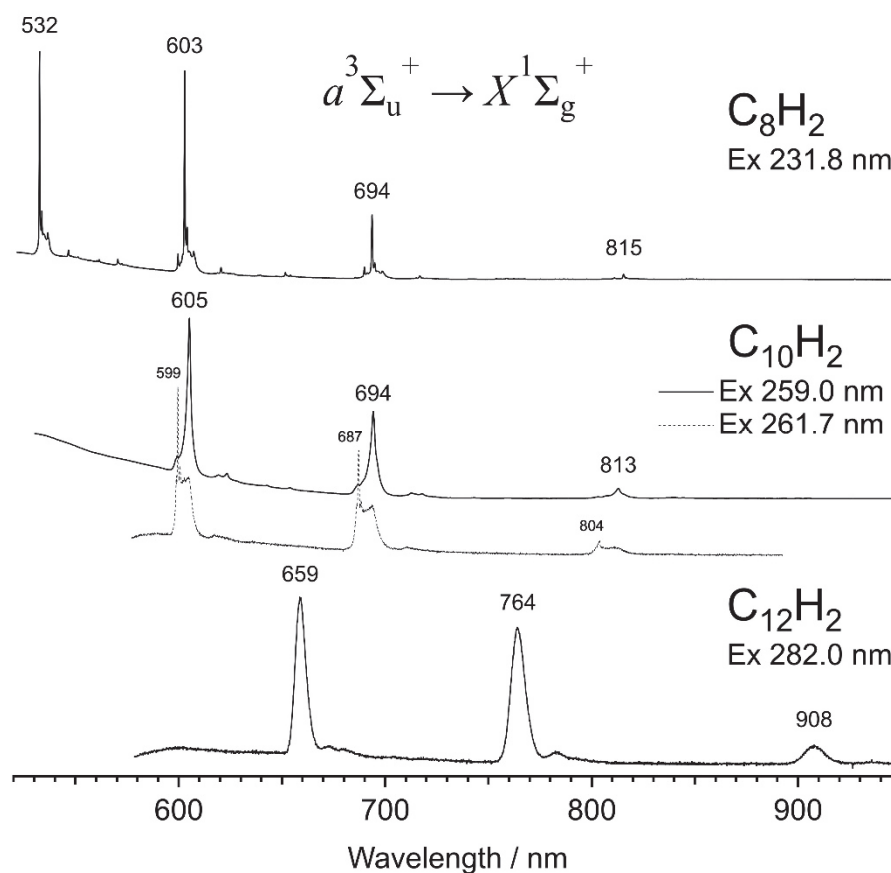


Figure 4. Dispersed phosphorescence spectra of C_8H_2 , $C_{10}H_2$, and $C_{12}H_2$ in solid hexane at 20 K.

Figure 5a shows the phosphorescence excitation spectrum obtained from the intensity of the 0–0 band of $C_{10}H_2$ in solid hexane at 20 K. The absorption spectra of $C_{10}H_2$ at ambient temperature are shown for comparison (b) in the solution of hexane and (c) in the gas phase. The measurement of the spectrum in the gas phase (c) is conducted as follows; a small amount of the concentrated solution of $C_{10}H_2$ in hexane was introduced into an evacuated quartz cell of 10 cm path length and the cell was set in the sample chamber of the double-beam UV spectrophotometer (Jasco, Hachioji, Japan, V-670). The 0–0 band peaked at $43,690\text{ cm}^{-1}$ (228.9 nm) in (c) and at $39,640\text{ cm}^{-1}$ (252.3 nm) in (b), indicating a solvent shift of -4050 cm^{-1} for hexane. In the excitation spectrum (a) for the hexane matrix at 20 K, the most intense band peaked at $38,728\text{ cm}^{-1}$ (258.2 nm), revealing a further redshift of -912 cm^{-1} from the peak in the hexane solution. In general, the tight packing of the solvent molecules in cryogenic solid matrices results in a stronger interaction between the host and guest molecules, and the electronically excited state of the guest polyyne molecule is stabilized further to redshift its absorption/excitation spectrum.

Figure 6 shows the phosphorescence excitation mapping of the 0–1 band of $C_{12}H_2$ (left) and an excitation spectrum (right) plotted using the phosphorescence intensity at 761.7 nm (solid line). The absorption spectrum in the solution at ambient temperature is overlapped (dashed line), showing the redshift of -840 cm^{-1} for the solid matrix relative to the liquid solution of $C_{12}H_2$ /hexane. Table 1 summarizes the observed peaks in the phosphorescence excitation spectra of C_8H_2 , $C_{10}H_2$, and $C_{12}H_2$, together with their absorption peaks in solutions and in the gas phase. Molecular constants in the electronically excited state, $^1\Sigma_u^+$, are listed in Table 2. Figure 7 plots the transition energies of the electronic $^1\Sigma_u^+ \leftrightarrow X^1\Sigma_g^+$ system of $C_{2n}H_2$ ($n = 4-6$), showing the solvent shift (gas–solution) and the matrix shift (solution–solid matrix).

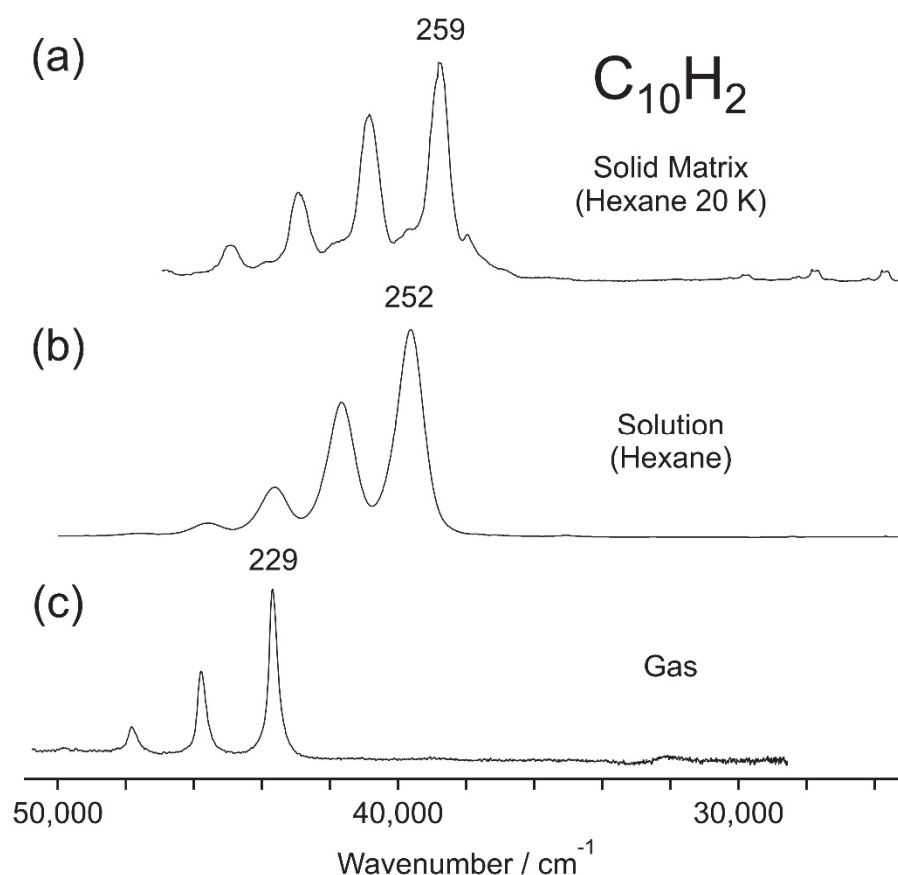


Figure 5. (a) Phosphorescence excitation spectrum of $C_{10}H_2$ in solid hexane at 20 K plotted by the emission intensity at 605 nm for the 0–0 band in the $a^3\Sigma_u^+ \rightarrow X^1\Sigma_g^+$ transition. Absorption spectra of $C_{10}H_2$, $^1\Sigma_u^+ \leftarrow X^1\Sigma_g^+$, (b) in the solution of hexane and (c) in the gas phase, are plotted for comparison. Numbers atop the peak maxima are the wavelengths in nm.

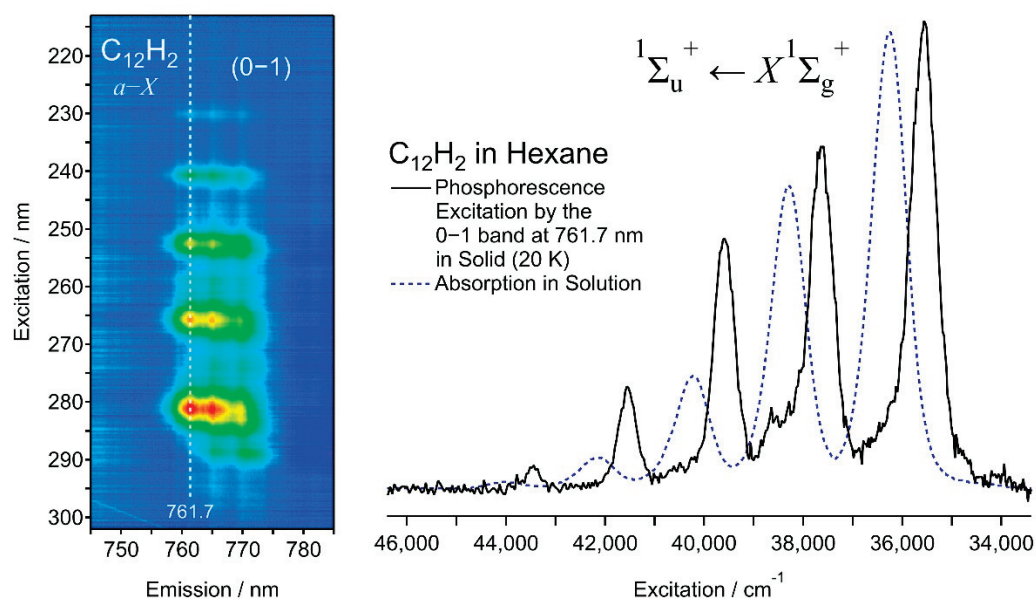


Figure 6. Phosphorescence excitation mapping (left) and the excitation spectrum probed by the emission intensity at 761.7 nm (right) of $C_{12}H_2$ in solid hexane at 20 K. Absorption spectrum of $C_{12}H_2$ in hexane solution at room temperature (dashed line in blue) is shown for comparison.

Table 1. Peaks in cm^{-1} (nm) for the phosphorescence excitation spectra of polyynes molecules, C_{2n}H_2 ($n = 4-6$), in solid hexane matrices at 20 K. Peaks in the absorption spectra in the hexane solution and in the gas phase are listed for comparison.

Molecule	Assignment ¹	Solid Matrix Hexane (20 K)	Solution ² Hexane	Gas Phase ²
C_8H_2	0-0	43,113 (231.9)	43,960 (227.5)	48,190 (207.5)
	1-0	45,243 (221.0)	46,080 (217.0)	50,280 (198.9)
	2-0		48,190 (207.5)	52,380 (190.9)
C_{10}H_2	0-0	38,728 (258.2)	39,640 (252.3)	43,690 (228.9)
	1-0	40,815 (245.0)	41,670 (240.0)	45,790 (218.4)
	2-0	42,909 (233.1)	43,630 (229.2)	47,820 (209.1)
	3-0	44,940 (222.5)	45,600 (219.3)	
C_{12}H_2	0-0	35,420 (282.3)	36,260 (275.8)	40,370 (247.7)
	1-0	37,511 (266.6)	38,300 (261.1)	42,340 (236.2)
	2-0	39,469 (253.4)	40,230 (248.6)	44,250 (226.0)
	3-0	41,457 (241.2)	42,160 (237.2)	
	4-0	43,292 (231.0)	44,010 (227.2)	

¹ Change in the symmetric stretching σ_g vibrational level in the ${}^1\Sigma_u^+ \leftarrow X^1\Sigma_g^+$ transition. ² Measurement at room temperature.

Table 2. Molecular constants in cm^{-1} of the electronically excited state, ${}^1\Sigma_u^+$, of polyynes molecules, C_{2n}H_2 ($n = 4-6$) in solid/liquid hexane and in the gas phase. Vibrational constants, ω_e' and $\omega_e x_e'$, are for the alternating CC stretching σ_g mode.

Molecule	Constant	Solid cm^{-1}	Solution cm^{-1}	Gas cm^{-1}
C_8H_2	$T^* 1$	42,048	42,896	47,145
	ω_e'	2130 ²	2130	2090 ²
	$\omega_e x_e'$	–	5	–
C_{10}H_2	$T^* 1$	37,663	38,626	42,614
	ω_e'	2129	2044	2170
	$\omega_e x_e'$	14	15	35
C_{12}H_2	$T^* 1$	34,361	35,237	39,362
	ω_e'	2141	2072	2030
	$\omega_e x_e'$	34	27	30

¹ $T^* = T_0 - \omega_e''/2 + \omega_e x_e''/4$. Zero-point energy in the electronic ground state is included. ² Difference in the transition energies for the 1-0 and 0-0 bands.

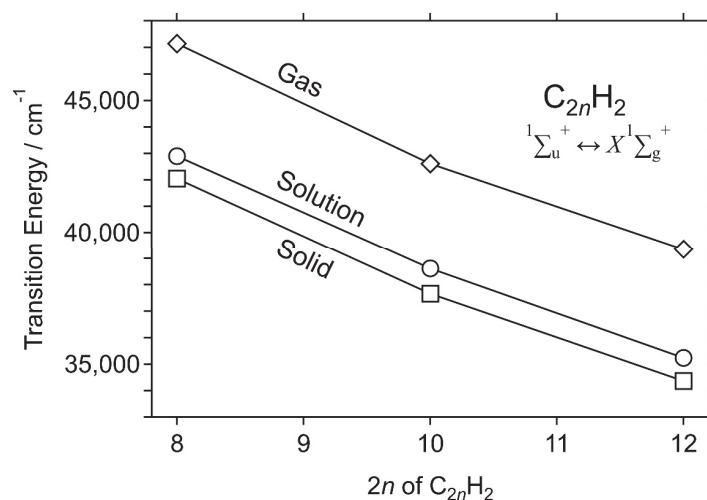


Figure 7. Transition energies of the electronic ${}^1\Sigma_u^+ \leftrightarrow X^1\Sigma_g^+$ system of C_{2n}H_2 ($n = 4-6$) under the three different conditions in the gas phase, hexane solutions, and solid hexane matrices.

3.2. Lifetimes

Figure 8 illustrates the typical decay profiles of phosphorescence intensity at 20 K for the 0–0 and 0–1 bands of C_8H_2 (red), $C_{10}H_2$ (black), and $C_{12}H_2$ (blue). From the slope of the logarithmic plot, phosphorescence lifetime was deduced for each trace by fitting to a single exponential component. The lifetime was ~ 31 ms for C_8H_2 , ~ 8.4 ms for $C_{10}H_2$, and ~ 3.9 ms for $C_{12}H_2$, showing a decreasing property as the number of carbon atoms in a molecule increases. A longer polyynic such as $C_{14}H_2$ should exhibit a weak phosphorescence signal at a longer wavelength.

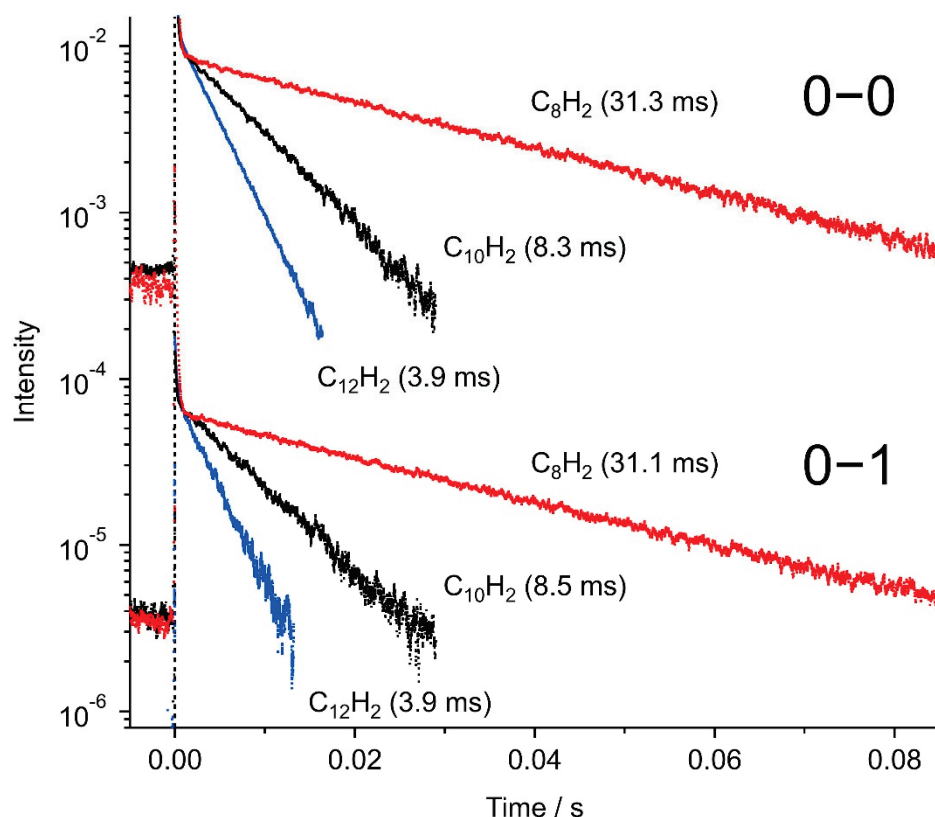


Figure 8. Temporal decay profiles of selected phosphorescence peaks in the 0–0 and 0–1 bands of C_8H_2 , $C_{10}H_2$, and $C_{12}H_2$ in solid hexane at 20 K. For C_8H_2 , plots are the emission peak intensities at 533 nm (0–0) and 603 nm (0–1) by the excitation at 231.0 nm. Similarly, the emission at 603 nm (0–0) and 692 nm (0–1) by the excitation at 257.0 nm for $C_{10}H_2$, and the emission at 660 nm (0–0) and 765 nm (0–1) by the excitation at 282.0 nm for $C_{12}H_2$.

For $C_{10}H_2$, depending on the phosphorescence peak wavelengths within the 0–0 band (599–605 nm), the observed decay rates deviated from 6 ms to 16 ms due to the different rates of intersystem crossing and/or internal conversion in the different trapping sites in the solid matrix host.

3.3. Vibrational Bands

Vibrational overtones and combinations in the dispersed phosphorescence in Figures 1 and 4 are summarized in Table 3. Figure 9 plots the observed vibrational levels for (a) C_8H_2 , (b) $C_{10}H_2$, and (c) $C_{12}H_2$. The electronic transition from the lowest triplet state to the ground state, $a^3\Sigma_u^+ \rightarrow X^1\Sigma_g^+$, is spin forbidden but the other conditions are common with the fully allowed transition, $^1\Sigma_u^+ \leftrightarrow X^1\Sigma_g^+$, because excited states in both transitions commonly stem from the single-electron HOMO–LUMO excitation. In this case, totally symmetric vibrational species tend to appear as overtones and combinations. The main progression with the increment of $2100\text{--}2200\text{ cm}^{-1}$ is associated with the alternat-

ing C≡C and C–C stretching σ_g mode of the *sp*-carbon chain, i.e., $\nu_2\sigma_g$ of C₈H₂, $\nu_3\sigma_g$ of C₁₀H₂, and $\nu_3\sigma_g$ of C₁₂H₂, in which all the triple bonds expand and all the single bonds shrink simultaneously, and vice versa. In Table 4, molecular constants deduced from the σ_g progression in the dispersed phosphorescence spectra are summarized for the electronic ground state, $X^1\Sigma_g^+$.

Table 3. Overtone and combination bands observed in the dispersed phosphorescence spectra of C_{2n}H₂ (*n* = 4–6) in solid hexane matrices at 20 K. Vibrational mode characteristics are noted for (a) the alternating C≡C and C–C stretching mode, σ_g (2100–2200 cm^{−1}), (b) the longitudinal breathing mode, σ_g' , (c) the even-numbered overtone of the *trans*-zigzag bending mode, π_g (~620 cm^{−1}), and (d) the even-numbered overtone of the *cis*-zigzag bending mode, π_g' for C₁₀H₂ and π_u' for C₈H₂ and C₁₂H₂ (~240 cm^{−1}).

Molecule	Observed Band cm ^{−1} (nm)	Difference Frequency cm ^{−1}		Vibrational Mode Assignment	
C ₈ H ₂	18,788 (532.3)	0	0 ₀ ⁰		0–0 band
	18,305		483 5 ₁ ⁰	σ_g'	breathing ^b
			and/or 16 ₂ ⁰	$\pi_u'^2$	<i>cis</i> -zigzag ^d
	17,819		969 16 ₄ ⁰	$\pi_u'^4$	<i>cis</i> -zigzag ^d
	17,540		1248 11 ₂ ⁰	π_g^2	<i>trans</i> -zigzag ^c
	16,597 (602.4)	2190	2 ₁ ⁰	σ_g	alternating CC str. ^a
	16,126		471 2 ₁ ⁰ 5 ₁ ⁰	$\sigma_g + \sigma_g'$	breathing ^b
			and/or 2 ₁ ⁰ 16 ₂ ⁰	$\sigma_g + \pi_u'^2$	<i>cis</i> -zigzag ^{a,d}
	15,646		951 2 ₁ ⁰ 16 ₄ ⁰	$\sigma_g + \pi_u'^4$	<i>cis</i> -zigzag ^{a,d}
	15,352		1245 2 ₁ ⁰ 11 ₂ ⁰	$\sigma_g + \pi_g^2$	<i>trans</i> -zigzag ^{a,c}
	14,426 (693.2)	2172	2 ₂ ⁰	σ_g^2	alternating CC str. ^a
	13,959		467 2 ₂ ⁰ 5 ₁ ⁰	$\sigma_g^2 + \sigma_g'$	breathing ^b
			and/or 2 ₂ ⁰ 16 ₂ ⁰	$\sigma_g^2 + \pi_u'^2$	<i>cis</i> -zigzag ^{a,d}
	13,183		1243 2 ₂ ⁰ 11 ₂ ⁰	$\sigma_g^2 + \pi_g^2$	<i>trans</i> -zigzag ^{a,c}
	12,268 (815.1)	2157	2 ₃ ⁰	σ_g^3	alternating CC str. ^a
	10,133 (986.9)	2136	2 ₄ ⁰	σ_g^4	alternating CC str. ^a
C ₁₀ H ₂	16,525 (605.1)	0	0 ₀ ⁰		0–0 band
	16,145		380 6 ₁ ⁰	σ_g'	breathing ^b
	16,042		483 15 ₂ ⁰	$\pi_g'^2$	<i>cis</i> -zigzag ^d
	15,560		965 15 ₄ ⁰	$\pi_g'^4$	<i>cis</i> -zigzag ^d
	15,293		1232 13 ₂ ⁰	π_g^2	<i>trans</i> -zigzag ^c
	14,405 (694.2)	2120	3 ₁ ⁰	σ_g	alternating CC str. ^a
	14,031		374 3 ₁ ⁰ 6 ₁ ⁰	$\sigma_g + \sigma_g'$	breathing ^{a,b}
	13,930		475 3 ₁ ⁰ 15 ₂ ⁰	$\sigma_g + \pi_g'^2$	<i>cis</i> -zigzag ^{a,d}
	13,456		949 3 ₁ ⁰ 15 ₄ ⁰	$\sigma_g + \pi_g'^4$	<i>cis</i> -zigzag ^{a,d}
	13,172		1233 3 ₁ ⁰ 13 ₂ ⁰	$\sigma_g + \pi_g^2$	<i>trans</i> -zigzag ^{a,c}
	12,300 (813.0)	2105	3 ₂ ⁰	σ_g^2	alternating CC str. ^a
	11,902		398 3 ₂ ⁰ 6 ₁ ⁰	$\sigma_g^2 + \sigma_g'$	breathing ^{a,b}
	11,847		453 3 ₂ ⁰ 15 ₂ ⁰	$\sigma_g^2 + \pi_g'^2$	<i>cis</i> -zigzag ^{a,d}
10,210 (979.4)	2090	3 ₃ ⁰	σ_g^3	alternating CC str. ^a	
C ₁₂ H ₂	15,178 (658.8)	0	0 ₀ ⁰		0–0 band
	14,869		309 7 ₁ ⁰	σ_g'	breathing ^b
	14,699		479 23 ₂ ⁰	$\pi_u'^2$	<i>cis</i> -zigzag ^d
	14,205		973 23 ₄ ⁰	$\pi_u'^4$	<i>cis</i> -zigzag ^d
	13,883		1295 15 ₂ ⁰	π_g^2	<i>trans</i> -zigzag ^c
	13,088 (764.1)	2090	3 ₁ ⁰	σ_g	alternating CC str. ^c
	12,765		323 3 ₁ ⁰ 7 ₁ ⁰	$\sigma_g + \sigma_g'$	breathing ^{a,b}
	12,602		486 3 ₁ ⁰ 23 ₂ ⁰	$\sigma_g + \pi_u'^2$	<i>cis</i> -zigzag ^{a,d}
	11,008 (908.4)	2080	3 ₂ ⁰	σ_g^2	alternating CC str. ^a
	10,699		309 3 ₂ ⁰ 7 ₁ ⁰	$\sigma_g^2 + \sigma_g'$	breathing ^{a,b}

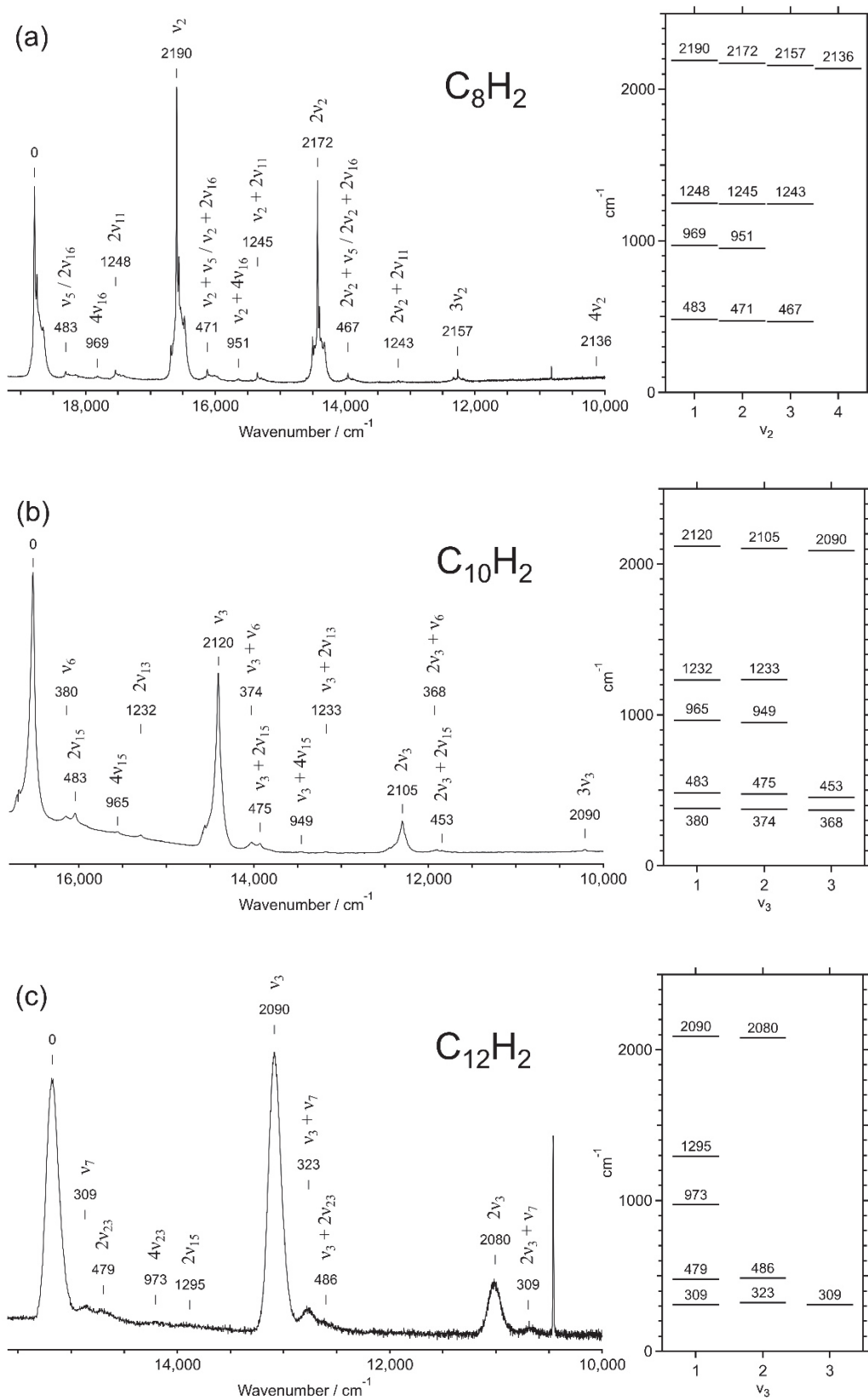


Figure 9. Vibrational features in the dispersed phosphorescence spectra for (a) C_8H_2 , (b) $C_{10}H_2$, and (c) $C_{12}H_2$ in solid hexane at 20 K.

Table 4. Molecular constants in cm^{-1} obtained from the analysis of the $a^3\Sigma_u^+ \rightarrow X^1\Sigma_g^+$ phosphorescence spectra for polyynes molecules, C_{2n}H_2 ($n = 4-6$), in solid hexane matrices at 20 K. Vibrational constants are deduced for the alternating CC stretching σ_g mode in the electronic ground state, $X^1\Sigma_g^+$.

Molecule	$T^* \text{ }^1$ cm^{-1}	ω_e'' cm^{-1}	$\omega_e x_e''$ cm^{-1}	Mode	Raman 2 cm^{-1}
C_8H_2	19,888	2205	8.1	$\nu_2\sigma_g$	2172
C_{10}H_2	17,590	2135	7.5	$\nu_3\sigma_g$	2123
C_{12}H_2	16,227	2100	5.0	$\nu_3\sigma_g$	2096

¹ $T^* = T_0 + \omega_e'/2 - \omega_e x_e'/4$. Zero-point energy in the lowest spin-triplet state, $a^3\Sigma_u^+$, is included. ² The Stokes Raman fundamental energy of the 1-0 transition in hexane solutions [24,25,28].

For candidates of the combination bands appearing between the peaks of the σ_g progression, totally symmetric species are possible by the other symmetric stretching σ_g modes and by even-numbered overtones of antisymmetric stretching modes or bending modes, i.e., $\sigma_u\sigma_u$, $\pi_g\pi_g$, or $\pi_u\pi_u$. Molecular orbital (MO) calculations predict harmonic frequencies for all modes, σ_g , σ_u , π_g , and π_u (see Figure S1 in Supporting Materials) [31]. Among them, frequencies for stretching σ_g and σ_u modes of lower frequencies, $<1600 \text{ cm}^{-1}$, are size dependent, i.e., lower frequencies for longer polyynes. Observed bands of frequencies at $\sim 480 \text{ cm}^{-1}$ for C_8H_2 , $\sim 380 \text{ cm}^{-1}$ for C_{10}H_2 , and $\sim 310 \text{ cm}^{-1}$ for C_{12}H_2 follow this tendency and are attributable to the longitudinal breathing mode of the carbon chain, namely σ_g' , having the lowest frequency among the σ_g modes, i.e., $\nu_5\sigma_g$ for C_8H_2 , $\nu_6\sigma_g$ for C_{10}H_2 , and $\nu_7\sigma_g$ for C_{12}H_2 . This mode is reasonably excited when the length of the molecule changes upon the $a^3\Sigma_u^+ \rightarrow X^1\Sigma_g^+$ transition (one of the HOMO-LUMO transitions), where the triple bonds are tightened and the single bonds are loosened.

The three polyynes share a common frequency of $1230-1290 \text{ cm}^{-1}$ for the observed highest-frequency combination band. According to the MO calculations, one of the highest-frequency bending modes of π_g stays at $650-700 \text{ cm}^{-1}$ independently of the molecular size for all the polyynes (see Figure S1 in Supporting Materials). This π_g mode promotes a deformation of the carbon chain into a *trans*-zigzag configuration, i.e., alternating displacements of adjacent carbon nuclei in opposite directions to each other perpendicularly to the molecular axis (see Figure S2 in Supporting Materials). The activation of the *trans*-zigzag bending motion of the carbon chain accompanies the electronic transition of $a^3\Sigma_u^+ \rightarrow X^1\Sigma_g^+$, when even numbers of vibrational quanta are excited, providing a totally symmetric species as $\pi_g \otimes \pi_g = \sigma_g^+ \oplus \delta_g$. Thus, the observed band separated by $1230-1290 \text{ cm}^{-1}$ from the band in the major progression of σ_g is attributable to the overtone of π_g^2 and its combinations with the alternating CC stretching mode, i.e., $n\nu_2\sigma_g$ for C_8H_2 , $n\nu_3\sigma_g$ for C_{10}H_2 , and $n\nu_3\sigma_g$ for C_{12}H_2 of $n = 1-4$.

Another series of combination bands with common frequencies at ~ 480 and $\sim 960 \text{ cm}^{-1}$ are noted for the excitation, once and twice, of an overtone of bending modes, π_g^2 or π_u^2 . The vibrational motion having a common harmonic frequency of $\sim 240 \text{ cm}^{-1}$ for different molecular size represents the *cis*-zigzag bending mode, namely π_g' for C_{10}H_2 and π_u' for C_8H_2 and C_{12}H_2 (see Figures S1 and S2 in Supporting Materials). Candidates for the possible excitations are $2\nu_{16}$ and $4\nu_{16}$ of π_u' for C_8H_2 , $2\nu_{15}$ and $4\nu_{15}$ of π_g' for C_{10}H_2 , and $2\nu_{23}$ and $4\nu_{23}$ of π_u' for C_{12}H_2 .

3.4. Annealing of Matrix Samples

To study the origin of satellite bands accompanying the main peak in the bands of the σ_g progression, the matrix sample in solid hexane was subjected to warming and cooling cycles between 20 K and 80 K, then warming up to 120 K, during which the spectra were recorded redundantly from one to the next. Figure 10 shows a series of spectra for the 0–0 band at 532 nm of C_8H_2 observed in the warming–cooling cycle, namely 20–60–20–80–20 K. The intensity of the main peak was reduced for vanishing by the warming up to 60 K, then recovered by cooling back to 20 K. In this cycle, a fraction of the intensity of the main peak was lost, while the intensity of the satellite bands was retained. The next cycle to 80 K affected the main peak by reducing its intensity to an order of magnitude less than the original intensity, even after cooling back to 20 K. Similar changes were observed for the other band of 0–1 in the σ_g progression. The recovery of the C_8H_2 molecule in a trapping site associated with the main peak is reproducible upon annealing partly but not completely.

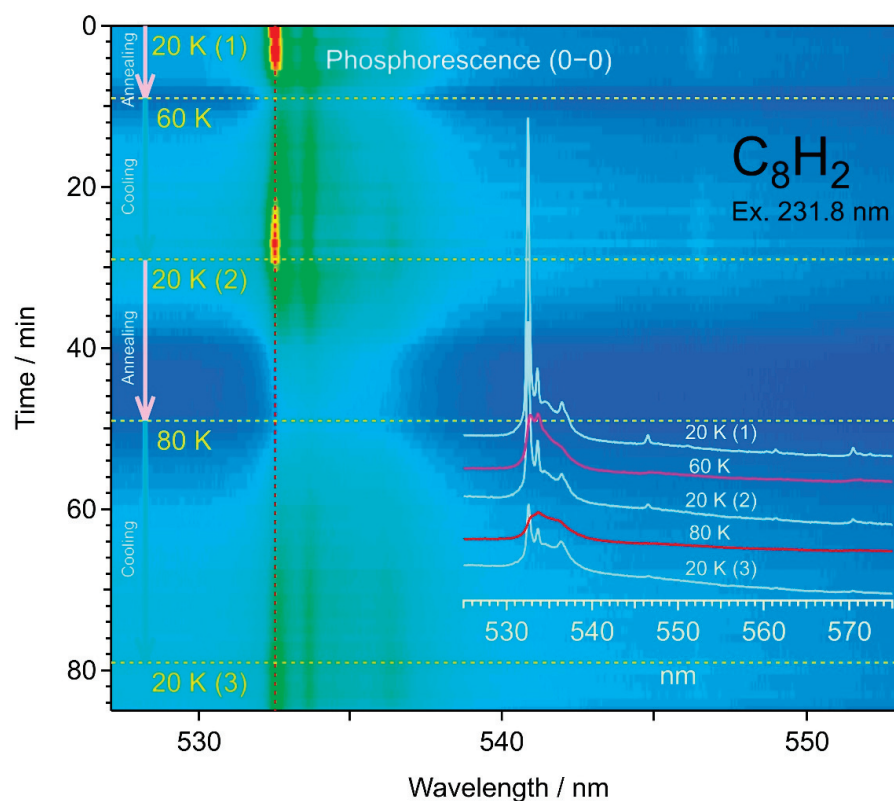


Figure 10. Spectral changes in phosphorescence 0–0 bands of C_8H_2 upon the warming–cooling cycle of the solid hexane matrix.

In Figure 11, the simple warming up of the matrix sample from 20 K to 120 K for the 0–1 band at 603 nm of C_8H_2 exhibited again the reduction in the intensity for the main peak up to 80 K, followed by the intensification of a broad band at 607 nm and the reduction of all the band features around 120 K, up to where the solid hexane matrix and the trapped molecules were lost by sublimation. The weaker features or satellite bands were associated with the 0–0 and 0–1 transitions in the phosphorescence of C_8H_2 molecules trapped in different circumstantial environments. The relatively sharp main peak corresponds to C_8H_2 molecules in a stable trapping condition.

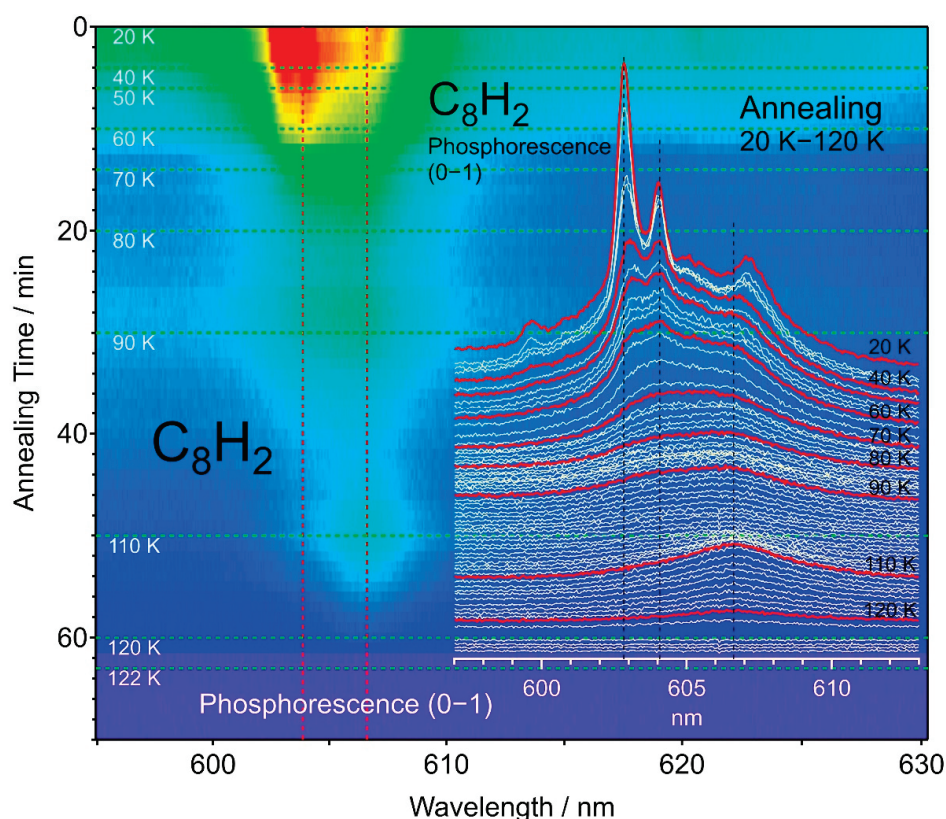


Figure 11. Spectral changes in the phosphorescence 0–1 band of C_8H_2 upon annealing of the solid hexane matrix from 20 K to 120 K, where the hexane matrix sublimates.

4. Discussion

4.1. Electronic Transition and Vibrational Excitation

Single-electron excitation from the highest occupied molecular orbital (HOMO) to the lowest unoccupied molecular orbital (LUMO) in a linear polyynes molecule in $D_{\infty h}$ point group symmetry, $H(C\equiv C)_nH$, provides three electronically excited states as spin-singlet states, i.e., $^1\Sigma_u^+$, $^1\Sigma_u^-$, and $^1\Delta_u$. Among them, the $^1\Sigma_u^+$ is the only state to which the optical transition is allowed from the ground state, $X^1\Sigma_g^+$ [32–34]. By the character of the electronic excitation from one degenerated molecular orbital to another, the excited state to which the optical transition is allowed, $^1\Sigma_u^+$, enjoys the highest transition energy among the three states stemming from the HOMO–LUMO excitation, while the others, $^1\Sigma_u^-$ and $^1\Delta_u$, come close at the lowest transition energies within the spin-singlet manifold [34]. The spin-flipped, lowest-energy triplet state, $a^3\Sigma_u^+$, also stemming from the HOMO–LUMO excitation, lies closer to or even lower in the transition energy relative to those for the latter two.

HOMO has electron densities on the triple bonds, $C\equiv C$, and nodes on the single bonds, $C-C$, of the polyyinic carbon chain, while LUMO has electron densities on the single bonds, $C-C$, and nodes on the triple bonds, $C\equiv C$. Thus, upon the transition of an electron between HOMO and LUMO, a vibrational mode in which all the triple bonds expand and all the single bonds shrink and vice versa is activated. Accordingly, a conspicuous progression for the alternating CC stretching σ_g mode constitutes a major feature in the spectra of absorption, $^1\Sigma_u^+ \leftarrow X^1\Sigma_g^+$ [9,10] and $^1\Delta_u \leftarrow X^1\Sigma_g^+$ [10,12,32], fluorescence, $^1\Delta_u \rightarrow X^1\Sigma_g^+$ [30], and phosphorescence, $a^3\Sigma_u^+ \rightarrow X^1\Sigma_g^+$, as shown in Figures 1 and 4. The relevant modes are $\nu_2\sigma_g$ for C_8H_2 , $\nu_3\sigma_g$ for $C_{10}H_2$, and $\nu_3\sigma_g$ for $C_{12}H_2$. Since the phosphorescence excitation spectra of $C_{10}H_2$ in Figure 5a corresponds to the absorption spectra in Figure 5b,c, the progression of the alternating CC stretching σ_g mode predominates the

spectral feature. The same discussion applies to the excitation spectra of C_8H_2 and $C_{12}H_2$ in Figures 3 and 6, respectively.

When the potential minimum changes or the length of the *sp*-carbon chain varies upon the electronic transition, this is accompanied by the excitation of the longitudinal breathing mode, namely σ_g' , where all the CC bonds expand then shrink repeatedly. The relevant modes are the lowest-frequency symmetric stretching mode of $\nu_5\sigma_g$ for C_8H_2 , $\nu_6\sigma_g$ for $C_{10}H_2$, and $\nu_7\sigma_g$ for $C_{12}H_2$. As the size of the carbon chain, n , increases, the vibrational frequency of the breathing mode decreases as $\sim n^{-1}$.

A sudden change in the molecular length upon the electronic excitation is to be relaxed and mitigated when some bending modes are excited simultaneously. A plausible mode which accompanies the alternating CC stretching motion is the *trans*-zigzag bending mode of π_g symmetry, in which the adjacent carbon atoms move in opposite directions transversely to the molecular axis. According to the MO calculations, another π_g mode of vibration, i.e., CH bending, has a similar harmonic frequency to that of the *trans*-zigzag bending π_g mode of the carbon chain. The calculated mode frequencies are so close that the order can be reversed depending on the theoretical model and the basis set used. Experimentally, the IR absorption spectra revealed the frequency for the CH-bending π_u mode at 625 cm^{-1} and its combination of $\pi_g + \pi_u$ at 1236 cm^{-1} for $C_{2n}H_2$ ($n = 3-6$), independently of the size, n [11,12,26]. Disregarding the anharmonicity and other effects of perturbation, the simple subtraction provides $\sim 611\text{ cm}^{-1}$ for the CH-bending π_g mode. On the other hand, the overtone frequency of $\sim 1232\text{ cm}^{-1}$ for π_g^2 observed in the dispersed phosphorescence spectrum is simply divided into two, providing the frequency of $\sim 616\text{ cm}^{-1}$ for the *trans*-zigzag bending π_g mode. The highest-frequency π_g mode is, by definition, ν_{10} for C_8H_2 , ν_{12} for $C_{10}H_2$, and ν_{14} for $C_{12}H_2$. This numbering of the mode, n of ν_n , has been applied to the CH-bending π_g mode in the IR absorption spectra [26] and also to the *trans*-bending π_g mode of the carbon chain in the laser-induced fluorescence spectra [30]. One might better refrain from the use of the numbering, n for ν_n , because of the close proximity of the vibrational frequencies for the CH-bending π_g mode and the *trans*-zigzag bending π_g mode. However, for convenience throughout this article, we dare to reserve for the CH-bending the numbering of the highest-frequency π_g mode, i.e., ν_{10} for C_8H_2 , ν_{12} for $C_{10}H_2$, and ν_{14} for $C_{12}H_2$, while for the *trans*-zigzag bending of the carbon chain the numbering of the second highest-frequency π_g mode, i.e., ν_{11} for C_8H_2 , ν_{13} for $C_{10}H_2$, and ν_{15} for $C_{12}H_2$. Having the same frequency and belonging to the same vibrational symmetry, both π_g modes can strongly couple to gain extra activity, appearing as conspicuous spectral features.

Another relaxation is obtained upon distortion induced by the electronic transition, provided the *cis*-zigzag bending mode is excited simultaneously. In this mode, displacements of the adjacent $C\equiv C$ units are in opposite directions transversely to the molecular axis. The symmetry of this mode is π_u for C_8H_2 and $C_{12}H_2$ or π_g for $C_{10}H_2$, namely π_u' for the $4n$ series and π_g' for the $4n + 2$ series. Having smaller number of nodes along the carbon chain, the vibrational frequency of $\sim 240\text{ cm}^{-1}$ for this *cis*-zigzag bending mode, π_u' or π_g' , is lower than that of $\sim 620\text{ cm}^{-1}$ for the *trans*-zigzag bending mode, π_g . They are $\nu_{16}\pi_u$ for C_8H_2 , $\nu_{15}\pi_g$ for $C_{10}H_2$, and $\nu_{23}\pi_u$ for $C_{12}H_2$. With the excitation of even-numbered vibrational quanta, the π_g and π_u modes provide a totally symmetric vibrational species as $\pi_g \otimes \pi_g = \pi_u \otimes \pi_u = \sigma_g^+ \oplus \delta_g$, and thus are excited simultaneously upon the electronic excitation with a transition moment parallel to the molecular axis, namely the $\Sigma-\Sigma$ transition. An example for the progression of the even-numbered vibrational quanta of a bending mode is reported for the $\Pi-\Sigma$ transition of a simple linear molecule of C_3 [35].

4.2. Phosphorescence Lifetimes

The observed lifetimes of 31 ms for C_8H_2 , 8.4 ms for $C_{10}H_2$, and 3.9 ms for $C_{12}H_2$ are comparable to the reported lifetimes of cyanopolyynes in solid rare gas matrices, i.e., 40 ms for HC_5N [13,16], 8.2 ms for HC_7N [15], and 3.9 ms for HC_9N [18]. In solid organic matrices at 20 K, phosphorescence lifetimes of HC_9N were ~ 9.7 ms in solid hexane and ~ 11.2 ms in solid acetonitrile, and the lifetime of $HC_{11}N$ was ~ 7.6 ms in solid acetonitrile [22]. These observations clearly show shorter lifetimes for larger species. The tendency of decreasing lifetimes for larger species is confirmed for both series of polyynes and cyanopolyynes. With an increasing number of vibrational degrees of freedom, particularly in low-frequency bending modes for longer polyynes, non-radiative decay is promoted from the upper singlet states, as well as from the lowest triplet state, $a^3\Sigma_u^+$, to vibrationally excited states of the singlet ground state, $X^1\Sigma_g^+$. The population in the electronically excited states decreases faster for larger molecules with a high density of vibrational states.

4.3. Phosphorescence versus Fluorescence

Laser-induced fluorescence spectra have been reported in the near-UV and visible regions for hydrogen-capped centrosymmetric polyyne molecules of $C_{2n}H_2$ ($n = 5-8$) in hexane solutions at ambient temperature, c.a. 25 °C, upon the excitation of the fully allowed transition, $^1\Sigma_u^+ \leftarrow X^1\Sigma_g^+$, in the UV [30]. The optical emission was attributed to the vibronic transition in the symmetry-forbidden electronic system of $^1\Delta_u \rightarrow X^1\Sigma_g^+$. The optical transition for the 0-0 band of $^1\Delta_u \leftrightarrow X^1\Sigma_g^+$ is strictly forbidden but becomes weakly allowed through vibronic coupling, when a particular vibrational mode, namely an inducing mode of π_g symmetry, is activated or deactivated simultaneously upon the electronic transition [32,33]. Under the room temperature condition of the solution, fluorescence was detectable but phosphorescence was not noticed [30], reasonably because of the fast relaxation via internal conversion at the elevated temperature. Only the fluorescence having a typical lifetime of at most a few nanoseconds could be detected. In the present work for the same series of molecules, $C_{2n}H_2$ ($n = 4-6$), with the same excitation energy but in the cold matrix of solid hexane at 20 K, the phosphorescence spectrum predominated while the fluorescence spectrum was not discernible.

4.4. Vibronic Bands in the Forbidden Transition

Figure 12 shows the detail of the phosphorescence mapping of $C_{10}H_2$, with an extension of the excitation wavelength in the near-UV range from 302 nm to 409 nm, in addition to the excitation in the UV range from 213 nm to 302 nm. In the UV excitation below 300 nm, bright spots are discernible in the map, which are attributable to the 0-1 band emission of the phosphorescence, $a^3\Sigma_u^+ \rightarrow X^1\Sigma_g^+$, upon the excitation of the allowed transition, $^1\Sigma_u^+ \leftarrow X^1\Sigma_g^+$. The bottom trace in light blue is the excitation spectrum for the emission at 693.5 nm, showing again the curve of UV absorption identical to the excitation spectrum by the 0-0 band at 605 nm in Figure 5a. In the middle trace, using the emission at 687.0 nm, another peak of the excitation at 262 nm appears as the small spot in the map, which corresponds to the emission peak of the dashed line in Figure 4. This excitation spectrum exhibits complex patterns, with two sharp peaks and some overlapping bands in the slightly longer wavelength region of 266-271 nm. The upper trace using the emission at 686.0 nm shows the excitation peak at 242 nm within a complex pattern of the excitation spectrum. All these patterns appear in the phosphorescence excitation mapping of $C_{10}H_2$ in solid hexane and they are reproducible for different matrix samples and for the mapping using the 0-0 band emission. Couples of electronic states are predicted below the excitation energy of the allowed transition, to which the electric dipole transition is symmetry forbidden but vibronically allowed by the mechanism of intensity borrowing [36-38].

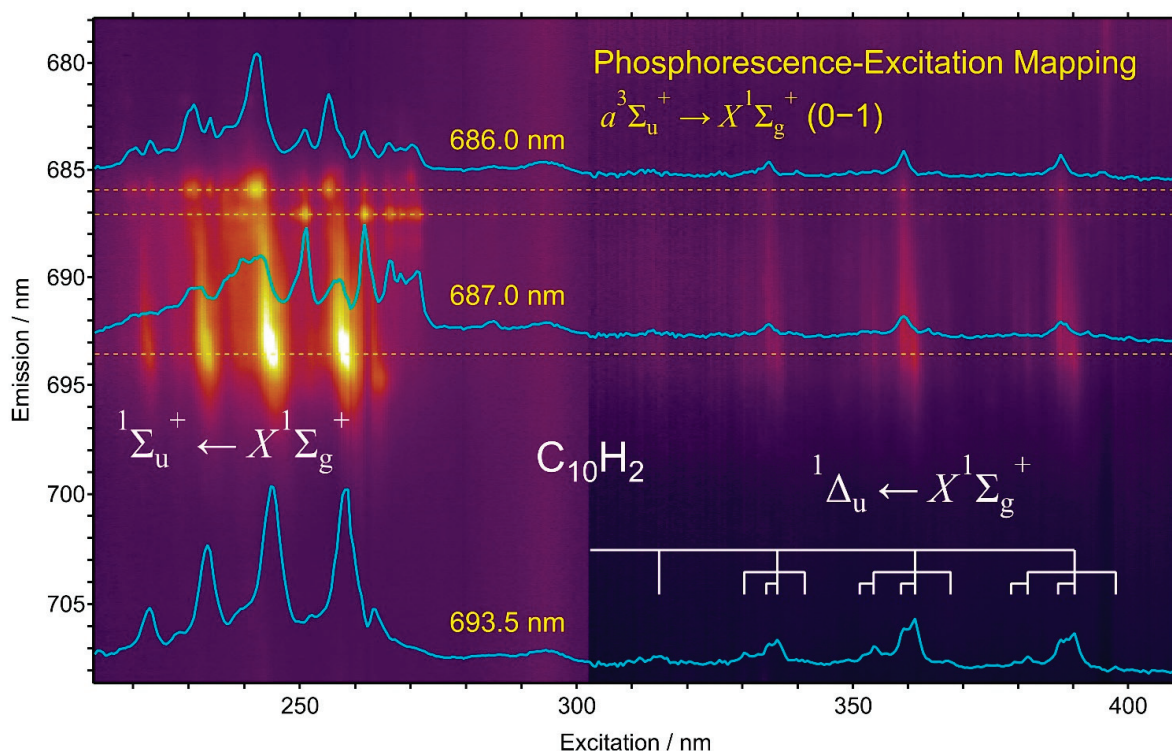


Figure 12. Phosphorescence excitation mapping of $C_{10}H_2$ polyynes in solid hexane matrix at 20 K. Three traces in light blue are the excitation spectra corresponding to the emission at 686.0 nm, 687.0 nm, and 693.5 nm, all belonging to the 0–1 band with the $\nu_3\sigma_g$ stretching-mode excitation in the phosphorescence, $a^3\Sigma_u^+ \rightarrow X^1\Sigma_g^+$. The main features in shorter wavelengths than 271 nm are bands in the allowed transition, $^1\Sigma_u^+ \leftarrow X^1\Sigma_g^+$, while the weak features in the excitation wavelengths of 310–395 nm are bands in the forbidden transition, $^1\Delta_u \leftarrow X^1\Sigma_g^+$.

In the near-UV excitation of 310–395 nm in Figure 12, four bands with an increment of $\sim 2050\text{ cm}^{-1}$ are found in the mapping using phosphorescence 0–1 band of $C_{10}H_2$. By the proximity to those observed as absorption bands in the symmetry-forbidden transition in solutions [10,30], these bands belong to the excitation of the $^1\Delta_u \leftarrow X^1\Sigma_g^+$ system of the HOMO–LUMO transition. Table 5 compares the observed bands in the forbidden transition by phosphorescence excitation in solid hexane at 20 K in the present work and those by absorption in hexane solutions at ambient temperature [30]. In the excitation spectrum using the phosphorescence 0–0 band in Figure 5a, identical features are discernible in $32,300\text{--}25,300\text{ cm}^{-1}$. The intensity of these features in the excitation spectrum in Figure 5a is relatively stronger than the intensity in absorption in the solutions shown in Figure 5b. The difference is rationalized as follows: in different wavelengths of UV, where the molecule strongly absorbs the incident light, and near-UV, where the molecular absorption is orders of magnitude weaker, the thickness of the sample is common for the transmission measurement of the absorption in solutions, while in the phosphorescence measurement, the penetration depth of the incident light for the excitation is different, i.e., thin for the UV and thick for the near-UV, to gain intensity for the near-UV relative to the UV.

Table 5. Observed peaks in nm for the excitation spectrum of C₁₀H₂ in solid hexane matrix at 20 K. For the vibronic transition in near UV, ${}^1\Delta_u \leftarrow X^1\Sigma_g^+$, absorption bands observed in hexane solution at ambient temperature are listed for comparison [30].

Transition	Excitation 686.0 nm	Excitation 687.0 nm	Excitation 693.5 nm	Separation cm ⁻¹	Solution ¹ nm	Mode	Symmetry
${}^1\Delta_u \leftarrow X^1\Sigma_g^+$	395.3	392.8	397.8				
			390.3	0			
	387.8	387.8	387.8	165	384	13 ₀ ²	π_g^2
			381.8	571			
			379.3	173			
	365.3	363.8	367.3				
			361.3	2057			
	359.3	359.3	359.3	154	357	3 ₀ ¹ 13 ₀ ²	$\sigma_g + \pi_g^2$
			353.8	587			
			351.8	161			
${}^1\Delta_u \leftarrow X^1\Sigma_g^+$	339.8	339.8	340.8				
			336.3	2058			
	334.8	334.8	334.8	133	333	3 ₀ ² 13 ₀ ²	$\sigma_g^2 + \pi_g^2$
			330.3	540			
${}^1\Delta_u \leftarrow X^1\Sigma_g^+$	312.8	313.8	314.8	2031	312	3 ₀ ³ 13 ₀ ²	$\sigma_g^3 + \pi_g^2$
	270.2	271.2					
	268.2	268.2					
${}^1\Sigma_u^+ \leftarrow X^1\Sigma_g^+$	266.2	266.2					
	261.7	261.7	258.8	0		0-0	
	255.3	257.3	245.3	2116		3 ₀ ¹	σ_g
	250.8	251.3	233.4	2084		3 ₀ ²	σ_g^2
	242.3	242.8	222.9	2008		3 ₀ ³	σ_g^3
	233.9	239.9					
	230.9	231.4					
	222.9						
220.5							

¹ Reference [30].

As the probing wavelength is shortened from 694 nm to 686 nm, the band shape of the forbidden transition changes, but rather simply compared with those in the allowed transition in shorter wavelengths. Since the appearance of the phosphorescence signal of the 0-1 band in 685-695 nm coincides well with the excitations of the allowed transition, ${}^1\Sigma_u^+ \leftarrow X^1\Sigma_g^+$, and the forbidden transition, ${}^1\Delta_u \leftarrow X^1\Sigma_g^+$, all the spectral features in Figure 12 belong to C₁₀H₂, despite the complex shifts in wavelengths and the alternating intensities.

4.5. Relevance to Interstellar Molecules

Finally, we briefly mention the relevance to interstellar molecules. Cyanopolyynes, H(C≡C)_nC≡N, have been a series of leading interstellar molecules since their discovery by radio astronomical observations in the late 1970s [3-7]. It is natural to consider that the simplest analog of hydrogen-end-capped polyynes, H(C≡C)_nH, shares the same place [8]. However, their detection in space has been limited by the selection rule for the pure rotational transition to take place, i.e., the detectable molecule must have a permanent electric dipole. Since the radio-frequency pure rotational transition for the centrosymmetric polyyne molecule, H(C≡C)_nH, is forbidden, vibrational transitions or electronic transitions are the possibilities for detection.

Infrared absorption has been reported in relevance to the abundance of hexatriyne, C₆H₂, and octatetrayne, C₈H₂, in the atmosphere of Titan [11,12]. In this case, vibrational modes associated with heteronuclear, dipolar CH bonding are detectable, i.e., the asymmetric CH stretching σ_u mode at ~ 3330 cm⁻¹ and the synchronized CH bending π_u mode at 622 cm⁻¹, and its combination of $\pi_u + \pi_g$ at ~ 1230 cm⁻¹. For the characteristic localized

vibration on the two terminal CH bonds, the vibrational frequencies of these modes are independent of the size of the carbon chain. On the other hand, transition energies of the electronic spectra are size dependent because of the property of the HOMO–LUMO excitation of the electron in the doubly degenerate π -orbitals on the carbon chain, as plotted in Figure 13. Absorption bands of vibronic transitions in the forbidden transition, ${}^1\Sigma_u^- \leftarrow X^1\Sigma_g^+$ and ${}^1\Delta_u \leftarrow X^1\Sigma_g^+$ [33], have been the subject of astronomical observation. Concerning the phosphorescence, $a^3\Sigma_u^+ \rightarrow X^1\Sigma_g^+$, the size-dependent property is clearly shown for the wavelength of their 0–0 bands, as demonstrated in Figures 4 and 13. Although the observable condition is limited to the place where the UV excitation occurs for cold molecules, phosphorescence in the visible and near-infrared regions can be a promising probe for the detection of centrosymmetric linear polyynes molecules of $C_{2n}H_2$ in space.

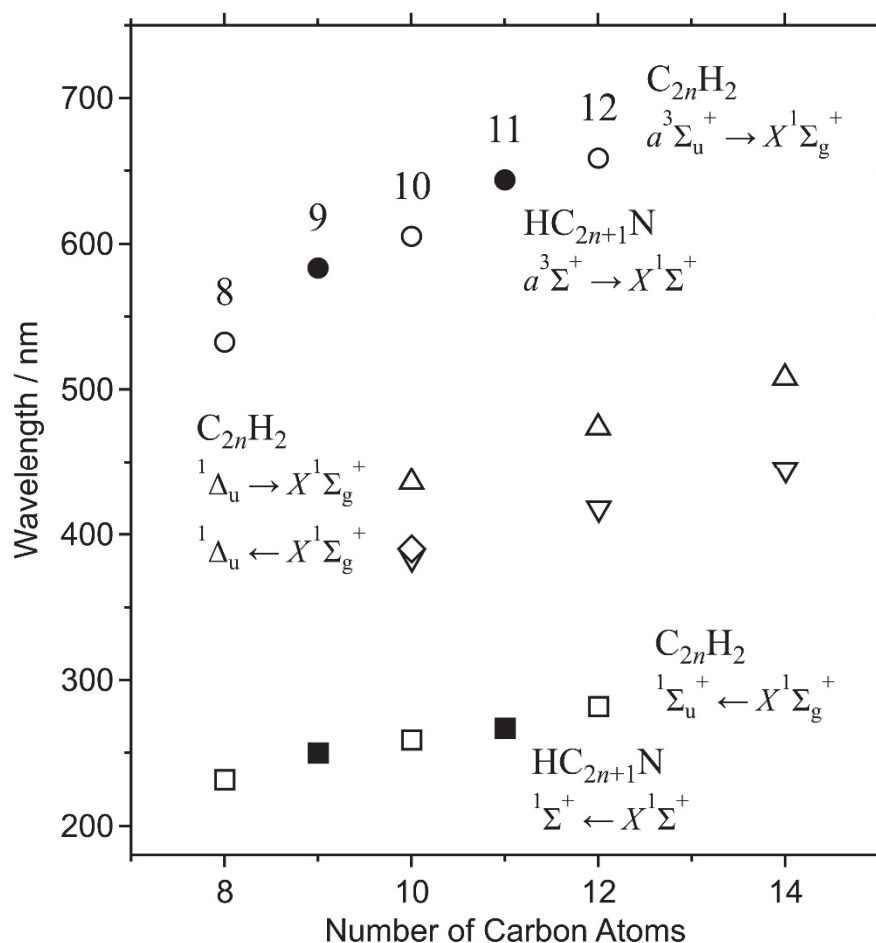


Figure 13. Wavelengths of the 0–0 band of phosphorescence (circles) and absorption (squares) of polyynes molecules, $C_{2n}H_2$, plotted as a function of molecular size, $2n$. The excitation wavelength of the forbidden transition of $C_{10}H_2$ in the solid hexane matrix in the present work (diamond) is plotted with emission and absorption wavelengths in solutions (triangles) [30]. Transition wavelengths of cyanopolyynes molecules, $HC_{2n+1}N$, are plotted for comparison (closed markers) [22].

Supplementary Materials: The following supporting information can be accessible at: <https://www.mdpi.com/article/10.3390/photochem2010014/s1>. For the assignment of vibrational modes in Figure 9 and Table 3, supplementary Figures S1 and S2 are available online. Figure S1 summarizes calculated harmonic frequencies and observed fundamentals and overtones. Figure S2 illustrates the displacement of atoms in the breathing mode (σ_g') and the *trans*-zigzag (π_g) and *cis*-zigzag (π_u' or π_g') bending modes for (a) C_8H_2 , (b) $C_{10}H_2$, and (c) $C_{12}H_2$.

Author Contributions: Conceptualization, T.W. and U.S.; validation, H.S. (Haruo Shiromaru), T.K. and M.H.; investigation, T.Y. and H.S. (Hal Suzuki); chemical resources, K.T., S.S., and K.O.; data curation, K.F. and R.O.; writing—original draft preparation, T.W.; writing—review and editing, U.S. and J.-C.G.; funding acquisition, T.W. All authors have read and agreed to the published version of the manuscript.

Funding: This research was funded by The Ministry of Education, Sports, Science and Technology (MEXT) of Japan grant number 20K05438 of Grant-in-Aid for Scientific Research C.

Institutional Review Board Statement: Not applicable.

Informed Consent Statement: Not applicable.

Data Availability Statement: To share the experimental data sets for further investigations, please contact to the corresponding author, T.W., wakaba@chem.kindai.ac.jp.

Conflicts of Interest: The authors declare no conflict of interest.

Sample Availability: Samples of polyynes in various organic solvents containing ~1 mg of C₈H₂, C₁₀H₂, or C₁₂H₂ are available for basic researches. For collaborations, please contact to the corresponding author, T.W., wakaba@chem.kindai.ac.jp.

References

- Cataldo, F. (Ed.) *Polyynes: Synthesis, Properties, and Applications*; CRC Press: Boca Raton, FL, USA, 2006. [CrossRef]
- Diederich, F.; Stang, P.J.; Tykwinski, R.R. (Eds.) *Acetylene Chemistry: Chemistry, Biology, and Material Science*; Wiley-VCH: Weinheim, Switzerland, 2004. [CrossRef]
- Broten, N.W.; Oka, T.; Avery, L.W.; MacLeod, J.M.; Kroto, H.W. The detection of HC₉N in interstellar space. *Astrophys. J.* **1978**, *223*, L105. [CrossRef]
- Snell, R.L.; Schloerb, F.P.; Young, J.S.; Hjalmarsen, A.; Friberg, P. Observations of HC₃N, HC₅N, and HC₇N in molecular clouds. *Astrophys. J.* **1981**, *244*, 45–53. [CrossRef]
- Bell, M.B.; Avery, L.W.; MacLeod, J.M.; Matthews, H.E. The excitation temperature of HC₉N in the circumstellar envelope of IRC+10216. *Astrophys. J.* **1992**, *400*, 551–555. [CrossRef]
- Truong-Bach, D.G. HC₉N from the envelopes of IRC+10216 and CRL2688. *Astron. Astrophys.* **1993**, *277*, 133–138.
- Loomis, R.A.; Shingledecker, C.N.; Langston, G.; McGuire, B.A.; Dollhopf, N.M.; Burkhardt, A.M.; Corby, J.; Booth, S.T.; Carroll, P.B.; Turner, B.; et al. Non-detection of HC₁₁N towards TMC-1: Constraining the chemistry of large carbon-chain molecules. *Mon. Not. R. Astron. Soc.* **2016**, *463*, 4175–4183. [CrossRef]
- Heath, J.R.; Zhang, Q.; O'Brien, S.C.; Curl, R.F.; Kroto, H.W.; Smalley, R.E. The formation of long carbon chain molecules during laser vaporization of graphite. *J. Am. Chem. Soc.* **1987**, *109*, 359–363. [CrossRef]
- Eastmond, R.; Johnson, T.R.; Walton, D.R.M. Silylation as a protective method for terminal alkynes in oxidative couplings—A general synthesis of the parent polyynes H(C≡C)_nH (*n* = 4–10, 12). *Tetrahedron* **1972**, *28*, 4601–4616. [CrossRef]
- Kloster-Jensen, E.; Haink, H.-J.; Christen, H. The electronic spectra of unsubstituted mono- to penta- acetylene in the gas phase and in solution in the range 1100 to 4000 Å. *Helv. Chim. Acta* **1974**, *57*, 1731–1744. [CrossRef]
- Shindo, F.; Bénilan, Y.; Chaquin, P.; Guillemin, J.-C.; Jolly, A.; Raulin, F. IR spectrum of C₈H₂: Integrated band intensities and some observational implications. *J. Mol. Spectrosc.* **2001**, *210*, 191–195. [CrossRef]
- Shindo, F.; Benilan, Y.; Guillemin, J.-C.; Chaquin, P.; Jolly, A.; Raulin, F. Ultraviolet and infrared spectrum of C₆H₂ revisited and vapor pressure curve in Titan's atmosphere. *Planet. Space Sci.* **2003**, *51*, 9–17. [CrossRef]
- Coupeaud, A.; Kołos, R.; Couturier-Tamburelli, I.; Aycard, J.P.; Piétri, N. Photochemical synthesis of the cyanodiacetylene HC₅N: A cryogenic matrix experiment. *J. Phys. Chem. A* **2006**, *110*, 2371–2377. [CrossRef] [PubMed]
- Crépin, C.; Turowski, M.; Ceponkus, J.; Douin, S.; Boyé-Péronne, S.; Gronowski, M.; Kołos, R. UV-induced growth of cyanopolyne chains in cryogenic solids. *Phys. Chem. Chem. Phys.* **2011**, *13*, 16780–16785. [CrossRef] [PubMed]
- Couturier-Tamburelli, I.; Piétri, N.; Crépin, C.; Turowski, M.; Guillemin, J.-C.; Kołos, R. Synthesis and spectroscopy of cyanotriacetylene (HC₇N) in solid argon. *J. Chem. Phys.* **2014**, *140*, 044329. [CrossRef]
- Turowski, M.; Crépin, C.; Gronowski, M.; Guillemin, J.-C.; Coupeaud, A.; Couturier-Tamburelli, I.; Piétri, N.; Kołos, R. Electronic absorption and phosphorescence of cyanodiacetylene. *J. Chem. Phys.* **2010**, *133*, 074310. [CrossRef] [PubMed]
- Turowski, M.; Crépin, C.; Douin, S.; Gronowski, M.; Couturier-Tamburelli, I.; Piétri, N.; Wasiak, A.; Kołos, R. Low temperature Raman spectra of cyanobutadiyne (HC₅N). *Vib. Spectrosc.* **2012**, *62*, 268–272. [CrossRef]
- Szczepaniak, U.; Crépin, C.; Gronowski, M.; Chevalier, M.; Guillemin, J.-C.; Turowski, M.; Custer, T.; Kołos, R. Cryogenic photochemical synthesis and electronic spectroscopy of cyanotetraacetylene. *J. Phys. Chem. A* **2017**, *121*, 7374–7384. [CrossRef]
- Szczepaniak, U.; Turowski, M.; Custer, T.; Gronowski, M.; Kerisit, N.; Trolez, Y.; Kołos, R. Infrared and Raman spectroscopy of methylcyanodiacetylene (CH₃C₅N). *ChemPhysChem* **2016**, *17*, 3047–3054. [CrossRef]

20. Szczepaniak, U.; Kołos, R.; Gronowski, M.; Guillemin, J.-C.; Crépin, C. Low temperature synthesis and phosphorescence of methyltriacetylene. *J. Phys. Chem. A* **2018**, *122*, 89–99. [CrossRef]
21. Turowski, M.; Szczepaniak, U.; Custer, T.; Gronowski, M.; Kołos, R. Electronic spectroscopy of methylcyanodiacetylene (CH₃C₅N). *ChemPhysChem* **2016**, *17*, 4068–4078. [CrossRef]
22. Szczepaniak, U.; Ozaki, K.; Tanaka, K.; Ohnishi, Y.; Wada, Y.; Guillemin, J.-C.; Crépin, C.; Kołos, R.; Morisawa, Y.; Suzuki, H.; et al. Phosphorescence excitation mapping and vibrational spectroscopy of HC₉N and HC₁₁N cyanopolynes in organic solvents. *J. Mol. Struct.* **2020**, *1214*, 128201. [CrossRef]
23. Tsuji, M.; Tsuji, T.; Kuboyama, S.; Yoon, S.-H.; Korai, Y.; Tsujimoto, T.; Kubo, T.T.; Mori, A.; Mochida, I. Formation of hydrogen-capped polyynes by laser ablation of graphite particles suspended in solution. *Chem. Phys. Lett.* **2002**, *355*, 101–108. [CrossRef]
24. Tabata, H.; Fujii, M.; Hayashi, M.; Doi, T.; Wakabayashi, T. Raman and surface-enhanced Raman scattering of a series of polyynes. *Carbon* **2006**, *44*, 3168–3176. [CrossRef]
25. Inoue, K.; Matsutani, R.; Sanada, T.; Kojima, K. Preparation of long-chain polyynes of C₂₄H₂ and C₂₆H₂ by liquid-phase laser ablation in decalin. *Carbon* **2010**, *48*, 4209–4211. [CrossRef]
26. Wada, Y.; Morisawa, Y.; Wakabayashi, T. Spectroscopic characterization of a series of polyyne-iodine molecular complexes H(C≡C)_nH(I₆) of *n* = 5–9. *Chem. Phys. Lett.* **2012**, *541*, 54–59. [CrossRef]
27. Sato, Y.; Kodama, T.; Shiromaru, H.; Sanderson, J.H.; Fujino, T.; Wada, Y.; Wakabayashi, T.; Achiba, Y. Synthesis of polyyne molecules from hexane by irradiation of intense femtosecond laser pulses. *Carbon* **2010**, *48*, 1673–1676. [CrossRef]
28. Wakabayashi, T.; Tabata, H.; Doi, T.; Nagayama, H.; Okuda, K.; Umeda, R.; Hisaki, I.; Sonoda, M.; Tobe, Y.; Minematsu, T.; et al. Resonance Raman spectra of polyyne molecules C₁₀H₂ and C₁₂H₂ in solution. *Chem. Phys. Lett.* **2007**, *433*, 296–300. [CrossRef]
29. Wakabayashi, T.; Saikawa, M.; Wada, Y.; Minematsu, T. Isotope scrambling in the formation of cyanopolynes by laser ablation of carbon particles in liquid acetonitrile. *Carbon* **2012**, *50*, 47–56. [CrossRef]
30. Wakabayashi, T.; Nagayama, H.; Daigoku, K.; Kiyooka, Y.; Hashimoto, K. Laser induced emission spectra of polyyne molecules C_{2n}H₂ (*n* = 5–8). *Chem. Phys. Lett.* **2007**, *446*, 65–70. [CrossRef]
31. *Gaussian 16*, Revision C.01; Gaussian, Inc.: Wallingford, CT, USA, 2019. Available online: <https://gaussian.com/gaussian16/> (accessed on 21 February 2021).
32. Ding, H.; Schmidt, T.W.; Pino, T.; Güthe, F.; Maier, J.P. Towards bulk behaviour of long hydrogenated carbon chains? *Phys. Chem. Chem. Phys.* **2003**, *5*, 4772–4775. [CrossRef]
33. Wakabayashi, T.; Wada, Y.; Iwahara, N.; Sato, T. Vibronic bands in the HOMO-LUMO excitation of linear polyyne molecules. *J. Phys. Conf. Ser.* **2013**, *428*, 012004. [CrossRef]
34. Nakai, H. Discovery of chemical principles: Symmetry rules of degenerate excitations. *J. Comp. Chem. Jpn.* **2012**, *11*, 1–16. (In Japanese) [CrossRef]
35. Čermák, I.; Förderer, M.; Čermáková, I.; Kalhofer, S.; Stopka-Ebeler, H.; Monninger, G.; Krätschmer, W. Laser-induced emission spectroscopy of matrix-isolated carbon molecules: Experimental setup and new results on C₃. *J. Chem. Phys.* **1998**, *108*, 10129–10142. [CrossRef]
36. Orlandi, G.; Siebrand, W. Theory of vibronic intensity borrowing. Comparison of Herzberg-Teller and Born-Oppenheimer coupling. *J. Chem. Phys.* **1973**, *58*, 4513–4523. [CrossRef]
37. Lin, S.H.; Eyring, H. Study of vibronic and Born-Oppenheimer couplings. *Proc. Nat. Acad. Sci. USA* **1974**, *71*, 3415–3417. [CrossRef] [PubMed]
38. Lin, S.H.; Eyring, H. Study of the Franck-Condon and Herzberg-Teller Approximations. *Proc. Nat. Acad. Sci. USA* **1974**, *71*, 3802–3804. [CrossRef] [PubMed]

Article

UV-Vis Spectrophotometer as an Alternative Technique for the Determination of Hydroquinone in Vinyl Acetate Monomer

Md Al Mamunur Rashid ^{1,*}, Mofizur Rahman ², ASM Obaidullah Mahmud ², Ali Shazzad Mohammad Morshed ², Md Masudul Haque ² and Md Mobarak Hossain ²

¹ Extreme Materials Research Center, Korea Institute of Science and Technology, Seoul 02792, Korea

² Research and Development Center, Berger Paints Bangladesh Limited, Dhaka 1230, Bangladesh; mofizur@bergerbd.com (M.R.); mahmud@bergerbd.com (A.O.M.); mmorshed@bergerbd.com (A.S.M.M.); masudul@bergerbd.com (M.M.H.); mobarak@bergerbd.com (M.M.H.)

* Correspondence: ndcmamun@kist.re.kr; Tel.: +82-10-9728-9732

Abstract: As an appropriate quantity of hydroquinone (HQ) is essential to safeguard inhibition characteristics by eliminating the risk of self-polymerization of vinyl acetate monomer (VAM), the determination of the HQ content in VAM is very crucial to ensure the stability of VAM during storage and transportation as well as to achieve the possibility of a proper polymerization reaction. In this study, a simple, cheap, time-saving, and easy method has been developed by which the HQ content in VAM can be measured quickly based on the measurement of UV-Vis absorbance of the HQ content at 293 nm using methanol as a blank. No color development is required for this determination process, and the HQ content in the VAM can be measured directly without any further processing. The limit of detection, limit of quantification, linearity range, accuracy, precision, robustness, and measurement uncertainty of this method have been measured and analyzed and found to be within the acceptable limit and range. The method shows linearity within 0.36–25.0 ppm HQ content in the solution range with a regression coefficient of 0.9999, a relative spike recovery of 101.35%, precision of 1.36%, relative bias of 0.55%, and robustness with a temperature variation of -5°C .

Keywords: vinyl acetate monomer; hydroquinone; polymerization; UV-visible spectrophotometer

Citation: Rashid, M.A.M.; Rahman, M.; Mahmud, A.O.; Morshed, A.S.M.; Haque, M.M.; Hossain, M.M. UV-Vis Spectrophotometer as an Alternative Technique for the Determination of Hydroquinone in Vinyl Acetate Monomer. *Photochem* **2022**, *2*, 435–447. <https://doi.org/10.3390/photochem2020030>

Academic Editors: Rui Fausto and Robert Koles

Received: 16 May 2022

Accepted: 13 June 2022

Published: 15 June 2022

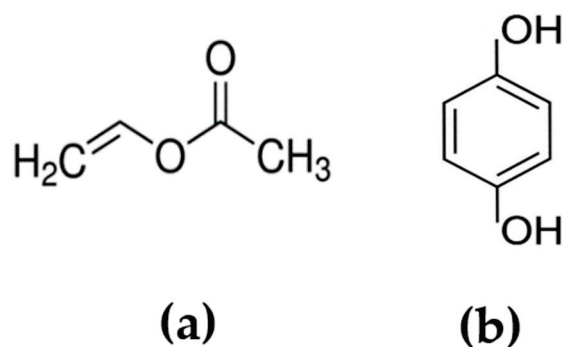
Publisher's Note: MDPI stays neutral with regard to jurisdictional claims in published maps and institutional affiliations.



Copyright: © 2022 by the authors. Licensee MDPI, Basel, Switzerland. This article is an open access article distributed under the terms and conditions of the Creative Commons Attribution (CC BY) license (<https://creativecommons.org/licenses/by/4.0/>).

1. Introduction

Vinyl acetate monomer (VAM) may undergo a free radical chain polymerization phenomenon under constant temperature to produce polymers and copolymers used in water-based paints, adhesives, paper coatings, non-woven binders, and various applications at moderate temperatures [1–5]. The stability of VAM (Scheme 1a) depends mainly on the concentration of the inhibitor present in the VAM, the temperature of the storage vessel, and other surrounding conditions. The rapid spontaneous polymerization of VAM is the second most frequent cause of runaway reaction accidents in the chemical industry because of cross contamination [6]. Uncontrollable polymerization of VAM can occur due to improper handling, absence of inhibitor, inhibitor depletion for a prolonged storage, or the lack of proper storage precautions. Typically, hydroquinone (HQ) (Scheme 1b), having the chemical formula $\text{C}_6\text{H}_4(\text{OH})_2$, is used in topical application in pharmaceuticals and as an inhibitor of the polymerization in VAM, including to prolong the shelf life of VAM for processing and safe transport and storage [7–9]. Most VAM shipped from the manufacturer should contain 3–5 ppm and up to 25 ppm HQ for regional shipments and for long-range shipments, respectively [8]. To avoid polymerization including cross contamination, the concentration of the HQ inhibitor should not decrease below a minimum effective level. Proper methods for accurate measurement of HQ content are highly desirable.



Scheme 1. Chemical structure of (a) VAM and (b) HQ.

There are several test methods for determining the HQ content in pharmaceutical products (e.g., cream), healthcare products (e.g., cosmetics), and various biological matrices by using UV, thin layer chromatography (TLC), micellar electrokinetic chromatography (MEKC), capillary electrochromatography (CEC), and high-performance liquid chromatography (HPLC) [10–15]. Moreover, in the United State Pharmacopeia (USP) monograph, HQ has been determined in the pharmaceuticals cream by 1cm cells at the wavelength of maximum absorbance at about 293 nm, with a suitable spectrophotometer, using methanol as a blank [16]. In the Metler Toledo application note, HQ has been measured by UV spectrophotometer at about 289 nm using 0.05 (M) sulphuric acid as a diluent [17]. In the British Pharmacopeia (BP) monograph, Tretinoin, HQ, and Hydrocortisone have been determined in pharmaceuticals cream by using HPLC [Column-Waters Spherisorb ODS 1 (250 mm × 4.6 mm, 5 μm), Mobile Phase-Methanol: water (9:1, v/v), Diluent-Mobile Phase, Detection-UV, 295 nm] [18]. These methods are expensive, sophisticated, and need extensive experimental skills. Moreover, we did not find any study on determining the amount of HQ in the VAM using any of the above-mentioned methods. Thus, developing a simple, easy, cheap, and suitable validated technique to determine HQ content is timely right now.

To the best of our knowledge, only two test methods are available for the determination of the HQ content in VAM. They are the titrimetric method in ASTM D2193 (withdrawn standard without replacement) and the liquid chromatographic method in the Vinyl Acetate Safe Handling Guide [8,18]. However, these two methods require many reagents and sample processing for the analysis of the HQ content in the VAM; they are also time-consuming. In this contribution, a quicker and easier validated test method has been developed to determine the HQ content in the VAM by using the Ultra-Violet Visible (UV-Vis) spectrophotometer at absorbance of 293 nm and with methanol as a blank. Neither the color development nor the special reagent is required for this technique, and a VAM sample can be analyzed directly without further processing. After the development of the method, an extensive method validation was conducted to ensure the entire testing process.

2. Materials and Methods

2.1. Principle

The Beer–Lambert Law (also called Beer’s Law), which is commonly applied to the measurements of chemical analysis, describes a relationship between the attenuation of light through a substance and the properties of the substance. The main principle of the law states that concentration and absorbance are directly proportional to each other [19,20]. The expression of the law is

$$A = k \times l \times c \quad (1)$$

where A is the absorbance, k is the proportionality constant, l is the path length, and c is the concentration of the absorbing chemical species.

2.2. Apparatus

- (i) Spectrophotometer, absorbance at 293 nm; UV 1800 Spectrophotometer (Shimadzu Corporation, Kyoto, Japan).
- (ii) Volumetric Flask, 50 mL and 100 mL capacity.
- (iii) Pipets or Auto-pipets, 1 mL or 2 mL.
- (iv) Quartz cuvette; Material: Q, Path Length: 10 mm, Match Code: 6 (Starna Scientific Ltd., Ilford, UK).

2.3. Reagents

All the reagents and chemicals in this study were of high purity. HQ (Certified Reference Material: Catalogue no-N-12192-1G, Lot-10614100, Purity-99.4 ± 0.5%) was obtained from Chem Service Inc., West Chester, PA, USA. Methanol (Analytical Grade: Catalogue no-1.06009.2500, Lot-10983509 046, Purity-99.9%) was obtained from Merck, Germany. VAM (Batch-05000107470, Purity-99.98%) was collected from AIK MOH Paints & Chemicals Pte Ltd., Singapore.

2.4. Methods

2.4.1. Calibration

0.10 g of HQ was weighed into a 100-mL volumetric flask containing approximately 50 mL of Methanol. The mixture was stirred well until the solution was completed, then diluted to the mark with methanol. This was used as the stock solution of the HQ (1000 ppm). A series of standards were prepared by pipetting the 0.25 mL, 0.50 mL, 0.75 mL, 1.00 mL, and 1.25 mL portions of the HQ stock solution into respective 50 mL volumetric flasks. Each flask was diluted to the mark with methanol and mixed well. These standards contained approximately 5 ppm, 10 ppm, 15 ppm, 20 ppm, and 25 ppm of the HQ, respectively. The absorbance of each of these standards was determined at 293 nm using methanol as the blank. The calibration curve was constructed on rectangular coordinate graph paper or software by plotting the absorbance of the standards at 293 nm.

2.4.2. Solution for Validation

A precision and robustness solution (15 ppm) was prepared from the standard stock solution of the HQ by diluting 0.75 mL of the HQ stock solution in 50 mL volumetric flasks containing 30 mL methanol. The solution was mixed well and diluted to the mark with methanol. Following the same process, ten samples were prepared for each precision and robustness analysis. Robustness was analyzed by checking the temperature impact at 25 °C, 30 °C, and 35 °C. Solutions for accuracy (spike recovery) were prepared by using 0.10 mL of HQ stock solution with 30 mL VAM sample in a 50 mL volumetric flask. The solution was mixed well and diluted to the mark with VAM sample. Seven samples were prepared for the accuracy (spike recovery) analysis. Solutions for accuracy (bias) were prepared in such a way as to contain 80%, 100%, and 120% of the target concentration of 15 ppm (0.60 mL, 0.75 mL and 0.90 mL of HQ stock, respectively) in respect to 50 mL volumetric flasks. Seven samples were prepared for each concentration of accuracy (bias) solution.

2.4.3. Determination of HQ

No sample preparation was required or measured directly. The absorbance of the solution was determined at 293 nm using methanol as a blank. From the calibration curve, the HQ content was determined corresponding to the absorbance obtained. In this study, a Shimadzu UV-VIS 1800 double-beam spectrophotometer was used for analysis.

3. Result and Discussion

3.1. Determination of λ_{max} of HQ

To determine the maximum absorption (λ_{max}), 20 ppm standard solution of the HQ was prepared. Scanning of the HQ in a wavelength range from 200 nm to 400 nm showed

a λ_{max} at 293 nm (Figure 1). It is noted that there was no inference of methanol within this range.

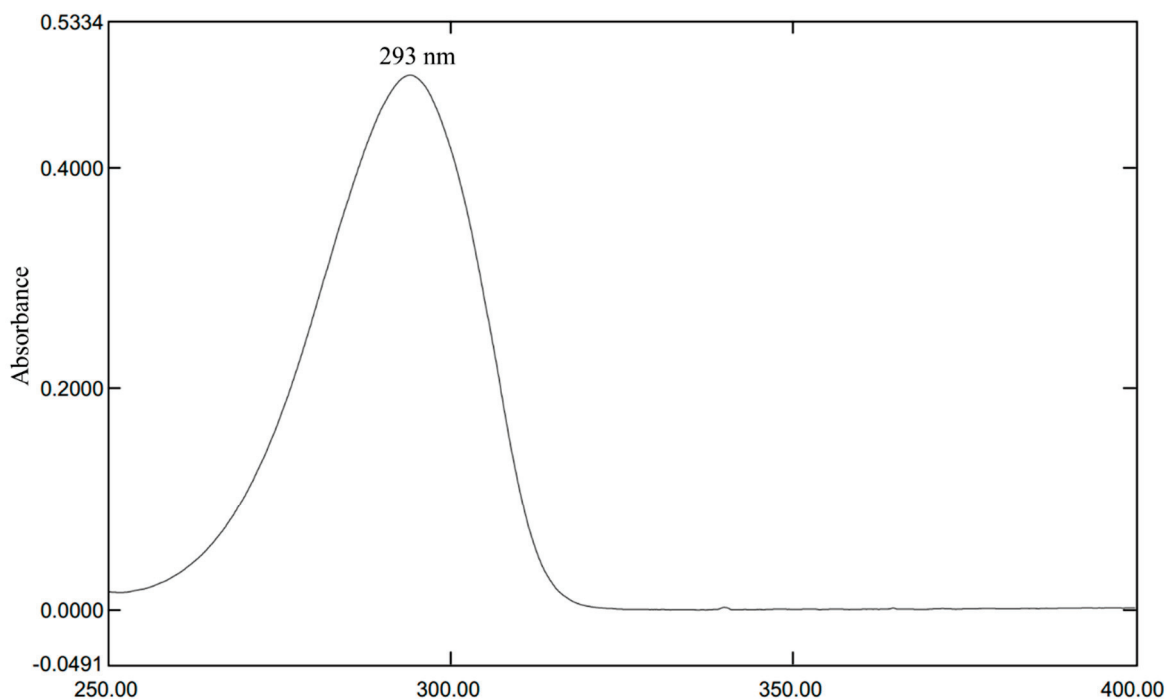


Figure 1. UV-Vis absorption spectra of the 20 ppm HQ standard solution within the range of 200~400 nm wavelength.

3.2. LOD (Limit of Detection)

LOD was analyzed with the lowest concentration of standard which can be detectable [21], as a blank sample has no response in the specified condition at 293 nm UV wavelength. A series of ten replicate measurements for the HQ content of 0.1 ppm and 0.2 ppm were analyzed, and a detectable response for 0.2 ppm was observed. The data of 0.2 ppm were used for the calculation of LOD as shown in Table 1. The LOD was found to be 0.14 ppm.

Table 1. Ten replicate measurements with respect to the theoretical concentration of the HQ at 0.2 ppm.

Absorbance of Sample	Experimental Concentration of HQ, ppm
0.005	0.142
0.006	0.167
0.005	0.106
0.005	0.116
0.005	0.131
0.005	0.115
0.005	0.118
0.005	0.125
0.005	0.123
0.005	0.120
Mean	0.126
Standard Deviation (SD)	0.017

LOD Calculation: Standard Deviation of LOD [22],

$$S' = SD \div \sqrt{n}; \quad (2)$$

For ten replicates, $n = 10$

$$\begin{aligned} \text{LOD} &= \text{LC}_{\text{Mean}} + 3S' \\ &= 0.126 + 3(0.017/\sqrt{10}) = 0.14 \text{ ppm} \end{aligned} \quad (3)$$

3.3. LOQ (Limit of Quantification)

LOQ data was analyzed with the lowest concentration of standard which can be quantifiable [21], as the blank sample had no response in the specified condition at 293 nm UV wavelength. A series of ten replicate measurements for the HQ content of 0.1 ppm, 0.2 ppm, and 0.3 ppm were analyzed, and a quantifiable response for 0.3 ppm was observed. The data of 0.3 ppm was used for the calculation of LOQ, which is presented in Table 2. The LOQ was found to be 0.36 ppm.

Table 2. Ten replicate measurements with respect to the theoretical concentration of 0.3 ppm HQ.

Absorbance of Sample	Experimental Concentration of HQ, ppm
0.006	0.264
0.007	0.316
0.007	0.293
0.007	0.293
0.006	0.271
0.006	0.267
0.008	0.325
0.007	0.318
0.007	0.289
0.007	0.290
Mean	0.293
Standard Deviation (SD)	0.022

LOQ Calculation: Standard Deviation of LOQ [22],

$$S' = \text{SD} \div \sqrt{n}; \quad (2)$$

For ten replicates, $n = 10$

$$\begin{aligned} \text{LOQ} &= \text{LC}_{\text{Mean}} + 10S' \\ &= 0.293 + 10(0.022/\sqrt{10}) = 0.36 \text{ ppm} \end{aligned} \quad (4)$$

3.4. Calibration Curve (Linearity and Range)

Under the optimum experimental conditions, a linear correlation was obtained between the UV-Vis absorbance and the HQ concentration within the range of 0.36~25 ppm. Concentrations of the standards against the respective absorbance were computed, and the linear regression curve was generated as shown in Figure 2. The regression coefficient $R^2 = 0.9999$ showed excellent linearity.

Regression line equation by the method of least squares $y = 0.0284x - 0.0005$

Regression coefficient, $R^2 = 0.9999$; slope = 0.0284 & y-intercept = 0.0005

3.5. Precision

3.5.1. Repeatability Data and Intermediate Precision Data

Analyst 1 was conducted repeatedly for determination of the HQ content by using ten samples (15 ppm standard solution). HQ content was measured from the corresponding absorbance for ten samples from the calibration curve. The percent of relative standard deviations (RSD) was calculated for analyst 1 using the following relationship:

$$\% \text{RSD} = \{(\text{Standard Deviation (SD)} \div \text{Mean (Avg.) Concentration}) \times 100\% \} \quad (5)$$

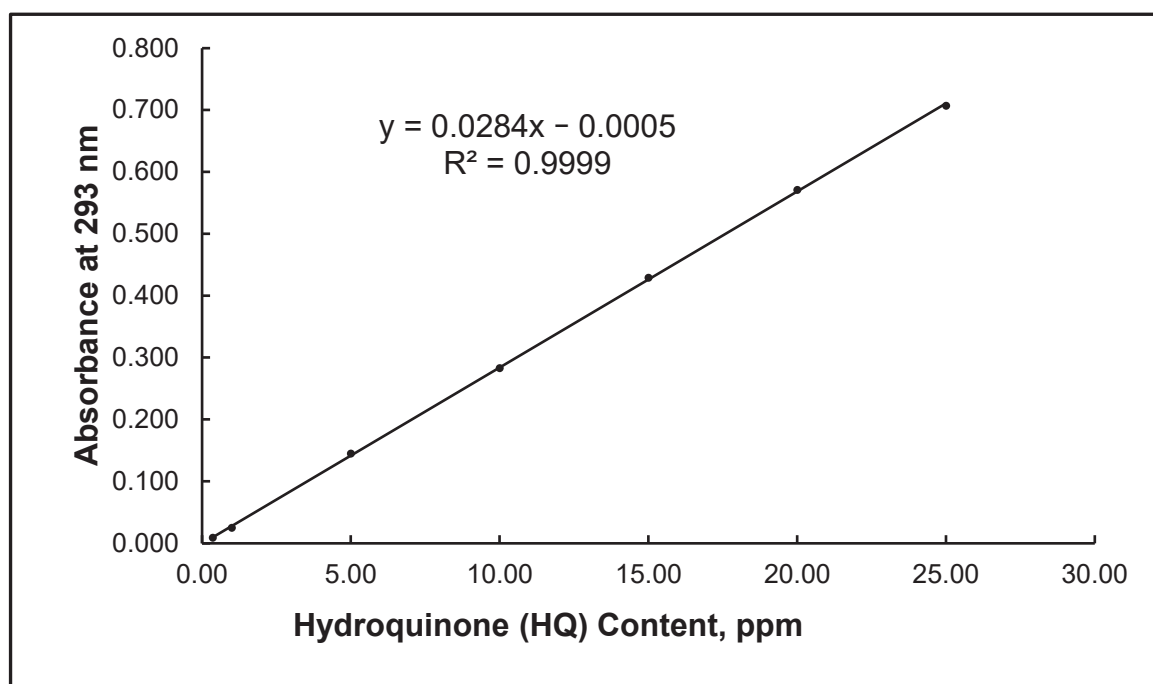


Figure 2. Linearity regression curve of UV-Vis absorbance and the HQ content within the range of 0.36–25 ppm.

The repeatability of the method was found to be 1.57%, whereas the acceptance criteria for the repeatability was 10% [23]. The percentage of RSD and is presented in Figure 3a. Separately, analyst 2 (second analyst) was measured with ten samples similarly to analyst 1. The HQ content was measured from the corresponding absorbance for each sample (15 ppm standard solution). The percentage of RSD was calculated for analyst 2 using the equation (5) and is shown in Figure 3b. The combination of the percentage RSD of analyst 1 and analyst 2 is called intermediate precision and is shown in Table 3. The intermediate precision of the method was found to be 1.36%, whereas the acceptance criteria for repeatability was 10% [24], ensuring that the repeatability and precision of this method are acceptable beyond a doubt.

Table 3. Intermediate precision data from 20 samples of 15 ppm HQ solution.

Content	Result
Average Content of HQ (ppm) of 20 Nos	15.14
Standard Deviation (SD) of 20 Nos	0.21
%RSD of 20 Nos measurements	1.36%

3.5.2. Inter-Laboratory Comparison (Reproducibility Test)

An inter-laboratory comparison was conducted for the reproducibility test with the following research laboratory. LAB A: Research & Development Center, Berger Paints Bangladesh Limited, Dhaka-Bangladesh; LAB B: Leather Research Institute, Bangladesh Council of Scientific and Industrial Research, Dhaka-Bangladesh; and LAB C: Wazed Miah Science Research Centre (WMSRC), Jahangirnagar University, Dhaka-Bangladesh. The data obtained from the three laboratories were shown in Table 4. The mean value of the HQ content was 15.37 ppm, which was very similar to our study, thus ensuring a satisfactory reproducibility for our method.

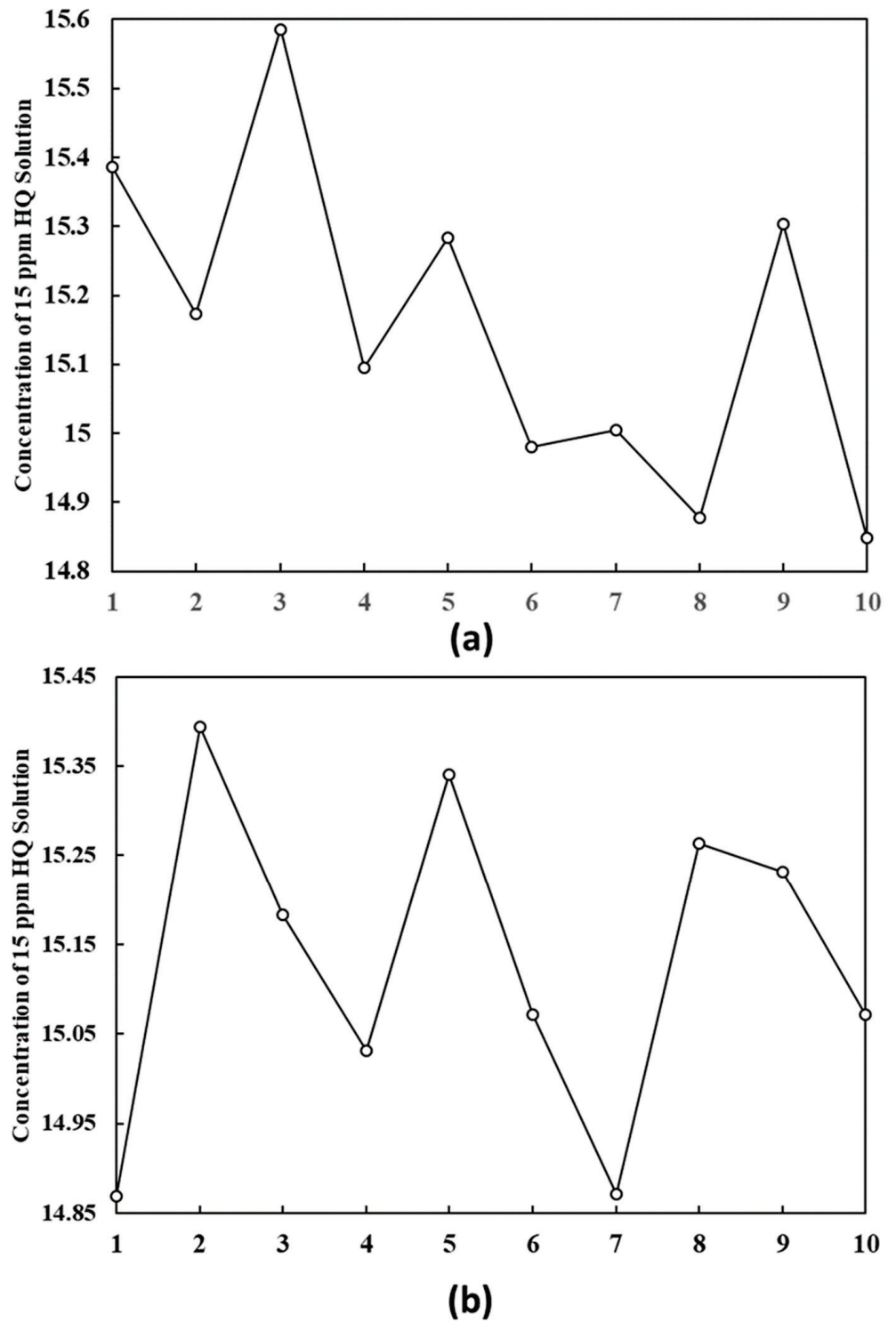


Figure 3. (a) Repeatability data for analyst 1 and (b) Intermediate precision data for analyst 2 for 15 ppm HQ content.

Table 4. Inter-laboratory comparison data of the reproducibility test.

Participant Laboratory	Obtained Result, ppm	Z Score = (Lab Result—Mean)/SD	Remarks
LAB A	15.44	0.167	Satisfactory
LAB B	15.75	0.906	Satisfactory
LAB C	14.92	−1.073	Satisfactory
Mean value	15.37	Acceptance Criteria: Z score ≤ 2.0	
Standard Deviation	0.4194		

3.6. Accuracy

3.6.1. Accuracy Data (Percentage of Spike Recovery)

Accuracy data were measured by adding known amounts of analyte to the sample solution (7 NOS solution samples prepared) and have been listed in Table 5. The concentration values were calculated from the corresponding absorbance for the sample and the spiked sample. The percentage of spike recovery was calculated using the following equation [24]:

$$\% \text{ Spike Recovery} = \left[\frac{(\text{Mean Value Spiked Sample} - \text{Mean Value Sample}) \div \text{Spiked Concentration}}{\text{Spiked Concentration}} \times 100 \right] \quad (6)$$

Table 5. Accuracy data (percentage of spike recovery in sample) with respect to spiked concentration 2 ppm.

Sample Details	Absorbance	Experimental Concentration	Mean Value	% Spiked Recovery *
Sample	0.438	15.382	15.372	Spike recovery of Hydroquinone = $(17.399 - 15.372)/2 = 101.35\%$
	0.438	15.381		
	0.437	15.366		
	0.437	15.371		
	0.437	15.363		
	0.438	15.372		
	0.437	15.370		
Spiked Sample	0.492	17.287	17.399	Spike recovery of Hydroquinone = $(17.399 - 15.372)/2 = 101.35\%$
	0.487	17.102		
	0.502	17.650		
	0.500	17.561		
	0.494	17.379		
	0.495	17.385		
	0.494	17.430		

* Acceptance criteria: the accuracy data (percentage of spike recovery) should be between −20.0% and 10.0% [25].

It is seen from Table 5 that the spike recovery of the HQ was found to be 101.35%, suggesting that this method is highly accurate for the determination of HQ content in VAM.

3.6.2. Bias

Bias samples were analyzed by adding known amounts of analyte to the blank solution at various concentrations, and three different concentrations of HQ (7 NOS samples for each concentration) were prepared. Concentration values were measured from the corresponding absorbance for the three concentrations [26]. The relative percentage of bias was calculated using the following formula and is listed in Table 6.

$$\% \text{ Bias} = \left[\frac{(\text{Mean for Experiment data} - \text{Theoretical Concentration}) \div \text{Theoretical Concentration}}{\text{Theoretical Concentration}} \times 100 \right] \quad (7)$$

Table 6. The results of percentage of bias.

Theoretical Concentration, ppm	Absorbance	Experimental Concentration, ppm	Mean Value	% Bias
12	0.353	12.400	12.086	0.72%
	0.347	12.182		
	0.341	11.957		
	0.338	11.860		
	0.341	11.966		
	0.345	12.091		
	0.346	12.147		
15	0.430	15.090	15.173	1.16%
	0.425	14.928		
	0.427	14.995		
	0.432	15.170		
	0.438	15.397		
	0.440	15.443		
18	0.506	17.798	17.959	−0.23%
	0.517	18.187		
	0.521	18.302		
	0.508	17.857		
	0.508	17.863		
	0.505	17.744		
	0.511	17.960		
			Mean	0.55%

The percentage of bias of the HQ was found to be 0.72%, 1.16%, and −0.23% for 12 ppm, 15 ppm, and 18 ppm, respectively. The relative (mean) bias was observed as 0.55%. The acceptance criteria of the accuracy data (percentage of spike recovery and bias) should be between −20.0% and 10.0% [27]. This confirms the accuracy of our method.

3.7. Robustness

Robustness data for this method were analyzed by maintaining a 5 °C temperature difference in samples of 15 ppm HQ standard solution. Single absorbance was measured for each of ten samples against 25 °C, 30 °C, and 35 °C temperature, respectively. The percentage of RSD was calculated for each temperature variance using the following relationship [28]:

$$\%RSD = [(\text{Standard Deviation (SD)} \div \text{Mean (Avg.) Concentration}) \times 100\%] \quad (8)$$

Figure 4 represents the robustness of the method, which was 0.83%, 0.73%, and 1.37% at 25 °C, 30 °C, and 35 °C temperature, respectively.

3.8. Measurement Uncertainty (MU)

MU is the expression of the statistical dispersion of the values attributed to a measured quantity. For the calculation of MU data, it is necessary to consider type A source (obtained from repeatability data) and type B source (obtained from certificate), which together represent the range of values that can reasonably be attributed to the quantity being measured. Type A source for MU data calculation was obtained from 10 replicate measurements. The repeatability of 10 (15 ppm HQ standard solution) test samples was determined by obtaining the type A uncertainty (Mean/√n, n = number of replicates), which has been represented in Figure 5. The expanded MU has been measured and listed in Table 7. It is observed from Figure 5 and Table 7 that the expanded MU of the method was found to be 15.15 ± 0.656 ppm and that the percentage of expanded uncertainty was 4.33% with a 95% confidence level. The following sources were considered in MU calculation: (standard uncertainty of type B obtained from certificate).

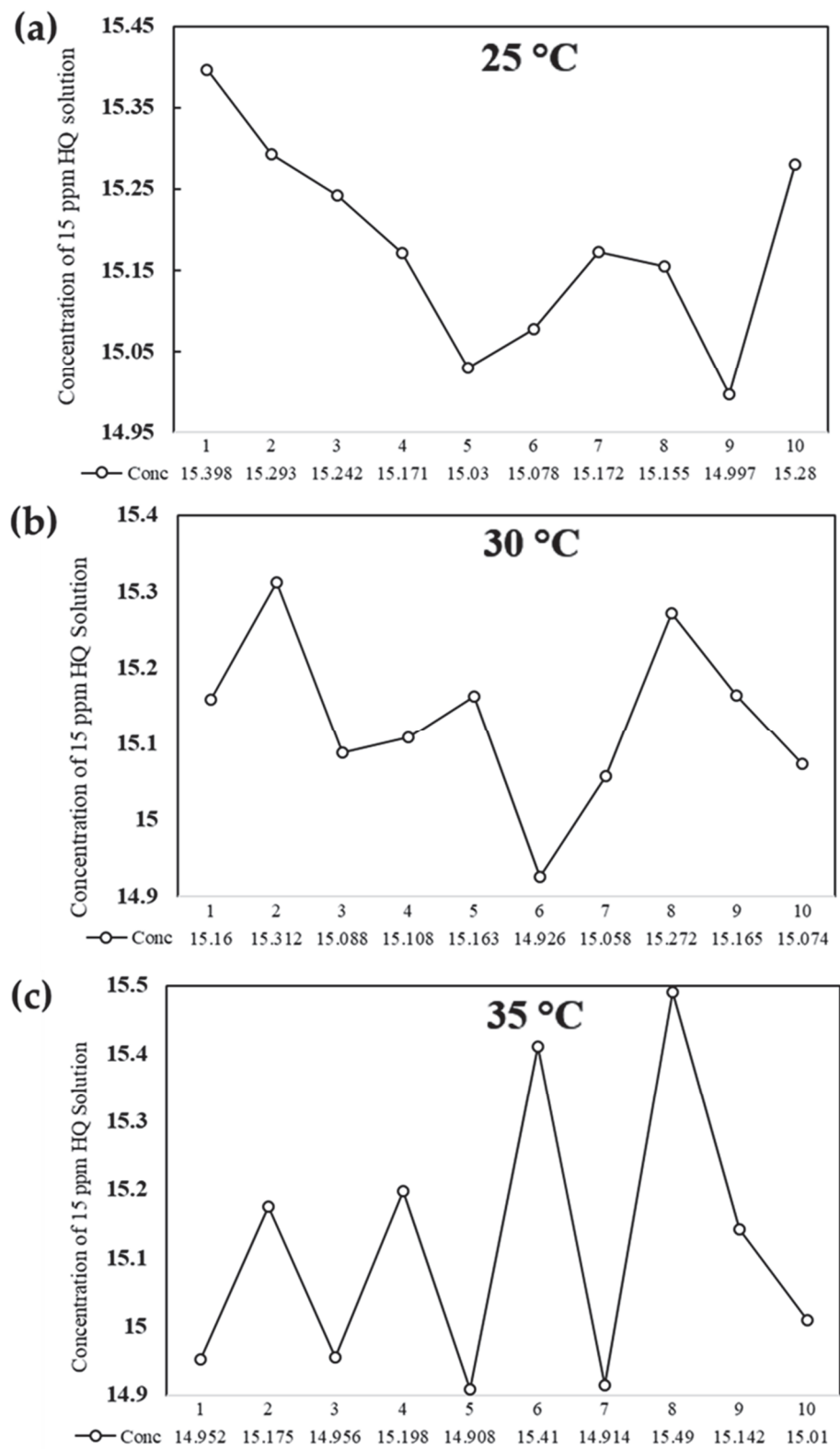


Figure 4. Robustness data at (a) 25 °C, (b) 30 °C, and (c) 35 °C temperature.

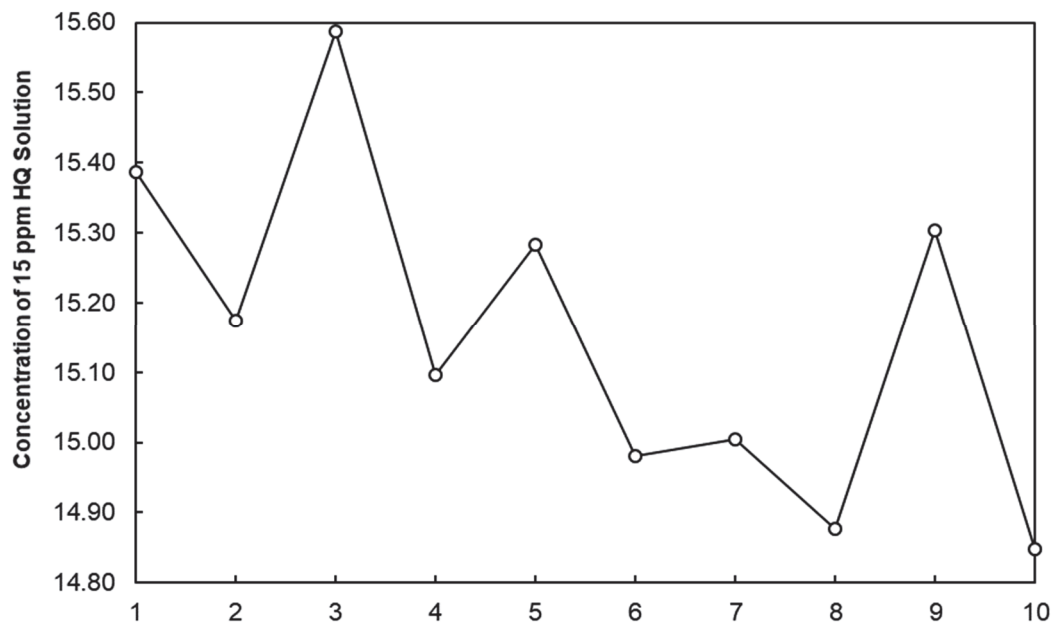


Figure 5. Measurement uncertainty data from type A source for ten standard HQ test samples.

Table 7. Expanded measurement uncertainty.

Sources of Uncertainty	Standard Uncertainty, δ	Divisor, x	Relative Uncertainty
Repeatability	0.0751	15.15	0.0050
Volumetric Flask	0.0300	50.00	0.0006
Balance	0.0010	0.0500	0.0200
Auto Pipette	0.0004	1.000	0.0004
Purity of CRM	0.2887	99.40	0.0029
Recovery %	−0.5931	100.00	−0.0059
Linearity curve	0.0001	1.00	0.0001
combined relative uncertainty			0.022
expanded uncertainty			0.656
% expanded uncertainty			4.33

Type B Source:

- Balance (uncertainty: 0.0010 g)
- Volumetric Flask (uncertainty: 0.0300 mL)
- Pipette (uncertainty: 0.0004 mL)
- Recovery (uncertainty: −0.5931)
- Certified reference material (uncertainty: 0.2887)
- Calibration curve linearity (uncertainty: $1 - 0.9999 = 0.0001$)

$$\text{Combined relative uncertainty} = \sqrt{\{(\delta_1/x_1)^2 + (\delta_2/x_2)^2 + \dots + (\delta_n/x_n)^2\}} \quad (9)$$

where δ = standard uncertainty of source, x = divisor, and n = number of source

$$\text{Expanded uncertainty} = \text{combined relative uncertainty} \times K \times \text{mean of type A data} \quad (10)$$

where coverage factor $K = 2$ for 95% confidence level

$$\text{Percentage of expanded uncertainty} = \text{expanded uncertainty} \times 100 / \text{Mean of type A data} \quad (11)$$

4. Conclusions

In this study, an alternative test method was developed for determining the HQ content in VAM by using a UV-Vis spectrophotometer. This method does not require

further sample processing or color development and excludes only methanol as reagent for standard HQ solution preparation. LOD, LOQ, linearity range, accuracy (spike recovery and bias), precision (repeatability, intermediate precision, and reproducibility), robustness under 5 °C temperature variation, and MU were found to be within the acceptable limit and required range. Therefore, this method has been extensively validated, and we believe that it will be very suitable for the accurate determination of the HQ content in VAM using a UV-Vis spectrophotometer. As the determination of the HQ content in VAM is a crucial factor for reducing unexpected polymerization for ensuring proper storage and transportation, industries and suppliers need an easy and quick method for measuring HQ content. Thus, this validated test method will be very useful to manufacturers and suppliers of VAM to ensure quality and give sustainability during storage and transportation.

Author Contributions: Writing—review & editing & Methodology, M.A.M.R.; Writing—original draft, Data curation, Formal analysis & Investigation, M.R.; Supervision & Funding acquisition, A.O.M.; Conceptualization & Project administration, A.S.M.M.; Formal analysis & Validation, M.M.H. (Md Masudul Haque); Resources & Validation, M.M.H. (Md Mobarak Hossain). All authors have read and agreed to the published version of the manuscript.

Funding: This work was financially supported by Berger Paints Bangladesh Limited, Dhaka, Bangladesh.

Institutional Review Board Statement: Not applicable.

Informed Consent Statement: Not applicable.

Data Availability Statement: Not applicable.

Acknowledgments: This experiment was conducted mainly at the laboratory of the Research and Development Center, Berger Paints Bangladesh Limited. The inter-laboratory testing comparison was conducted at the government-owned laboratory of the Leather Research Institute, Bangladesh Council of Scientific and Industrial Research and at the Wazed Miah Science Research Centre (WMSRC), Jahangirnagar University.

Conflicts of Interest: The authors declare no conflict of interest.

References

1. Young, M.E.; Murray, M.; Cordiner, P. *Stone Consolidants and Chemical Treatments in Scotland*; Historic Scotland: Edinburg, TX, USA, 1999.
2. Amann, M.; Minge, O. Biodegradability of Poly(vinyl acetate) and Related Polymers. *Adv. Polym. Sci.* **2012**, *245*, 137–172.
3. Coggins, C.R.E.; Jerome, A.M.; Lilly, P.D.; McKinney, W.J.; Oldham, M.J. A comprehensive toxicological evaluation of three adhesives using experimental cigarettes. *Inhal. Toxicol.* **2013**, *25*, 6–18. [CrossRef] [PubMed]
4. Van den Berg, G. Dutch-Type Cheeses. In *Encyclopedia of Dairy Sciences*; Roginski, H., Ed.; Elsevier: Oxford, UK, 2002; pp. 371–378.
5. Staudinger, H.; Frey, K.; Starck, W. Hochmolekulare Verbindungen, 9. Mitteilung: Über Poly-vinylacetat und Poly-vinylalkohol. *Ber. Dtsch. Chem. Ges.* **1927**, *60*, 1782–1792. [CrossRef]
6. Gustin, J.L.; Laganier, F. Understanding Vinyl Acetate Polymerization Accidents; Icheme Symposium 144. November 1998. Available online: <https://www.icheme.org/media/10280/xiv-paper-30.pdf> (accessed on 15 May 2022).
7. Shaffei, K.A.; Moustafa, A.B.; Hamed, A.I. The Emulsion Polymerization of Each of Vinyl Acetate and Butyl Acrylate Monomers Using bis (2-ethylhexyl) Maleate for Improving the Physicomechanical Properties of Paints and Adhesive Films. *Int. J. Polym. Sci.* **2009**, *2009*, 731971. [CrossRef]
8. Vinyl Acetate Council. Vinyl Acetate Safe Handling Guide. March 2019. Available online: www.lyondellbasell.com/globalassets/documents/chemicals-technical-literature/vam-safety-and-handling-guide-english-3293.pdf (accessed on 15 May 2022).
9. U.S. Pharmacopeia. USP monograph- Hydroquinone and Determination of Hydroquinone in Cream. January 2007. Available online: www.pharmacopeia.cn (accessed on 15 May 2022).
10. BP monograph- Tretinoin, Hydroquinone and Hydrocortisone Cream—BP 2018. Available online: <https://www.pharmacopeia.com> (accessed on 15 May 2022).
11. Elferjani, H.S.; Ahmida, N.H.S.; Ahmida, A. Determination of Hydroquinone in Some Pharmaceutical and Cosmetic Preparations by Spectrophotometric Method. *Int. J. Sci. Res.* **2017**, *6*, 2219.
12. Agorku, E.; Waansa-Ansah, E.; Voegborlo, R.; Amegbletor, P. Is it possible to optimize the protein production yield by the generation of homomultimeric fusion enzymes? *SpringerPlus* **2016**, *5*, 316.
13. Kaur, S.; Kaur, T.; Kaur, G.; Verma, S. Development and validation of a UV-spectrophotometric method for estimation of hydroquinone in bulk marketed cream and prepared NLC formulation. *Int. J. Appl. Pharm.* **2017**, *9*, 102–108. [CrossRef]

14. Siddique, S.; Parveen, Z.; Ali, Z.; Zaheer, M. Qualitative and quantitative estimation of hydroquinone in skin whitening cosmetics. *J. Cosmet. Dermatol. Sci. Appl.* **2012**, *2*, 224–228. [CrossRef]
15. Seokmin, J.; Yongseong, K. Analysis of hydroquinone and its ether derivatives by using micellar electrokinetic chromatography (MEKC). *Bull. Korean Chem. Soc.* **2005**, *26*, 819–822.
16. Desiderio, C.; Ossicini, L.; Fanali, S. Analysis of hydroquinone and some of its ethers by using capillary electrochromatography. *J. Chromatogr. A* **2000**, *887*, 489–496. [CrossRef]
17. Khoshneviszadeh, R.; Bazzaz, B.S.F.; Housaindokht, M.R.; EbrahimHabibi, A.; Rajabi, O. UV spectrophotometric determination and validation of hydroquinone in liposome. *Iran. J. Pharm. Res.* **2015**, *14*, 473–478. [PubMed]
18. Jogarami, R.; Jain, P.; Sharma, S. Validated UV spectrophotometric method development for simultaneous estimation of tazarotene and hydroquinone in gel preparation. *J. Pharm. Res.* **2012**, *5*, 2273–2275.
19. Metler Loledo Application Note: Hydroquinone in Cosmetics Using UV/VIS Spectroscopy. Available online: https://www.mt.com/kr/ko/home/supportive_content/ana_chem_applications/uvvis/M9113.html (accessed on 15 May 2022).
20. British Pharmacopoeia Monograph. Tretinoin, Hydroquinone and Hydrocortisone Cream–BP 2018. Available online: <https://www.pharmacopoeia.com/document/example-test-results?page=3&page-size=30&sort-by=issued-date> (accessed on 15 May 2022).
21. *ASTM D2193-06*; Standard Test Method for Hydroquinone in Vinyl Acetate. ASTM International: West Conshohocken, PA, USA, 2022.
22. Swineharf, F. The Beer-Lambert Law. *J. Chem. Educ.* **1962**, *39*, 333. [CrossRef]
23. Kocsis, L.; Herman, P.; Eke, A. The modified Beer–Lambert law revisited. *Phys. Med. Biol.* **2006**, *51*, N91. [CrossRef] [PubMed]
24. Barwick, V. (Ed.) *Planning and Reporting Method Validation Studies*; A Supplement to Eurachem Guide on the Fitness for Purpose of Analytical Methods; Eurachem: Gembloux, Belgium, 2019.
25. Magnusson, B.; Örnemark, U. (Eds.) *Eurachem Guide: The Fitness for Purpose of Analytical Methods—A Laboratory Guide to Method Validation and Related Topics*, 2nd ed.; Eurachem: Gembloux, Belgium, 2014; ISBN 978-91-87461-59-0.
26. *UNODC Guideline: Guidance for the Validation of Analytical Methodology and Calibration of Equipment used for Testing of Illicit Drugs in Seized Materials and Biological Specimens—ST/NAR/41*; Laboratory and Scientific Section United Nations Office on Drugs and Crime: Vienna, Austria, 2009; ISBN 978-92-1-148243-0.
27. ICH Guideline Validation of Analytical Procedures: Text and Methodology Q2 (R1). International Conference on Harmonization of Technical Requirements for Registration of Pharmaceuticals for Human Use, Version 4. 2005. Available online: [https://www.scirp.org/\(S\(i43dyn45teexjx455qlt3d2q\)\)/reference/ReferencesPapers.aspx?ReferenceID=1584467](https://www.scirp.org/(S(i43dyn45teexjx455qlt3d2q))/reference/ReferencesPapers.aspx?ReferenceID=1584467) (accessed on 15 May 2022).
28. 2002/657/EC—Council Directive 96/23/EC concerning the performance of analytical methods and the interpretation of results. *Off. J. Eur. Commun.* **2002**, *221*, 8–36.

MDPI
St. Alban-Anlage 66
4052 Basel
Switzerland
www.mdpi.com

Photochem Editorial Office
E-mail: photochem@mdpi.com
www.mdpi.com/journal/photochem



Disclaimer/Publisher's Note: The statements, opinions and data contained in all publications are solely those of the individual author(s) and contributor(s) and not of MDPI and/or the editor(s). MDPI and/or the editor(s) disclaim responsibility for any injury to people or property resulting from any ideas, methods, instructions or products referred to in the content.



Academic Open
Access Publishing

mdpi.com

ISBN 978-3-7258-1209-7